Identifying fast hadrons with silicon detectors

Martin van Beuzekom

The work described in this thesis is part of the research program of the 'Stichting voor Fundamenteel Onderzoek der Materie (FOM)', which is financially supported by the 'Nederlandse organisatie voor Wetenschappelijk Onderzoek (NWO)'.

RIJKSUNIVERSITEIT GRONINGEN

Identifying fast hadrons with silicon detectors

Proefschrift

ter verkrijging van het doctoraat in de
Wiskunde en Natuurwetenschappen
aan de Rijksuniversiteit Groningen
op gezag van de
Rector Magnificus, dr. F. Zwarts,
in het openbaar te verdedigen op
vrijdag 19 mei 2006
om 14:45 uur

door

Martinus Gerardus van Beuzekom

geboren op 25 juni 1967
te Amsterdam

Promotor:	Prof. dr. G. van der Steenhoven
Copromotor:	Dr. J.J.M. Steijger
Beoordelingscommissie:	Dr. E.H.M. Heijne
	Prof. dr. H. Löhner
	Prof. dr. H.W.E.M. Wilschut

ISBN: 90-367-2551-8

Ter herinnering aan mijn vader

Contents

Chapter 1

Introduction

Particle detectors have always been extremely important in high-energy and nuclear physics experiments because the human senses are not suited to detect the invisibly small particles involved in these experiments. There is a nice synergy between experimental research at the frontier of science and detector development since new or improved detection techniques enable on the one hand more sophisticated experiments, while on the other hand, the need for advanced experiments is a driving force for the development of ever better detectors.

The earliest particle detectors that were used around the turn of the 20th century were photographic emulsion and phosphorescent screens. The latter are the precursors of scintillation detectors. A gas filled radiation detector was invented by Geiger in 1908 and it enabled electronic registration of the counter signals. With the invention of the photomultiplier tube in 1930 also scintillation signals could be efficiently recorded in counting experiments.

The discovery of semiconductor detectors, more than sixty years ago, was another major breakthrough for particle physics experiments. It started in 1945 with the observation of electrical signals in silver-chloride crystals [1] when they were irradiated by α-particles, electrons or X-rays. This observation was followed by similar measurements on diamond and germanium crystals [2, 3]. However, due to the poor charge collection efficiency of the crystals, which was caused by trapping and recombination effects, it took almost ten years before semiconductor crystals were applied in counting applications. By that time, high purity silicon and germanium crystals could be produced, which showed a better energy resolution compared to the gaseous and scintillating type detectors. Hence, the main applications for these semiconductor detectors were nuclear, alpha, neutron and gamma spectroscopy [4]. The semiconductor detectors in those days consisted of small crystals with an area of typically less than 1 cm^2. It is interesting to note that already in 1962 silicon detectors were applied for identifying slow protons, deuterons and helium nuclei [5] by measuring their energy deposition. Another technique that was used for identifying particles with silicon is pulse shape discrimination [6], but this is only applicable for low energy particles.

The first monolithic segmented detectors appeared in 1961 [7], providing position information in addition to the energy deposition signal. In 1966 a Dutch group [8] constructed the first double-sided detectors by depositing a pattern of gold strips on

the front surface, and aluminium strips in the orthogonal direction on the back surface. This 'checkerboard' detector was the first true two-dimensional silicon detector. However, is was not until the early 1980s that highly segmented position sensitive detectors (microstrip detectors) became commonly used in high energy physics experiments. Especially, the research on short-lived particles for which high precision track information is required [9] pushed the development of silicon detectors. These detectors were used to detect minimum ionizing particles and were shown to be suited for reconstructing the position of the interaction and the decay vertex. The sensitive area of the silicon microstrip sensors used was 20×30 mm^2 and the strip pitch was 200 μm.

With the introduction in 1982 of Charge Coupled Devices (CCD) in high energy physics experiments [10], a new technique was introduced which provided high precision monolithic two-dimensional detectors. This development was followed in 1989 by hybrid pixel detectors in which the sensitive highly segmented detector is attached to a multichannel readout chip by means of bump bonding. These hybrid pixel detectors are essential in high count-rate applications where microstrip or CCD sensors cannot be used. More recent developments also include monolithic active pixel sensors in which the sensitive detection layer is integrated into the same wafer as the associated readout electronics. Although these monolithic pixel sensors became popular relatively recently, they were already proposed in 1988 [11].

Nowadays every major high energy physics experiment uses silicon strip and pixel (hybrid or CCD) detectors in the first detector layers surrounding the interaction point. In the largest experiments these detectors consist of several millions strips and almost a hundred million pixels [12]. Single silicon sensors are constructed from crystals with a surface area as large as 10×10 cm^2, and readout of the sensors is accomplished by custom developed integrated circuits. The main goal of semiconductor detectors in these experiments is to provide accurate spatial coordinates in order to reconstruct the tracks in the vertex region with a resolution of several micrometers. Even though the energy deposition of the particles in the detectors is almost always measured, the information is only used to improve the resolution of the particle tracks.

One branch of experimental particle physics where silicon detectors were hardly used until recently is the investigation of the quark-gluon structure of the nucleon [13, 14]. By scattering high-energy leptons off nuclear targets these experiments have, over the years, accurately determined the momentum distribution of the quarks and gluons in the nucleon, and more recently the contribution of the quark spins to the nucleon spin [15]. However, the sum of all experimentally determined contributions to the nucleon spin do not add up to precisely $\frac{1}{2}\hbar$ which is the spin of the nucleon as a whole. Therefore, an additional contribution to the nucleon spin is required, which could come from the gluon spin [16] or the orbital angular momentum of the quarks and gluons. In order to quantify the latter contribution, new experiments are needed which must be operated at new high luminosity facilities and which use high-density polarized targets.

The best way to gather information on the orbital angular momentum of the quarks in the nucleon is by studying the Deeply Virtual Compton Scattering (DVCS) process which requires measurements enabling the identification of exclusive processes. Unfortunately, the resolution of the main forward spectrometer in such deep inelastic scattering experiments is typically about 1%, which is not enough to ascertain the exclusivity of

these processes. The latter requirement can be accomplished by making use of an additional detector in the target area of the experiment. Such a so-called recoil detector must detect and identify the relatively low-energy hadrons that emerge from the final state of the interaction (and background processes). Given the many constraints in the target area of such an experiment, the use of silicon detectors to accomplish this task is likely to be the best option, especially if it can be proved to be possible to identify recoiling protons up to momenta of 1.3 GeV·c^{-1}. In this thesis it is investigated to what extent a recoil detector consisting of only a few layers of silicon detectors can be used to identify recoiling protons in DVCS measurements at future high-intensity DIS facilities. For this purpose several detector techniques are compared, Monte Carlo simulations are performed for the chosen solution and an experiment has been performed at CERN to investigate the particle identification capability of the proposed detector concept.

This thesis is organized as follows. In chapter 2 the key concepts of Deep Inelastic Scattering are introduced including a discussion on how the contribution of the orbital angular momentum of the quarks to the nucleon spin can be measured. In that light, the concept of generalized parton distributions is introduced which provides the mathematical framework to access the orbital angular momentum via the observation of exclusive processes. The second part of this chapter elaborates on the experimental environment that is needed to conduct such experiments. More specifically the possibility of employing a recoil detector in the target area is addressed. The influence of background events, which are numerous due to the use of a dense target, are also discussed in some detail.

Chapter 3 starts with an overview of the various detection techniques that can be used for particle identification, followed by a detailed discussion of energy deposition measurements in silicon. This chapter also gives the necessary background for dE/dx measurements with silicon detectors. The statistical analysis methods, which are used in dE/dx-based particle identification procedures and which are used in the remaining chapters, are also discussed.

The subject of chapter 4 is the Monte Carlo study which has been done to determine whether a recoil detector at a future fixed-target deep inelastic scattering experiment can be built from a stack of silicon detectors only. The simulations are used to explore the various detector configurations and to predict its particle identification capabilities. Realistic models for both the silicon sensors and the readout electronics are used in terms of charge collection efficiency and noise. The benefits and drawbacks of operating a silicon recoil detector in a magnetic field, which will be present in the (polarized) target region of such an experiment, are also discussed.

Chapter 5 describes an experiment that has been conducted at CERN in order to confirm the particle identification capabilities of a multi-layer silicon telescope in the momentum range of 0.8 to 1.3 GeV·c^{-1}. The chapter begins with a description of the experimental set-up and is followed by a discussion of the analysis of the data from a time-of-flight system consisting of four scintillators. This time-of-flight system provides independent particle identification which is needed to qualify the performance of the dE/dx silicon telescope. The second part of this chapter deals with the analysis of the data obtained with two different sets of four double-sided silicon detectors that were used in the experiment. These detectors provide the dE/dx information for the particle identification which is the last subject in this chapter.

Finally, chapter 6 gives the conclusions of the studies presented in this thesis. Furthermore, an outlook is given on those aspects of this study that need to be pursued in the future in order to come to a complete conceptual design of a full scale recoil detector that can be used in future experiments aimed at measuring the parton orbital angular momentum in the nucleon.

Chapter 2

Deep Inelastic Scattering

In this chapter several aspects of deep inelastic lepton scattering experiments are discussed. In the first part of this chapter the kinematics and formalism associated with the unpolarized and polarized structure functions are introduced, followed by a presentation of the rather new concept of Generalized Parton Distributions (GPD). In the second section of this chapter the experimental environment which is needed to investigate these Generalized Parton Distributions is described. One of the difficulties of such future experiments is the anticipated high background in the target region. This subject will be discussed in some detail in order to obtain information on the working environment of any future detector in the target area. The conclusions obtained in this chapter are summarized in the last section.

2.1 Kinematics and formalism

Deep inelastic lepton scattering (DIS) off protons (or neutrons) is the most common method to study the quark-gluon structure of nucleons and more generally the nature of the strong interaction, i.e. Quantum Chromo Dynamics (QCD). In the following the focus is on electron (or positron) scattering off nucleons. Neutrino scattering is not treated as the detector design discussed in the remainder of this thesis only applies to measurements using electromagnetic probes. Moreover, a detailed treatment of DIS is beyond the scope of this thesis. A more comprehensive discussion of DIS can be found in [17, 18].

In DIS, a lepton l with four-momentum k^μ scatters off a nucleon N with four-momentum p^μ as depicted in Fig. 2.1. The final state of this reaction consists of the scattered lepton l' and the hadronic fragmentation products X. The exchanged virtual vector boson[1] γ^* carries a four-momentum $q^\mu = k^\mu - k'^\mu$. The first component of q^μ is the energy transfer $\nu = E - E'$ with E being the energy of the incoming lepton l and E' the energy of the scattered lepton. To describe the kinematics of the process in the laboratory reference frame, the following variables are introduced.

- $Q^2 = -q^2$, the negative of the exchanged four-momentum squared.

[1] In DIS the exchanged boson is either a γ or Z^0 boson in neutral current interactions, or a $W^\pm$ boson in charged current interactions.

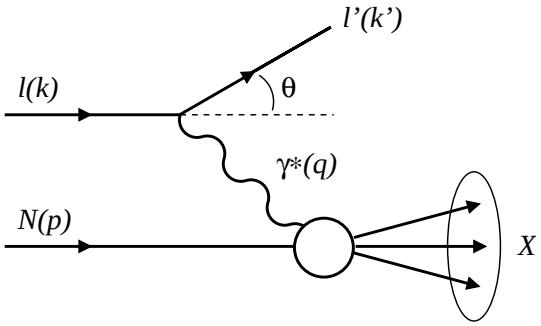

Figure 2.1: *Schematic diagram of deep inelastic lepton scattering. A lepton (l) scatters off a nucleon (N) by exchanging a virtual photon γ^*.*

- $x = \frac{Q^2}{2p\cdot q} = \frac{Q^2}{2M\nu}$, the Bjorken scaling variable, which describes the fraction of the nucleon momentum carried by the struck quark.
- $W^2 = (p+q)^2$, the invariant mass squared of the virtual-photon nucleon system.
- $y = \frac{p.q}{p.k} = \frac{\nu}{E}$, the fraction of the initial lepton energy transferred to the boson.

Neglecting the mass of the electron, the expressions for Q^2 and W^2 can be transformed into

$$Q^2 = 4EE' \sin^2(\theta/2), \tag{2.1}$$

and

$$W^2 = M^2 + 2M(E - E') - Q^2, \tag{2.2}$$

where M is the mass of the nucleon and θ is the scattering angle in the laboratory reference frame. Large Q^2 values correspond to small distance scales, which means that the constituents of the hadron (quarks) are probed rather than the hadron as a whole. At small distance scales, the quarks act as almost free particles and because the interactions are relatively weak at those scales, perturbative QCD techniques can be used. A typical lower Q^2 limit for which perturbative QCD is applicable, is 1 GeV^2. Similarly, to avoid contributions from the baryonic resonance region a minimum invariant mass W of 2 GeV is usually imposed on the data.

In DIS, three types of events are distinguished: (i) inclusive events, where only the scattered lepton is detected; (ii) semi-inclusive events, where apart from the lepton also a hadron is detected; and (iii) exclusive events, where all reaction products are identified.

2.1.1 Unpolarized DIS cross section and structure functions

The unpolarized DIS cross section can be expressed as

$$\frac{d^2\sigma}{dxdQ^2} = \frac{4\pi\alpha^2}{Q^4} \cdot \Big[F_1(x,Q^2)\cdot y^2 + \frac{F_2(x,Q^2)}{x} \cdot (1 - y - \frac{Mxy}{2E})\Big], \tag{2.3}$$

where α is the electromagnetic fine structure constant ($\approx 1/137$), and F_1 and F_2 are two dimensionless structure functions.

Because quarks have spin $\frac{1}{2}$, the two structure functions F_1 and F_2 are related by the Callan-Gross relation,

$$2xF_1(x,Q^2) = F_2(x,Q^2). \tag{2.4}$$

In the quark parton model (QPM), the structure functions are independent of Q^2 for point-like quarks, and are only functions of the scaling variable x. Experimental data [19] show sizeable deviations from the assumed Q^2-independence, which are known as scaling violations. The deviations are due to gluon radiation and the creation of quark-antiquark pairs. These deviations are only prominent at low values of x ($< 10^{-2}$), and are well described by pQCD calculations, in which the quark and gluon distributions are used as free parameters.

In this framework, the structure function F_1 can be interpreted as the parton density distribution which is given by the incoherent sum of the parton momentum distributions $q_f(x)$ for each quark flavor f,

$$F_1 = \frac{1}{2}\sum_f e_f^2 q_f(x). \tag{2.5}$$

Here e_f is the (fractional) electric charge of each of the quark flavors. Similarly, F_2 is the sum weighted by x, which is the momentum fraction carried by the parton,

$$F_2 = \sum_f x e_f^2 q_f(x). \tag{2.6}$$

For unpolarized beams and targets, the parton momentum distribution is defined as

$$q_f(x) = q_f^{\vec{\rightarrow}}(x) + q_f^{\vec{\leftarrow}}(x), \tag{2.7}$$

where $q_f^{\vec{\rightarrow}}(x)$ and $q_f^{\vec{\leftarrow}}(x)$ represent the probability to find a parton of type f with its spin aligned parallel or anti-parallel to the nucleon spin, respectively[2]. Most experimental results on structure functions are obtained by inclusive measurements.

2.1.2 Polarized structure functions

In analogy to the unpolarized structure functions F_1 and F_2, the polarized structure functions g_1 and g_2 contain information on the helicity dependent contribution to the DIS cross section. To access these structure functions, a polarized target and a polarized beam are needed. Results are obtained by measuring the difference in cross section for a parallel ($\vec{\Rightarrow}$) or anti-parallel ($\vec{\Leftarrow}$) orientation of the spins of the struck nucleon and the lepton. A measure for the helicity dependent contributions to the cross section is obtained by evaluating the asymmetry $(\sigma^{\vec{\Rightarrow}} - \sigma^{\vec{\Leftarrow}}) \,/\, (\sigma^{\vec{\Rightarrow}} + \sigma^{\vec{\Leftarrow}})$. This is called a double spin asymmetry[3].

[2]It is noted that the discussion here is limited to the longitudinal spin, i.e. parallel to the direction of motion of the proton. Therefore, the spins mentioned in the text actually correspond to helicities.

[3]Similarly, in case of a single spin asymmetry either the target or the beam is polarized, while the other is unpolarized.

The nucleon is a spin $\frac{1}{2}$ particle and has a total spin that is given by the sum of the angular momentum components of its constituents. The total longitudinal spin of the nucleon is given by

$$\frac{1}{2} = \frac{1}{2}\Delta\Sigma_q + \Delta G + L_z, \tag{2.8}$$

where $\Delta\Sigma_q$ is the contribution of the quark spins, ΔG represents the gluon polarization, and L_z is the (possible) contribution coming from the orbital angular momentum of the quarks and gluons. The longitudinal quark spin contribution $\Delta\Sigma_q$ is given by the sum over all flavors of the quark helicity distributions Δq_f,

$$\Delta\Sigma_q = \sum_f \int_0^1 \Delta q_f(x) dx, \tag{2.9}$$

with

$$\Delta q_f(x) = q_f^{\rightarrow}(x) - q_f^{\leftarrow}(x). \tag{2.10}$$

The distribution $\Delta q_f(x)$ can be interpreted as the probability to find a quark with flavor f in the same helicity state as the nucleon. For already some time it is known that the sum of the quark spins only accounts partially for the nucleon spin [20].

The inclusive scattering cross section gives access to g_1, which is the sum of helicity distributions for different quark flavors weighted by the electric charge e_f squared,

$$g_1 = \frac{1}{2}\sum_f e_f^2 \Delta q_f. \tag{2.11}$$

The helicity distributions for different quark flavors can be determined via semi-inclusive measurements where the observed (leading) hadron gives a tag of the flavor of the struck quark.

By determining the double spin asymmetry in semi-inclusive DIS for hadrons with a different quark composition, the helicity distributions of the individual quark flavors can be determined. The most recent results on this flavor decomposition of the nucleon spin are given in [15]. The integrated values of Δu and Δd obtained from these data over the measured x-range are 0.60 and -0.23, respectively, and the contribution of the sea quarks ($\Delta\overline{u}$, $\Delta\overline{d}$ and Δs) is found to be about zero. As the sea quarks do not seem to contribute to the total longitudinal spin of the nucleon, other carriers of angular momentum are needed to explain the nucleon spin.

The contribution of the gluon spin ΔG to the nucleon spin can be determined from events created in the photon-gluon fusion process. In this process, the virtual photon interacts with a gluon from the nucleon by splitting into a $q\overline{q}$ pair. The first measurements of this type are summarized in [21] showing that $\Delta G \approx 0.5$, with uncertainties of similar size.

The remaining contribution to the nucleon spin, if any, comes from the orbital angular momentum of the quarks and gluons (L_z). As the sum of the present best values for $\frac{1}{2}\Delta\Sigma_q$ and ΔG cannot make up for the spin of the nucleon, it is likely that quarks and gluons also carry a non-zero amount of orbital angular momentum. Although a direct measurement of L_z is not possible, is has been shown by Ji [22] that exclusive

Deeply Virtual Compton Scattering (DVCS) can be used to measure the total angular momentum J carried by the quarks and gluons. Because $J = S + L$ with $S = \frac{1}{2}\Delta\Sigma_q$, the value of L can be derived from such data. In the next subsection it will be explained how DVCS measurements can be used to obtain information on L_z.

Analogously to the polarized structure functions defined for the longitudinal quark spin distribution, also a transverse structure function, h_1, can be defined, which describes the distribution of quarks in a proton that is polarized in a direction perpendicular to the direction of motion. First measurements of the corresponding leading order structure function $h_1(x)$, known as the transversity distribution, start to emerge [23]. The interest in $h_1(x)$ stems from the fact that it probes the spin structure of the nucleon while 'switching off' the gluon contribution.

2.1.3 Generalized parton distributions

A new set of distributions known under the name of Generalized Parton Distributions (GPD) was recently reintroduced [24, 25]. These GPDs are an extension of the previously mentioned (forward) distribution functions in the sense that they also describe the correlations between the partons within the nucleons. The previously described structure functions appear as moments of the GPDs.

For each quark flavor a set of four distributions is defined; two unpolarized distributions $H(x', \xi, t)$ and $E(x', \xi, t)$, and two polarized distributions $\tilde{H}(x', \xi, t)$ and $\tilde{E}(x', \xi, t)$. The H and $\tilde{H}$ distributions conserve helicity and the E and $\tilde{E}$ distributions are associated with an helicity flip of the nucleon. The kinematic variables x' and ξ represent the longitudinal momentum fraction and t, one of the Mandelstam variables, is related to the transverse momentum transfer, $t = (p' - p)^2$. Note that $x' = x$ (Bjorken scaling variable) for quarks, and $x' = -x$ for antiquarks. The relation of the variables ξ and x' is given by $\xi = \frac{1}{2}(x'_{initial} - x'_{final})$ and hence $x'_{initial} = x' + \xi$ and $x'_{final} = x' - \xi$.

In the limit of $\xi \to 0$ and $t \to 0$, the (ordinary) quarks distributions $q(x)$ and $\Delta q(x)$ are obtained,

$$H(x', 0, 0) = q(x), \qquad \tilde{H}(x', 0, 0) = \Delta q(x). \tag{2.12}$$

As was mentioned before, the structure functions F_1 and F_2 are given by the first moments in x of the GPDs,

$$\int_{-1}^{1} dx H(x', \xi, t) = F_1(t), \qquad \int_{-1}^{1} dx E(x', \xi, t) = F_2(t). \tag{2.13}$$

According to Ji's sum rule, the total angular momentum of the quarks (J_q) is related to the second moment of generalized parton distributions $H()$ and $E()$ in the limit $t \to 0$:

$$\lim_{t\to 0} \frac{1}{2} \int_{-1}^{1} dx\, x[H(x', \xi, t) + E(x', \xi, t)] = J_q. \tag{2.14}$$

Using the information of the GPDs one can isolate the contribution of the quark orbital momentum to the total spin via $\frac{1}{2} = J_q + J_g = (\Delta\Sigma_q + L_q) + (\Delta G + L_g)$.

2.2 Measuring generalized parton distributions

Deeply Virtual Compton Scattering (DVCS) is one of the processes that give access to the GPDs[4]. Figure 2.2a shows a schematic diagram, known as the handbag diagram, of the DVCS process. In the Bjorken limit ($Q^2 \to \infty$ at fixed x), a virtual photon γ^* is absorbed by one of the quarks in the nucleon which almost immediately returns to the original state, thereby emitting a real photon. The nucleon is left intact. There is,

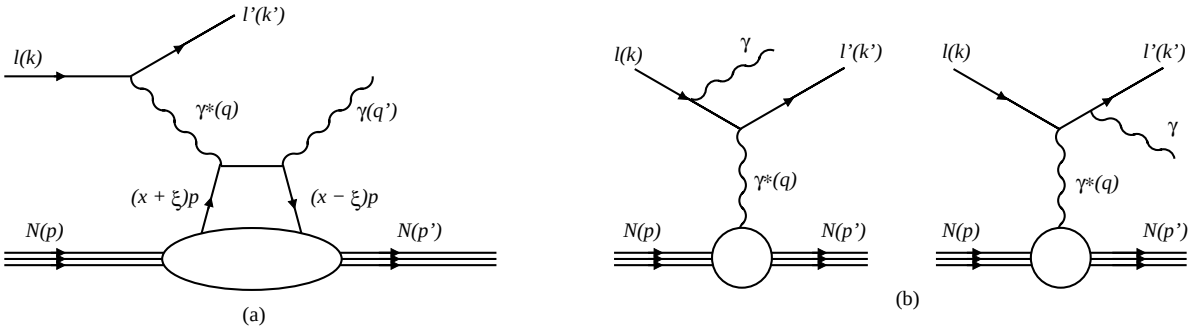

Figure 2.2: *(a) Deeply Virtual Compton Scattering, where a virtual photon interacts with one of the quarks in the nucleon. (b) Bethe-Heitler process, where the incoming or scattered lepton emits a photon in the electromagnetic field of the nucleon.*

however, another process which has the same particles in the final state as the DVCS process: the Bethe-Heitler process which is shown in Fig. 2.2b. Here, the incoming or scattered lepton emits a photon in the electromagnetic field of the nucleus. Hence, these photons carry no information on the structure of the nucleon. The Bethe-Heitler process is dominant with respect to the DVCS process for small values of t. Unfortunately this is exactly the domain where Eq. 2.14 needs to be evaluated. However, by virtue of the interference between the two processes, the weak amplitude of DVCS can still be accessed.

Another possible way to obtain information on GPDs is through hard exclusive meson production. This is, however, a theoretically less clean method to study GPDs as compared to DVCS, because the (in general not exactly known) wave function of the meson contributes as well.

The schematic diagram of the meson production process is shown in Fig. 2.3. The final state meson can either be an uncharged particle like a π^0, η^0 or ρ^0_L meson, or a charged particle like a π^+ or ρ^+ meson. For charged mesons the struck proton from the target converts into a neutron.

In most of the analyses aimed at studying GPDs, the asymmetry of the yield with respect to the azimuthal angle for different target or beam polarizations is determined. Figure 2.4 illustrates the azimuthal angle for the hard exclusive meson production process. The scattering plane is defined by the incoming and scattered lepton. The recoiling nucleon (N) and the newly produced meson (M) define the production plane. The angle between the production plane and the scattering plane defines the azimuthal angle.

[4]The process is deeply virtual in the kinematic regime where the virtuality Q^2 of the exchanged photon γ^* is large.

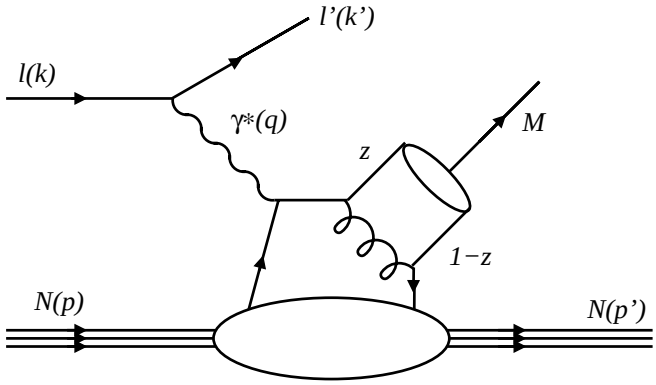

Figure 2.3: *Hard exclusive meson production. A vector meson is produced by scattering a virtual photon off one of the quarks in the target nucleon.*

From the yield measurements for different target polarizations, the yield asymmetry with respect to the azimuthal angle can be determined. The most common method

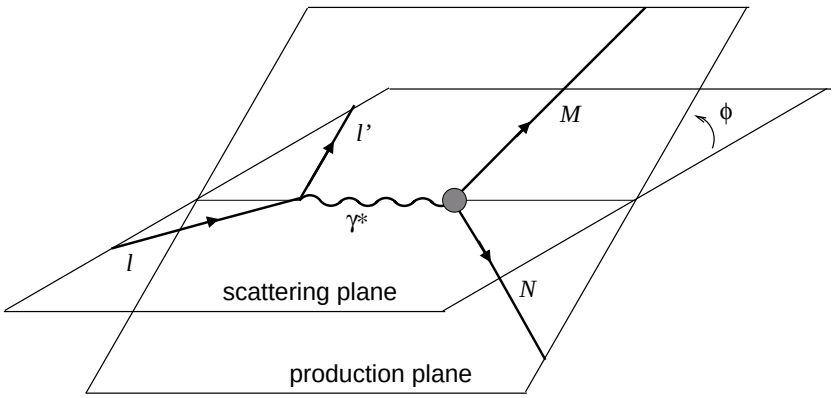

Figure 2.4: *The azimuthal angle ϕ is defined as the angle between the scattering plane, given by the incoming and scattered lepton, and the production plane defined by the meson M and the recoiling nucleon N (or γ^*).*

(and presently the only one used) to measure the single-spin asymmetries is via semi-inclusive measurements. In this case, the nucleon (N) goes undetected and identification of the exclusivity of the reaction is based on the determination of the missing mass of the reaction. This can be done by measuring the momentum and identifying the type of all particles reconstructed by the forward spectrometer typically used in such experiments. However, future experiments will use lepton beams with energies of the order of hundreds of GeV or more. As the missing mass resolution of the main spectrometer in these experiments is typically 1%, it will not be possible to guarantee exclusivity. By placing a so-called recoil detector in the target region, the relatively slowly recoiling target protons can be observed as well and the exclusivity of the reaction can be guaranteed. Exclusivity is a key factor in measuring GPDs via Deeply Virtual Compton Scattering or hard exclusive meson production, as a contamination of the signal by some non-exclusive processes will -at best- dilute the signal or -at worst- make the measurement impossible.

2.2.1 Kinematics of recoiling particles

A recoil detector, designed for the observation of exclusive processes such as the DVCS process discussed in the previous section, must detect and identify the relatively low energy protons which are emitted at large angles. Figure 2.5 shows the angle versus momentum correlation of the recoiling proton at an incident lepton energy of 27 GeV [13]. The top side of the plot shows the correlation for the DVCS events and for the events associated with the DVCS/Bethe-Heitler interference. The bottom left plot is for exclusive ρ^0 vector meson production and the bottom right plot shows the correlation for background processes where an intermediate Δ resonance is produced. From the

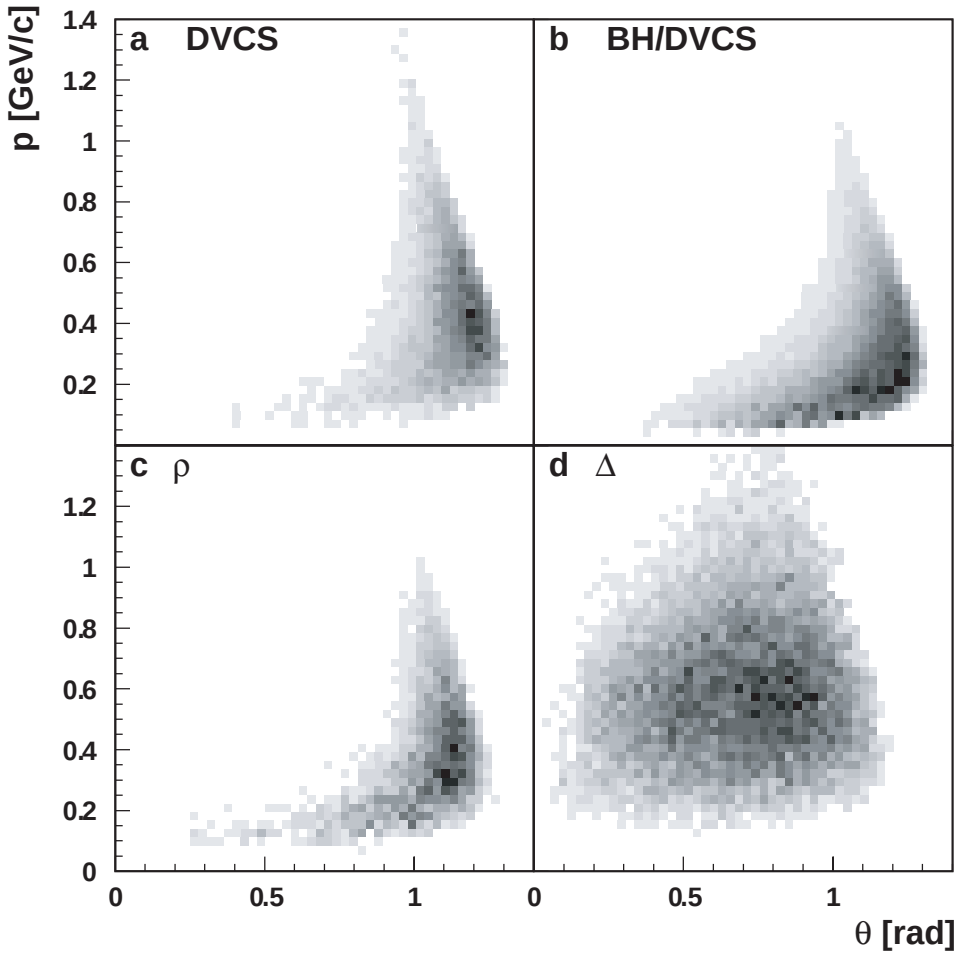

Figure 2.5: *Kinematics of recoil protons in exclusive processes. The momentum of recoil particles versus (scattering) angle is shown for (a)* DVCS*, (b)* DVCS*-Bethe-Heitler interference, (c) ρ^0 production and (d) the Δ resonance [13].*

figure it is clear that the momentum of the recoiling proton in the DVCS process never exceeds 1.3 GeV·c^{-1} and most of the events even stay in the range below 0.8 GeV·c^{-1}. For ρ^0 production the momentum limit of the recoil protons amounts to 1.1 GeV·c^{-1}. It is concluded that a proton recoil detector for future DIS experiments aimed at the study of GPDs (and hence the value of L_z) should be able to determine the proton recoil

momentum up to 1.3 GeV·c^{-1}. In case of the HERMES experiment [13] this is realized by combining the information from silicon detectors and scintillating fibers, making the experiment bulky. The silicon detectors in the HERMES recoil project are used for the identification of protons up to 0.65 GeV·c^{-1}. In future DIS facilities (to be discussed in the next section), the same momentum restriction applies, but the amount of space available in between the poles of the magnet is much less since the required field strength is much higher. This consideration has inspired the goal of the present thesis, i.e. to find a configuration of silicon detectors that makes it possible to identify protons up to 1.3 GeV·c^{-1}. It is noted that the basic features of Fig. 2.5 remain unchanged when the incident lepton energy is increased to several 100 GeV.

Another design requirement of a recoil detector that can be extracted from Fig. 2.5 is the angular acceptance. It is clear from Fig. 2.5 that an angular acceptance from about 0.2 to 1.3 rad is sufficient for observing all relevant processes.

2.2.2 Future DIS facilities

Many proposals for new experiments or extensions of existing experiments aimed at studying GPDs have been presented in recent years [26, 27, 28, 29, 30]. Of the newly proposed experiments, TESLA-N [27], which is a fixed target experiment at the proposed 500 GeV electron-positron collider TESLA [31], has been developed in most detail. It is clear that, given the high cost of such a machine, only one such a linear electron-positron collider will be built worldwide. Therefore, the research efforts for an e^+-e^- collider, are now combined in a global project known as the International Linear Collider (ILC) [32]. A common feature of all the proposals is the need for a high-energy polarized lepton beam which, together with a dense target, gives a luminosity in the order of 10^{35}cm^{-2}·s^{-1}. Very recently, a new initiative was taken to also explore the possibility for a fixed target experiment at the ILC [32, 33].

An overview of the kinematic domains accessible at the various experiments is given in Fig. 2.6. The label 'ELFE' maps out the kinematic domain for several possible future high luminosity experiments [29, 30]. Another possible future DIS experiment is the TESLA-N experiment. This experiment enables measurements down to very low values of the Bjorken scaling variable. Two of the kinematic constraints shown in Fig. 2.6 are the 1 GeV restriction on Q^2 and the minimum requirement on the invariant mass (W) of the hadronic final state in order to avoid contributions from the baryonic resonance region. These constraints apply to all experiments. On the low x side, the kinematic domain of the various experiments is limited by the energy of the lepton beam and the maximum value of y (the maximum energy transferred to the boson). The curves which limit the kinematic domains of the HERMES and COMPASS experiments are due to the limited integrated luminosity of these experiments and hence these boundaries are only indicative.

In the present and following subsections an overview of a possible future fixed target experiment is given. Examples and calculations are based on, but not limited to, the TESLA-N experiment. The idea is to sketch the operational environment of a recoil detector at such an experiment. TESLA-N is used as a starting point of the discussions since the features of any future fixed-target experiment will be close to that of the

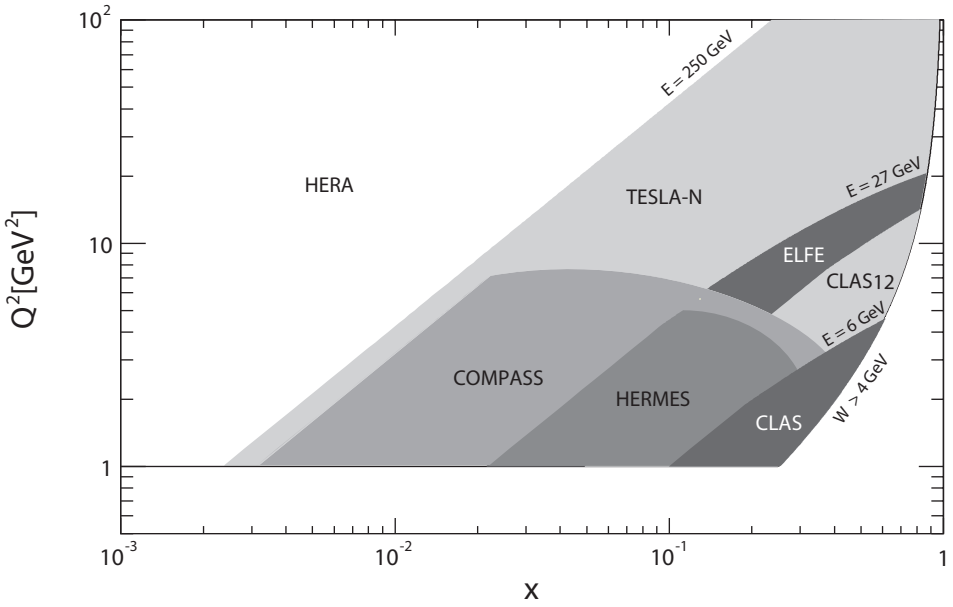

Figure 2.6: *Overview of the kinematic domain as covered by existing and possible future* DIS *experiments.*

TESLA-N project. The calculations presented in the section 2.2.4 give an estimate of the background count rates in the detectors and should be interpreted accordingly.

The TESLA beam

The proposed TESLA-N experiment is a relatively small fixed target experiment using only one arm of the proposed TESLA collider [31]. The electron beam for TESLA-N is accelerated in parallel with the main positron beam which eases the separation of the electron beam for TESLA-N and the main beam for the colliding experiment. Although the full beam energy is 250 GeV, it is envisaged to have extra ejection points along the accelerator giving access to beams with energies from 25 to 100 GeV.

The TESLA beam is composed of five bursts every second, and each burst consists of 2830 bunches with an inter-bunch timing of 337 ns as depicted in Fig. 2.7. The inter-bunch time of 337 ns corresponds to 440 buckets and only one of the buckets is filled for the main TESLA beam. To reduce the number of piled-up events in the TESLA-N experiment the beam current for TESLA-N should be spread over the largest possible number of beam buckets. Spreading the charge over all 440 buckets will give an almost continuous beam for TESLA-N with a lower intensity. The total number of filled buckets for the TESLA-N experiment is $6.2 \cdot 10^6$ per second. The lower intensity is compensated for by using a relatively large polarized fixed target, which is the subject of the next subsection. The average electron beam current is 20 nA which is only 0.04% of the (positron) current of the main beam; each bucket contains $2 \cdot 10^4$ electrons. The center of mass energy for a 250 GeV electron beam on a fixed target is $\sqrt{s} \approx \sqrt{2E_e m_p} = 21.7$ GeV.

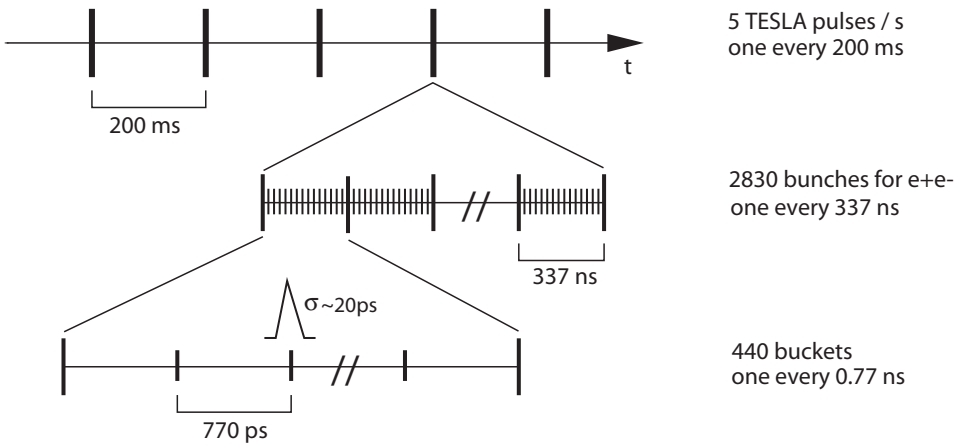

Figure 2.7: *Time structure of the beam as proposed for the* TESLA-N *experiment.*

The TESLA-N experiment

The TESLA-N detector [27], of which a schematic diagram is shown in Fig. 2.8, consists of three spectrometer stages similar to the two stage spectrometer of COMPASS [34]. Each stage covers a different region of x and uses a big C-type dipole magnet. The integrated field for the first magnet (SM1) is 1 Tm while the second and third stage (SM2/SM3) have fields of 5 Tm each. Because of the high particle rates and the quasi

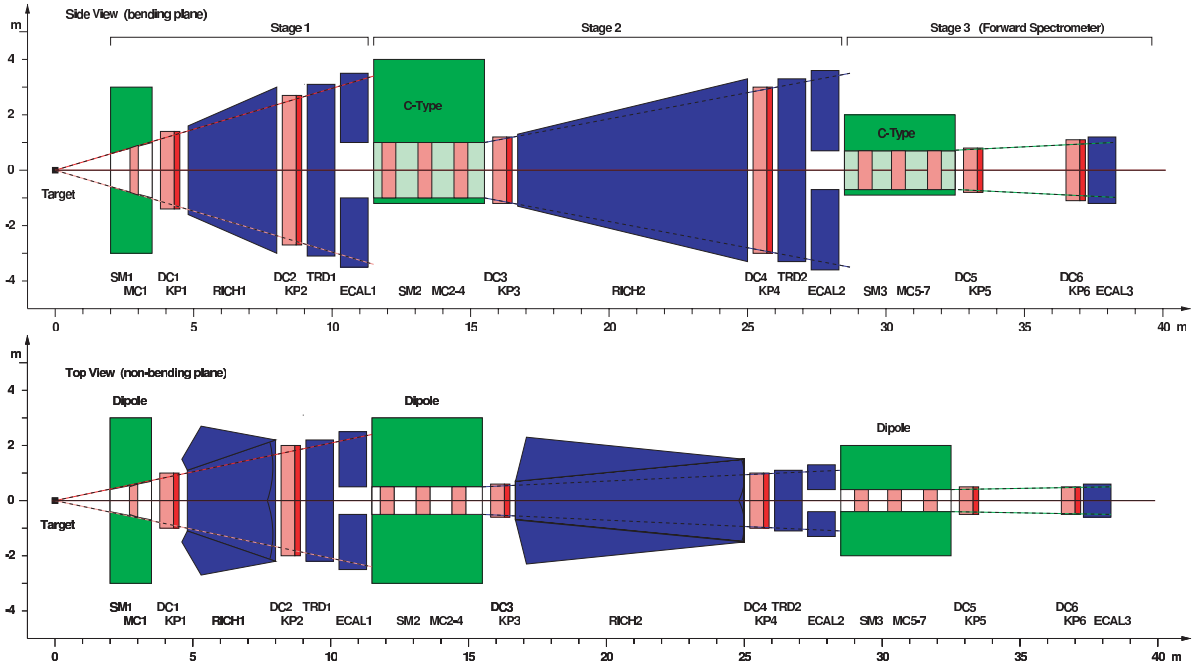

Figure 2.8: *Schematic side and top view of the proposed* TESLA-N *experiment [27]. The magnetic spectrometer consists of three sections covering complementary (x,Q^2) domains.*

continuous beam, the precise tracking detectors, consisting of drift chambers (DC) are complemented by fast, less accurate, tracking detectors (labeled KP) which could, for

instance, consist of planes of scintillating fibers. The first stage of the spectrometer will identify particles up to a momentum of 10 GeV·c^{-1}. It consists of a transition radiation detector (TRD1), an electromagnetic calorimeter (ECAL1) for electron identification, and a ring imaging Cherenkov (RICH1) for hadronic particle identification. The second stage uses the same detector types as the first stage, but will cover a higher momentum range and will have a smaller angular coverage. The third stage only consists of an electromagnetic calorimeter. As can be seen from Fig. 2.9, the three stages of the spectrometer together have a large coverage in the (Q^2, x)-plane which is essential for studying GPDs.

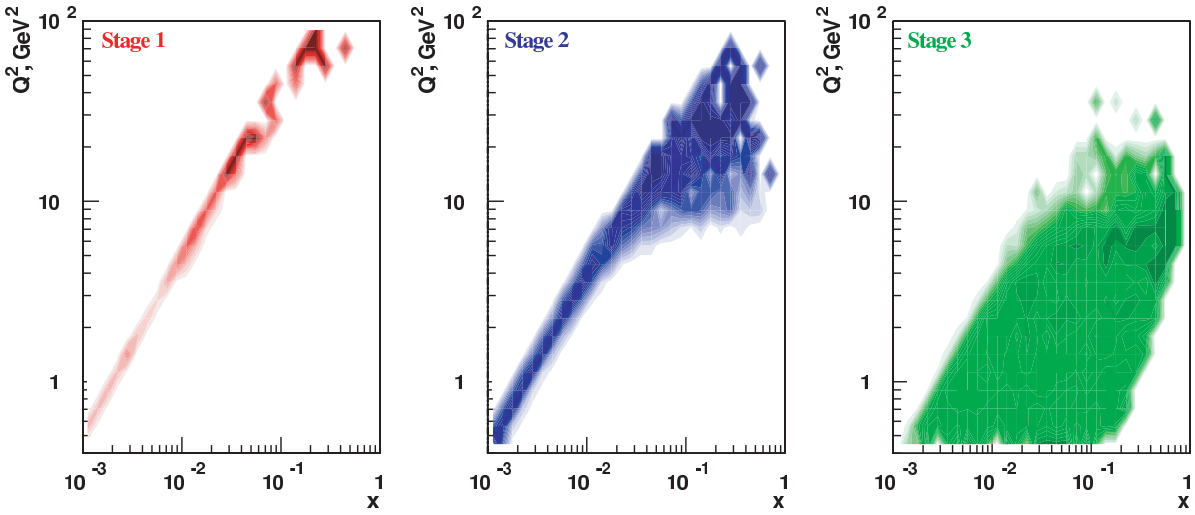

Figure 2.9: *Acceptance of the scattered lepton for the three spectrometer stages of the proposed* TESLA-N *detector [27], expressed as a (Q^2, x) correlation.*

2.2.3 Polarized target

Given the low intensity of the beam, a relatively thick polarized target is needed to obtain enough luminosity. The set-up of the E143 experiment [35] is chosen as a baseline for the target. This target consists of a cylinder of frozen ammonia (NH_3) or lithium-deuteride (^{6}LiD). These materials are selected because they have the lowest dilution by unpolarized nucleons in combination with a high radiation tolerance.

The thin-walled target cylinder has a length of 3 cm and a diameter of 2.5 cm. The target material is a suspension of small particles in a bath of liquid helium needed for cooling. An areal density in the order of 1.25 g·cm^{-2} can be obtained in this way [36]. The corresponding areal electron density for the ^{6}LiD target amounts to $3.77 \cdot 10^{23}$ e$^-$·cm^{-2}. Although the target length and composition yield an areal density of 1.25 g·cm^{-2}, the density used in the following calculations is only 1 g·cm^{-2}, because it matches with the value used in the proposal [27].

Polarization of the target is obtained via Dynamic Nuclear Polarization (DNP). At thermal equilibrium, the proton polarization is only 0.5%, but by irradiating the target with microwaves of the appropriate frequency, the polarization of the free electrons,

which is about 99%, can be transferred to the protons. The orientation of the polarization depends on the microwave frequency being higher or lower than the Larmor frequency. In order to preserve the polarization, the target needs to be operated at a temperature of about 1 K which is achieved with a ^{4}He evaporator cryostat.

A high magnetic field of about 5 T, which can be generated by a superconducting Helmholtz type magnet, is needed to maintain the target polarization in a given direction. The Larmor frequency needed for this field strength is about 140 GHz. The target is designed for maintaining longitudinal polarization, i.e. orienting the spin direction of the target protons parallel to the beam direction, but it must be compatible with transverse polarization, i.e. orthogonal to the beam direction, as well. It was calculated that the heat load on the target due to energy deposition and photon absorption from bremsstrahlung and synchrotron radiation is well below the available cooling power of 1 Watt at 1 K [36].

Luminosity

With a charge of $2 \cdot 10^4$ electrons in each bunch (bucket), $6.2 \cdot 10^6$ bunches per second, and an areal density of the target of 1 g·cm^{-2} a luminosity $\mathcal{L} = 7.5 \cdot 10^{34}$ cm^{-2}·s^{-1} is obtained. If a conservative total uptime of machine and experiment of 0.25 is assumed, an integrated luminosity of 600 fb^{-1} per year can be achieved, which is sufficient for the proposed physics program [27].

2.2.4 Background

In this subsection, the background processes in the target region are evaluated, which is important because the recoil detector, being close to the dense target, will see a sizeable fraction of the large number of background events. When discussing the detection and identification of the recoiling protons, it must be verified that these protons can be detected and identified amongst the high number of background events.

The most important processes contributing to the background events are Møller scattering and bremsstrahlung. Another source of background events is synchrotron radiation due to the passing of the beam through the magnetic field of the target. In this section the background rates for a detector in the target area will be calculated. In addition, estimates for count rates and radiation levels will be given. Note that the count rate numbers are indicative only because the background consists of a significant number of low-energy particles. Hence, the number of particles seen by the recoil detector depends on the exact design of the target. Part of the low-energy background can be removed by introducing a thin layer of aluminium in between the target and the recoil detector at the cost of an increase of the lower detection threshold for recoiling particles. Some electrically conductive material (like beryllium or aluminium) should anyhow be present around the target in order to shield against the RF wakefields created by the passing of the beam.

Møller electrons

Elastic $e^-e^- \rightarrow e^-e^-$ scattering, known under the name of Møller scattering, is characterized by the symmetric scattering angle of the two electrons in the laboratory system. For a 250 GeV beam, this scattering angle is $\theta_0 = \arctan\sqrt{2m_e/(E+m_e)} = 2.02$ mrad in the laboratory system, which corresponds to a $\pi/2$ scattering angle in the Center-of-Mass (CM) system. In this expression m_e and E are the mass of the electron and the energy of the beam, respectively. The Møller cross section in the CM system can be expressed as [37]

$$\Big(\frac{d\sigma}{d\Omega}\Big)_{CM} = \frac{r_e^2 m_e^2}{s}\Big[\frac{3+\cos^2\theta_{CM}}{\sin^4\theta_{CM}}\Big], \tag{2.15}$$

where $s = 2m_e(E+m_e)$ is the square of the center of mass energy and r_e is the classical electron radius. The scattering angles in the laboratory system ($\theta_{LAB,1}$, $\theta_{LAB,2}$) and the angle in the CM system (θ_{CM}) are related by

$$\tan\theta_{LAB,1} = \gamma_{CM}\tan\frac{\theta_{CM}}{2} \qquad \text{and} \qquad \tan\theta_{LAB,2} = \frac{\gamma_{CM}}{\tan\frac{\theta_{CM}}{2}}, \tag{2.16}$$

where $\gamma_{CM} = (E+m_e)/\sqrt{s}$ is the Lorentz factor of the CM system. Transforming the Møller cross section to the laboratory system and integrating over the azimuthal angle yields

$$\Big(\frac{d\sigma}{d\theta}\Big)_{LAB} = 2\pi\sin\theta_{CM}\cdot\frac{2\gamma_{CM}(1+\tan^2\theta_{LAB})}{1+\gamma_{CM}\tan^2\theta_{LAB}}\cdot\Big(\frac{d\sigma}{d\Omega}\Big)_{CM}. \tag{2.17}$$

Here, the CM scattering angle θ_{CM} is obtained from Eq. 2.16 as

$$\theta_{CM} = 2\arctan(\frac{\tan\theta_{LAB}}{\gamma_{CM}}). \tag{2.18}$$

The first factor in the laboratory cross section of Eq. 2.17 comes from the conversion of the solid angle to scattering angle θ and the second factor is the derivative of the CM scattering angle with respect to the laboratory scattering angle ($d\theta_{CM}/d\theta_{LAB}$).

A plot of the Møller cross section as a function of the laboratory scattering angle is shown in Fig. 2.10. Virtually all Møller type interactions will produce an electron in the very forward direction with an energy close to that of the initial beam, in addition to the recoiling electron emitted at a large angle. These forward scattered electrons are 'beam-like' and can therefore participate in a second interaction. The number of recoil electrons is thus larger than in case of only a single interaction per primary (beam) electron. Hence, to calculate the number of Møller electrons, the thin target approach is appropriate even though the target is thick with respect to the mean free path for Møller interactions.

The total cross section for the production of Møller electrons for the angular range from 0.2 to 1.3 rad is about 3.2 barn. This large cross section in combination with the high electron density of the target (about $3\cdot10^{23}$ $e^-\cdot cm^{-2}$) results in a large number of electrons emitted in the direction of the recoil detector.

Fortunately, most of the recoiling electrons have a low kinetic energy, and many are stopped when traversing the target. A plot of the kinetic energy of the recoil electrons

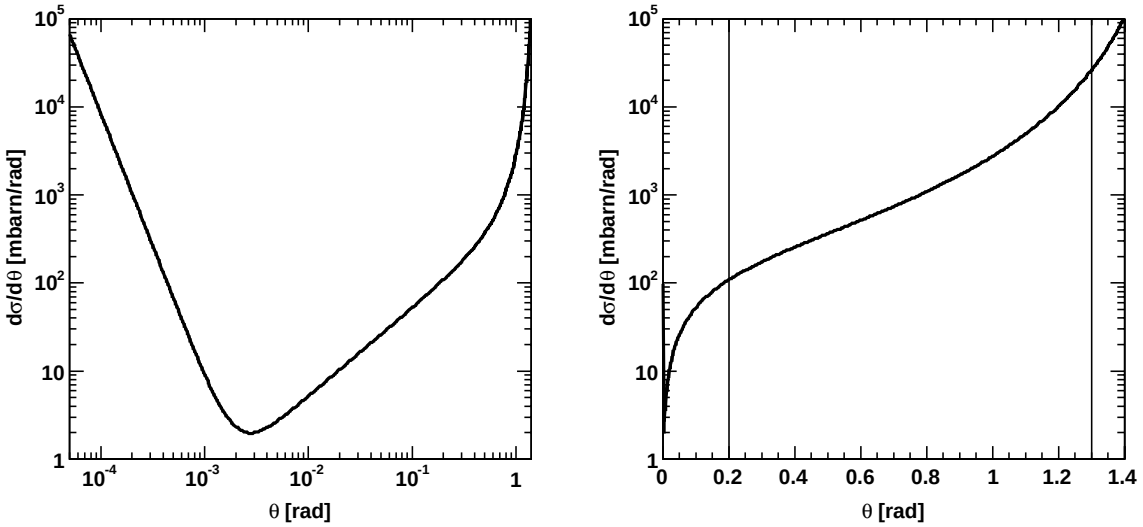

Figure 2.10: *Møller cross section versus scattering angle for a 250 GeV beam on a logarithmic (left) and linear scale (right). The angular coverage required for the proposed recoil detector is indicated by vertical lines.*

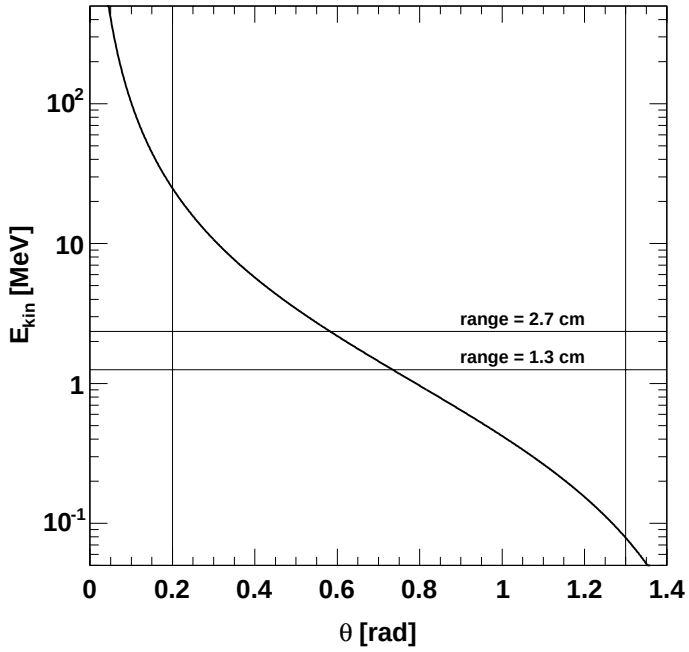

Figure 2.11: *Kinetic energy of recoiling electrons from the Møller process as a function of scattering angle for a 250 GeV beam. The angular coverage of the recoil detector is indicated by vertical lines. The horizontal lines indicate the stopping energies of electrons corresponding to a path length of 1.3 and 2.7 cm, respectively.*

as a function of scattering angle is shown in Fig. 2.11. Given the proposed radius of the target cell of 1.25 cm, the path length of the recoiling electrons through the target ranges

from 1.3 to 2.7 cm for electrons emitted at the beginning of the target. The horizontal lines indicate the stopping energies corresponding to these path lengths. Møller electrons which are produced close to the end of the target will travel only over a short distance in the target. Hence, even electrons with a very low-energy will not be stopped in the target. Since the number of low energy electrons is very large, a substantial fraction of the background is due to these Møller electrons originating from the end of the target.

Using a Monte Carlo simulation it has been determined that without a magnetic field about 1600 electrons per bunch can reach the recoil detector. As the TESLA-N experiment will be operated with a polarized target, the strong (5 T) holding field will change the trajectory of the recoiling electrons and these electrons will travel a longer distance through the target. This will stop an additional fraction of the recoiling electrons. The number of electrons that can still reach the recoil detector depends on the orientation of the magnetic field. As the low-energy electrons will coil around the magnetic field lines with a small radius, these electrons will travel in the direction of the field.

In case of a longitudinal field, the low-energy electrons will therefore travel in the beam direction and most of them will go undetected because of the minimum opening angle of a recoil detector (0.2 rad). By means of a Monte Carlo simulation it has been determined that for the longitudinal field configuration less than 3.5% of the Møller electrons (compared to the field-less configuration) will give a signal in the detector. The longitudinal magnetic field very effectively sweeps away the low-energy Møller electrons and only 58 electrons per bunch will end up in the recoil detector.

For the transverse field, however, the electrons will not be swept away, and will travel in the direction of the recoil detector. The reduction of Møller electrons is only a factor of 2.3 compared to the field-less case; about 700 electrons per bunch will penetrate the recoil detector[5].

The Møller electrons will be the dominant source of background for the recoil detector except in case of a longitudinal magnetic field. Other sources are reviewed briefly in the following paragraphs.

Other sources of background

Apart from Møller scattering, the beam electrons will also elastically scatter off the target nucleons. However, the cross section for elastic $e^- p \rightarrow e^- p$ scattering is insignificant as compared to that of Møller scattering and hence elastic $e^- p$ scattering will hardly contribute to the background.

Several other processes, such as bremsstrahlung and synchrotron radiation, will create energetic photons which can either reach the recoil detector directly or generate particles via subsequent interactions like electron-positron pair production, Compton- and Rayleigh scattering.

[5] About 30% of these remaining Møller electrons will end up in a small surface area, because of the 'focussing' due to the transverse field.

Bremsstrahlung

The main source of photons created by the interaction of the electron beam with the target material is bremsstrahlung, i.e. the emission of EM radiation in the electric field of the nucleus. The cross section for bremsstrahlung depends on the screening parameter [38]

$$\zeta = \frac{100 m_e c^2 h\nu}{E E' Z^{1/3}}, \tag{2.19}$$

where E and E' are the total energy of the incident and scattered electron, respectively, and $h\nu$ is the energy of the emitted photon. The screening parameter accounts for the screening of the EM field of the nucleus by the atomic electrons. For almost the complete photon spectrum, the value of ζ is close to zero except for the highest photon energies, i.e. $\zeta \approx 0$ corresponds to complete screening. Hence, it is assumed that the nucleus is completely screened by the atomic electrons. The bremsstrahlung cross section for complete screening of the nucleus by the atomic electrons, is given by

$$\frac{d\sigma}{dh\nu} = \frac{4Z^2 r_e^2 \alpha}{h\nu}\Big[\Big(1+\epsilon^2-\frac{2\epsilon}{3}\Big)\Big(\ln(183Z^{-1/3}) - f(Z)\Big) + \frac{\epsilon}{9}\Big]. \tag{2.20}$$

Here, ϵ is the ratio E'/E and $f(Z)$ is a correction factor which reads [38]

$$f(Z) \approx a^2[(1+a^2)^{-1} + 0.20206 - 0.00369a^3 + 0.0083a^4 - 0.002a^6], \tag{2.21}$$

where $a = Z/137$. For the bremsstrahlung calculations in the next section, Eq. 2.20 is used.

Synchrotron radiation

When the electron beam passes through the magnetic field of the target, the electrons will be bent from the straight line path. The radius of curvature of the electron path (in meters) in a field of strength B (in Tesla) is given by

$$R = \frac{p}{0.3B} \approx \frac{E}{0.3B}, \tag{2.22}$$

with p in GeV·c^{-1} and E in GeV. Here, p is the momentum of the electron which is almost equal in magnitude to the energy E for the TESLA-N beam. Due to the acceleration of an electron in the magnetic field, synchrotron radiation will emerge. The mean number of photons emitted by a particle traveling along a circular path of length l is given by [39]

$$\frac{d\overline{N}}{dh\nu} = \frac{\sqrt{3}}{2\pi}\alpha\frac{l\gamma}{R}\frac{1}{\omega_c}\int_{\omega/\omega_c}^{\infty} K_{5/3}(\eta)d\eta, \tag{2.23}$$

where $K_{5/3}$ is a fractional order modified Bessel function, and ω_c is the critical energy

$$\omega_c = \frac{3\hbar c\gamma^3}{2R}. \tag{2.24}$$

Half of the radiated power is carried by photons with an energy larger than ω_c. For a 250 GeV beam, synchrotron radiation will only be emitted at very small angles with

respect to the beam axis and the synchrotron photons can thus not reach the recoil detector directly.

Figure 2.12 shows the photon yield of the bremsstrahlung and the synchrotron processes per second of the TESLA-N beam. Most of the low-energy photons are due to synchrotron radiation, while the very high-energy photons are almost solely due to bremsstrahlung. As was explained before, the photons, both from the bremsstrahlung

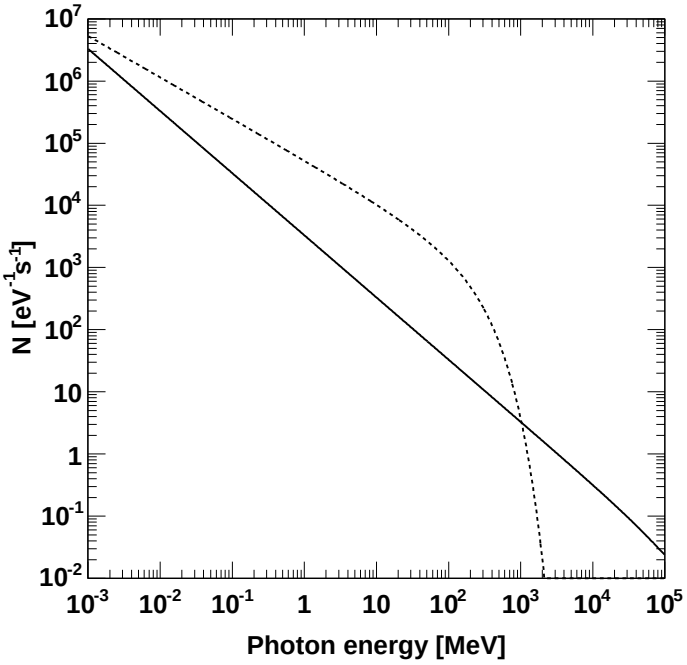

Figure 2.12: *Number of photons per second from bremsstrahlung produced in a 1 g·cm^{-2} target (solid line), and synchrotron radiation in the 5 T target field (dashed line). The beam energy is 250 GeV and the beam current is 20 nA.*

and the synchrotron radiation process, are emitted in the very forward direction and are therefore not seen directly by the recoil detector. However, due to interactions of the photons in the target, reaction products might still reach the recoil detector and contribute to the background. The three most important interactions of photons are the photo-electric effect, Compton scattering and pair production. The cross sections of these processes multiplied by the target density yield the interaction probability of the photons, which is shown in Fig. 2.13. The cross sections are obtained from the EPDL97 library [40]. At low photon energies, the photo-electric effect is dominant, and below an energy of about 10 keV all photons will be stopped in the target. In the intermediate energy range, the Compton process dominates and in the high energy range the most likely interaction is electron-positron pair production. Note that for high energies, the probability to create an electron-positron pair is independent of the photon energy.

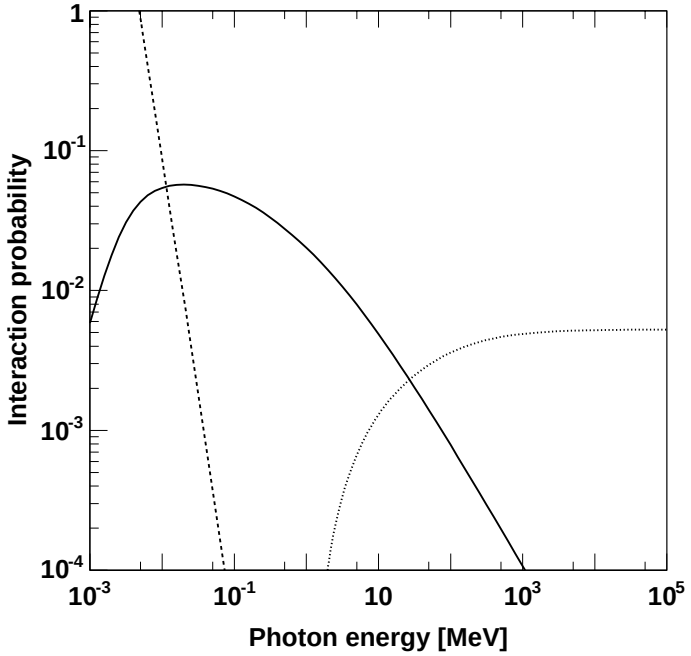

Figure 2.13: *Interaction probability of photons in the target. At low energies, the photo-electric effect dominates (dashed line) and at high-energy pair production is most likely (dotted line). The solid line represents the interaction probability of the Compton process.*

Background events due to bremsstrahlung and synchrotron radiation

By means of a Monte Carlo program the effect has been determined of the photonic interactions in the target on the number of background events in the recoil detector. For the field-less target configuration and the configuration with the longitudinal magnetic field, about 135 bremsstrahlung photons per bunch crossing will reach the recoil detector[6]. About 25% of these photons have an energy larger than 100 keV and only a small fraction of these high-energy photons will interact with the detector material[7]. The bremsstrahlung photons with an energy less than 100 keV will almost all be stopped in the recoil detector. However, half of these low-energy photons carry an energy less than 12 keV and will therefore only induce a small signal in the detector compared to a minimum ionizing particle.

Effectively only about 50 photons per bunch crossing will show up as background hits in the detector. Some of the bremsstrahlung photons will interact already within the target and produce low-energy charged particles, but the energy of these particles is so low that virtually all of them will be stopped in the target. Hence, the number of background events from tertiary (charged) particles is negligible.

[6]The number of synchrotron photons is negligible in case of a longitudinal field because the magnetic field lines are parallel to the beam.

[7]For a 300 μm silicon sensor for example, only one in a thousand photons with an energy larger than 1 MeV will interact with the detector.

The configuration with the transverse field is different because of the production of a large number of photons as synchrotron radiation. This field configuration effectively yields 100 photons per bunch crossing with an energy in the range from 12 to 100 keV. In addition, about 65 electrons from Compton scattering will give rise to hits in the detector.

Note that the list of background sources is only limited to sources which originate in the target region of the experiment. In addition to this experiment-related background, also backgrounds originating from beam handling may appear. This could be for instance synchrotron radiation from beam bending and focusing and also scattering products from collimators upstream of the experiment. Estimating the backgrounds from the accelerator is impossible, given the amount of information available. The machine background should, however, be small compared to the background from Møller scattering in the target.

2.2.5 Count rate

From the previous sections it has become clear that the number of background hits in a recoil detector can be high. The expected number of hits from a single bunch, in the angular range from 0.2 to 1.3 rad, is 1650 for the field-less configuration, and 108 and 865 for a longitudinal and transverse field, respectively. If the effect of the time resolution of the detector and the readout electronics is taken into account, the number of particles that traverse the detector within a certain amount of time is an order of magnitude larger than the number of hits per bunch. For silicon detectors, for example, the response time of sensor plus readout electronics is in the order of 20 ns. Within this 20 ns, a total of $4.3 \cdot 10^4$ particles enter the recoil detector, which is more than an order of magnitude larger than the maximum of $1.7 \cdot 10^3$ hits per bunch. When using very fast readout electronics one might gain a factor of two in shaping time at the cost of a lower signal to noise ratio, but much larger factors cannot be achieved due to the finite charge collection time of planar silicon strip detectors. Details on signal development in silicon strip detectors can be found in section 3.4.4.

In order to be able to distinguish the very large number of events quoted above, the detector has to be subdivided in small detector elements. If an occupancy of 1% per detector segment is assumed[8], the minimum required number of detector segments per layer must then be close to four million for non-polarized running. Note that even in case of non-polarized running, one should consider using a longitudinal magnetic field to sweep out the low-energy Møller electrons. This will reduce the count rate by a factor 15, and therefore also reduce the total required number of detector elements with the same factor. Given the small surface area of the recoil detector one can only use pixel type detectors if a large number of detector elements is needed.

The high (angle integrated) count rate is only a peak count rate during the 1 ms of beam. The average count rates are a factor of 200 lower because of the low duty cycle of

[8]This number assumes perpendicular tracks, while almost all tracks will be inclined with respect to the detector surface. The real strip occupancy will thus be higher by a factor of 2 to 4. An occupancy of 1% is commonly used for microstrip detectors; for pixel type detectors with a sequential readout of the pixels, the occupancy should be less than 1‰.

the TESLA accelerator. This alleviates the requirements on the data acquisition system somewhat. The design and operation of a recoil detector would clearly be much simpler when operated at a continuous beam. For application at a (quasi) continuous beam, the recoil detector can be built from microstrip detectors instead of pixel detectors. A more detailed presentation on the required readout architecture for a recoil detector is given in section 6.2.

2.2.6 Radiation damage

The high background count rates do not only give a high occupancy of the detectors and front-end electronics, but could potentially also induce radiation damage in the sensor and in the readout electronics. For a silicon sensor, the most important radiation damage is the displacement damage caused by Non Ionizing Energy Loss (NIEL) [41]. This type of damage is mainly due to hadronic particles and not so much due to leptons and photons. The larger fraction (by far) of the background for the recoil detector consists of (Møller) electrons and photons. Damage to the sensor will therefore not be a primary concern.

For the readout electronics on the other hand, the most important type of damage is caused by ionizing energy loss. The ionization will introduce a positive charge build-up in the oxide of the field effect transistors in the front-end electronics. As a consequence, the thresholds and thereby the characteristics of the transistor change. Ionization induced damage is proportional to the total ionizing dose. Electrons, photons and charged hadrons will all contribute to the damage in the oxide.

The worst case configuration for radiation damage is the one where the magnetic field is absent because in this case the number of background tracks is largest. Although the magnetic field is needed for momentum determination of the particles entering the recoil detector, it is useful to consider the radiation effects without the presence of a magnetic field. At small polar angles, the Møller electrons will be minimum ionizing, but particles emerging at angles larger than about 0.5 rad have, on average, an energy below 1 MeV. These particles will deposit more energy in the readout electronics and consequently contribute more to the radiation damage.

To estimate the order of magnitude of the radiation level, it is assumed that all particles lose an amount of energy equal to twice that of a minimum ionizing particle. Given the 6.2 million bunches per second, the 1650 particles per bunch traversing the recoil detector, and assuming beam for 25% of the time, a total of about $3 \cdot 10^{15}$ particles will hit the recoil detector every year. The estimated surface area of the first detector layer is about 400 cm^2. The annual radiation dose in the silicon oxide will thus be in the order of 3 kGy. These radiation levels require the use of radiation hard integrated circuits for the electronics close to the detector.

2.3 Conclusions

In order to determine the contribution of the orbital angular momentum of the quarks to the total longitudinal spin of the nucleon, accurate measurements of generalized parton distributions are needed, which can be achieved at new high-luminosity deep inelastic

scattering facilities. Experimental information on generalized parton distributions can be obtained from exclusive deeply virtual Compton scattering. The exclusivity of the reaction, i.e. singling out the transition to the proton final state only, is crucial for a clean interpretation of the data. Given the limited energy resolution of the forward angle spectrometers in future fixed-target deep inelastic scattering experiments, exclusivity can only be guaranteed by employing a recoil detector in the target region of the experiment. This recoil detector will have to detect the low-momentum large-angle particles emitted in DVCS. It also has to provide hadronic particle identification as a stand-alone detector. The angular range which must be covered by the recoil detector is 0.2 to 1.3 rad, and the maximum momentum for proton identification is 1.3 $\mathrm{GeV{\cdot}c^{-1}}$. Moreover, the detector surface must be subdivided in many ($\sim 4 \cdot 10^6$) small detector elements to be able to handle the background rates, and radiation hard readout electronics must be used to withstand the high radiation levels anticipated. In the following chapters it is investigated whether it is possible to realize a recoil detector given these and other environmental constraints in the target region.

Chapter 3

Particle identification

In the previous chapter it was concluded that the requirements on the design of a recoil detector for the study of generalized parton distributions are severe. The recoil detector must accomplish momentum determination and particle identification (PID) as a stand-alone detector in the limited space available in the target region of a future high-luminosity DIS facility. Moreover, the detector must operate in vacuum and is exposed to a large number of background events. If a detector is placed outside the vacuum chamber, the amount of material between the particle vertex and the detector increases the lower (momentum) limit for detection which then becomes too large in view of the physics described in chapter 2. A combination of detectors both inside and outside of the vacuum is not excluded if a large momentum range is required. However, the possibility to detect recoiling particles with a stand-alone detector that fits within the target magnet is preferred as it leads to a more compact design. A summary of the design requirements and anticipated operating conditions of a recoil detector for a future fixed target DIS experiment is listed below:

- Stand-alone tracking in a magnetic field: a minimum of four space points on each track is needed.
- Stand-alone particle identification for protons up to 1.3 GeV·c^{-1}.
- Coverage of the scattering angle from 0.2 to 1.3 rad.
- Operation in the vacuum of the (lepton) beam.
- Presence of a 5 Tesla magnetic field.
- Space available in the target region: 20×20×20 cm^3.

This chapter starts with a brief introduction of the various particle detector types and techniques in an effort to select the most suitable technique for a future recoil detector. Thereafter, the chapter focuses on ionization measurements with silicon detectors. After a review of the energy loss of fast charged particles in silicon, several statistical techniques for particle identification by means of ionization measurements are presented. These techniques are used to analyze the data of both the Monte Carlo simulations and the experimental study which are the subjects of chapter 4 and 5, respectively. Finally, the models to simulate the response of a realistic detector and readout electronics are introduced; these models are used in the Monte Carlo simulations described in chapter 4.

3.1 Overview of particle identification techniques

In High Energy Physics (HEP) many particle identification techniques are applied. An overview of the main techniques and the typical momentum range in which they can be used for pion-proton separation is depicted in Fig. 3.1. Each technique is briefly reviewed in the subsequent subsections, where it must be kept in mind that the future recoil detector needs to be operated in vacuum and be small as it must fit in the limited space available in the target area.

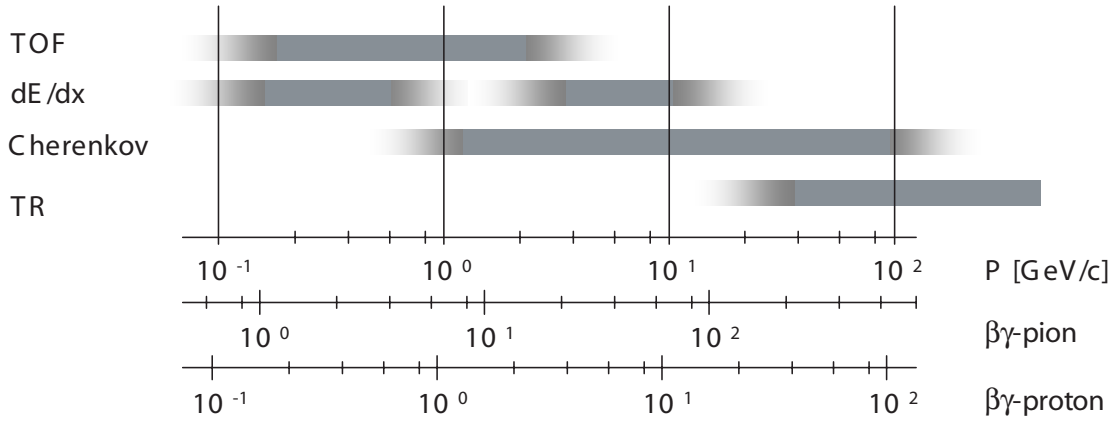

Figure 3.1: *Overview of the typical ranges of application (in momentum) of various particle identification techniques. See the text for an explanation of the gap in the dE/dx band.*

3.1.1 Time of flight

Hadrons can be identified by measuring their mass via the relation $\beta\gamma = p/Mc$, where p is the momentum of the particle, M is its rest mass and c is the speed of light in vacuum. Apart from a precise measurement of the momentum p via the curvature of the tracks in a magnetic field, which is the subject of section 4.2, a measurement of the velocity v of the particle is required to determine $\beta = \frac{v}{c}$ and $\gamma = 1/\sqrt{1-\beta^2}$. A direct measure of the velocity can be obtained from the time-of-flight (TOF) of the particle. For a given resolution of the time measurement, the best mass resolution is obtained by placing the detectors sufficiently far apart. With a detector separation of several meters, pions and protons can be identified up to a momentum of about 5 GeV·c^{-1}. The *difference* in the time-of-flight of two particles with masses M_1 and M_2 over a linear distance l is given by

$$\Delta t = \frac{l}{c}\left[\sqrt{1+\frac{M_1^2c^2}{p^2}} - \sqrt{1+\frac{M_2^2c^2}{p^2}}\right]. \tag{3.1}$$

The minimum guaranteed distance between two detecting elements in the current application is 10 cm due to the limited space in between the poles of the target magnet. Assuming a minimum measurable time difference of 200 ps, separation of pions and kaons is possible up to 0.37 GeV·c^{-1}. Protons and kaons can be separated up to 0.57 GeV·c^{-1}.

These upper limits are below the required momentum range of the recoil detector. Note that to measure a time difference of 200 ps with reasonable accuracy, the resolution of the time measurement should be at least a factor four better.

With the development of multi-channel Time to Digital Converter (TDC) chips for the Large Hadron Collider (LHC) experiments, the use of the time-of-flight technique for highly granular detectors such as vertex detectors is becoming more realistic. An example of a TDC chip with a 500 ps time resolution is given in [42][1]. Although the time-of-flight technique alone is not suited for the current application, it is in general a good complementary technique to ionization measurement.

3.1.2 Cherenkov detectors

If a charged particle travels through a dielectric medium with a velocity larger than the speed of light in that medium, Cherenkov light is emitted. The axis of the Cherenkov light cone is in the direction of motion of the particle and the half apex of the light cone is given by $\cos\theta = \frac{1}{\beta n}$, where n is the refractive index of the medium. The threshold for light emission corresponds to the condition $v > \frac{c}{n}$ which implies the use of radiators with a high refractive index for low momentum particle identification. Materials with a high refractive index which are applied in Cherenkov detectors are either liquid C_6F_{14} ($n = 1.27$) [43] or fused silica ($n = 1.47$) [44]. For true particle identification one would like to have a positive identification which means that particles must leave a signal in the detector[2]. In the current application, protons must be detected over the whole momentum range, even down to a few hundred MeV·c^{-1}. The threshold for light emission by protons is 1.2 GeV·c^{-1} for liquid C_6F_{14} and 0.87 GeV·c^{-1} for fused silica. So even with a solid radiator, protons with a momentum of less than 0.87 GeV·c^{-1} will go undetected. Hence, particle identification by detecting Cherenkov light is not possible for the current application.

3.1.3 Transition radiation detectors

Transition radiation (TR) is the emission of X-rays arising when a charged particle crosses the boundary between two materials with different dielectric constants. As the probability of radiating an X-ray at the boundary is very low (∼0.01), hundreds of boundaries (layers) are needed for an efficient detector. Transition radiation detectors can only be used for highly relativistic particles with $\gamma > 500$, which is only the case for electrons in the current application. Transition radiation detection is therefore not suited for hadronic particle identification around 1 GeV·c^{-1}. A detailed discussion on transition radiation detectors is given in [45].

[1] The resolution is not limited by the technology but by the requirement of the application.

[2] This is in contrast to threshold based identification where only one of the particle types to be identified generates a signal in the detector.

3.1.4 dE/dx

Another method to identify particles is by a difference in their energy deposition. The energy dE lost by a particle over a distance dx depends on its momentum and on its type. Figure 3.1 shows two regions where this so called dE/dx method can be applied. In the intermediate momentum range, dE/dx cannot be used because the dE/dx curves of light particles cross the curves of heavier particles in this domain (see also Section 3.2.3 and Fig. 3.3). Identification in the low momentum region is possible with either semiconductor, gaseous or scintillation detectors. At higher momenta only gaseous detectors can be used because of the greater value of the relativistic rise in the dE/dx curve. The relativistic rise is almost absent for solid detectors because of the density effect (see Section 3.2.3). Hence, the dE/dx curves completely overlap for relativistic energies and particles can no longer be identified by their energy deposition.

Gaseous detectors cannot be used for the current application for several reasons. The measured ionization in gaseous detectors is based on a low number of primary ionizations. Hence the fluctuation in the ionization, and thus in the measured energy deposition, is larger than for a typical solid state detector. This can be overcome by using a large gas volume and a large number of ionization samples (layers), but clearly this is not possible for the current application because of the small volume in the bore of the target magnet. Moreover, gaseous detectors are difficult to operate in the beam vacuum if the amount of material of the gas envelope should be minimized to meet the lower detection threshold of a few hundred MeV·c^{-1} for protons. An example of particle identification with gaseous detectors is described in [46, 47], where pions and protons are separated up to momenta of 6 GeV·c^{-1} with a large Time Projection Chamber.

Semiconductor detectors on the other hand, have been shown to work in the beam vacuum [48], but their useful momentum range for dE/dx based particle identification is smaller than for gaseous detectors because the region of the relativistic rise cannot be used. For the current application, however, the maximum required momentum is only as high as 1.3 GeV·c^{-1} which is still below the cross-over point of the dE/dx curves for hadronic particles[3]. The possibility to use silicon detectors for dE/dx particle identification is explored in the remainder of this work.

3.2 Physics foundations of dE/dx particle detection

Particle identification by means of measuring the energy deposition in silicon sensors seems to be the best option for a recoil detector and will be further explored in the rest of this work. A good understanding of the energy loss mechanism is of decisive importance, and for that reason the physics behind dE/dx particle identification is considered in some detail in this section.

Charged particles passing through matter lose energy by interaction with atomic electrons and nuclei. Particles heavier than electrons mainly lose their energy by inelastic collisions with the atomic electrons resulting in ionization. In the ionization process also

[3]The silicon detector in the HERMES recoil project is used for the identification of protons up to 0.65 GeV·c^{-1}. Higher momenta protons are identified by a detector consisting of scintillating fibers.

more energetic electrons, called δ-rays, may be emitted which subsequently release their energy until they are captured or undergo a reaction with a nucleus.

In silicon detectors, the deposited energy liberates charge by moving electrons from the valence to the conduction band. This mobile charge can move freely through the lattice and is collected by the readout electrodes of the detector. Exact determination of the energy deposition enables the identification of the particle that passed the detector, most notably in case the incident particle is non-relativistic.

In the next subsections the collision cross section is presented, followed by a description of the Bethe-Bloch equation. In subsection 3.2.4 the Landau and Vavilov energy loss straggling functions are described. The scaling of the energy deposition with path length is the subject of subsection 3.2.5.

3.2.1 Introduction

In the description of the energy loss of heavy charged particles, the only interactions taken into account are the Coulomb interactions with the atomic electrons. Nuclear interactions are disregarded as they occur infrequently[4]. Correlated energy loss effects such as channeling [49, 50] will be neglected as well, because they are only important at specific angles of incidence (and only for materials with a crystal lattice like silicon).

The probability of a single interaction of a charged particle with an atomic electron is described by the doubly differential cross section $\sigma(E, k)$, where E is the energy lost in an interaction with momentum transfer k. In absorbers with a thickness larger than several micrometers, a particle will in general experience multiple (n) collisions and suffer a total energy loss

$$\Delta = \sum_{i}^{n} E_i. \tag{3.2}$$

The energy loss straggling function $f(d, \Delta)$ describes the probability of losing an amount of energy Δ when traversing a detector of thickness d. This straggling function differs from an energy deposition straggling function (also called *restricted* energy loss straggling function) as recorded by an ideal detector due to the escape of high-energy δ-rays from the active detector volume. To calculate the energy loss straggling function $f(d, \Delta)$ one needs (i) the probability for the occurrence of n collisions and (ii) the probability for a particular energy loss E_i. The latter is given by the singly differential cross section $\sigma(E)$ which will be described in more detail in the next subsection. The number of collisions is given by a Poisson distribution with a mean value $\mu = dM_0$, where M_0 is given by

$$M_0 = N_e \int_0^\infty \sigma(E) dE, \tag{3.3}$$

in which N_e is the number of electrons per unit volume.

The theoretical derivation of the collision cross section $\sigma(E)$ is determined separately for close and distant collisions, small and large energy and momentum transfers, and longitudinal and transverse excitations. A full review is beyond the scope of this work;

[4]The nuclear interaction length in silicon is 106 g·cm^{-2} and a (typical) 300 μm thick silicon sensor is 7·10^{-2} g·cm^{-2}. Hence, the probability of a nuclear interactions in a sensor is less that 1‰.

interested readers are referred to [51, 52, 53]. The main constituent of the total collision cross section is the cross section for large energy transfers, which is presented in the next subsection.

3.2.2 Collision cross section for large energy transfers

For large energy transfers, the *non-relativistic* differential Rutherford cross section [51]

$$\sigma_{nr}(E) = \frac{2\pi z^2 e^4}{m_e v^2 E^2} \tag{3.4}$$

describes the collision probability of a heavy charged particle with charge ze, speed v and rest mass M[5] in collision with a free electron with rest mass m_e. In this case, the electron receives all the energy E lost by the particle and the corresponding momentum transfer k equals $\sqrt{2m_eE}$ [6]. By including a term for the maximum energy transfer, the equation becomes valid for relativistic particles. The *relativistic* (differential) Rutherford cross section [54] then reads

$$\sigma_{rr}(E) = \sigma_r(E)\Big[1 - \beta^2 \frac{E}{E_m}\Big], \tag{3.5}$$

with the maximum energy transfer E_m defined by

$$E_m = \frac{Mc^2\beta^2\gamma^2}{M/2m_e + m_e/2M + \gamma}. \tag{3.6}$$

Here, M and m_e are the rest mass of the incident particle and of the (free) electron, respectively, β is the ratio of the velocity of the particle to the speed of light and $\gamma = 1/\sqrt{1-\beta^2}$.

Equation (3.5) describes the collision cross section for charged particles incident on free electrons, while in the detector material the electrons are bound to the nucleus. Including the binding energy of the electrons for energy transfers greater than a certain threshold (E_a in Table 3.1) yields the empirical cross section [51]

$$\sigma_u(E) = \sigma_r(E)\Big[1 - \beta^2 \frac{E}{E_m}\Big] \sum_l Z_l \Big[1 + \frac{d_1}{E} + \frac{d_2}{E^2}\Big], \tag{3.7}$$

where Z_l is the number of electrons in the sub-shell l. The coefficients d_1 and d_2 for each (sub)shell are listed in Table 3.1. Note that Eq. 3.7 represents the cross section per atom of the stopping material.

Definition of moments

The collision cross section for large energy transfers (σ_u) described in the previous section is the main constituent to the total differential cross section σ. The other constituents

[5] The rest mass M of the incident particle does not appear in the cross section for $M >> m_e$.

[6] The nuclear recoil is zero by definition for a free electron.

Table 3.1: *Shell dependent constants of Eq. (3.7) for silicon; the corrections are valid for energy transfers greater than E_a [51].*

Shell	Z_l	E_a[eV]	d_1[eV]	d_2[eV^2]
K	2	20000	3340	0
$L-2s$	2	4000	369	$1.94 \cdot 10^6$
$L-2p$	6	3000	448	$2.07 \cdot 10^6$
M	4	150	9.4	31.2

are due to the longitudinal and transverse excitations. If a description of the total cross section differential in E, including the excitation cross sections, is available, a set of moments can be defined:

$$M_m = N_v \int_0^\infty E^m \sigma(E) dE. \tag{3.8}$$

Here, N_v is the number of atoms in a unit of volume[7] (for silicon: $4.99 \cdot 10^{22}$ cm^{-3}). The mean number of collisions per unit length is given by the zeroth moment M_0. The first moment M_1 is the stopping power, which gives the mean energy loss $\langle E \rangle$ when multiplied by the detector thickness. The stopping power obtained using Eq. (3.8) gives the same results as the Bethe-Bloch equation discussed in the next subsection. The second moment M_2 is related to the width of the energy loss straggling distribution. This quantity is only useful for a symmetric (Gaussian) energy loss distribution, and cannot be used for skewed energy loss distributions like the Landau or Vavilov distribution (see section 3.2.4).

3.2.3 Bethe-Bloch equation

The slowing down of particles in thin layers of material is described by the Bethe-Bloch equation. Although it does not directly lead to energy deposition straggling functions needed for particle identification, it nicely describes the mean energy loss for different momenta of the particle. For particles heavier than electrons, the Bethe-Bloch equation for the stopping power dE/dx reads [38]

$$\frac{dE}{dx} = 2\pi N_a r_e^2 m_e c^2 \rho \frac{Z}{A} \frac{z^2}{\beta^2} \Big[\ln\Big(\frac{2 m_e \gamma^2 v^2 E_m}{I^2} \Big) - 2\beta^2 - \delta - 2\frac{C}{Z} \Big], \tag{3.9}$$

where:

- N_a is Avogadro's number, $6.022 \cdot 10^{23}$ atoms·mole^{-1}.
- $r_e = \frac{e^2}{m_e c^2}$ is the classical electron radius, $2.817 \cdot 10^{-15}$ cm.
- $m_e c^2$ is rest mass of the electron.
- ρ is the density of the stopping material (2.33 g·cm^{-3} for silicon).

[7] The integrated cross section is multiplied by the number of atoms in the stopping material and not by the number of electrons because the cross section for large energy transfers σ_u contains a sum over all electrons in the (silicon) atom.

- Z, A are the atomic number and weight of the stopping material (14 and 28.09 for silicon, respectively).
- I is the mean ionization potential (173 eV for silicon).
- z is the charge of the particle in units of electron charge.
- $\beta = \frac{v}{c}$ is the particle speed as a fraction of the speed of light.
- γ is the Lorentz factor $\left(= \sqrt{1-\beta^2}^{-1}\right)$.

The maximum energy E_m that can be transferred in a single collision is given by Eq. (3.6). The term $2\frac{C}{Z}$ is the shell correction [55, 56, 57] which reduces the stopping power at energies where the velocity of the particle is comparable to that of the atomic electrons. This reduction in dE/dx is caused by atomic electrons moving along with the particle, thereby screening the electromagnetic field of the particle. The orbital speed of the atomic electrons can be approached by $Z\alpha c$, from which the particle momenta are calculated where the shell correction becomes significant. For protons the correction is necessary for $p \lesssim 96$ MeV·c^{-1}, equivalent to a stopping range of 240 μm in silicon.

At low energies, the stopping power dE/dx decreases with the logarithm of the particle energy. After a broad minimum at $\beta\gamma = 3.0 \ldots 4.0$, the stopping power increases with $\ln(\beta^2\gamma^2)$ due to the increase of the transverse electromagnetic field of the particle moving at a relativistic velocity. The density correction (δ) lowers the $\ln(\beta^2\gamma^2)$ dependence to $\ln(\beta\gamma)$ because the stopping material is polarized by the field of the passing particle, thereby reducing the effect of distant collisions. This effect is stronger for materials with a higher electron density and is therefore called the density effect. Studies by Sternheimer [58] led to the following parameterization:

$$\delta = \begin{cases} 0 & X < X_0 \\ 4.6052X + C_0 + a(X_1 - X)^m & X_0 < X < X_1 \\ 4.6052X + C_0 & X > X_1 \end{cases} \tag{3.10}$$

where $X = \log_{10}(\beta\gamma)$ and

$$C_0 = -\left(2\ln\frac{I}{h\nu_p} + 1\right). \tag{3.11}$$

In this equation, I is the ionization potential which was already introduced before and ν_p is the plasma frequency given by

$$\nu_p = \sqrt{\frac{N_e e^2}{\pi m_e}}. \tag{3.12}$$

Here, N_e is the electron density of the stopping material. The values of various parameters entering Eq. 3.10 are listed in Table 3.2 for silicon as stopping material.

Although the Bethe-Bloch formula is accurate, it cannot be used directly in particle identification applications because it calculates the mean energy loss of the propagating particle, and not the mean energy deposition. These quantities differ due to the escape

Table 3.2: *Constants for Sternheimer's density effect correction (Eq. 3.10) in silicon [58].*

a	C_0	I[eV]	m	X_0	X_1
0.1492	-4.44	173	3.25	0.2014	2.87

of δ-electrons from the sensitive detector volume[8]. The restricted energy loss formula, which describes the mean energy deposition, is obtained from Eq. 3.9 by imposing an upper threshold on the energy of these δ-rays

$$\frac{dE}{dx} = 2\pi N_a r_e^2 m_e c^2 \rho \frac{Z}{A}\frac{z^2}{\beta^2}\Big[\ln\Big(\frac{2m_e\gamma^2 v^2 E_{cut}}{I^2}\Big) - \beta^2\Big[1+\frac{E_{cut}}{E_{max}}\Big] - \delta - 2\frac{C}{Z}\Big]. \qquad (3.13)$$

The value of E_{cut} is the energy of an electron with a range equal to the thickness of the detector, with $E_{cut} < E_{max}$ as defined in Eq. (3.6). Figure 3.2 shows the original Bethe-Bloch curve for the energy loss of protons in silicon together with the restricted energy loss curve. An energy cut of 230 keV was used for the restricted loss curve which corresponds to the stopping energy of an electron in a 300 μm thick silicon detector. Clearly visible is the difference in energy loss and energy deposition for relativistic particles due to the escape of δ-rays from the detector.

Figure 3.2 also shows some of the existing data from energy deposition measurements in silicon [59, 60, 61, 49, 62, 63, 64, 65].

The group of points close to the minimum (Bak [60]) are measurements with a detector thickness in the range of 32 μm to 1 mm. The insert shows the increase in restricted dE/dx with increasing detector thickness. The six solid lines represent the restricted energy loss curves as calculated with Eq. 3.13 using an energy cut corresponding to the detector thickness. The measurements are systematically low compared to the calculations. For the top four points this can be explained from the limited range of the energy deposition plots in the original article which results in an underestimated mean deposition because the tail of the distribution is missing. The two lowest points, however, corresponding to 32 μm and 51 μm thick sensors, are well below the curves even after correcting for the cut-off tails. Another characteristic shown in Fig. 3.2 is that the relativistic rise is almost absent in dense materials like silicon. The mean restricted energy loss for very high energies is only 10% larger than the minimum energy loss.

Particle identification by means of dE/dx sampling exploits the difference in energy deposition of different particles for a given momentum. Figure 3.3 shows the mean energy deposition of pions, kaons and protons as a function of momentum. The actual energy deposition varies around this mean value. The difference in mean energy deposition for pions and kaons is very small for a momentum of 1 GeV·c^{-1} or more. Hence, particle identification at these momenta is only possible using many dE/dx samples. Identification of protons is possible up to slightly higher energies.

[8]Even the mean energy deposition is difficult to measure because it depends on the dynamic range of the readout electronics. A limited dynamic range of the readout equipment cuts the tail of the distribution and thereby lowers the (measured) mean energy deposition.

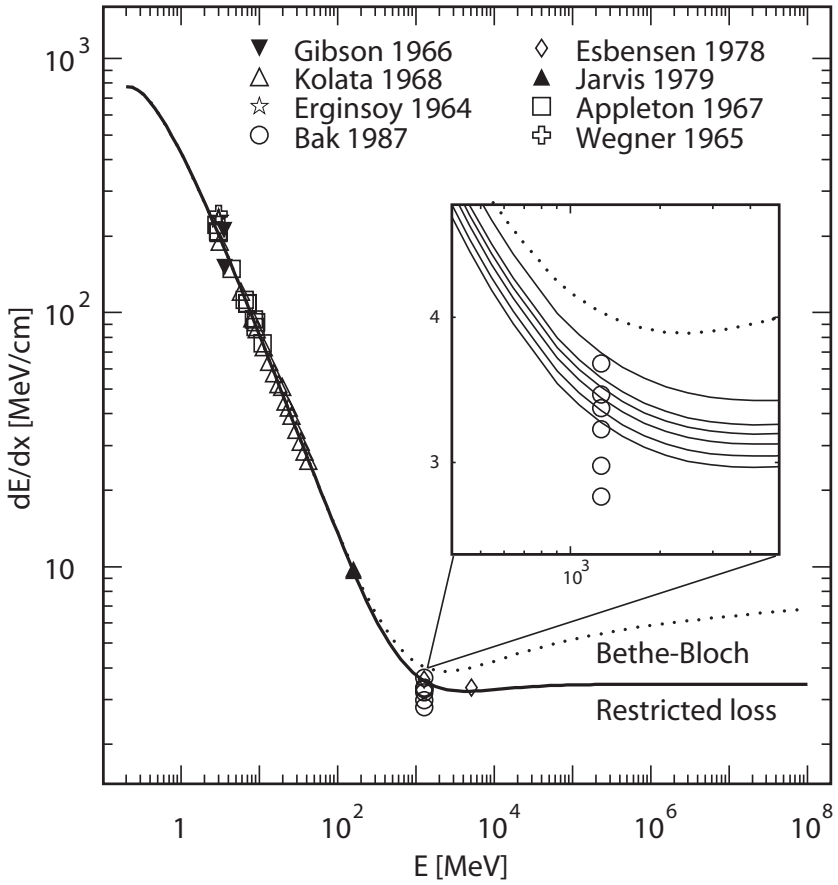

Figure 3.2: *Mean energy loss and mean restricted energy loss of protons in silicon. An energy cut of 230 keV was used for the restricted energy loss curve. The insert shows the area around the minimum. The solid lines are the restricted energy loss curves corresponding to different cut values, matching the detector thickness (32 μm to 1 mm) in the Bak data.*

3.2.4 Landau and Vavilov distribution

The energy loss of particles for a given, fixed, momentum is not constant but fluctuates around the mean value which is described by Eq. 3.13. For a thin layer of the stopping material and high-energy charged particles, the most probable energy loss is also not equal to the mean energy loss. The energy loss distribution is skewed, with a long tail towards the high energy side, originating from single collisions with large energy transfers. Landau theoretically worked out this problem for a thin layer of material, where thin is defined through a requirement on the parameter k:

$$\kappa \equiv \frac{\xi_L}{E_m} < 0.01, \tag{3.14}$$

with

$$\xi_L = \frac{2\pi z^2 e^4}{m_e c^2 \beta^2} N_a d\rho \frac{Z}{A}. \tag{3.15}$$

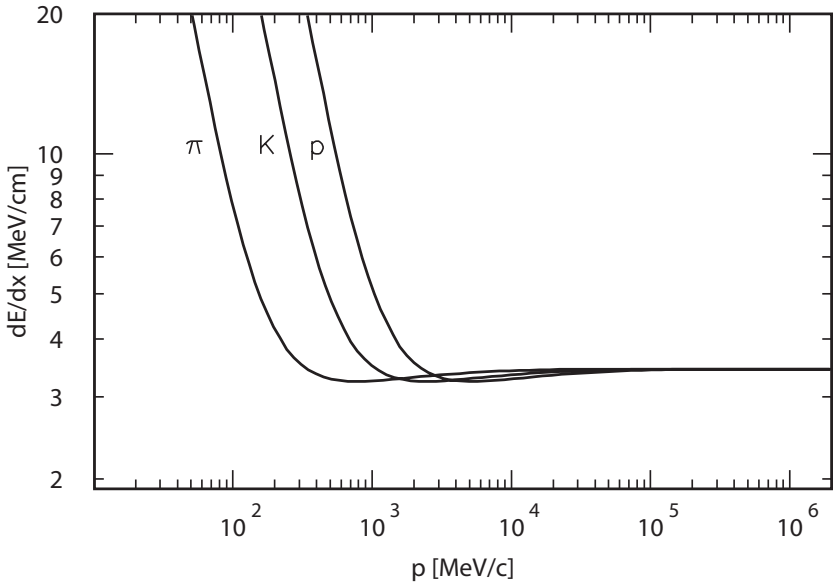

Figure 3.3: *Mean energy deposition as a function of momentum for pions, kaons and protons.*

Here, E_m is the maximum energy transfer in a single collision (Eq. 3.6), and d is the thickness of the detector. The numerical value of ξ_L for silicon is $17.83dz^2/\beta^2$ eV, with d in μm.

Landau derived his expression from the non-relativistic Rutherford cross section, Eq. 3.4, by writing the energy loss in a thin layer as a transport equation [66]. He solved this equation using Laplace transformations and obtained the following expression for the energy loss straggling function which depends on the single variable λ

$$f_L(d, \Delta) = \frac{\Phi(\lambda)}{\xi_L}, \tag{3.16}$$

where

$$\Phi(\lambda) = \frac{1}{2\pi i} \int_{\sigma+i\infty}^{\sigma-i\infty} e^{[u \ln u + \lambda u]} du \tag{3.17}$$

and

$$\lambda = \frac{\Delta - \xi_L(\ln \frac{\xi_L}{\epsilon} + 1 - C)}{\xi_L}, \tag{3.18}$$

with

$$\ln \epsilon = \ln \left[\frac{(1-\beta^2) I^2}{2 m_e v^2} \right] + \beta^2 \tag{3.19}$$

and C=0.577 is Euler's constant.

Landau's function does not describe the energy loss distribution of a fast particle very accurately. This is mainly due to:

- The use of the non-relativistic Rutherford cross section, i.e. no limitation on the maximum energy transfer.

- The assumption that the atomic electrons are free particles, i.e neglecting the binding of the atomic electrons by the nucleus. This underestimates the width of the distribution.

Vavilov [67] used the relativistic version of the Rutherford cross section (Eq. (3.5)) to obtain energy loss distributions for somewhat thicker layers corresponding to values of κ up to $\kappa = 10$. The difference between the Vavilov and the Landau distribution for relativistic particles is very small. Still, Vavilov's description of the energy loss straggling function yields a distribution that is too narrow because the binding of atomic electrons has been neglected. A practical solution to the problem is to convolute the Landau or Vavilov distribution with a Gaussian distribution to correct for electronic binding [51, 68]:

$$f(x,\Delta) = \frac{1}{\sigma\sqrt{2\pi}} \int_{-\infty}^{\infty} f_L(x,\Delta') e^{-(\Delta-\Delta')^2/2\sigma^2} d\Delta'. \tag{3.20}$$

A parameterization of the width of the Gaussian is [69]

$$\sigma^2 = \frac{8}{3}\xi_L(2.319 + 0.67\ln\beta)\cdot 10^{-3}. \tag{3.21}$$

Note that the width of the Gaussian scales with the square root of the thickness d of the layer of material through which the particle is passing (see Eq. 3.15). Hence, a thin silicon sensor gives a relatively broad energy loss straggling function.

An example of a fit using a pure Landau function and a fit using a Landau function convoluted with a Gaussian is shown in Fig. 3.4. The distribution shown is obtained from a GEANT4 simulation with 2 GeV·c^{-1} protons and a 100 μm detector. The most important shortcoming of the pure Landau function is its narrow width, but also the most probable value of the fit is too low.

If the detector is very thick or if the energy of the impinging particle is very low, the corresponding energy loss straggling function obtains a pure Gaussian shape. This can be understood from the fact that for a large number of collisions the resulting distribution must become Gaussian as prescribed by the central limit theorem.

As a reference, Table 3.3 lists the minimum momentum for pions, kaons and protons where the Landau or Vavilov function describes the energy loss straggling in a 300 μm silicon detector.

Table 3.3: *Minimum momenta (in MeV·c^{-1}) for pions, kaons and protons for which the Landau or Vavilov distribution is the appropriate energy loss distribution assuming a 300 μm silicon detector. The criteria are $\kappa = 0.01$ and $\kappa = 10$ for the Landau and Vavilov distribution, respectively.*

	Pion	Kaon	Proton
Landau	142	502	952
Vavilov	21	75	143

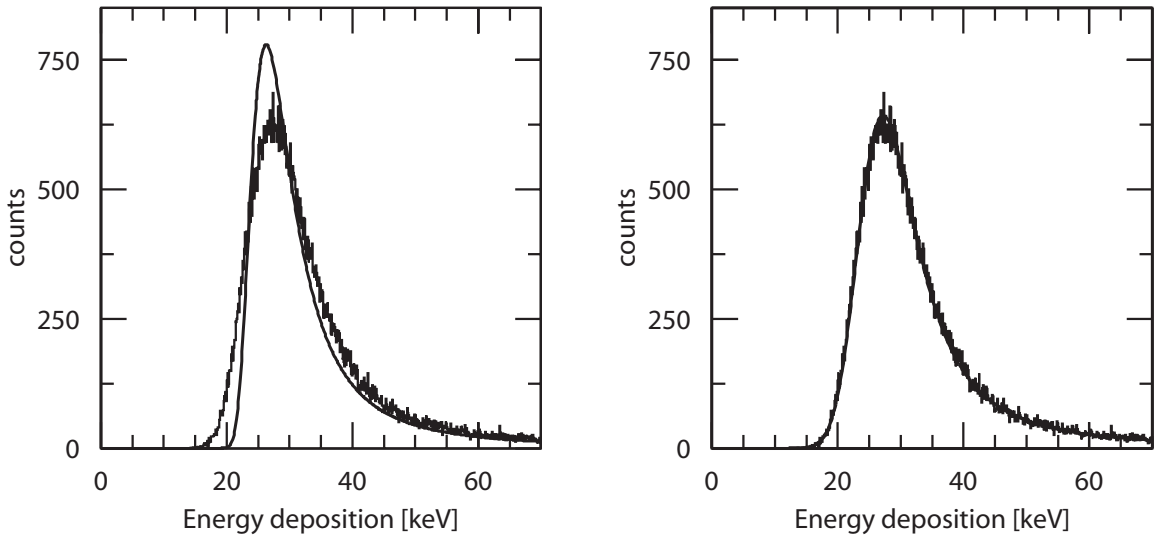

Figure 3.4: *Energy deposition distribution with a pure Landau fit (left) and with a convolution of a Landau and Gaussian (right). The data represent the results of a* GEANT4 *simulation for 2 GeV·c^{-1} protons incident on a 100 μm silicon detector.*

3.2.5 Scaling of energy deposition with path-length

Particles crossing the silicon detectors under various angles traverse different amounts of material. For particle identification it is easiest if one can use a simple scaling rule so that all energy deposition samples can be compared to the same distribution. As already explained in Section 3.2.3, the mean energy deposition per unit length depends on the thickness of the detector due to the escape of δ-rays. This thickness dependence also exists for the most probable (restricted) energy deposition as shown in Fig. 3.5. The most probable number of electron-hole pairs generated along the track decreases with detector thickness. Several data from beam measurements [60] are also plotted for comparison. It should be noted that the measured value for the 32 μm thick sensor is low compared to the simulation [60]. The most probable energy deposition Δ_{mp} and thus the number of electron hole pairs increases with thickness as $d(a+\ln(d))$ [70], with d in μm. A reduction of the sensor thickness gives a more than linear reduction in the detected signal. Moreover, because the width of the energy deposition straggling function (Section 3.2.4) scales with the square root of the sensor thickness, the ratio of the width of the distribution to the most probable value increases even more for thin silicon sensors.

3.3 Particle identification with silicon detectors

The particle identification task of the recoil detector is to distinguish pions, kaons and protons with momenta up to 1.3 GeV·c^{-1}. The identification is based on the information obtained from the energy deposition of the particles. At low particle energies this deposition strongly depends on the energy and the velocity of the particle. Identification of these low energy particles is then obtained from the correlation of the energy deposition

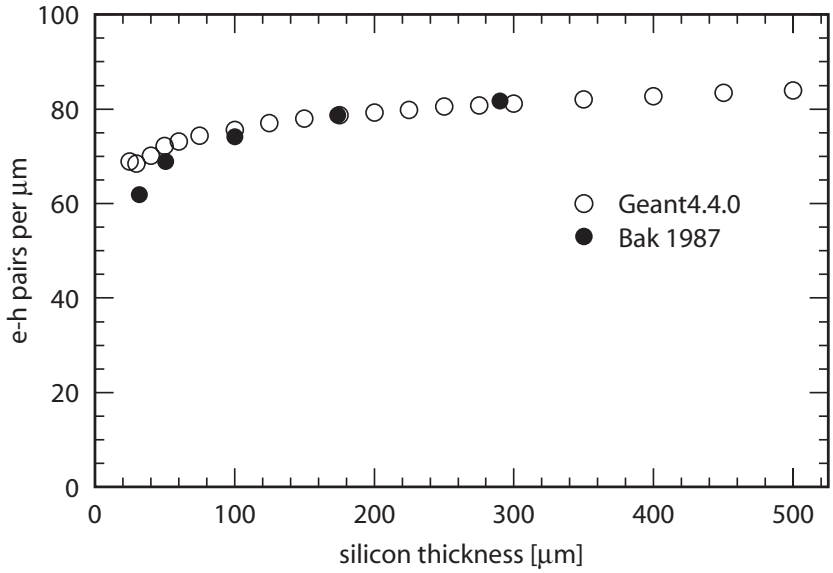

Figure 3.5: *Most probable number of electron-hole pairs per micrometer versus the thickness of the detector, for 2 GeV·c^{-1} protons.*

in two silicon sensors. This ΔE-E method is described in the following subsection. At higher energies the difference in energy deposition of various particles becomes smaller, and finally the particles become indistinguishable in the relativistic regime. Because of this smaller difference in energy deposition, more than two energy deposition measurements are needed to reliably identify particles. This multiple dE/dx sampling and the corresponding statistical analysis methods are described in subsections 3.3.2 to 3.3.5.

3.3.1 ΔE-E

Very-low energy particles stop in the first few hundred microns of silicon and the particle type can in this case be reconstructed directly from their energy deposition in the first two layers. An example plot of this ΔE-E method is shown in Fig. 3.6. The energy deposition in the, 150 μm thick, first layer is plotted horizontally, while that of the, 300 μm thick, second layer is plotted vertically. After correction for the angle of incidence, different particle-types end up in well-separated bands in the plot. Each triangular band has three distinct regions. The bottom side of the triangle corresponds to particles that are stopped in the first layer. Particles stopping in the second layer contribute to the right side of the triangle and particles that pass through both layers end up on the left side of the plot.

Clearly visible are the bands of the kaons and the protons. The pions cannot easily be identified because they decay when stopping in the detector and they overlap with the signals of protons and kaons passing both silicon layers. When a negatively charged pion is stopped it decays into a slow muon with a kinetic energy of 4.1 MeV. This muon will in turn deposit a large fraction of its energy in the detectors. The angle of the muon track with respect to the direction of the incident pion is isotropic. Hence it is well possible that also a part of the muon energy is lost in the first layer, which explains

the scattering of the pion data in the plot. The decay of kaons on the other hand results in muons with an energy of 142 MeV, or in pions of 108 MeV. These particles escape the detector while only depositing a small amount of energy. Hence, this only widens the kaon band somewhat.

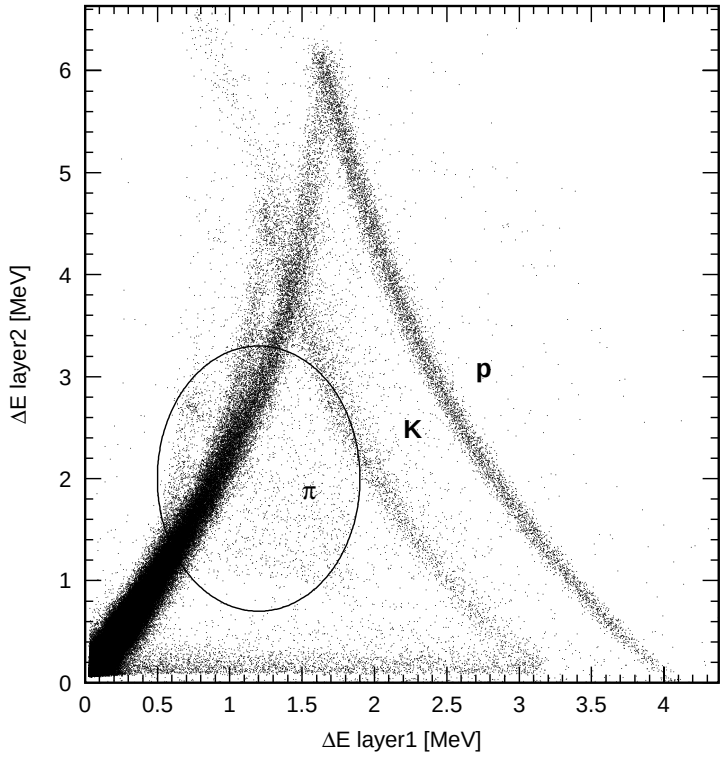

Figure 3.6: *Simulated energy deposition of pions, kaons and protons in a thick (300 μm) layer ('layer2') as a function of the energy deposition in a thin (150 μm) layer ('layer1'). Low-energy protons and kaons can easily be identified, while pions cannot easily be identified because they decay into low-energy muons. Energy depositions from pions mostly show up in the region outlined by the ellipse.*

At very low energies, the energy deposition can be expressed as [71]

$$\Delta E = E - \left(E^{\beta} - \frac{d}{C_R}\right)^{\frac{1}{\beta}}. \tag{3.22}$$

Here, E is the energy of the particle on entering the detector, d is the thickness of the silicon layer and β and C_R are constants obtained from tables [71]. In Ref. [48] it has been shown that, in this energy regime, the energy deposition scales with angle of incidence as $(\cos\alpha)^{1/\beta}$, where α is the angle of incidence with respect to the normal. By using this scaling relation, all inclined tracks can be treated as perpendicular tracks and a correlation plot like Fig. 3.6 is obtained.

As energy depositions are large for the ΔE-E method, the noise of the read-out electronics can be neglected. It should be noted that although the residual momentum of the particle can be determined with great accuracy, the initial momentum of the

particle is not well known due to the large uncertainty in energy deposition in the thick target. This problem mainly affects the low momentum particles.

At higher momenta, particle identification is generally much more difficult if only silicon detectors are available. In this thesis it is investigated whether it might still be possible to do particle identification by making multiple dE/dx measurements[9]. Particle identification in this (higher) energy region is based on the characteristics of the energy deposition distributions of the different particles.

3.3.2 dE/dx sampling

The use of multiple-sampling ionization detectors is up to now mainly restricted to large volume gaseous detectors. The low value of the density effect is exploited to allow for particle identification at relativistic energies up to the Fermi plateau. Examples of detectors with hundreds of layers are readily available [72, 73, 46]. Solid state detectors on the other hand have a much larger density effect which limits their use in the relativistic region. Due to the large radiation length of silicon the number of layers must also be limited and the number of (thin) layers will in general not exceed ten. Nevertheless it seems advantageous to use a silicon multi-sampling ionization detector for the current application. An application with five silicon layers is given in [74].

In dE/dx sampling, particles are identified using the statistical information from the samples. The statistical techniques most commonly used are the TRuncated Mean method (TRM), the Maximum Likelihood Method (MLM) and the Kolmogorov-Smirnov test, which are discussed below in separate subsections. A survey of other methods is given in [75].

3.3.3 Truncated mean

The truncated mean method distinguishes particles by comparing their mean energy deposition, calculated from a selected set of dE/dx samples, against a threshold. As the Landau or Vavilov type energy deposition distributions are highly skewed, the mean value strongly depends on tails of these distributions. The mean value is larger than the most probable value and also depends on the dynamic range of the read-out electronics because it truncates the tail of the distribution. Hence, the mean energy deposition, as calculated from a set of samples, is not a good signature of a particle. A better parameter is the most probable energy deposition which can be approximated by calculating the mean energy deposition from an ordered subset of the samples: the truncated mean. By removing the samples with the highest values from a set, the influence of the tail is reduced and the (truncated) mean value approaches the most probable value.

Figure 3.7 shows how much the most probable value of the truncated mean distribution deviates from the most probable (simulated) energy deposition. The plot shows the ratio of the (most probable) truncated mean Δ_{TRM} over the most probable value Δ_{MP} of the single sample distribution, versus the fraction of samples removed from the

[9] Strictly speaking, the correct term for dE/dx sampling would be $\Delta E/\Delta x$ sampling as neither the energy deposition nor the path length is infinitesimal. However, to conform to the terminology used in the literature, the term dE/dx will be used throughout this work.

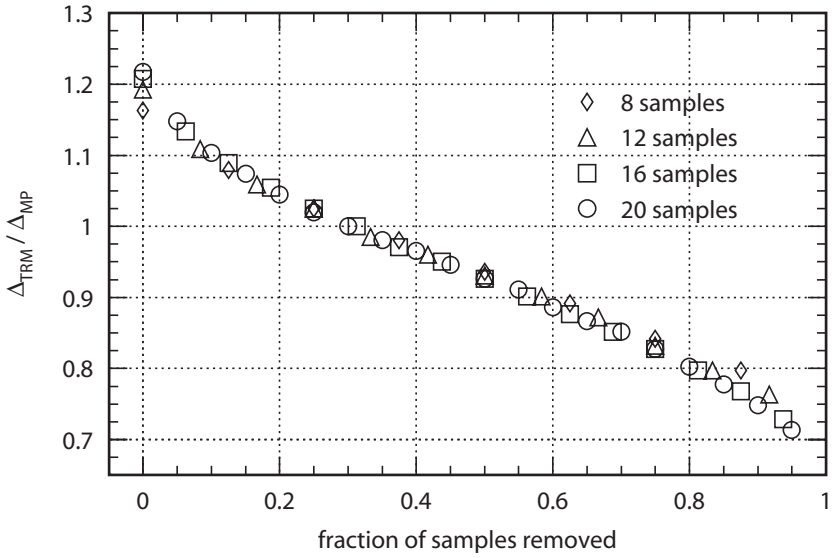

Figure 3.7: *Ratio of the truncated mean energy deposition and the most probable energy deposition from a simulation of 1 GeV·c^{-1} protons in 100 μm silicon for different values of the truncation factor.*

calculation. All samples are taken from a simulated restricted energy deposition distribution of 1 GeV·c^{-1} protons that was generated with the GEANT4 toolkit [76] for a 100 μm thick detector. For a fixed momentum, the relation between Δ_{TRM} and Δ_{MP} does not depend on the size of the original set of samples. The Δ_{TRM} with 30% of the samples removed, is the best estimator of the most probable energy deposition.

The question is what fraction of the samples should be removed when calculating the truncated mean to get the best particle identification. For a Gaussian distribution one often defines the ability to distinguish between two particle species, the resolution, as the number of standard deviations by which two closely lying peaks can be separated. However, for an asymmetric distribution the standard deviation is not a good figure of merit. Because the TRM distribution is fairly symmetric in the region of interest (near the optimum resolution), the Root Mean Square (RMS) value of the distribution will be used here as figure of merit in the comparison. Figure 3.8 shows the ratio of the RMS of the truncated mean distribution and the (most probable) truncated mean value (Δ_{TRM}) of the same distribution versus the fraction of samples removed, again for protons of 1 GeV·c^{-1}. For low fractions, the high-energy tail of the distribution enlarges the RMS which results in a large RMS to Δ_{TRM} ratio. If a large fraction of the samples is removed, the ratio increases again due to limited statistics. Increasing the number of samples leads to a smaller RMS to MP ratio, but the position of the minimum remains fixed at about 0.4.

The result for a fixed number of 16 samples as a function of the proton momentum is shown in Fig. 3.9. Low momentum particles have a nearly Gaussian energy deposition distribution and the effect of the truncation is much smaller than for particles with a higher momentum which have an asymmetric distribution. Towards higher momenta, it is more beneficial to take a lower truncation factor. Based on these results a truncation factor of 0.3 is chosen for the truncated mean method used in the Monte Carlo study

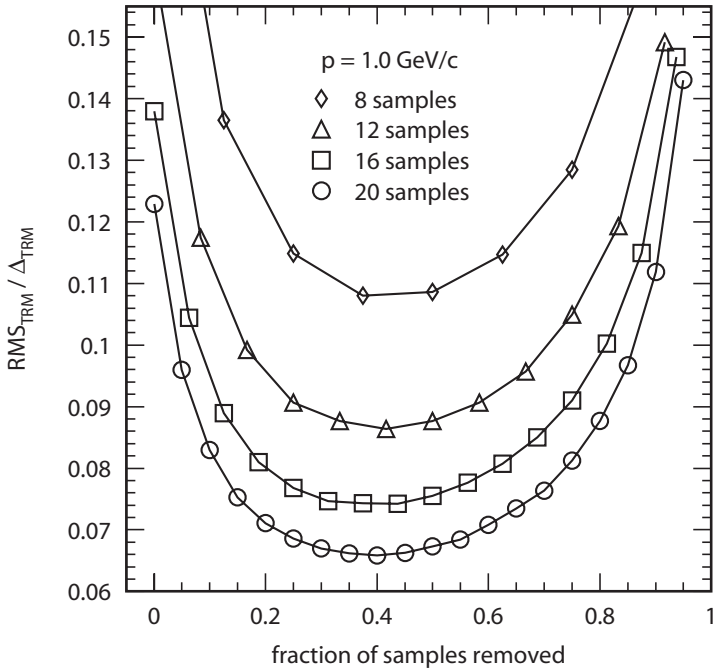

Figure 3.8: *Ratio of the* RMS *of the truncated mean distribution and the most probable truncated mean value from a simulation of 1 GeV·c^{-1} protons in 100 μm silicon for a different number of samples as a function of the truncation factor.*

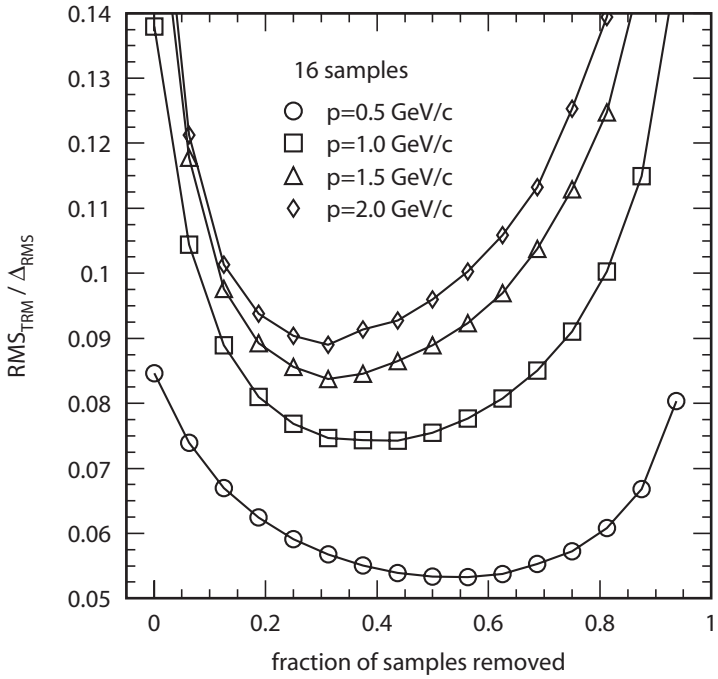

Figure 3.9: *Ratio of the* RMS *of the truncated mean energy deposition distribution and the most probable truncated mean value for different proton momenta as a function of the truncation factor. The sample size used in this simulation is fixed at 16.*

presented in Section 4.3.

The truncated mean method discriminates particles by comparing the calculated TRM energy deposition with a threshold. Because the threshold value is a function of the momentum of the particle, a rough determination of the momentum of the particle is necessary, especially in the high-energy region, as will be discussed in more detail in section 4.2. An example of the truncated mean method applied to data obtained from a GEANT4 simulation of 0.7 GeV·c^{-1} particles incident on 100 μm thick detectors is shown in Fig. 3.10. The TRM is obtained by taking 9 out of 12 samples. The top

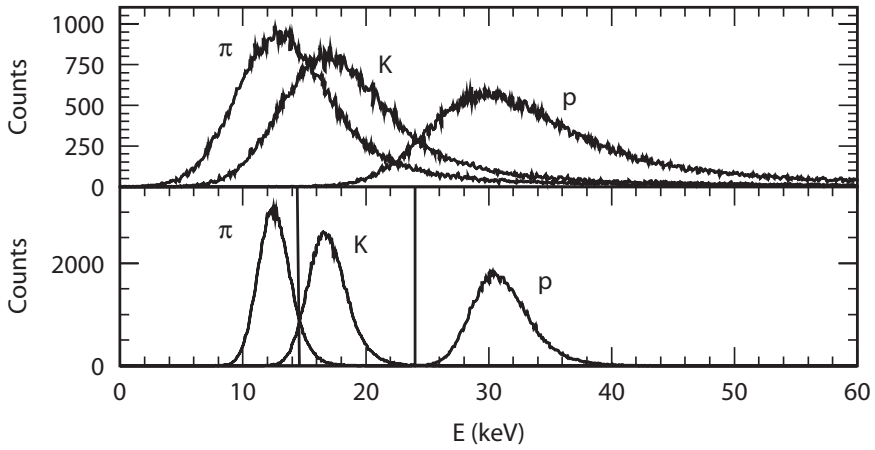

Figure 3.10: *The simulated energy deposition distributions of pions, kaons and protons of 700 MeV·c^{-1} incident on a single 100 μm silicon detector are shown in the top panel. The curves in the bottom panel are the (truncated) mean values of 9 samples with the lowest values out of a set of 12 samples. The discrimination thresholds for π-K and K-p separation are indicated by the vertical lines.*

panel shows the simulated energy deposition straggling of pions, kaons and protons for a single 100 μm silicon detector, while the bottom panel shows the distribution of the truncated mean values. Vertical lines indicate the chosen discrimination thresholds for π-K and K-p separation. The example demonstrates the usefulness of the TRM method.

3.3.4 Maximum likelihood method

The second statistical method under consideration is the maximum likelihood method. For each set of energy deposition samples Δ_i the likelihood L_p is calculated for all relevant particle types p

$$L_p = \prod_{i=0}^{n} f_p(\Delta_i), \tag{3.23}$$

where f_p is the normalized energy deposition straggling function for particle type p [77]. The largest of the likelihood values L_p determines the particle type. The maximum likelihood method will give a large likelihood value if all samples Δ_i are close to the most probable value of the straggling function f_p. However, the probability that *all* samples are close to the most probable value of the distribution is not very high. In

other words, the value L_p does not give the absolute likelihood that a set of dE/dx samples belongs to a straggling function f_p. This is no problem for clean sample sets that are generated by a Monte Carlo program, but could be a problem for real detector signals which might be deteriorated by common mode noise.

The Kolmogorov-Smirnov test, which is the subject of the next subsection, does not have this problem and gives an absolute probability whether a set of samples belongs to a given energy deposition distribution or not. Another minor drawback of the maximum likelihood method (and the Kolmogorov-Smirnov test) is that the complete straggling functions for a large number of momenta should be known a priori. These functions can be obtained from Monte Carlo simulations as will be shown in chapter 4.

3.3.5 Kolmogorov-Smirnov test

The Kolmogorov-Smirnov test provides a goodness-of-fit which can be used for unbinned distributions of a single variable. It is especially suited in case only a small number of observations is obtained, far less than necessary to create a (frequency) histogram. This is in contrast to the more commonly used χ^2 test which determines the goodness-of-fit of a frequency histogram using a theoretical function.

From the observed values Δ_i the estimated cumulative probability of the reference distribution is obtained by summing (counting) all values with $\Delta < \Delta_i$ divided by the sample size. This cumulative probability $S(\Delta_i)$ is the probability of obtaining a value smaller than Δ_i and can be described by

$$S(\Delta_i) = \frac{1}{N} \sum_{j=1}^{i} n(\Delta_j < \Delta_i). \tag{3.24}$$

If all values of Δ_i are unique, the estimator $S(\Delta_i)$ is equal to the position of Δ_i in the (increasing) ordered list, divided by the sample size. This estimator should be compared to the cumulative probability distribution $p(\Delta)$ of the reference function $f(z)$ defined as

$$p(\Delta) = \int_0^{\Delta} f(z)dz, \tag{3.25}$$

where, in the present application, $f(z)$ depends on the particle type. The largest distance between the observed and reference cumulative distributions is called the D-statistic,

$$D_m = \max |S(\Delta_i) - p(\Delta_i)| \qquad \forall \Delta_i. \tag{3.26}$$

The distribution of this value can be calculated when the sample is taken from the reference distribution. The significance of the identification (Q) is [78]:

$$Q(\lambda) = 2 \sum_{j=1}^{\infty} (-1)^{j-1} e^{-2j^2\lambda^2}, \tag{3.27}$$

where λ is approximated by[10] [79]

$$\lambda = D_m \sqrt{N}. \tag{3.28}$$

[10] An alternative form $\lambda = \left[\sqrt{N} + 0.12 + \frac{0.11}{\sqrt{N}}\right] D$ is given in [78].

The probability P to find a value $D > D_m$ is $Q(\lambda)$. Values of $P < 0.05$ are considered significant [80] and lead to the rejection of the hypothesis that the data Δ_i are drawn from the distribution $f(\Delta_i)$. By comparing the value of the D-statistic against a reference value, the null hypothesis (i.e. the sample distribution belongs to the reference distribution) is either rejected or accepted. In the current application, the D-statistic is calculated for each particle type and the smallest value of D gives the most probable particle type.

3.4 Silicon detectors and readout

The particle identification techniques presented in the previous sections used ideal energy deposition straggling functions. In a real detector, however, the measured dE/dx samples are not sampled from an ideal restricted energy loss straggling function, but are modified by various experimental effects caused by the sensors and the readout electronics. Figure 3.11 shows the steps in the detection process that transform the energy deposition straggling function into the straggling function obtained after readout. The

Figure 3.11: *Different steps that transform an energy deposition straggling function into an observed ionization straggling function.*

first two blocks cover all the information of the physics interaction process and are independent of the readout of the detector. This subject was discussed in Section 3.2. In the signal formation block, the influence of the geometry and operating conditions of the silicon sensors on the observed signals is considered. Effects like (intrinsic) resolution, diffusion, drift and charge collection play a role here. These subjects are covered in subsections 3.4.1, 3.4.2 and 3.4.3. The effects of charge sharing and noise which are caused by the readout electronics are presented in sections 3.4.3 to 3.4.6. All of these aspects must be included in a Monte Carlo model in order to get a realistic prediction of the performance of a highly segmented multi-layer silicon dE/dx detector. Such a full Monte Carlo simulation of a future recoil detector system is the subject of Chapter 4.

3.4.1 Intrinsic energy resolution

The ability of a detector to distinguish two distinct energy depositions, i.e. the energy resolution, is ultimately limited by the statistics of the ionization process. For a fixed energy deposition the signal charge is equal to the number of liberated electrons N_Q. As this is a statistical process, the number of electrons will fluctuate around a mean value. For silicon, the average energy w required to produce one electron-hole pair is 3.61 eV, which is significantly larger than the band-gap energy of silicon of 1.12 eV. This additional energy is lost in excitation of the lattice, i.e. phonon production, needed to conserve momentum in the collision. Many of these excitation modes have energy

transfers smaller than the band-gap. Because of the large difference in energy between ionization and excitation, sufficient degrees of freedom exist to dissipate exactly the amount of energy deposited by a particle. Hence, the variance of the number of electron hole pairs created is, for a fixed energy deposition, smaller than expected from Poisson statistics; the variance is $\sigma_Q^2 = FN_Q$. The reduction factor F is called after Fano, who worked out the problem theoretically [81]. For silicon the measured value of the Fano factor amounts to 0.1.

Energy deposition measurements in HEP experiments generally give worse resolutions than expected by evaluating σ_Q^2 due to noise in the fast readout electronics. Moreover, in case the particle is not stopped in the detector, as is almost always the case, the energy deposition is not fixed but fluctuates as described by either the Gaussian, Landau or Vavilov distributions discussed in Section 3.2.4. The width of these distributions is (much) larger than the intrinsic resolution of the silicon sensor. Therefore, the intrinsic resolution is not the limiting factor for a silicon detector in the envisaged application.

3.4.2 Drift and diffusion

The movement of the charge liberated by the passing particle depends on the electric field to which the charge is exposed. In a fully depleted silicon detector the electric field as a function of the depth y inside the detector is found by solving the Poisson equation, yielding

$$E_d(y) = \frac{2yU_{fd}}{d^2} + \frac{U_{det} - U_{fd}}{d}, \tag{3.29}$$

where U_{det} is the voltage across the detector, U_{fd} is the full-depletion voltage and d is the thickness of the crystal. The first term of Eq. (3.29) describes the field due to the uncovering of the space charge. It is a function of the doping concentration of the material which enters the equation via the full-depletion voltage U_{fd}. Applying a voltage to the detector larger than the full-depletion voltage (over-depleting) results in an additional flat field component given by the second term of Eq. (3.29).

The relation between the drift velocity v and the electric field from Eq. (3.29), i.e. the mobility μ, is given by

$$v(y) = \mu E_d(y). \tag{3.30}$$

At room temperature the mobility of electrons and holes in very pure (sensor) silicon is 1450 and 450 $\mathrm{cm^2V^{-1}s^{-1}}$, respectively [82]. For very high electric fields the drift velocity saturates, but the field strength in a silicon detector is generally much less, except for highly irradiated sensors. Charge generated at point y_0 drifts towards the electrode in a time t which follows from Eq. (3.29) and (3.30):

$$t(y_0) = \frac{-d^2}{2\mu U_{fd}} \ln\left(1 - \frac{2U_{fd}(d - y_0)}{(U_{det} + U_{fd})d}\right). \tag{3.31}$$

A passing particle is presented by a charge deposition along the y-axis at $t = 0$ and at position x=z=0. In absence of the drift field, the charge will diffuse into the detector which leads to a charge distribution [83]

$$C(x, z, t) = \frac{q}{2\pi D_h t d} e^{-\frac{x^2+z^2}{4D_h t}}, \tag{3.32}$$

where D_h is the transverse diffusion coefficient of the charge carriers. The diffusion coefficient is given by the Einstein relation $\frac{kT}{e}\mu$, where T is the *effective* temperature of the charge carriers, which is higher than the ambient (lattice) temperature due to the velocity of the charge carriers. A value of 390 K was found from a fit to experimental data [83]. For strip-detectors with their strips aligned along the z-axis the charge will distribute along x. The amount of charge per strip is obtained by integrating Eq. (3.32) over the z-direction. Typical values for the width of the charge cloud at the collecting electrodes are 5 to 10 μm depending on the thickness of the detector and the applied bias voltage.

Charge sharing due to diffusion

If a particle traverses the detector in between two strips, the charge liberated by the particle will drift towards the strips. Because of the non-zero width of the charge cloud due to diffusion, the charge will be shared by two or more strips. The fraction of charge collected by a strip as a function of the distance to the strip is described by a so-called η-function. The ratio of the charge collected on the two nearest strips can be used to refine the position of the impact point of the particle. The resolution of a silicon sensor can be improved by implanting intermediate strips in between the readout strips. The fraction of the total charge seen on the readout strips in these detectors is to a large extent determined by the capacitive network formed by the strips and by the η-function. A drawback of this technique is that some of the charge remains (temporarily) on the intermediate strips. Therefore, the sum of the charge collected on the readout strips is not exactly equal to the liberated charge and, hence, to the energy deposited.

Charge sharing due to diffusion is an effect which is intrinsic to silicon sensors. The magnitude of the effect depends on the geometry of the strips in the sensor and the applied bias voltage. Another effect which influences the distribution of the signal over the strips is due to a combination of the detector capacitance and the readout electronics. This is the subject of section 3.4.6.

3.4.3 Lorentz angle

The electrons and holes that are liberated by the passing particle drift towards the collecting electrodes under influence of the electric field. If a magnetic field is present, the direction of motion of the electrons and holes is changed due to the Lorentz force. The magnetic field that surrounds the recoil detector is the holding field of the polarized target and has a maximum strength of 5 T. It can be directed either parallel or perpendicular to the electron beam to facilitate running both in longitudinal and transverse polarized mode [27, 36]. The equation of motion for an electron or hole in the presence of both an electric (drift) field and a magnetic field is given by

$$m\frac{d\boldsymbol{v}}{dt} = e\boldsymbol{E} + e\boldsymbol{v} \times \boldsymbol{B} - \frac{m\boldsymbol{v}}{\tau(v)}, \tag{3.33}$$

where the last term corresponds to the friction that the free charge undergoes in the crystal lattice with $\tau(v)$ being the mean free time between collisions.

In the situation where $\boldsymbol{E} \perp \boldsymbol{B}$ (see Fig. 3.12) the Lorentz angle becomes

$$\tan\theta_L = \mu_H \boldsymbol{B}. \tag{3.34}$$

The Hall mobility μ_H of electrons is about 15% larger than the drift mobility at room temperature [84, 85]. Holes, on the other hand, have a Hall mobility of only 70% of the drift value. Assuming the worst case situation where the magnetic field, with a

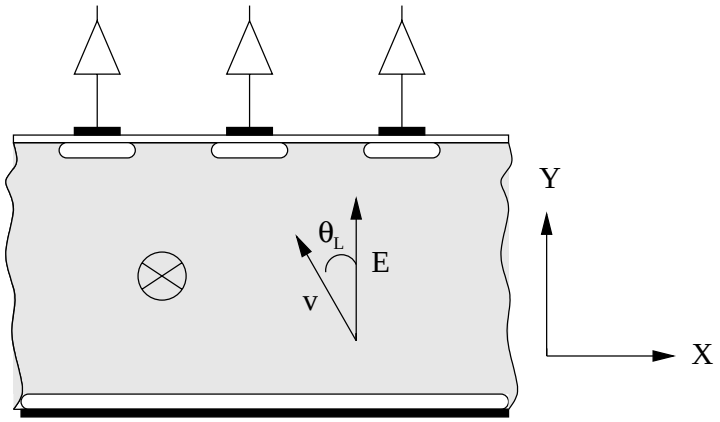

Figure 3.12: *Cross section of strip-detector with definition of coordinate axes and fields.*

magnitude of 5 Tesla, is perpendicular to the drift field, the Lorentz angles for electrons and holes are 38 and 9 degrees, respectively. Hence, the charge in a 300 μm detector will spread over a distance of 234 μm and 48 μm, respectively.

Charge Collection

Under influence of a drift field in the y-direction and a magnetic field in the z-direction (see Fig. 3.12) the charge drifts at the Lorentz angle relative to the y-direction. By integrating along y the charge distribution at the strips becomes[11]

$$f(x) = \frac{1}{d\sqrt{4\pi D_h}} \int_0^d \frac{dy}{\sqrt{t}\exp(-\frac{(x-y\tan\theta_L)^2}{4D_h t})}. \tag{3.35}$$

Figure 3.13 shows the distribution of charges along the x-axis, for a 300 μm detector in a 5 T magnetic field in the z-direction, obtained from Eq.(3.35). The distribution in absence of the magnetic field is shown as reference. The displacement of the charge is much less for holes than for electrons because of the lower mobility of holes in silicon. Note that Fig. 3.13 shows the worst and the best case of charge displacement. In an actual recoil detector, the orientation of the magnetic field with respect to the drift field will depend on the orientation of the sensors. To cover the total angular range, the sensors will be oriented with their normal both along the, and perpendicular to the direction of the magnetic field lines. Hence, the charge distribution due to the Lorentz angle depends on the orientation of the sensors.

[11] The width of the initial charge distribution can be incorporated into Eq. 3.35 by replacing t with $t + t_0$.

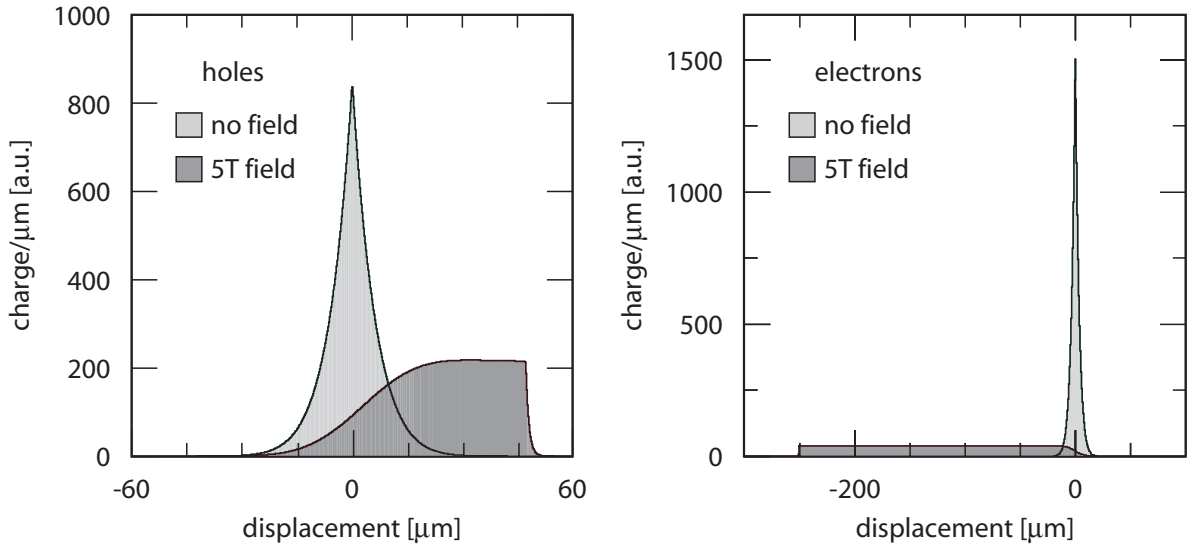

Figure 3.13: *Charge distribution in the x (strip) direction due to diffusion and drift in the presence of a 5T magnetic field.*

3.4.4 Signal induction

The signal induced on a readout strip of the detector by the moving charge depends on the geometry of the readout electrodes (strip implants). The current induced in the electrode by a single point charge is described by the Shockley-Ramo theorem [86]

$$i = -e\boldsymbol{v}\boldsymbol{E_w}, \tag{3.36}$$

where e is the unit of charge, $\boldsymbol{v}$ is the velocity of the electrons or holes given by Eq. (3.30) and $\boldsymbol{E_w}$ is the value of the weighting field[12] at the position of the moving charge. This weighting field $\boldsymbol{E_w}$ is the field in the detector which is obtained by raising the collecting electrode to unit potential while grounding all other electrodes. The weighting field has no relation with the drift field E_d which is determined by the bias voltage on the detector and by the doping profile of the silicon. The total current flowing into the electrode is

$$i(t) = \sum_Q Q(x, y, z, t)\boldsymbol{v}\boldsymbol{E_w}. \tag{3.37}$$

Here, Q is the distribution of the charge carriers in the detector due to the energy deposited by the passing particle. For an actual strip detector geometry both the weighting field and the drift field can be calculated by a Finite Element Analysis program like POISSON [87].

Figure 3.14 shows a simulation of the induced current in an n-type silicon strip detector with a strip width of 50 μm and a pitch of 100 μm. The full depletion voltage of the 300 μm thick detector was assumed to be 50 V and the operating voltage of the detector was taken to be 100 V. The track of the particle went through the center of the strip, and the ionization density along the track was assumed to be uniform. The

[12]The weighting field is not a conventional electric field; it is normalized to 1 and the unit is m^{-1} instead of $\mathrm{V{\cdot}m}^{-1}$.

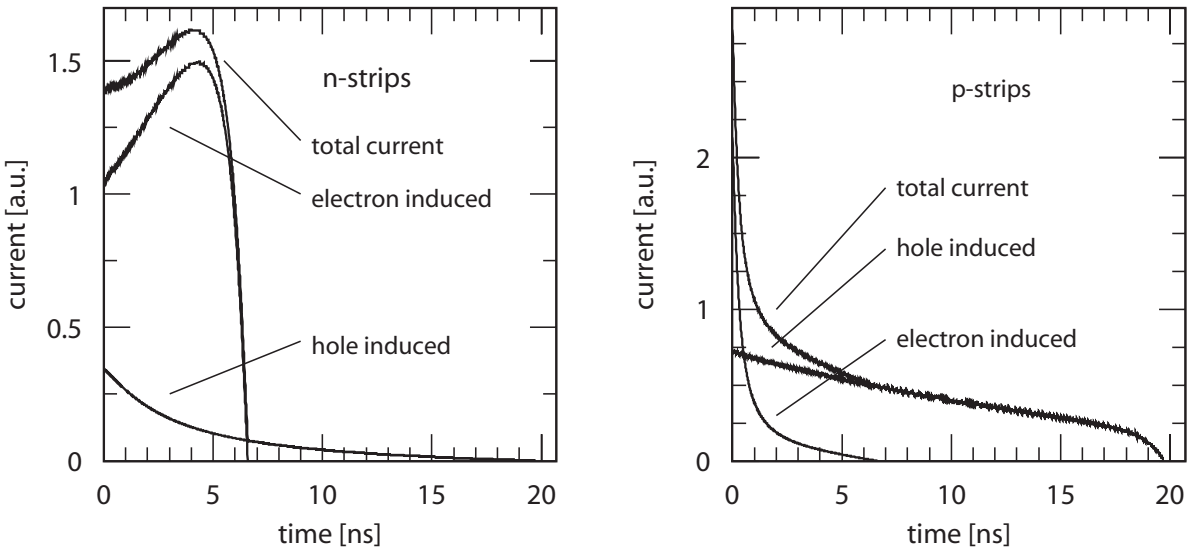

Figure 3.14: *Simulation of the induced current in the n-side strips (left plot) and p-side strips (right plot) of a 300 μm silicon detector. The total current is the sum of the electron induced and the hole induced currents.*

electron induced current dominates at the ohmic (n-strip) side of the detector, giving a $> 90\%$ charge collection within 7 ns. On the junction side (p-strips) the hole induced current contributes most to the total current and complete charge collection takes up to 20 ns because of the lower mobility of holes.

The silicon lattice was assumed to be perfect, i.e. trapping of charge carriers was not taken into account. For irradiated detectors this assumption is not valid and complete charge collection will not occur within the shaping time of the front-end amplifier.

3.4.5 Strip-detector capacitance

The detector-strip capacitance is an important parameter of a detector because it (i) may contribute to the charge sharing between the strips and (ii) determines the amplification of the thermal noise in the readout amplifier. The capacitance of a strip in a detector consists of two parts, the interstrip capacitance (C_{int}) and the strip-to-back capacitance (C_{back}). The corresponding empirical formulae are [88]:

$$C_{int} = 0.03 + 1.62\frac{w + 20\mu\text{m}}{p} \quad [\text{pF} \cdot \text{cm}^{-1}] \tag{3.38}$$

and

$$C_{back} = \epsilon_r\epsilon_0 \frac{p}{d + p[0.355(\frac{w}{p})^2 - 0.651(\frac{w}{p}) + 0.240 + 0.586(\frac{p}{w}) - 0.00111(\frac{p}{w})^2]} \quad [\text{pF}\cdot\text{cm}^{-1}], \tag{3.39}$$

where p and w are the pitch and the width of the strips, d is the thickness of the detector and $\epsilon_r\epsilon_0 = 1.05$ pF·cm^{-1} is the permittivity of silicon. Typical values of C_{int} and C_{back} range from 0.5 to 2, and from 0.2 to 0.8 pF·cm^{-1}. Equations 3.38 and 3.39

can be combined into a single expression, which can be used to estimate the total strip capacitance

$$C_{strip} = 0.83 + 1.67\frac{w}{p} \quad [\mathrm{pF} \cdot \mathrm{cm}^{-1}]. \tag{3.40}$$

The influence of these capacitances is further discussed in the next subsection.

3.4.6 Noise and charge sharing

Noise will degrade the accuracy of the measured amount of ionization. The main sources of noise are:

- Noise from the readout electronics.
- Noise from the leakage current of the detector.
- Noise due to trapping of charge in an irradiated detector.
- Noise from external causes, e.g. electromagnetic interference, ground reference currents.

Other noise sources which will be neglected are bias resistor noise, and noise due to the finite conductance of the metal interconnects.

It is very difficult to estimate the noise contribution from electromagnetic interference and other external noise sources. Often, this type of noise shows up as common mode noise which can be reduced effectively in the digitizing electronics. Furthermore, these sources often have a highly non-Gaussian character. In a well shielded and grounded detector the contribution of these noise sources is small. In the Monte Carlo study of Chapter 4 these noise sources are not modeled, but will be covered by the safety margin.

Noise in the readout electronics

Before going into some detail on noise in the readout electronics, a very brief introduction into charge sensitive read-out electronics is necessary. The focus will be on front-end electronics designed in CMOS processes. A functional diagram of a charge sensitive amplifier is depicted in Fig. 3.15. The front-end consists of an integrating preamplifier followed by a semi-Gaussian (RC-CR) shaper. The main source of noise is the noise

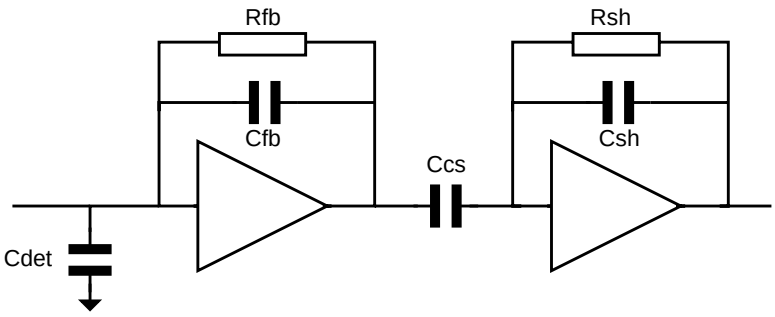

Figure 3.15: *Functional diagram of a charge sensitive amplifier consisting of an integrating preamplifier and a semi-Gaussian shaper.*

of the transistor at the input of the amplifier. The shaper is a band-pass filter which reduces the amount of noise from the preamplifier as seen on the output of the front-end.

The biggest noise sources of the input transistor are the channel noise and the flicker noise. Thermal channel noise is due to the resistance of the channel and has a white (flat) spectrum. Flicker noise depends on many parameters among which are the quality of the surfaces and interfaces in the transistor. It has a $1/f^x$ power density spectrum (with f representing the noise frequency) where x is close to unity. The contribution of the flicker noise to the total noise is independent of the time constant τ of the semi-Gaussian shaper[13]. For fast shaping front-ends the thermal channel noise is dominant and the noise power scales as [89, 90]:

$$\frac{i^2_{therm}}{df} = c_0 C_{in} \frac{\gamma_n kT}{g_m \tau}. \tag{3.41}$$

Here, γ_n is the combined excess noise factor plus a process dependent scaling factor which increases for deep sub-micron technologies [91], k is the Boltzmann constant, T is the absolute temperature, g_m is the transconductance of the first amplifier stage, τ is the characteristic shaping time of the semi-Gaussian shaper and C_{in} is the total capacitance seen at the input of the amplifier. The constant c_0 includes all other technology and circuit dependent factors. The simplest way to reduce the noise is to minimize the capacitance seen by the input of the amplifier, which can be done by making the detector elements smaller. The best example of this optimization is a pixel detector. The noise in strip and pixel detectors typically differ by a factor 10 which is mainly due to the small capacitance of a pixel compared to that of a strip. Noise can also be reduced by lowering the temperature; an example of a low-noise fast-shaping multi-channel amplifier operated at cryogenic temperatures is described in [92]. Increasing the shaping time τ of the front-end is a simple solution for lowering the noise in applications with a low strip occupancy, but is not possible for the proposed recoil detector due to the high background rate (see section 2.2.5). Another way to minimize the noise is to maximize the transconductance g_m of the preamplifier. For CMOS input stages operated in the weak-inversion region, the transconductance scales linearly with the current through the amplifier. The current should be maximized within the boundaries set by the power consumption.

Noise due to detector reverse bias current

The leakage current in the detector is a source of shot noise. The current spectral noise density of the source is [93]

$$\frac{\langle i^2 \rangle}{df} = 2eI, \tag{3.42}$$

where I is the DC-current through the detector segment and e is the unit of charge. This white noise only makes a significant contribution if the current in a single strip is high, for instance in a highly irradiated detector, or if the area of the detector strip is

[13] This can be understood from the fact that the difference of the logarithms of the corner frequencies of the shaper is a constant. Calculation of the noise by integrating the 1/f relation consequently results in a constant noise contribution.

very large. It will be neglected from now on because the sensors in the proposed recoil detector will be highly segmented, and also the total radiation dose will be modest (see section 2.2.6).

Charge sharing and equivalent noise charge

The noise seen at the output of the charge sensitive amplifier (Fig. 3.15) scales with the detector capacitance C_{det}. A larger value of C_{det} increases the noise contribution via the increase of the closed loop gain factor which is, in first order, determined by $1 + C_{det}/C_{fb}$.

A second effect related to the detector capacitance is charge sharing. Note that this is not the only cause for the sharing of charge over multiple strips. The sharing of charge due to diffusion is explained in section 3.4.2. Which of the two charge sharing effects dominates, depends on many factors like the detector geometry and the input impedance of the readout electronics.

The charge collected on a detector strip is divided capacitively between different amplifiers. Figure 3.16 represents the silicon strip detector and the read-out amplifiers as a network of capacitors. The quantities C_{int} and C_{back} represent the interstrip and strip-to-back capacitances of the detector as described in Section 3.4.5. The input impedance

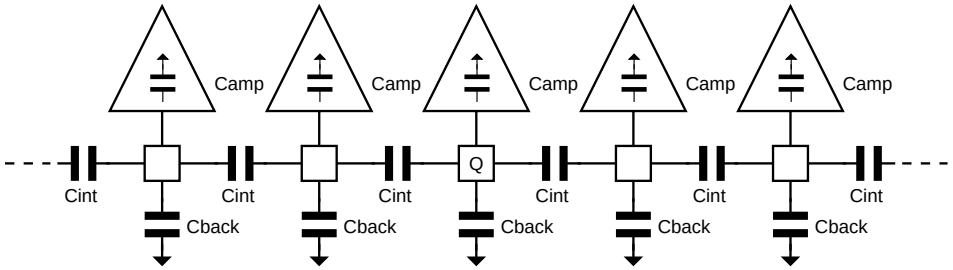

Figure 3.16: *Capacitive charge sharing in a strip-detector with matching read-out amplifiers.*

of the amplifier is taken into account in the capacitance C_{amp}[14]. This impedance depends on the value of C_{fb} and on the open loop gain of the amplifier and can only be assumed constant for a fixed shaping time τ. In the limit of a detector with an infinite number of strips, the fraction of the charge collected by the amplifier, connected to the strip that collected charge Q, can be shown to be

$$Q_{amp} = \frac{C_{amp}}{\sqrt{(C_{amp} + C_{back})^2 + 4C_{int}(C_{amp} + C_{back})}} Q. \tag{3.43}$$

The combined effect of increased noise and fractional charge gathering of the amplifier due to the detector capacitance is expressed in the Equivalent Noise Charge (ENC) specification. The ENC defines the noise in terms of the input charge which allows for a direct comparison to the amount of charge liberated in the detector. The ENC formula consists of a noise offset, which is a collection of various noise sources, and a noise slope

[14]For the frequency band of interest, the real input impedance is ohmic and not capacitive.

which denotes the dependence on input capacitance. Modern multichannel fast-shaping read-out chips for silicon strip detectors, such as the BEETLE [94] and SCTA[95], have an ENC figure of about 500 e^- + 50 $e^- \cdot pF^{-1}$. Readout chips for pixel detectors have noise levels in the order of 150 e^-.

Chapter 4

Monte Carlo studies

Particle identification via dE/dx sampling using multiple silicon layers seems to be the most viable option for the design of a recoil detector at a future fixed target DIS experiment. In this chapter the performance of such a silicon recoil detector is studied using Monte Carlo simulations. The results of several initial simulations are compared with published data on energy deposition in thin silicon detectors. Next, the set-up for the Monte Carlo studies is presented, followed by a discussion on the principle and limits of the momentum determination that can be achieved with a small multi-layered silicon detector. The second part of this chapter discusses the particle identification capabilities of a silicon dE/dx detector.

4.1 Some Monte Carlo aspects

4.1.1 Generating δ-rays

In GEANT4 [76], the Monte Carlo engine chosen for this project, the modeling of energy loss consists of two parts. Depending on the amount of energy lost by a particle, either a δ-ray is generated or the energy is deposited at the current position along the track. The threshold for generating δ-rays is under user control via a range cut. This cut determines the minimum range of a δ-ray (in meters) beyond which it will be tracked. GEANT4 converts the range cut to the corresponding minimum energy of a δ-ray. The default global cut-value of GEANT4 is 0.7 mm, which is too high to get a realistic energy deposition distribution in silicon. In order to reduce the simulation time, the number of δ-rays generated in the simulation should be chosen as low as possible, but should be high enough to produce realistic energy deposition straggling functions.

Figure 4.1 shows the simulated energy deposition distribution of 2 GeV$\cdot$c^{-1} protons in a 300 μm silicon sensor for different values of the range cut. Choosing a very high value of the cut overestimates the energy deposition because the escape of δ-rays from the sensitive detector volume is not taken into account. A very low cut value, on the other hand, drastically increases the simulation time. It has been determined that the shape of the energy deposition distribution remains almost the same, for a range cut of 20 μm and less. The range cut used for all the Monte Carlo simulations discussed in this chapter is 10 μm.

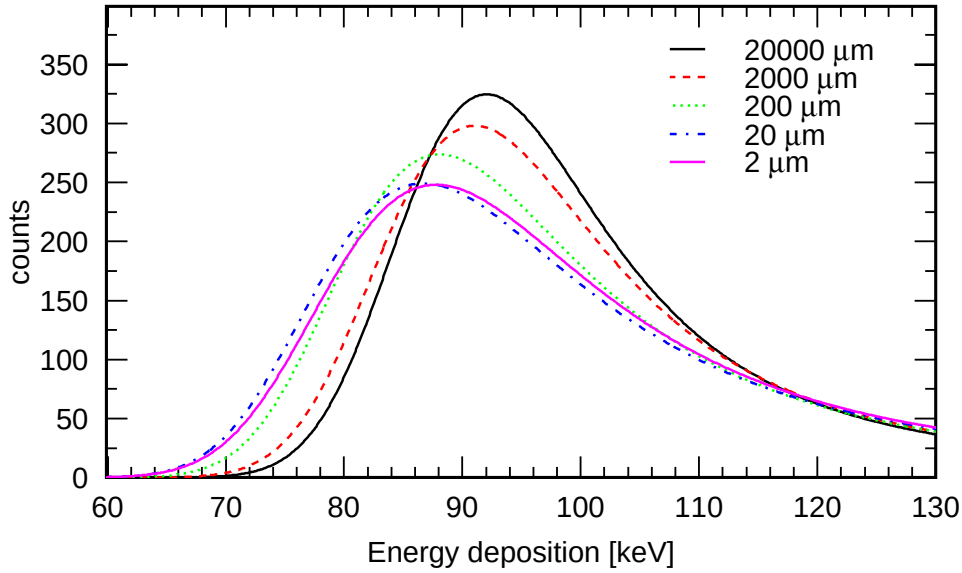

Figure 4.1: *Energy deposition distribution of 2 GeV·c^{-1} protons in 300 µm silicon for different values of the range cut in* GEANT4*. Using a high range cut, the escape of δ-rays from the sensitive detector volume is limited, which overestimates the energy deposition.*

4.1.2 Comparison to published measurements

Many articles on energy loss straggling in silicon have been published in the last 60 years, both on theoretical aspects and on measurements performed [66, 52, 51, 68, 96, 60]. For the current application, the interesting measurements are those on the energy deposition of pions, kaons and protons in the energy range of 100 MeV to 2 GeV. Many publications concern measurements for either much lower energies ($<$ 100 MeV), higher energies ($>$ 2 GeV), different particles (e^-,α) or do not include a proper calibration which renders them useless for comparison to the results of a Monte Carlo simulation.

Table 4.1 shows published data for pions and protons in the momentum range of interest. For some of the data, only a few characteristics such as the most probable energy deposition (Δ_{MP}) and the full width at half maximum of a distribution (ω) are given, while for others a complete plot of the energy deposition distribution is available. The latter type of information is preferred because this allows for a comparison of the full shape of the Monte Carlo distribution with a measured distribution, while for the (key) characteristics the shape of the Monte Carlo results and the measured distribution not necessarily have to match. Moreover, in some of the measurements listed in Table 4.1, very thick sensors were used which makes the comparison to the thin sensor used in the present Monte Carlo simulations difficult because energy deposition does not scale linearly with path length (see section 3.2.5). If we skip all these non-ideal data only a few measurements remain.

A comparison between two measurements (Hancock [68] and Bak [60]) and the corresponding GEANT4 results is shown in Fig. 4.2. The measured average energy deposition of 0.736 GeV·c^{-1} protons in a 300 μm thick sensor, as shown in the left plot, is higher than the simulated energy deposition. The difference cannot be explained by the accu-

Table 4.1: *Overview of published proton and pion data in the range of 0.2 to 2 GeV·c^{-1}.*

particle	p [GeV·c^{-1}]	thickness [μm]	Δ_{MP} [keV/mm]	data	reference
p	0.736	300	649	plot	[68]
p	1.000, 1.916	300	425, 313	$\Delta_{\mathrm{MP}}, \omega$	
p	0.679, 0.883	300	689, 499	$\Delta_{\mathrm{MP}}, \omega$	[69]
p	1.219, 1.343		370, 352		
p	1.522		332		
π^-	0.593	500, 1150, 1950	280, 293, 304	$\Delta_{\mathrm{MP}}, \omega$	[97]
p	0.831	2160	615	plot	[96]
p	1.379	464, 1772	337, 371	plot	[98]
π	0.490	1931	311	plot	[99]
p	1.379	2060	381	plot	
π^+/π^-	2.00	900	295, 288	Δ_{MP}	[49]
$\mathrm{p}/\overline{\mathrm{p}}$	2.00	900	315, 292	Δ_{MP}	[49]
π^+	2.00	32.0, 50.9, 100.3	219, 230, 258	plot	[60]
		174, 290, 1040	273, 268, 292		
p	2.00	32.0, 50.9, 100.3	224, 231, 269	plot	[60]
		174, 290, 1040	281, 284, 308		

racy of the measurements, which is claimed to be 6%. Also indicated in Fig. 4.2 is the most probable energy deposition from calculations [51]. The correspondence between the Monte Carlo simulation and the calculations of [51] is good.

Another comparison is shown in the right hand plot of Fig. 4.2, but now for 2 GeV·c^{-1} protons and a 100 μm sensor. This plot is representative for all data from reference [60]. The most probable energy deposition matches very well, but the width of the GEANT4 distribution is slightly smaller than the measured distribution, even after folding in the noise of the experiment as reported in [60]. The other data from Table 4.1 have also been compared to the Monte Carlo simulations and the correspondence is reasonably good. Although the amount of evidence is not overwhelming, the energy deposition straggling functions produced by GEANT4 are a good starting point for studying the performance of a future silicon dE/dx detector.

4.1.3 Configuration of simulated set-up

The proposed detector design consists of four concentric barrel silicon layers around the cylindrical target, complemented by four wheel shaped Si-detectors in the forward direction. The radius of the innermost barrel layer is 4 cm and the radius increases by 2 cm for each successive layer. The length of the barrel is 10 cm. The wheel shaped detector layers have a radius of 12 cm and are placed at equidistant positions between 12 to 18 cm from the target. A sketch of the set-up used in the Monte Carlo simulations is depicted in Fig. 4.3.

The total thickness of the four detector layers was kept constant; 1.28% X_0 for

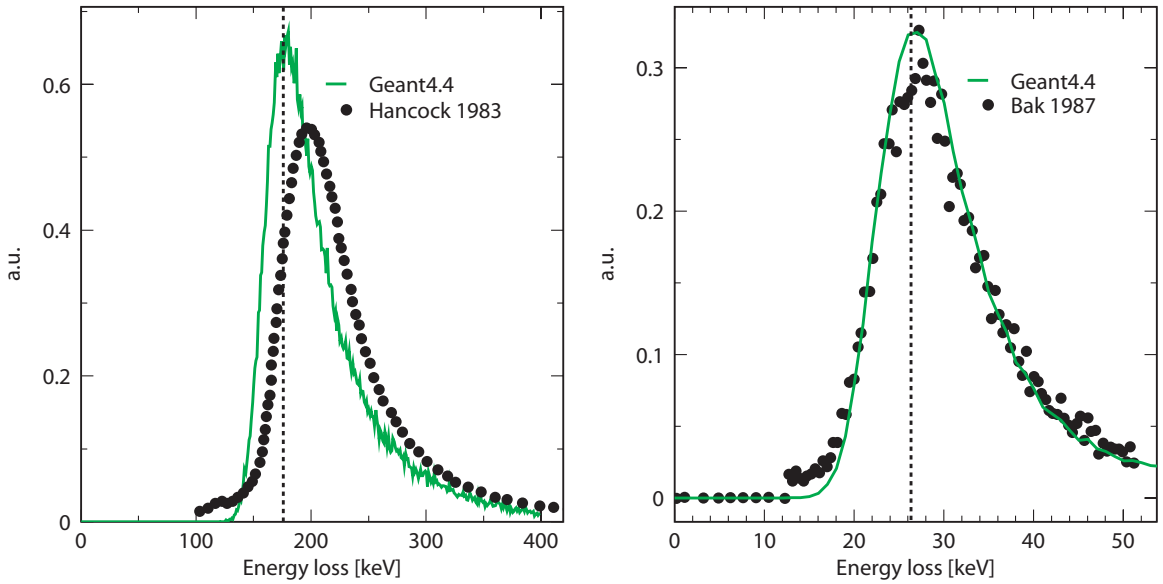

Figure 4.2: *Comparison of energy deposition distributions generated by a* GEANT4 *simulation with measurements reported in the literature. The left panel shows 0.736 GeV·c^{-1} protons in a 300 μ detector [68] and the right panel shows 2 GeV·c^{-1} protons in a 100 μm detector [60]. The data in the right panel is representative for all data from ref [60].*

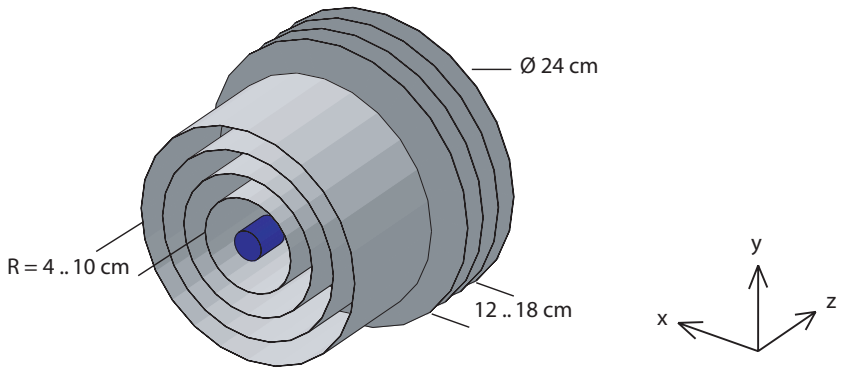

Figure 4.3: *Detector configuration used in the Monte Carlo simulations, consisting of four barrel layers surrounding a cylindrical target, complemented by four forward wheels.*

tracks at normal incidence, where X_0 denotes the radiation length in silicon. The configurations under study always consisted of four detector layers with a thickness equivalent to 300 μm of silicon per layer. Each layer consisted of either one, two or three silicon crystals with a thickness of 300, 150 and 100 μm, respectively, as shown in Fig. 4.4. For a fair comparison of the different configurations, the total number of readout strips per detector layer was kept constant, while the pitch is varied accordingly from 50 μm for the 300 μm crystals to 150 μm for the 100 μm crystals.

To reduce the simulation time of the Monte Carlo studies, not all studies are done by means of a full GEANT4 simulation but are done by sampling predefined energy deposition straggling functions. These energy deposition straggling functions have been

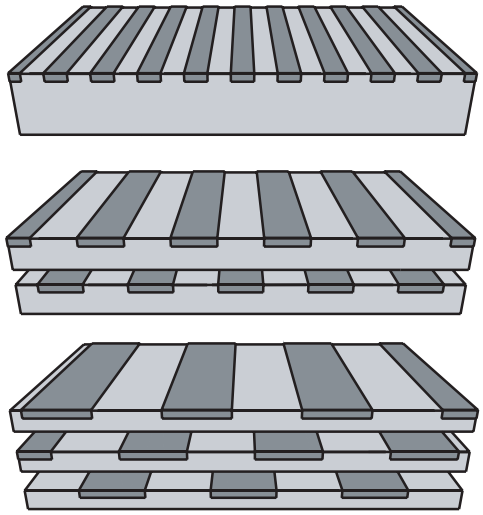

Figure 4.4: *Configuration of each detector layer used in the Monte Carlo simulation; one layer consists either of one, two or three silicon crystals with a thickness of 300, 150 and 100 μm, respectively. The pitch is adapted accordingly to keep the total number of strips constant.*

generated for electrons, pions, kaons and protons at 50 MeV·c^{-1} momentum intervals. The results of these sampling Monte Carlo studies have been verified at certain points and agree within 1% with a full GEANT4 simulation.

Noise and signal reconstruction

To make the simulations more realistic, several effects of the detectors and the read-out electronics are taken into account. A strip length of 10 cm is assumed, and the detector capacitance, calculated with Eqs. 3.38 and 3.39, is about 1.6 pF·cm^{-1} for a width to pitch ratio of 1:2. This results in a noise figure of 1300 electrons. A total noise of 1500 electrons is used in the simulations to have some safety margin which includes all other noise sources mentioned in the previous chapter. Note that this margin is as large as 750 electrons for uncorrelated sources.

Almost all of the tracks in the simulation cross the sensors at a non-perpendicular angle, and for most of the tracks the charge will therefore be deposited on more than one detector strip. The signal in neighboring strips must be added for a complete signal reconstruction, which increases the noise and thereby reduces the signal to noise ratio. For the sampling Monte Carlo studies, the signal is scaled linearly with path length; the small error introduced in this way (<0.5%, see section 3.2.5) has a negligible effect on the results. Noise is added to all strips that collected (a fraction of the) charge, both in the full GEANT4 simulation and in the sampling Monte Carlo.

Lorentz angle

The presence of a magnetic field causes the liberated charge in the sensors to drift at the Lorentz angle with respect to the direction of the electric field (see section 3.4.3). As a result, the charge will spread over more than one strip. In the Monte Carlo model, the charge is assumed to be collected on the junction side which has the least charge spread because the signal is mainly induced by the movement of holes which drift at a smaller Lorentz angle. A Lorentz angle of 9 degrees is used in all simulations; the corresponding width of the charge distribution at the collecting electrode is 3.2 μm·T^{-1} per 100 μm of

detector thickness. The charge spread due to diffusion adds another 5 to 10 μm to the width of the distribution. If the distance from the center of the track to the boundary of the strip is smaller than the width of the charge distribution, the charge is shared with the neighboring strip.

4.2 Momentum determination

In the envisaged detector configuration at a future high-luminosity fixed-target DIS experiment, the recoil detector is the only one covering large detection angles, and is not backed by any other detector because of the large amount of material in the target magnet. For dE/dx-based particle identification, the momentum of the particle must be determined because it is used for selecting the proper energy deposition distributions which are needed for the identification methods described in section 3.3.4 and 3.3.5. Hence, the recoil detector must also determine the momentum of particles emerging at large angles. This can be accomplished by measuring the curvature of the tracks in the 5 T magnetic holding-field of the target.

Charged particles traveling through a constant magnetic field describe helical paths. For a known magnetic field, the momentum of the particle can be determined from the parameters that describe this path. If the momentum of the particle is constant, it can be expressed as

$$p = \frac{0.3BR}{\cos\alpha}, \tag{4.1}$$

where B is the magnetic field strength in Tesla, R is the radius of the circle that can be drawn through the coordinates of the particle trajectory orthogonal to the direction of the field, and α is the pitch angle (which is defined in Eq. 4.2). If the direction of the field is assumed to be along the z-axis, the radius R can be obtained by fitting a circle through the x- and y-coordinates. The fast circular fit routine that is used in this study is documented in [100]. The pitch angle is given by

$$\alpha = \arctan(\frac{1}{R\lambda}), \tag{4.2}$$

where λ is the slope of the line through the z-ϕ points. Here, ϕ is defined as $\arctan(\frac{y-y_0}{x-x_0})$, where x_0 and y_0 are the centers of gravity of the x- and y-coordinates, respectively.

The accuracy of the momentum determination depends on the resolution of the coordinates as determined by the silicon sensors. Moreover, the interaction of the charged particle with the detecting material gives rise to deviations from the ideal helical path and, hence, also reduces the accuracy of the momentum determination. These deviations are primarily caused by multiple Coulomb scattering and, to a lesser extent, by the energy loss. The energy loss reduces the momentum of the particle and thereby the radius R of the circle. However, the slowing down of particles due to energy loss is only significant for very low energy particles and in these cases momentum determination needs not to be very accurate because the particles can be identified by their differences in energy deposition in the Si-sensors, as explained in Section 3.3.1.

The Gaussian approach to multiple scattering for small angles as defined by the Molière formalism is [70]

$$\theta_{plane}^{rms} = \frac{13.6\text{MeV}}{\beta cp} z \sqrt{\frac{d}{X_0}} \left[1 + 0.038 \ln\left(\frac{d}{X_0}\right) \right]. \tag{4.3}$$

Here, p is the momentum of the particle and X_0 and d are the radiation length and the thickness of the absorber, respectively; the other quantities are defined in Section 3.2.3. Multiple scattering increases towards low momenta due to the dependence on p and β.

The reconstructed momentum will be different from the true momentum of the particle due to the resolution of the measured coordinates, multiple scattering and energy loss. The distribution of the reconstructed momentum resembles a Gaussian shape and therefore the standard deviation (σ_p) of a fit to this distribution is used as a measure for the accuracy. The mean of the (fit of) the distribution is equal to the true momentum.

Figure 4.5 shows the width of the distribution of the reconstructed momentum as a function of momentum, obtained with the detector configuration shown in Fig. 4.3 consisting of four layers of 300 μm silicon. The angles of the various particles were

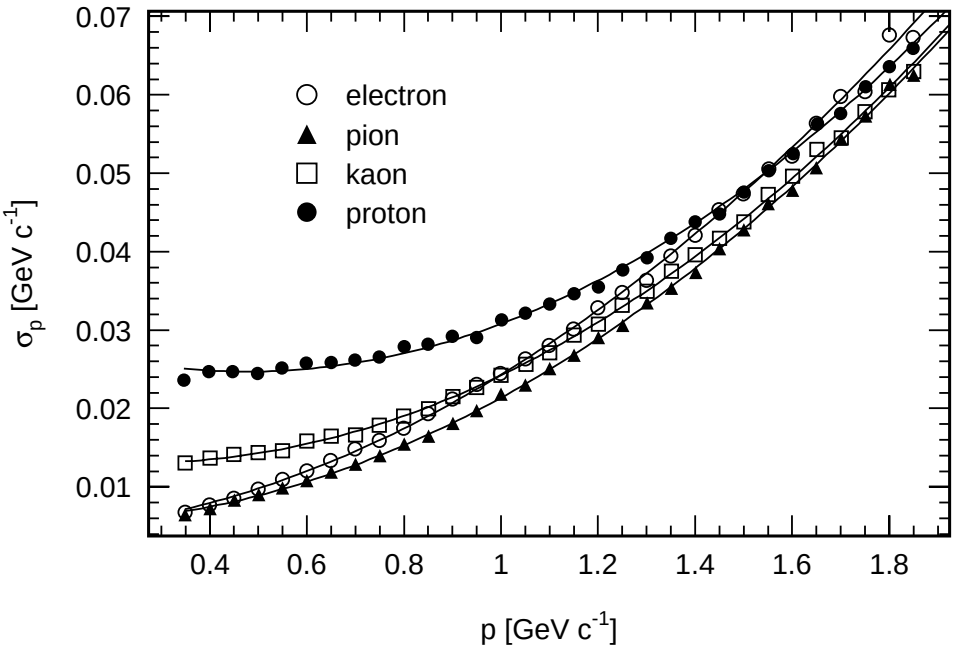

Figure 4.5: *Width of the reconstructed momentum distribution versus the (reconstructed) momentum for the simulated detector configuration of Fig. 4.3. The (statistical) error bars are too small to be visible.*

generated isotropically in the lab-frame with a polar angle range of 0.175 to 1.4 radians. The magnetic field was oriented in the z-direction and the target was absent.

The coordinates that are needed for the momentum reconstruction algorithm are derived from the digitized strip information. When more than one strip in a detector layer is hit, which is the case for most of the tracks, the coordinates are determined by the center of gravity method where the weight factors are given by the amount of energy deposited in the strips.

At low particle momenta the increase of the width of the distribution due to multiple scattering is compensated for by the decrease of the radius of curvature (R), i.e. for small radii the sensitivity for the accuracy of the spatial coordinates is less. At high particle momenta, the accuracy of the reconstructed momentum decreases because of the accuracy of the spatial coordinates prevents a precise determination of the weak curvature.

The curves of the hadronic particles merge at large momenta because the effect of multiple scattering becomes independent of the particle type (and also becomes very small). Hence, the momentum resolution only depends on the geometry of the set-up. The electron curve, however, shows a steeper increase with momentum which is due to bremsstrahlung. For the bremsstrahlung process, the amount of radiated energy increases with momentum and hence the deviation from the ideal helical path becomes larger. The effect is only significant for electrons in the envisaged momentum range. Similar figures were obtained for the transverse magnetic field configuration.

The momentum resolution that can be obtained with a 4 layer detector in a strong (5T) magnetic field ranges from 25 MeV·c^{-1} for 0.8 GeV·c^{-1} protons to 40 MeV·c^{-1} for 1.3 GeV·c^{-1} protons.

4.3 Particle identification

In order to compare different particle identification algorithms, a definition of terms is necessary. The results using different analysis algorithms as described in Sections 3.3.3, 3.3.4 and 3.3.5 will be expressed in terms of efficiency and purity. These parameters, adapted from [101], are derived from the probabilities and flux factors in the following subsections. In subsections 4.3.3 and 4.3.4 the sensitivity of these particle identification parameters to various aspects of the proposed detector system are investigated.

4.3.1 Definition of efficiency, contamination and purity

As the performance of the detector depends on the kinematics of the particles, all of the parameters are functions of momentum and angle. To simplify the reading of the definitions, these dependencies are implicitly assumed. For every particle we now define the true particle type which is known from the Monte Carlo simulation[1]. The identification algorithm assigns a reconstructed particle type to every particle. In case the algorithm cannot uniquely identify a particle, the particle is labeled as X.

The simplest observable is N_t^r, the number of particles of true type t that are identified as reconstructed type r. In our case where we want to distinguish between pions, kaons and protons, these numbers comprise the 4×3 matrix shown below.

$$\mathbf{N} = \begin{pmatrix} N_\pi^\pi & N_K^\pi & N_p^\pi \\ N_\pi^K & N_K^K & N_p^K \\ N_\pi^p & N_K^p & N_p^p \\ N_\pi^X & N_K^X & N_p^X \end{pmatrix} \tag{4.4}$$

[1] In an actual detector this information can only be obtained from other particle identifying detectors and from decaying particles with known decay products.

Flux factors

The flux factor Φ_t is defined as the number of true type particles that cross the detector in a given time interval, independent of the particle type obtained from reconstruction:

$$\Phi_t = \frac{\sum_i N_t^i}{\Delta t}. \tag{4.5}$$

A more convenient definition is the relative flux factor ϕ_t, being the number of true type particles in the total particle sample,

$$\phi_t = \frac{\sum_i N_t^i}{\sum_j \sum_i N_j^i}. \tag{4.6}$$

The relative flux factor is a dimensionless quantity.

Probability and efficiency

The probability P_t^r to identify a particle of true type t as a particle of type r, is defined as

$$P_t^r = \frac{N_t^r}{\sum_i N_t^i}. \tag{4.7}$$

This gives a matrix $\mathbf{P}$ which can be derived from matrix $\mathbf{N}$ (Eq. 4.4) by normalizing over the columns. The fields on the main matrix diagonal are the identification efficiencies ϵ_t for the various particles,

$$\epsilon_t = P_t^t. \tag{4.8}$$

Note that the efficiencies do not depend on flux factors because of the column-wise normalization.

Only the efficiency of the PID algorithm is taken into account, i.e. detector efficiencies are assumed to be unity for all particles.

Contamination and purity

Normalization over the rows of matrix $\mathbf{N}$ (Eq. 4.4) leads to the so called true type probabilities Q_t^r. This is the probability that a particle which is identified as type r really is of type t

$$Q_t^r = \frac{N_t^r}{\sum_i N_i^r}. \tag{4.9}$$

The off-diagonal elements are the contaminations c of true-type particles t in a dataset of reconstructed particle type r

$$c_t^r = Q_t^r \qquad t \neq r. \tag{4.10}$$

Contaminations depend on the flux factors as can be seen from

$$c_t^r = \frac{P_t^r \phi_t}{\sum_i P_i^r \phi_i}. \tag{4.11}$$

The purities $\mathcal{P}$ are the diagonal elements of the $\mathbf{Q}$ matrix

$$\mathcal{P}_t = Q_t^t. \tag{4.12}$$

4.3.2 PID performance

The results presented below are either analyzed with the truncated mean method (see section 3.3.3) or with the maximum likelihood method (section 3.3.4). The results of the Kolmogorov-Smirnov test are not shown explicitly because they are very similar to the maximum likelihood method for Monte Carlo data, except for the momentum dependence which is the subject of section 4.3.4. The estimated statistical uncertainty is less than 1% and the maximum difference between the Monte Carlo distributions and the published data [60] is estimated to be smaller than 3%.

Table 4.2 shows the results of the Monte Carlo simulations analyzed with the maximum likelihood method. The figures in the table represent the maximum momenta at

Table 4.2: *Maximum momenta in GeV·c^{-1} up to which particle identification is possible with an efficiency of 0.8 based on the maximum likelihood method. The numbers in parentheses are the corresponding purities assuming the same flux factors for all particles. The estimated error is less than 0.01 GeV·c^{-1} .*

	Efficiency ϵ=0.8		
	100 μm	150 μm	300 μm
e^-	0.21 (0.83)	0.21 (0.83)	0.20 (0.85)
π	0.22 (0.78)	0.22 (0.77)	0.22 (0.76)
K	0.78 (0.72)	0.79 (0.71)	0.77 (0.68)
p	1.44 (0.64)	1.44 (0.63)	1.42 (0.58)

which particle identification is possible with an efficiency of 0.8, which is assumed to be the minimum efficiency for meaningful particle identification. All numbers are mean values averaged over angles from 0 to 45 °. Also the average of the results with B-fields of 0 and 5 Tesla is taken. The numbers in parentheses are the corresponding purities.

Separating pions from electrons is virtually impossible for momenta larger than 0.2 GeV·c^{-1}. This will, however, not be a problem as the main purpose of the recoil detector is proton identification. The maximum momentum at which kaons and protons can be identified with an efficiency of 0.8 is marginally different for the three configurations under study. However, the configuration with the 100 μm detectors has a better purity compared to the 300 μm configuration.

The proton identification efficiency and purity as a function of particle momentum are shown in Fig. 4.6 for the three simulated configurations. Both the efficiency and the purity are close to 1 for momenta up to 1 GeV·c^{-1}. Although the difference in efficiency for the different configurations is small, a better purity (and a slightly better efficiency) is obtained by using 8 detectors of 150 μm or 12 detectors of 100 μm.

Looking at the results of a similar analysis using the truncated mean method instead (see Table 4.3), we see a 10% improvement for the kaon and proton case when decreasing the detector thickness. The efficiency and the purity are in this case both fixed at 0.8. Comparing the truncated mean results with the maximum likelihood results presented in Table 4.2, while taking into account the trade-off between efficiency and purity, gives similar results for thin detectors.

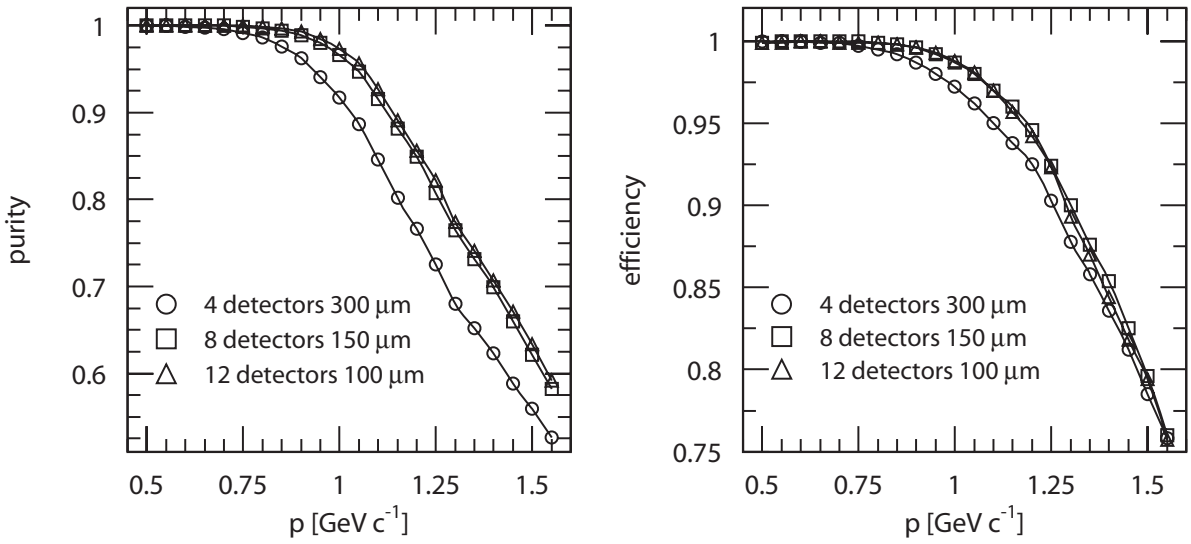

Figure 4.6: *Proton identification purity and efficiency as a function of momentum for the three different detector configurations. In this analysis the maximum likelihood method was used. There is no significant difference for $n = 8$ or $n = 12$ detectors. The estimated error is less than 0.01 GeV·c^{-1} .*

Table 4.3: *The maximum momenta in GeV·c^{-1} up to which particle identification is possible with an efficiency and purity of 0.8 using the truncated mean method.*

	Efficiency ϵ=0.8 and Purity $\mathcal{P}$=0.8		
	100 μm	150 μm	300 μm
e^-	0.22	0.22	0.21
π	0.22	0.22	0.21
K	0.75	0.73	0.67
p	1.35	1.32	1.18

4.3.3 Noise and thickness dependence

In all the Monte Carlo simulations, the noise was fixed at 1500 electrons and the total amount of material was also kept constant at 1.28% X_0. In this section the dependence of the identification efficiency on the total noise and on the amount of material is looked into. The simulation data are analysed with the maximum likelihood method.

Figure 4.7 shows the dependence of the maximum momentum for identifying kaons versus the number of layers and versus the noise, under the condition that the efficiency is at least 0.8. The number of layers in the left plot ranges from 4 to 16 layers of 150 μm, which is from half to double the number of layers compared to the default configuration. The noise in this left-hand plot is fixed at 1500 electrons. For a large number of layers the maximum momentum slowly saturates at the momentum where the straggling function of the kaons overlaps with that of the (relativistic) pions and electrons. If the number of detectors is less than four, the efficiency drops rapidly.

The dependence of the maximum momentum for particle identification as a function

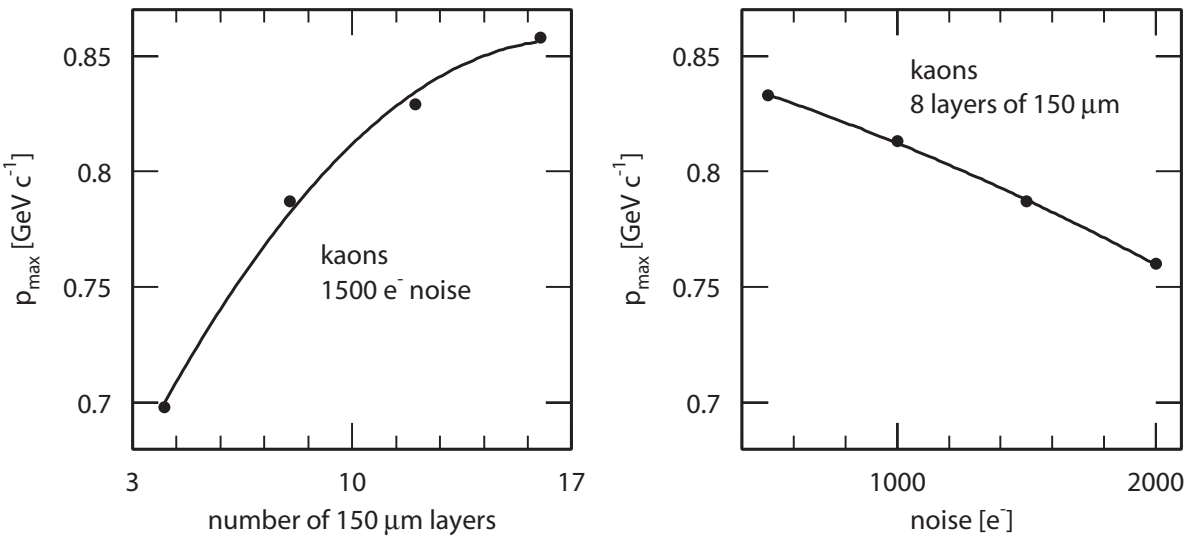

Figure 4.7: *The maximum momentum up to which identification of kaons is possible versus the number of 150 µm Si layers (left plot) and the amount of noise (right plot) for an efficiency of 0.8. Lines are drawn to guide the eye.*

of noise level is shown in the right hand side of Fig. 4.7. A 3% gain in the maximum momentum can be achieved by a 30% reduction in the noise (reduction from 1500 to 1000 e^-). The dependence on noise is not very strong because the noise only adds to the width of the already wide energy deposition distribution.

4.3.4 Sensitivity to momentum determination

The momentum of the particle must be determined by the envisioned recoil detector because it is needed to select the correct reference distribution for both the maximum likelihood method and the Kolmogorov-Smirnov test. In section 4.2 the accuracy of the momentum determination has been studied and the standard deviation on the reconstructed momentum of protons was found to vary from 25 MeV·c^{-1} for low momenta to about 40 MeV·c^{-1} for the required upper momentum limit of the recoil detector (1.3 GeV·c^{-1}).

The purity and efficiency for proton identification using the maximum likelihood method with an offset (Δp) on the reconstructed momentum (p) is shown in Fig. 4.8. Underestimating the momentum (negative Δp) drastically decreases the efficiency. Overestimating the momentum slightly increases the efficiency, but at the cost of a reduction in purity. Note that the situation presented in Fig. 4.8 is an extreme case because the momentum is over- or underestimated for *all* events in a run. The -50 MeV·c^{-1} offset corresponds to a 2σ error which is only the case for 2.3% of the events.

The sharp drop in efficiency at *low* proton momenta seems to be counterintuitive, but can be explained by the fact that the proton straggling function is a strong function of the momentum in this momentum range. Comparing the dE/dx samples to a reference distribution which belongs to a too low momentum means that many of the dE/dx samples will be smaller than the most probable value of the reference distribution.

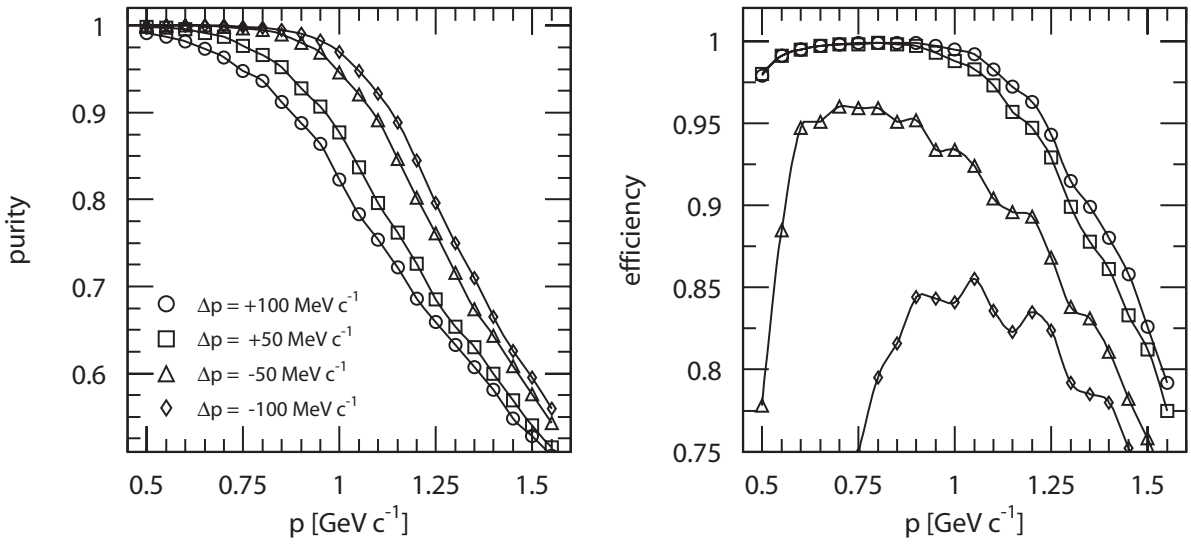

Figure 4.8: *Proton purity and efficiency as a function of momentum for various offsets (Δp) on the reconstructed momentum. The Monte Carlo data are analyzed using the maximum likelihood method. The drop in efficiency is discussed in the main text.*

Because the slope of an energy deposition distribution is steep on the low energy side, some of the dE/dx samples will be assigned a probability of zero. The likelihood is defined as the product of the probabilities of the samples, thus a single sample with probability zero will yield a zero total likelihood. Hence, the events with zero proton likelihood will be identified as kaons because the kaon likelihood will not be zero due to the long tail of the (kaon) distribution on the high energy side.

The Kolmogorov-Smirnov (KS) test is somewhat less sensitive to outlying samples. Figure 4.9 shows the momentum dependence of the efficiency and purity when using the KS-test. Although the efficiency drop at low momenta is smaller than for the maximum likelihood method, also the KS-test misidentifies slow protons.

4.4 Summary

Identification of protons with momenta up to 1.3 GeV·c^{-1} and with an efficiency of more than 0.8 seems to be possible with a detector consisting of four silicon layers. Given a fixed material budget, it is slightly advantageous to use 8 layers of 150 μm thick silicon instead of 4 layers of 300 μm.

To evaluate the total proton identification efficiency, the efficiency as a function of momentum, shown in Fig. 4.6, should be folded with the momentum distribution of the processes under study. Estimating the total (proton) purity is much more difficult because for that purpose the relative fluxes of all particles in all processes, including the background processes, need to be known.

The influence of the noise of the readout electronics on the maximum achievable momentum for a given efficiency is modest. A 30% decrease in noise only gives a 3% increase of the momentum limit at a PID efficiency of 80%. If was found that the

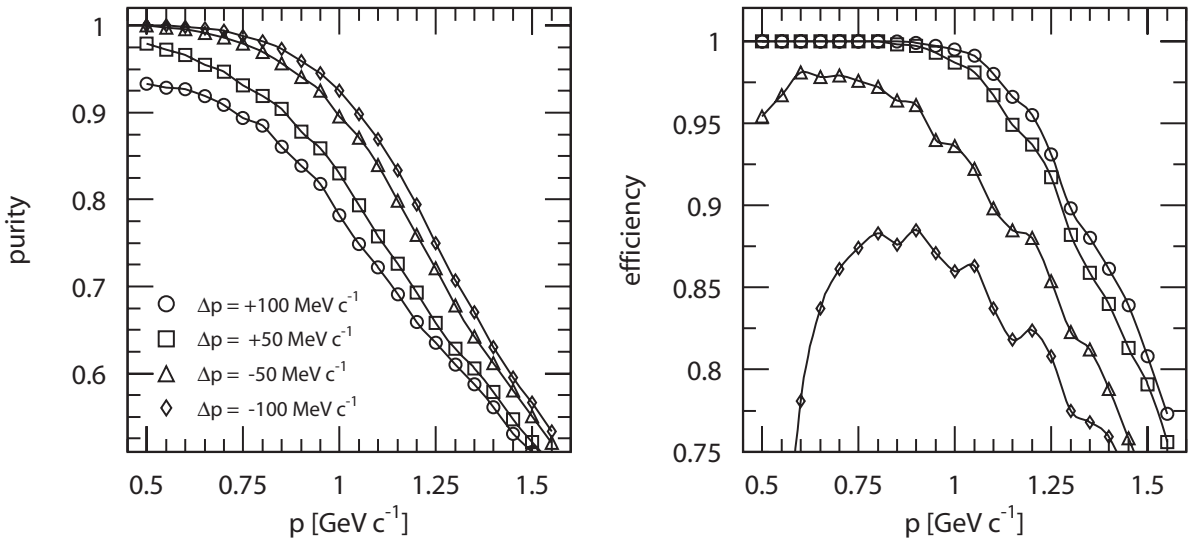

Figure 4.9: *Proton purity and efficiency as a function of momentum for various offsets (Δp) in the reconstructed momentum. The Monte Carlo data are analyzed using the Kolmogorov-Smirnov test.*

momentum resolution that can be achieved with a four layer silicon telescope ranges from 25 to 40 MeV·c^{-1} for charged particles with a momentum of 0.8 and 1.3 GeV·c^{-1}, respectively.

It should be noted that all results in this chapter are obtained from Monte Carlo simulations. The energy deposition distributions generated by Monte Carlo simulation have been compared to energy deposition data published in the literature. The number of published energy deposition measurements in the energy regime considered in this thesis is, however, limited. Hence, the Monte Carlo results should be confirmed by further experimental data. The next chapter describes an experimental study of pion-proton separation in a multi-layer silicon telescope.

Chapter 5

Experimental study of proton-pion separation in a multi-layer silicon telescope

In the previous chapter the feasibility of particle identification based on energy deposition in silicon was studied by carrying out Monte Carlo simulations. Identification of protons seems to be possible with an efficiency of 80% up to a momentum of 1.3 GeV·c^{-1}. However, these results strongly depend on the energy deposition distributions produced by GEANT4. The lack of a wide range of calibrated energy deposition data other than the mean value of the energy deposition, makes the validity of the Monte Carlo studies uncertain. Additional experimental data on the energy deposition distributions of pions and protons in silicon are needed to validate the conclusions obtained in the previous chapter.

This chapter describes an experiment that has been carried out at one of the CERN Proton Synchrotron (PS) beams. The aim of the experiment is to accurately determine the energy deposition distributions of pions and protons in silicon at selected momenta between 0.8 and 1.3 GeV·c^{-1}. These energy deposition distributions are subsequently used to determine the particle identification capability of a detector consisting of several layers of silicon sensors.

Important factors in the experiment and the subsequent analysis are the accurate determination of the energy deposition in the sensors and the independent particle identification by means of the time-of-flight technique. Tracking of the particles with a high accuracy is not needed because it is only used to resolve hit ambiguities which are rare because of the low beam intensity.

This chapter is organized as follows. The chapter starts with a description of the experimental set-up followed in section 5.2 by a discussion of the analysis of the time-of-flight data, which provides independent information on the particle type. The second part of the chapter focuses on the analysis of the data from the silicon detectors. Section 5.3 describes the calibration of the silicon data and in section 5.4 the energy deposition distributions are determined and compared to the Monte Carlo distributions presented in the previous chapter. The chapter ends with a study on the particle identification capabilities of the silicon telescope used in this experiment.

5.1 Experimental set-up

5.1.1 Beam-line

The experimental set-up was operated at the CERN T11 beam-line in the PS east hall complex. Figure 5.1 shows the T11 beam-line, from the extraction point at the PS machine to the focus point in the experimental area. The 20 GeV·c^{-1} proton beam

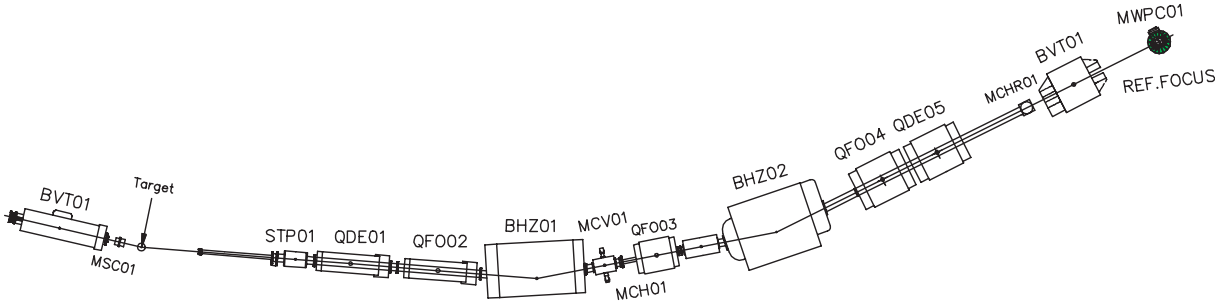

Figure 5.1: *Layout of the* T11 *beam-line. The production target on the left is common for beam-lines* T11, T10 *and* T9. *The latter two beam-lines are not shown. Magnet* BHZ01 *and collimator* MCV01 *determine the momentum of the particles in the experimental area.*

from the PS is directed onto a production target common for beam-lines T9, T10 and T11. Magnet BHZ01 and collimator MCV01 are used for momentum selection of the secondary particles. The mean momentum at the focus point can be tuned by changing the current of the momentum selecting magnet (BHZ01). Operating the collimator MCV01 with a default slit opening of 7 mm gave a $\Delta p/p$ of about 1%. Table 5.1 lists the other main specifications of the T11 beam.

Also shown in Fig. 5.1, in front of the last (vertical) bending magnet, is a Cherenkov counter (MCHR01). The walls of the Cherenkov detector are constructed from three layers of mylar foil with a thickness of 0.7 mm each. The Cherenkov counter was operated at atmospheric pressure with air as detection gas, which gives a detection threshold corresponding to a boost factor γ of about 50. This means that only positrons (and electrons) will emit Cherenkov light. The Cherenkov detector is therefore used as a positron veto in the analysis.

The Multi Wire Proportional Chamber (MWPC01), shown on the right-hand side of Fig. 5.1, was not operational but was present in the path of the beam. It has a radiation length equivalent to 0.1 mm of aluminium.

Mixed particle beam

The secondary beam was produced by bombarding an aluminium target with 20 GeV·c^{-1} protons. Two targets have been used; an Al target of 200 mm thickness, and a 100 mm Al target followed by a 3 mm tungsten plate. The latter target gives an electron enriched beam for very forward angles. Because the T11 beam-line has a production angle of 149.5 mrad with respect to the primary beam, only a small fraction of the particles

Table 5.1: *Main specifications of the* T11 *beam-line at the* CERN PS *accelerator complex.*

Maximum design momentum [GeV·c^{-1}]	3.5
Length at reference focus [m]	28
Horizontal production angle [mrad]	148.36
Vertical production angle [mrad]	16.06
Horizontal angular acceptance [mrad]	± 6.2
Vertical angular acceptance [mrad]	± 19.7
Horizontal magnification at momentum slit	3.6
Dispersion at momentum slit [mm / %$\Delta p/p$]	7.5
Theoretical momentum resolution (%)	1.9
Optical characteristics at reference focus:	
Horizontal dispersion [mm / %$\Delta p/p$]	0
Vertical dispersion [mm / %$\Delta p/p$]	1.1
Horizontal magnification	0.7
Vertical magnification	1.3
Calculated beam cross section for full beam angular acceptance and $\Delta p/p = \pm 1\%$ [mm^2]	18(hor.)×10(vert.)

traversed the tungsten plate and hence no significant difference in beam composition was seen for the two target types.

The beam was composed of positively charged particles; mainly protons, pions and positrons. Some other positive particles like deuterons, kaons, muons and alpha particles are also present in the beam, but their numbers are very low.

During the experiment, the PS-cycle had a period of 16.8 seconds. The T11 experimental area received its beam from a slow extraction cycle in which a burst of about 2×10^{11} protons were dumped on the target in a time of 600 ms.

Silicon detector set-up

The silicon detector set-up was positioned 2 meters behind the reference focus point, i.e. 30 meters downstream from the production target. A schematic diagram of the detector set-up is shown in Fig. 5.2. The set-up consisted of eight silicon detectors to measure the energy deposition and four scintillators to generate the trigger and to measure the Time-of-Flight (TOF) of the particles. The first scintillator was placed in front of the first silicon module and the second scintillator right after the last silicon module. The other two scintillators were placed at a distance of more than 4 meters behind the first scintillator to make a sufficiently long path for the TOF system. More details about the TOF measurement are given in section 5.2.

The first four silicon sensors are part of two so-called Lambda Wheels (LW) modules, which are described in more detail in section 5.1.2. Although two sensors mechanically constitute one LW module, they will be treated as two separate units; the LW modules are labeled LW1 to LW4. The other four sensors, labeled BT1 to BT4, belong to a Beam Telescope; these modules are described in section 5.1.3.

The silicon detectors were enclosed (as a group) by a light-tight aluminium box.

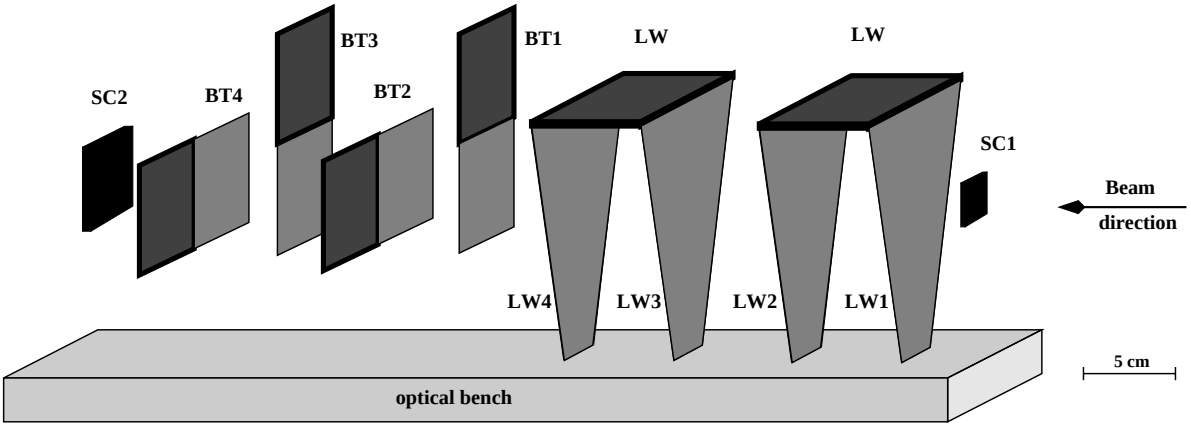

Figure 5.2: *Schematic drawing of the experimental set-up. The set-up consisted of eight double sided silicon detectors used for the energy deposition measurements. The active area of the silicon counters is indicated in light gray. The dark gray, framed, rectangles show the position of the front-end electronics. Two small trigger scintillators, one in front of and one behind the silicon stations, are mounted on the same optical rail.*

Holes were made in the front and back side of the box at the height of the beam to reduce momentum straggling and multiple scattering. The holes were covered with black plastic foil with a thickness of 100 μm.

Cooling of the front-end electronics was achieved by circulating air inside the box with fans. The surface area of the box was large enough to remove the heat ($\sim$25 Watts) with an acceptable rise in temperature. By measuring the dark current of the silicon sensors, we found that the temperature of the air inside the box increased by 6 to 8 degrees when switching on the readout electronics[1].

Material in the beam-line

The distance from the momentum selecting slit to the first scintillator is about 19 meters. As the beam runs through air, its momentum decreases over this distance, on average, by 15 MeV$\cdot$c^{-1} for protons with an initial momentum of 0.8 GeV$\cdot$c^{-1}. For pions with the same initial momentum, the momentum decrease amounts to 6 MeV$\cdot$c^{-1}.

Slowing down of the particles within the set-up is another source of momentum reduction and spread. In order to be able to calculate these effects a list of materials, other than air, in the path of the beam and their position relative to the front side of the first trigger scintillator is given in Table 5.2.

5.1.2 Lambda Wheels modules

The Lambda Wheels (LW) modules are part of a wheel shaped array of silicon detectors of the HERMES experiment [102]. This detector [103] has been designed and constructed

[1]The ratio of the dark currents at two temperatures T_1 and T_2 is given by [93] $\frac{I(T_1)}{I(T_2)} = (\frac{T_1}{T_2})^2 \exp(-\frac{E}{2k_b}\frac{T_1-T_2}{T_1T_2})$, where E is the activation energy which has a value of 1.15 eV and 1.2 eV for non-irradiated and irradiated detectors, respectively, and k_b is the Boltzmann constant.

Table 5.2: *List of materials in the trajectory of the beam. The position of the silicon sensor is that of the sensitive area, relative to the front side of Scintillator1.*

device	thickness [cm]	material	position [cm]
Cherenkov	0.42 (walls)	mylar	-470
MWPC	0.01	aluminium	-212
Focus	-	-	-200
Foil	0.01	plastic	-10
Scintillator1	0.2	NE102	0.0
LW1	0.03	silicon	12.5
LW2	0.03	silicon	17.5
LW3	0.03	silicon	27.7
LW4	0.03	silicon	32.7
BT1 (x)	0.03 + 0.02 + 0.004	silicon+mylar+copper	39.2
BT2 (y)	0.03 + 0.02 + 0.004	silicon+mylar+copper	48.2
BT3 (x)	0.03 + 0.02 + 0.004	silicon+mylar+copper	57.3
BT4 (y)	0.03 + 0.02 + 0.004	silicon+mylar+copper	66.4
Scintillator2	0.3	NE102	88.5
Foil	0.01	plastic	100
Scintillator3	1.0	NE102	408
Scintillator4	1.0	NE102	415

several years ago to increase the acceptance of the HERMES experiment for (relatively) slowly decaying particles (such as Λ^0 hyperons) in the forward direction. Figure 5.3 shows a schematic diagram of a LW silicon sensor. The sensor is wedge shaped with an apex of 30 °, a base of 85.3 mm and a top of 23.2 mm. Strips are implanted on both sides of the 300 μm thick n-type sensor, and are oriented parallel to the oblique sides. The strips are AC-coupled to the readout electronics via integrated coupling capacitors on the sensor. Bias voltage to the strips is supplied via integrated 2 MΩ poly-silicon resistors. The sensor has 516 strips on each side, of which the 17 shortest strips are not connected to readout pads. The strip implants are 60 μm wide and the strip pitch is 160 μm. More information on the LW modules is given in [104, 105].

The LW sensors are readout along the base by HELIX chips [106]. Connection of the sensor strips to the HELIX chips is realized by means of a flexible kapton foil. A HELIX chip contains 128 charge sensitive preamplifiers followed by a semi-Gaussian shaping stage with a peaking time of 50 ns. The pulse that is obtained after integration and shaping, is sampled by a 10 MHz clock and subsequently stored in an analog pipeline. A detailed technical description of the HELIX is given in [90]. Upon receipt of a trigger, the required samples are restored from the pipeline and sequentially sent out for digitization to a custom built analog to digital converter unit called HADC [107]. One of the two LW modules used in the present experiment was a prototype module which has sub-optimal characteristics. The other LW module is one of the spares for use in the HERMES experiment.

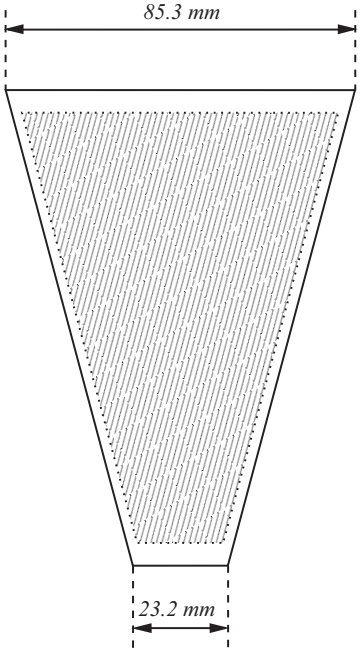

Figure 5.3: *Wedge shaped silicon sensor of a Lambda Wheels module. The strips on the double sided sensor are oriented parallel to the oblique sides.*

5.1.3 Beam Telescope modules

The Beam Telescope (BT) modules were built as general purpose reference detectors for high-precision track reconstruction. For the experiment described here, only the silicon detectors and the associated readout electronics of the Beam Telescope have been used. A detailed description of the whole Beam Telescope set-up can be found in [108].

Each BT detector module consists of a double sided n-type silicon sensor with AC-coupled readout strips. The active area of the detector is 57.6 by 57.6 mm^2 and the silicon thickness is 300 μm. The p-strips (junction side) are aligned parallel to the edge of the detector, and the strips on the n-side (ohmic side) have a stereo angle of 40 mrad with respect to the junction side. Each detector side has 512 readout strips with a strip to strip pitch of 112.5 μm. All strips, except for the first 20, have equal length. The length of the first 20 strips increases from 0 to 57.6 mm. In between the readout strips two intermediate strips are implanted.

The silicon sensor is readout by Analog Pipeline Chips (APC) [109]. An APC contains 64 charge sensitive amplifiers followed by an analog pipeline. The output of the (integrating) preamplifier is sampled at a frequency of 10 MHz and the samples are stored in a 32 cell deep analog memory. Writing to and reading from this memory is under control of an external controller which is common for all APC chips. Once this controller is triggered, the sampling process is paused and the charge stored on two pipeline columns is read back. The columns correspond to time samples taken 400 ns before, and 400 ns after the passing of the particle. By taking the difference of the two samples, all slow baseline variations of the preamplifier are removed. A group of eight APCs reads one side of a silicon sensor via a daisy chain connection. The signals are

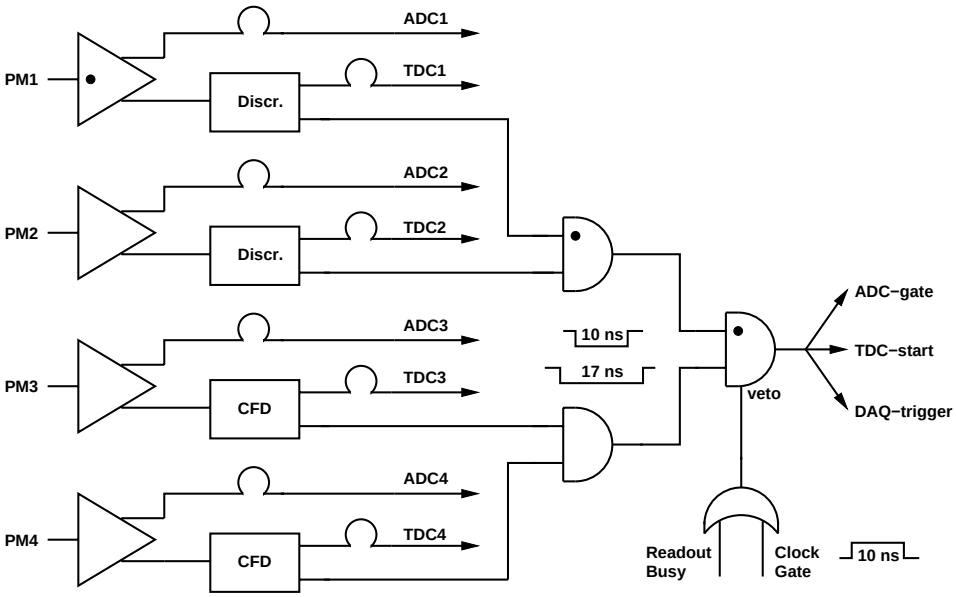

Figure 5.4: *Trigger diagram of the experimental set-up. The timing of the trigger is determined by the first scintillator. Triggers are only accepted during the proper phase of the 10 MHz sampling clock. During readout, all triggers are blocked. The black dots in the symbols denote the inputs that determine the phase of the corresponding output signals.*

digitized at a frequency of 1.25 MHz.

Depending on its mounting, a BT module can measure either the x or y position of a track accurately. The BT modules were oriented x-y-x-y when looking along the beam direction. By combining the strip information of the front side (x) and the back side (x'), a coarse measure of the position in the perpendicular direction is obtained. With a stereo angle of 40 mrad the digital resolution in this direction is 0.81 mm.

5.1.4 Trigger

A simplified diagram of the trigger logic is shown in Fig. 5.4. A trigger is created from a four-fold coincidence of the scintillator signals. Scintillator SC1, connected to photomultiplier PM1, determines the timing of the trigger. The analog signals of all photomultiplier tubes are delayed to enable the implementation of a common start for the TOF measurement.

In addition, the PM signals are integrated using an ADC of type LeCroy-1149A. This energy deposition information is used for the time walk corrections of the discriminators, which is described in more detail in section 5.2.1. Upon receipt of a trigger, the data acquisition system is started and further triggers are blocked until all silicon and TOF data are read out. Triggers are only accepted if the trigger coincides with the proper phase of the sampling clock of the HELIX chips in the LW modules. A 10 ns wide window out of a 100 ns clock period was selected.

5.1.5 Data acquisition

The data acquisition consisted of a PC running linux, reading a VME and a CAMAC crate. The Analog to Digital Converters (ADCs) of the LW modules, called HADC, have a 10 bit resolution and run at a sampling frequency of 10 MHz. Each HADC houses four ADCs and digitizes the data of one LW module, consisting of two double sided silicon sensors. The BT modules use CAEN type V550 ADCs, running at a conversion frequency of 1.25 MHz. The ADCs are 10 bits wide and each V550 unit digitizes the signals of two BT modules.

The time of arrival of the scintillator and Cherenkov signals with respect to the trigger was measured using a LeCroy-2228A Time to Digital Converter (TDC) which has a resolution of 50 ps. To measure the time relation between the trigger and the HELIX clock, a TDC with a resolution of 250 ps was used. The data collected in the spill were kept in memory, and written to disk after the spill to increase the number of events captured. Data have been collected in runs of 1000 events each. The typical collection time of a run was 4 to 5 minutes.

For monitoring purposes the rate of several signals and (sub) triggers was registered. Typical count rates per spill are given in Table 5.3. On average, about 50 triggers

Table 5.3: *Typical count rates per 600 ms long spill for the Cherenkov detector, scintillators and the various (sub)triggers.*

signal	counts per spill
Cherenkov	12k
PM1	20k
PM2	20k
PM3	35k
PM4	35k
PM1&PM2	11k
PM3&PM4	33k
PM1&PM2&PM3&PM4	5k
Cherenkov&PM1&PM2&PM3&PM4	600
accepted triggers	50

per spill were accepted by the DAQ system, which corresponds to only 1% of the tracks passing through all four scintillators. The rate of accepted triggers is mainly determined by the relatively long readout time of the ADC units.

The total number of events collected during the entire experiment is listed in Table 5.4. Also shown is the fraction of the total number of events that is either a proton, pion or positron. The identification of the particles is obtained from the time-of-flight system which is described in the next section. The proton to pion flux ratio in the beam decreases with increasing energy. To level the number of proton and pion events, the threshold of the discriminator of PM3 was increased. A higher threshold rejects more pions (and positrons) because of their lower average energy deposition. Proton enriched runs were taken for momenta of 1.1 to 1.3 GeV·c^{-1}.

Table 5.4: *Overview of the acquired number of events per momentum (set point). Also shown is the fraction of the total number of events that is either a proton* (p)*, pion* (π) *or positron* (e^+)*. Note that the data sets for 1.1 to 1.3 GeV·c^{-1} are proton enriched.*

p_{beam} [GeV·c^{-1}]	events	fraction p [%]	fraction π [%]	fraction e^+ [%]
0.8	443k	29	45	26
1.0	525k	23	61	16
1.1	481k	25	63	12
1.2	489k	38	53	9
1.3	773k	39	52	9

The data sets at each momentum setting contain at least 100k protons which is enough to determine a good quality energy deposition distribution for each detector plane.

5.2 Time of flight

The information of the TOF system is used as an independent particle identification detector which serves as a reference for the qualification of the PID capabilities of the dE/dx based particle identification. Therefore, an accurate analysis of the TOF information is important. This is the subject of the present section.

The Time-of-Flight (TOF) system consists of four scintillators, one of which is placed in front of the silicon stations, while the other three are positioned behind the silicon at distances of 88.5, 408 and 415 cm away from the first scintillator. The sensitive area of the first scintillator is 2×2 cm^2, that of the second one is 4×4 cm^2 and those of the last two are 10×10 cm^2. An increasing scintillator size is chosen to reduce the loss in trigger efficiency due to multiple scattering.

As was already mentioned in section 5.1.4, a trigger is created from the coincidence of all four scintillators, where PM1 determines the timing. The analog signal of each photomultiplier was integrated by an ADC to be used by the off-line time walk correction.

In the following subsections various aspects of the TOF system are described. First, the time walk corrections of the scintillator signals are looked into. In section 5.2.2, the momentum of the beam particles is determined using these corrections on the time-of-flight data. Finally a description of the beam composition, as determined by the TOF system, is given in section 5.2.3.

5.2.1 Time walk correction

Time walk is an instrumental effect which is caused by the finite rise time of the photomultiplier signals in combination with a fixed threshold of the discriminator. Time walk corrections serve two purposes: better separation of proton and pion peaks in the time-of-flight spectrum, and an improved determination of the momentum of the particles in the beam.

Figure 5.5 depicts the origin of the time walk. The moment when the output of the discriminator fires depends on the amplitude of the input signal. Large pulses give short response times. As can be seen in Fig. 5.5, the time between the start of the pulse (t_0)

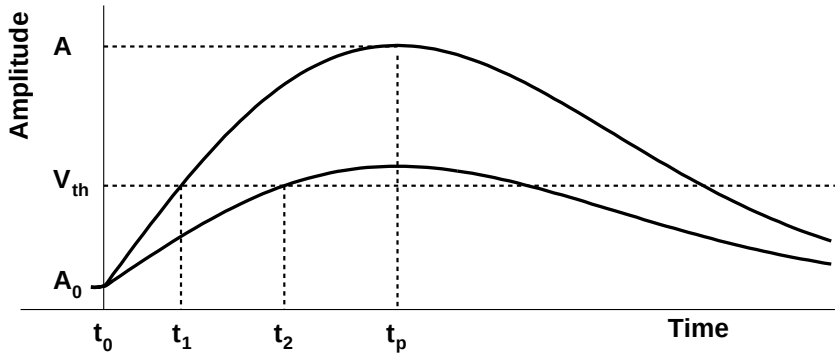

Figure 5.5: *Schematic diagram explaining the origin of time walk. The moment when the signal passes a threshold V_{th} depends on the amplitude of the pulse, on the peaking time $t_{\rm p}$ and on the baseline offset A_0.*

and the time when the signal crosses the threshold (t_1, t_2) depends on the amplitude (A) of the signal, on the peaking time ($t_{\rm p}$) of the pulse, and on the baseline offset (A_0).

A first order approach for the description of time walk is to assume a linear rising edge of the pulse, which gives a $\frac{1}{A}$ dependence of the time walk on the pulse amplitude (A) for a fixed value of $t_{\rm p}$ and for a fixed value of the threshold V_{th}[2]. The function that describes the time versus amplitude relation is

$$t_x = t_0 + \frac{k}{A - A_0}, \tag{5.1}$$

where k, A_0 and t_0 are the scale factor, an amplitude (baseline) offset and a time offset, respectively.

The time walk *correction* (Δt) applied to the data is then

$$\Delta t = -\frac{k}{A - A_0}. \tag{5.2}$$

The two parameters k and A_0 have been determined from fits to the analog data of the scintillators.

Alternatively, one can use a Constant Fraction Discriminator (CFD) which exhibits little time walk. We used CFDs for PM3 and PM4 because these photomultiplier tubes have longer peaking times than the ones used for the small scintillators. A short explanation of the CFD functioning is given in appendix A.

As shown in the trigger diagram of Fig. 5.4, the phase of the TDC start signal is determined by the first scintillator and the TDC-spectrum of PM1 should therefore be very narrow. Unfortunately this is not the case as can be seen from Fig. 5.6. Besides the narrow distribution, the TDC-spectrum has a wide shoulder on the left hand side of

[2]For pulse amplitudes close to the threshold (V_{th}), the first order approach is no longer valid.

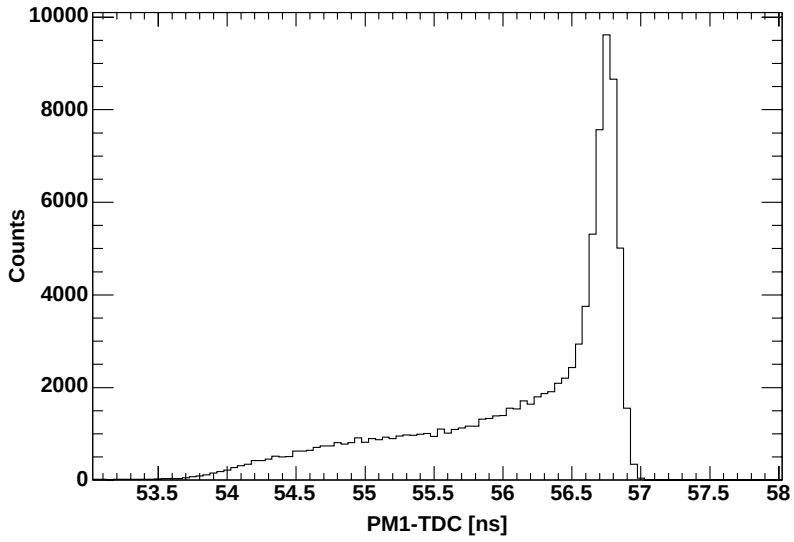

Figure 5.6: *Time spectrum of* PM1*. The spectrum should have been very narrow but due to limitations in the coincidence logic a shoulder on the left hand side of the spectrum appears.*

the spectrum. Similar spectra are obtained for the other three scintillators. The events contributing to the left hand side of the spectra are correlated which implies a common cause of the shoulder in the four time spectra. As the TDC start is common to these four spectra, it is likely that the shoulder is caused by a (frequently occurring) erratic delay of the TDC-start signal.

The erratic delay of the TDC-start signal is attributed to the behavior of the veto input of the coincidence unit (LeCroy-465) that has been used in the trigger. This behavior will be explained with the help of Fig. 5.7. Proper operation of the veto would yield a flat horizontal distribution over the whole range of the clock TDC as the timing of PM1 should not be correlated to the HELIX clock. Apparently, the veto only worked correctly for clock TDC values of less than 134 ns. However, if the leading edge of the scintillator trigger arrives near the start of the clock gate, the output signal of the coincidence unit is delayed, which leads to shorter times measured by the scintillator TDCs. For early scintillator triggers relative to the clock, the edge of the coincidence signal is determined only by the clock gate instead of by PM1. In this case, the PM1 TDC value shown in Fig. 5.7 varies for a fixed clock TDC (indicated by the vertical lines).

In the region between the two extremes (output timing determined by PM1 only, and output timing determined by the HELIX clock only), the timing of the coincidence logic is a function of the time difference between the rising edge of PM1 and the (HELIX) clock gate. The behavior of the veto input of the LeCroy-465 unit has been verified after the experiment and the result of a laboratory measurement is indicated by the dots in Fig. 5.7, showing agreement with the experimental data.

Another feature shown in Fig. 5.7 is the double band structure which must be caused by a problem in either the start or the stop signal of the clock TDC. At the position of the vertical line(s), the TDC start signal is determined solely by the clock gate and

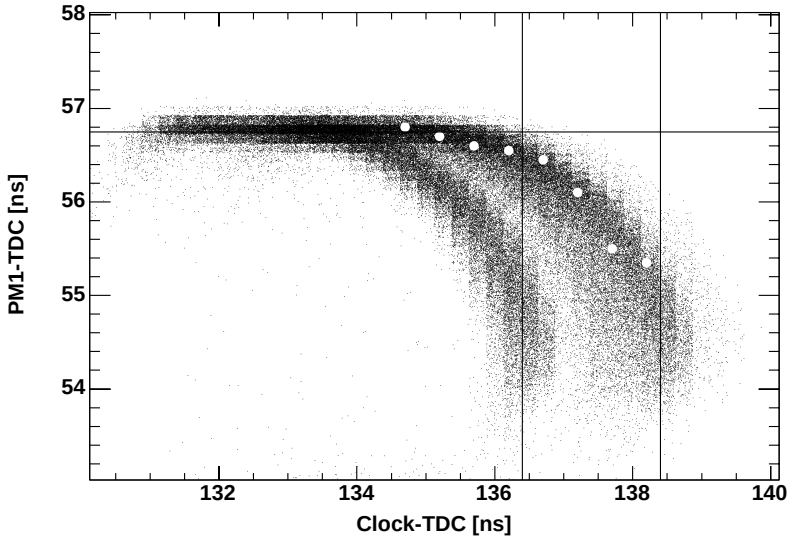

Figure 5.7: *Correlation between the time measured by* PM1 *and the* HELIX *clock* TDC. *The dependence shown is caused by a non-optimally operating veto input of the coincidence unit. The dots represent a laboratory measurement on the coincidence unit, which confirms the erratic behavior of the unit.*

not by one of the scintillator inputs. Hence, the most probable explanation for the two vertical lines in Fig. 5.7 is a jump of about 2 ns in the stop signal of the clock TDC with respect to the start signal. The 2 ns jump could be due to clock jitter, because the time as measured by the clock TDC is larger than the clock period of 100 ns and hence, the TDC start and stop signals originate from different clock edges. The 2 ns error in the clock phase has little effect on the analysis of the LW dE/dx data. This is explained in more detail in section 5.3.3. In all further analyses, the time-of-flight is determined by taking the difference of TDC4 and TDC1 because this removes the problem caused by the veto input of the trigger logic.

Correction parameters

In order to determine the time walk correction Δt, all the proton and pion data sets were first fitted using the function of Eq. 5.1 with three free parameters. The time offset parameter t_0 of Eq. 5.1 is different for the protons and the pions because of their difference in flight time. Moreover, t_0 is also a function of the particle momentum. Next, the mean value for parameters k and A_0 have been determined. Note that the same k and A_0 parameters for the proton and pion correction should be used to avoid bias in the time walk correction. Figure 5.8 shows the time walk correction function for PM1 (left) and PM4 (right). Each point in the plot is the mean value from a Gaussian fit to the TDC spectrum of that ADC bin[3]. The correction function for PM4 has the opposite sign as compared to that of PM1 because the time difference of PM1 and PM4 is taken.

[3]Note that a Gaussian function is only a coarse approximation. The actual distribution is not symmetric but skewed. A Gaussian fit was used to reduce the effect of outlying data points in the determination of the mean.

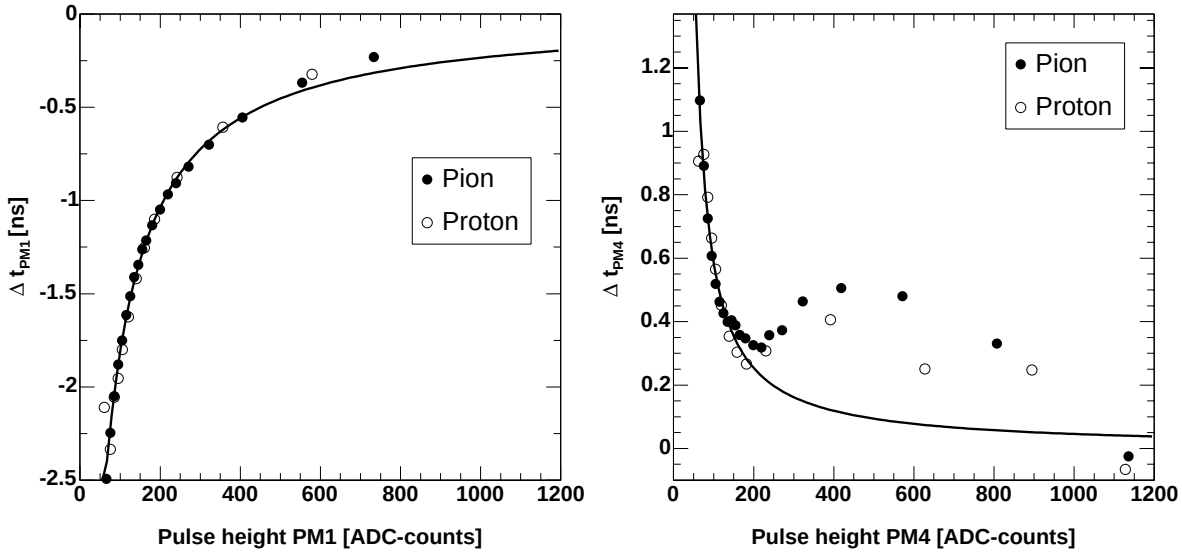

Figure 5.8: *Time walk of* PM1 *(left) and* PM4 *(right) for pions and protons together with the time walk correction function (solid curve). The time walk correction function for* PM4 *reveals a problem with the Constant Fraction Discriminator.*

Using this time difference instead of the *raw* TDC value when determining the time walk parameters for PM4 (PM1) does not introduce a dependence on PM1 (PM4) by virtue of the independence of the energy deposition in PM1 and PM4. This has been verified by determining the time walk parameters of PM1 for different ADC bins of PM4 at the cost of a reduction in statistics.

The figure shows the offset subtracted data together with the time walk correction function (solid curve). For PM1, the correction function describes the time walk reasonably well, but for PM4 the match is poor for large ADC values. Note that PM4 should hardly exhibit time walk because of the use of CFDs. It seems that the CFD was not properly tuned and that it acts as a (normal) discriminator with significant time walk for low ADC values. This behavior is explained in appendix A.

The parameters of the time walk correction function are given in Table 5.5. Errors

Table 5.5: *Parameters of the time walk correction function (Eq. 5.2). The values listed are the average taken over the 5 momenta bins considered in this experiment.*

Signal	k [ns×ADC-counts]	A_0 [ADC-counts]
PM1	-278 ± 17	-45 ± 3
PM4	38.8 ± 3.7	33 ± 3

are due to the parameter spread in the fits from different beam momenta. Despite the relatively large uncertainties of the parameters, the effect on the momentum calculation is small because the time walk corrections are small with respect to the actual pion-proton time difference.

The effect of the time walk correction on the time spectra of one of the 1.3 GeV·c^{-1} runs is shown in Fig. 5.9. The corrected spectrum is represented by the dotted line. Each of the two spectra consists of a pion peak (left) and a proton peak (right). The (negative) offset of the time axis is arbitrary because of the cable delay in the TDC start and stop signals. A better separation of the two peaks is obtained after applying the

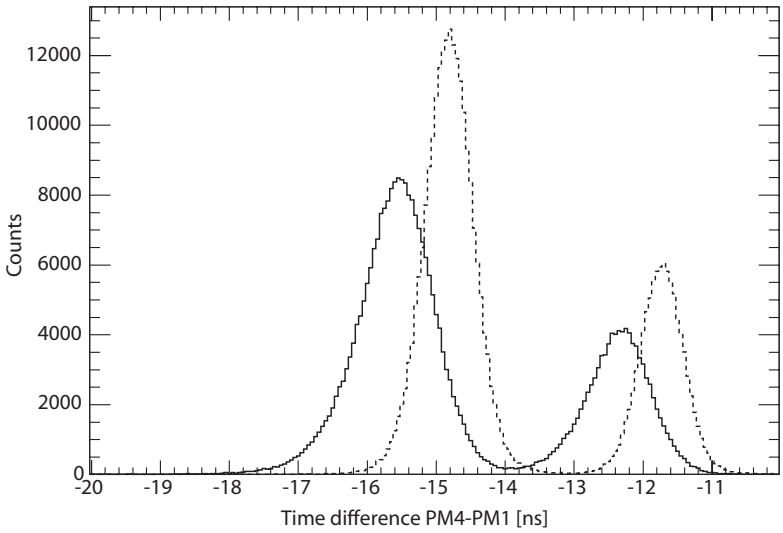

Figure 5.9: *Time difference of* PM4 - PM1 *after applying time walk correction (dotted line) and before the correction (solid line) for 1.3 GeV·c^{-1} particles. The peaks in the corrected spectrum are narrower and are better separated.*

time walk correction, together with a narrower peak and thus a better time resolution. The mean shift of the corrected spectrum is large compared to the relative shift of the two peaks within the corrected spectrum.

Time resolution

The time resolution (σ_t) obtained from a Gaussian fit to the distributions of Fig. 5.9 gives 0.37 ns for pions of 1.3 GeV·c^{-1} while for protons a resolution of 0.32 ns is found. The resolution varies from run to run, but it is always better than 0.44 ns and 0.37 ns for pions and protons, respectively. The proton resolution is always better than that of the pion which is due to the larger average amplitude of the proton signal in the scintillator. Larger signals pass the threshold more steeply thus giving less time jitter. Setting equal cuts on the signal amplitude yields the same resolution for pions and protons.

After correction for time walk, the proton and pion peaks are well separated. Even at 1.3 GeV·c^{-1} the peaks are separated by more than 4σ and hence the efficiency of the TOF method is essentially 100%. The purity is around 0.996 if a single threshold (in time) is used to separate pions from protons. Whenever a more pure dataset is required the selection criterion is narrowed down to a $\pm 2\sigma$ window around the mean time of the pion and proton distribution.

5.2.2 Beam momentum

The beam momentum is determined from the mean time difference of the pion and proton peaks. Assuming the same momentum p for the protons and the pions contained in the beam, the *difference* in TOF values of the particles is given by

$$\Delta t = \frac{l}{c}\left[\sqrt{1+\frac{M_p^2c^2}{p^2}} - \sqrt{1+\frac{M_\pi^2c^2}{p^2}}\right], \tag{5.3}$$

where l is the distance traveled, c is the speed of light and M_p and M_π are the rest masses of the proton and pion, respectively. The time difference Δt is most sensitive to the momentum of the proton, which can be seen from the dominance of the first term in Eq. 5.3. The assumption that the proton and pion momenta are the same introduces a small error because the average momentum of the proton will be lower than that of the pion due to the material present in the path from the momentum slit to the last scintillator in the TOF system. On average, protons lose more energy than pions in this flight path. The momentum difference between pion and proton is largest at the lowest beam momentum. If the proton momentum is 800 MeV·c^{-1}, the corresponding pion momentum is about 825 MeV·c^{-1}. However, the difference in TOF of pions with momenta of 800 and 825 MeV·c^{-1} is only 12 ps which is negligible. Hence, this effect has not been corrected for.

Solving Eq. 5.3 for the momentum p yields

$$p = l\sqrt{\frac{c^2\Delta t\left(M_\pi^2+M_p^2\right) - 2c\sqrt{l^2(M_p^2-M_\pi^2)^2 + M_\pi^2M_p^2c^2\Delta t^2}}{\Delta t\left(-4\,l^2+c^2\Delta t^2\right)}}. \tag{5.4}$$

Applying Eq. 5.4 to the TOF data gives the beam momenta as listed in Table 5.6. The subscripts *notcorr* and *corr* denote the time-of-flight (and corresponding momentum) before and after applying the time walk correction. The quoted momentum is that of the proton.

Table 5.6: *Time-of-flight and corresponding beam momentum with and without time walk correction. The quoted momentum is that of the proton.*

p_{set}[GeV·c^{-1}]	$\Delta t_{notcorr}$[ns]	$p_{notcorr}$[MeV·c^{-1}]	Δt_{corr}[ns]	p_{corr}[MeV·c^{-1}]
0.8	7.53	784	7.32 ± 0.10	797 ± 7 ± 7
1.0	5.16	982	4.95 ± 0.10	1007 ± 12 ± 10
1.1	4.35	1084	4.18 ± 0.10	1110 ± 15 ± 10
1.2	3.74	1190	3.57 ± 0.10	1212 ± 19 ± 11
1.3	3.22	1284	3.09 ± 0.10	1313 ± 23 ± 11

The uncertainty introduced by the time walk correction is less than 100 ps. In addition, the systematical uncertainty is shown for the calculated corrected momentum. It consists of the uncertainty in the length of the flight path, estimated to be less than 1 cm, and the uncertainty in the calibration of the TDC which is about 1.5%.

5.2.3 Particle spectrum

After application of the time walk correction, the composition of the beam can be determined. Figure 5.10 shows the particle spectrum as determined by the time-of-flight system for a momentum of 1.3 GeV·c^{-1}. The top part of the plot shows the correlation between the ADC and TOF data, and the bottom part is the projection of that plot on the time axis. From left to right, the peaks correspond to pions, protons,

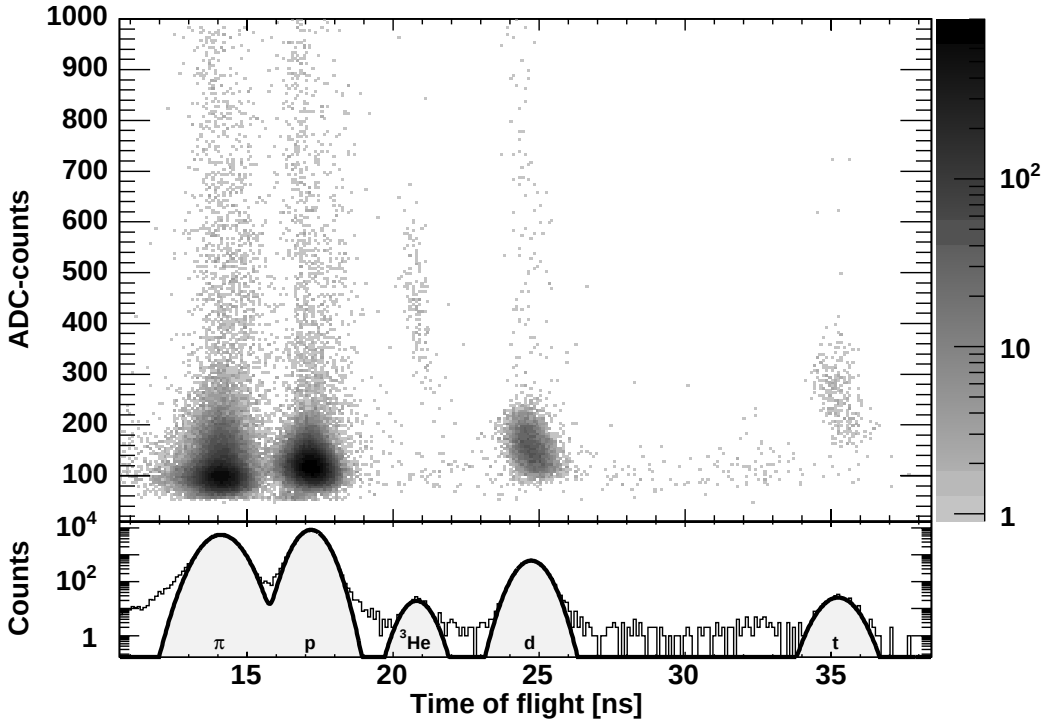

Figure 5.10: *Time-of-flight spectrum (bottom) and* TOF *versus* ADC *value of* PM4 *(top) of data taken with a 1.3 GeV·c^{-1} beam. From left to right, the peaks contributing to the spectrum are pions, protons, ^{3}He nuclei, deuterons and tritons.*

^{3}He nuclei, deuterons and tritons. The time axis is offset such that the mean of the pion peak corresponds to the expected TOF for 1.3 GeV·c^{-1} pions. Pions were chosen for this calibration because they suffer least from TOF variation caused by momentum spread (largest β). It has been verified that the flight times of the other particles obtained from the fits in Fig. 5.10 match the calculated flight times within 3%.

It is clearly visible that ^{3}He nuclei deposit, on average, more than four times as much energy as protons. This higher energy deposition is due to the double charge of ^{3}He and the quadratic dependence of the energy loss on charge (see Eq. 3.13). The ^{3}He particles have twice the momentum of the other particles because the magnetic deflection scales linearly with charge. Note that the ADC versus TOF correlations for ^{3}He, deuterons and tritons exhibit a small slope which is caused by the imperfect time walk correction of PM4.

The ratio of the number of pions to protons in this plot does not represent the ratio in production cross sections because the data shown have been taken from a run with a

high PM3 threshold which increases the proton yield. Moreover, positrons are excluded from the spectrum by using a cut on the Cherenkov TDC.

Hardly any kaon is present in the spectrum because of the small production cross section [110] combined with a short life time and a relatively large distance from the target to the detector. The expected yield of kaons is much smaller than 1% of the pion yield. This small kaon contribution to the spectrum cannot be separated from the pion peak due to the limited time resolution of the TOF system.

Alpha particles

The deuteron peak in Fig. 5.10 is possibly contaminated by α particles. Looking at the time-of-flight spectrum, there seems to be a fairly large number of events with a high energy deposition in PM4 for the time-of-flight range of 23 to 27 ns. However, a significant part of these events with a high energy deposition are due to nuclear interactions in the scintillator material. The number of nuclear interactions is not negligible given the use of a 1 cm thick detector ($\cong$ 1 g·cm^{-2}) and a nuclear interaction length of 82 g·cm^{-2} [70].

However, if a high energy deposition occurs simultaneously in all four scintillators it could be caused by an α particle. Table 5.7 lists the number of events per scintillator for an ADC cut equal to about four times the most probable energy deposition of a MIP. The most probable energy deposition of a deuteron and an α particle is about 2 and 7 times that of a MIP, respectively.

Table 5.7: *Number of α particle candidates for different* PM-ADC *cuts. The* ADC *threshold corresponds to a signal of 4* MIP *for each of the* PMs.

cut	number of particles	Observed Particle/Proton [%]
no cuts	5954	7.55
PM4ADC $>$ 4×MIP	95	0.12
PM3ADC $>$ 4×MIP	47	0.06
PM2ADC $>$ 4×MIP	11	0.01
PM1ADC $>$ 4×MIP	11	0.01
all cuts combined	10	0.01

The number of α candidates for this run is determined to be 10. Although the number of candidates is low, it is very unlikely that these 10 events are random coincidences. Given the yield for each PM-ADC-cut as listed in Table 5.7, the probability to find events surviving all four ADC cuts would be $8{\cdot}10^{-11}$ and the expected number of particles would be 0, while 10 events are found (= 0.16% of deuteron yield). The probability that a deuteron deposits more energy than four times the most probable energy of a MIP in *all* four scintillators[4] is less than $1{\cdot}10^{-15}$.

[4]The probability of an energy deposition in excess of 4 MIP in a 2 mm scintillator is about $5.5{\cdot}10^{-3}$, while for a 10 mm scintillator the probability is (much) less than $1{\cdot}10^{-5}$.

Particle yield

The particle yield, expressed as a fraction of the proton yield, is listed in Table 5.8 for a 1.3 GeV·c^{-1} beam. As an indication, the relative production cross sections are listed for the values of energy and angle found in the literature nearest to those of the present experiment. Pions are excluded from the table because their number is biased by the high cut on PM3, as was already mentioned before. The numbers from [111] are

Table 5.8: *Observed relative particle yield (normalized to the proton yield) in the 1.3 GeV·c^{-1} secondary beam of the present experiment. In the third column the relative yield from references [111] and [112] are listed for comparison.*

Particle	Observed Particle/Proton [%]	From ref. [111, 112]
Proton (normalization)	100	100
^{3}He	0.19	0.14
Deuteron	7.55	4.56
Triton	0.39	0.50
Alpha	0.01	(5% of 0.14) 0.01

for 10.1 GeV·c^{-1} protons incident on an Al target, and viewed at a scattering angle of 61 mrad. For the α particles, the expected yield is obtained by taking 5% of the ^{3}He yield as reported in [112]. The measured numbers in this experiment match the values found in the literature within a factor two, which is reasonable given the differences in energy and production angle.

Muons from pion decay

Because the pion is an unstable particle, some of them will decay in flight. The principal decay mode is $\pi^+ \rightarrow \mu^+ + \nu_\mu$ and the muons are created with p=29.8 MeV·c^{-1} in the Center-of-Mass frame. Due to the forward boost, the momentum of the muons in the laboratory ranges from 743 to 1302 MeV·c^{-1} for pions with p_π=1.3 GeV·c^{-1} and from 456 to 803 for p_π=0.8 GeV·c^{-1}. The maximum decay angle (in the lab-frame) is 30.0 and 49.2 mrad for 1.3 and 0.8 GeV·c^{-1} pions, respectively.

Depending on where the pion decays, the muon has a certain probability to hit the silicon detectors and trigger the DAQ. Most of the muons from pions decaying before the last bending magnet, will not traverse the silicon because they are either removed by the momentum selecting magnet (and slit) or the distance to the silicon is so large that even a small decay angle is enough to miss the detectors. However, a significant fraction (several tens of percent) of the muons from a decay in between the first and last trigger scintillator can still reach the last trigger scintillator. The time-of-flight of these muons is in the same range as that of the pions in the beam and hence these muons cannot be distinguished from pions by the TOF. In every meter of beam-line, 1.36 (2.18)% of the 1.3 (0.8) GeV·c^{-1} pions decay, and therefore it is very likely that the sample of pions contains in the order of a few percent of muons. The energy deposition of these relativistic muons is very close to the energy deposition of relativistic pions and hence the muons will not affect the analysis of the silicon dE/dx measurements.

5.3 Analysis of silicon data

The acquired silicon signals contain the information about the energy deposited in the wafer by the traversing particle, but the information is obscured by offset and noise of the readout electronics. In its most general form the relation between the ADC value $s(c,i)$ and the real charge deposition $q(c,i)$ for strip c in event i is given by:

$$s(c,i) = k(c) \cdot q(c,i) + p(c) + w_r(c) \cdot n_r(c,i) + w_{CM}(c,i) \cdot n_{CM}(i). \tag{5.5}$$

The charge signal is modified by a channel dependent gain factor ($k(c)$), which is discussed in section 5.3.3, and pedestal value $p(c)$. The latter is assumed to be the same from event to event. Slow variations of the pedestal, e.g. due to changes in temperature, are corrected for by regular recalculations of the pedestal.

In addition to the pedestal, the signal is modified by noise. Noise contributions are split in two parts, a random ($n_r(c,i)$) and a common mode part ($n_{CM}(i)$). Here, the noise weight factors w_r and w_{CM} are written explicitly, but can also be integrated into the noise terms n_r and n_{CM}. The random part changes from event to event, and this contribution is highly Gaussian. The main contribution to the random noise comes from the thermal noise of the preamplifier of the readout electronics. Random noise cannot be corrected for, and determines the final S/N (signal to noise) ratio. The magnitude of the random noise can be a function of strip number due to their difference in length and hence their strip capacitance.

The Common Mode (CM) noise ($n_{CM}(c,i)$) is a noise contribution which is correlated with other channels. The correlation can exist for a single readout chip, a whole detector or even the whole set-up. Once the correlation between the strips is determined, a large fraction of the CM noise can be subtracted. Contrary to random noise, CM noise can be highly non-Gaussian. It is assumed that, after correction, the mean value of this CM noise distribution is zero. Any deviation from zero will add to the pedestal value.

In the following subsections, the aforementioned effects will be described in more detail. First, the calculation of the pedestals is discussed in subsection 5.3.1, followed by a discussion of the common mode noise in subsection 5.3.2. The calculation of the various gain factors is the subject of subsection 5.3.3. The criteria used for selecting hits are discussed in subsection 5.3.4. Finally, section 5.3.5 addresses the correlation of signals in the ohmic and the junction side of the same sensor, and the sharing of the signal charge between neighboring readout strips.

5.3.1 Pedestal calculation

Calculating the mean of Eq. 5.5 for each channel over all events yields the pedestal,

$$\begin{aligned} p(c) &= \frac{1}{n}\sum_i^n s(c,i) - \frac{1}{n}\sum_i^n k(c) \cdot q(c,i) - \\ &\quad - \frac{1}{n}\sum_i^n w_r(c) \cdot n_r(c,i) - \frac{1}{n}\sum_i^n w_{CM}(c,i) \cdot n_{CM}(i). \end{aligned} \tag{5.6}$$

The average value of the noise terms is zero by definition, and therefore the two last terms do not contribute to the pedestal. The pedestal is usually determined if the real

signal is zero, which can be achieved with dedicated pedestal runs when the beam is switched off or by taking data in between the spills. Alternatively, the pedestal can be determined in the presence of the signal; the latter option was chosen in this experiment. In first order one can neglect the average signal contribution because of the low strip occupancy. The beam is rather wide and hence the strip occupancy ranges from 0 to 1% depending on position. The sign of the charge signal $k(c) \cdot q(c,i)$ is always the same and will thus give rise to an overestimated pedestal value if the small average signal contribution is neglected. Without further correction, the reconstructed charge will be too low. However, the common mode correction which is described in the next subsection, will remove part of the pedestal-error.

Pedestal drift: the LW case

Figure 5.11 shows the pedestal of a single strip in one of the LW modules versus run-number. The pedestal shown is the moving average of 10000 events and the size of the variation is about 10% of the most probable signal of a MIP. Other strips show a similar drift which implies a common cause. In this case, the drift is very likely due to temperature variation in the hall where the silicon sensors were located in combination with temperature variations in the control room where the HADCs were installed. If

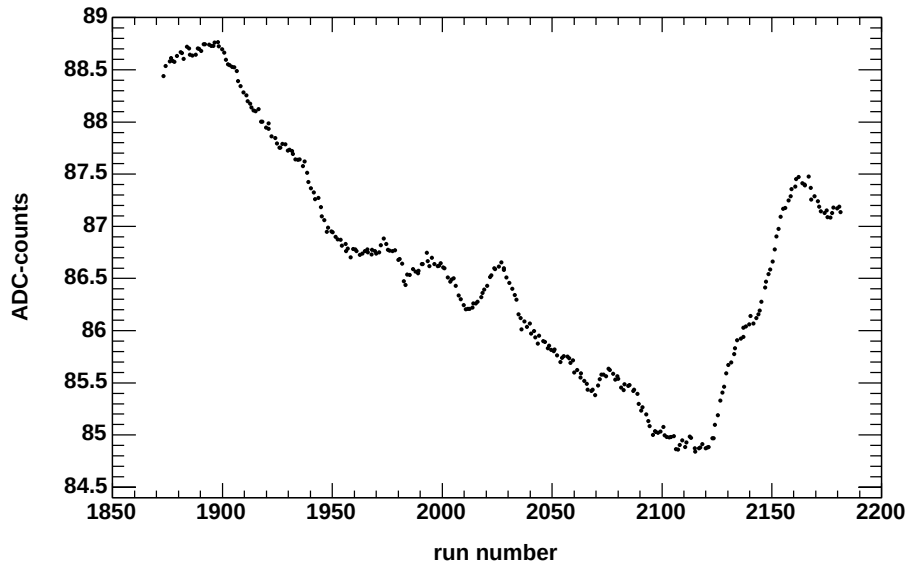

Figure 5.11: *Pedestal drift as a function of run number for a single strip of a* LW *module. The size of the pedestal drift amounts to about 10% of a* MIP *signal.*

the pedestal of all channels within a chip drift in the same direction, the common mode correction algorithm will correct for it. The pedestals are nevertheless recalculated every 10000 events.

5.3.2 Common mode noise calculation

The common mode noise is calculated by taking the average of a selection of channels for a single event. The selection used in the following analysis is the number of channels in one readout chip, i.e. 64 in the analysis of the BT data and 128 for the LW data. Starting from Eq. 5.5, the CM noise is calculated from

$$n_{CM}(i) = \frac{1}{n}\sum_{c}^{n}(s(c,i) - p(c)) - \frac{1}{n}\sum_{c}^{n} k(c)\cdot q(c,i) - \frac{1}{n}\sum_{c}^{n} w_r(c)\cdot n_r(c,i). \qquad (5.7)$$

The last term, which is the mean random noise in n channels, is very small because the mean of the random noise is $\sqrt{n}$ times smaller than the noise of a single channel. Moreover, because this mean noise is uncorrelated with the noise of a single channel it will only increase the random noise of a single channel by 0.8% in case of a 64 channel average; this is considered insignificant.

Depending on where the common mode interferes, the common mode noise term $w_{CM}(c,i)\cdot n_{CM}(i)$ can be simplified to $w_{CM}(c)\cdot n_{CM}(i)$. This is, for instance, possible when the noise couples into the silicon strips; the weighting factors are then correlated with the strip length. The weighting factors contain the channel dependence and the common noise (n_{CM}) is simply the mean value per event of all channels in the chip. The common mode weight factors ($w_{CM}(c)$) are obtained from the correlation of the pedestal subtracted signal ($s-p$) versus n_{CM}. Extracting the weight factors can be done without knowledge of the functional dependence. This common mode noise correction method was chosen for the Beam Telescope data.

It is also possible that a common mode signal interferes with the sequential readout. In that case the simplification mentioned before cannot be used. The weight factor $w_{CM}(c,i)$ changes from event to event. For this situation, a fit is made to a group of strip signals for every event; commonly used fit functions are first or second order polynomials. A strip length dependence will then show up as correlation in the fit parameters. This common mode subtraction method was used for the LW data.

The number of channels used in calculating the common mode value is less than the number of events used in the pedestal calculation which implies a risk of bias in case of a large signal in the sensor. The bias can be reduced by using an iterative procedure. First, the common mode noise is calculated as the mean value of all non-dead strips. Secondly, the common mode noise is recalculated by excluding strips that have a signal greater than three times the random noise of that channel[5].

Common mode noise: the LW case

The common mode noise in the LW modules is calculated with a first order polynomial in channel number. A first order polynomial is sufficient because the strip length of the wedge shaped silicon detectors decreases linearly with strip number in the region of the beam spot. Before calculating the parameters, strips with hits and other spurious

[5]If the CM noise is small compared to the random noise, the threshold can already be applied in the first step.

signals are removed by applying a threshold equal to the mean value plus three times the RMS of all channels in this event.

The distributions of the two parameters of the polynomial are shown in Fig. 5.12 for the second chip of one of the LW modules. A correlation of the two fit parameters

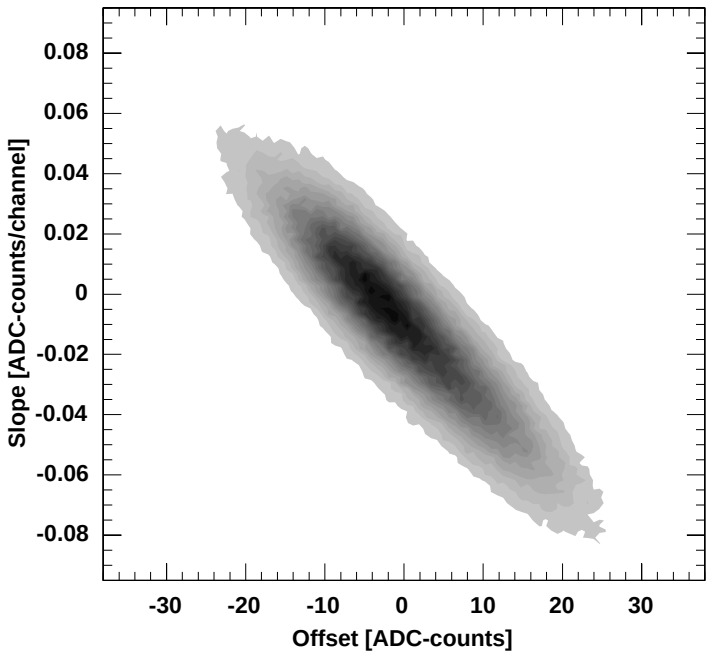

Figure 5.12: *Distribution of the parameters of a first order polynomial fit to the* LW *common mode noise. The offset and slope are strongly correlated which indicates that the noise pickup is related to the length of the silicon strips.*

indicates that the common mode pick-up is related to the length of the strips on the silicon sensor[6]. The magnitude of the LW common mode noise is about 20% of a MIP.

Common mode noise: the BT case

For the BT modules, a single common mode value per chip and per event is determined from the pedestal subtracted ADC values using the two step procedure described before. Next, for each channel in the chip, the correlation between the single CM noise value and the pedestal subtracted ADC value is determined for all events. From the correlation, the common mode weight factors for all channels are extracted. The weight factors are normalized via the relation

$$\frac{1}{n}\sum_{c}^{n}\omega_c = 1, \tag{5.8}$$

where ω_c is the weight factor of a single channel and n is the number of non-dead channels in the chip.

[6] A non-orthogonal set of polynomials was used in the fit which affects the correlation of the fit parameters.

Figure 5.13 shows the magnitude of the common mode noise (σ_{cm}) of all channels on the ohmic side of detector BT2 after correction with the weight factors. Other BT

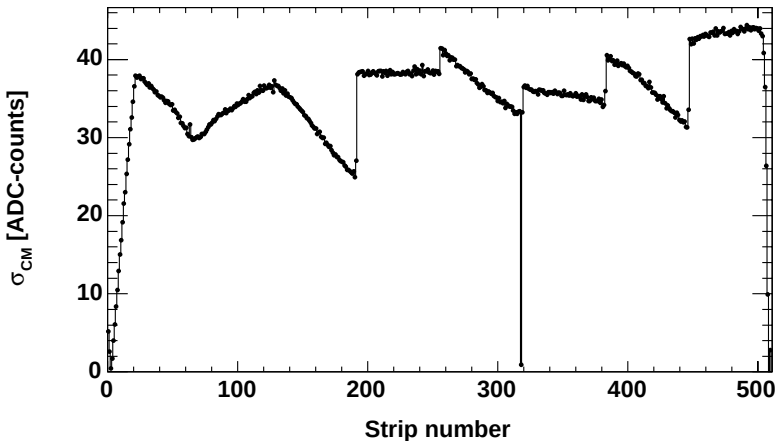

Figure 5.13: *Common mode noise versus strip number for the ohmic side of detector* BT2*. Some* APC *chips show a variation in* CM *noise of 20%. The low value at channel 318 is caused by a broken bond.*

modules show similar patterns. The boundaries of the different regions in the plot match with the 64 channel boundaries of the APC chips. Some of the APC chips have a strong channel number dependent CM noise while others show almost no dependence. The pattern cannot be explained by the geometry of the detector, except for the first 20 strips. For these strips, the length, and correspondingly the amount of noise picked up, decreases to zero towards the sensor's edge (see also section 5.1.3).

Random noise in the LW modules

After correction for the common mode noise, the random noise (per channel) remains. The random noise as a function of strip number for two of the LW sensors is shown in Fig. 5.14. Four sections in each plot can be distinguished, corresponding to the four HELIX chips. The noise in LW1 is equal for the ohmic and junction sides and shows a gradual decrease towards high numbered strips. High numbered strips are shorter, have less capacitance and therefore the preamplifier is less noisy.

The dual band structure in the second chip of LW4 represents a regular pattern of strips with high noise and extra high noise. The pattern correlates with the size of the test pulse capacitors in the HELIX. It seems as if a small test pulse was injected into these chips for some of the events. Removal of this signal structure is described in the hit selection section (5.3.4). No cause was found for the high noise level in the third and fourth chip. However, these chips contain almost no hits from tracks and hence do not significantly degrade the energy deposition measurement of this sensor.

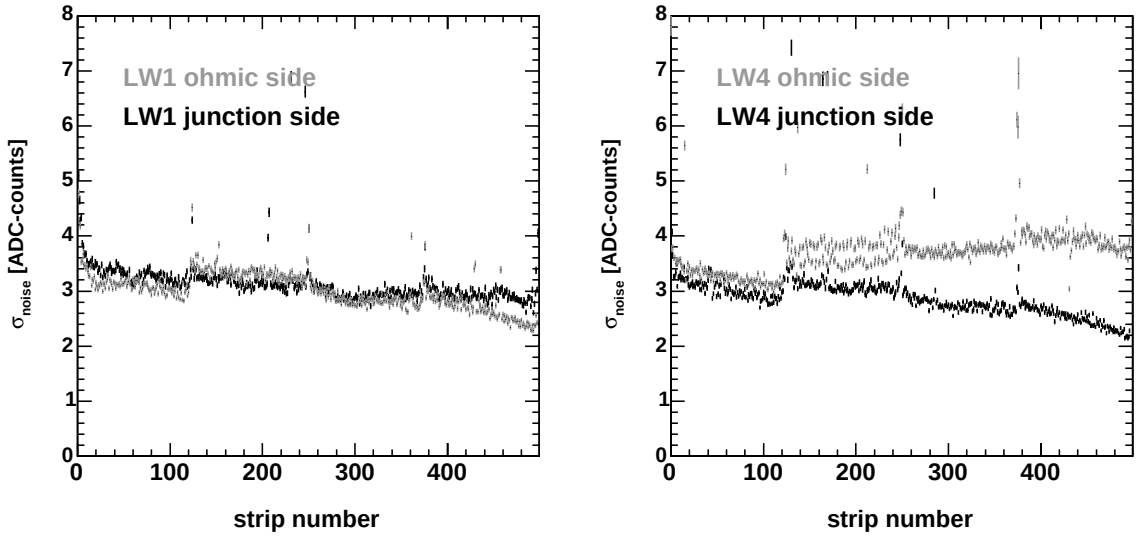

Figure 5.14: *Noise versus strip number for two of the* LW *sensors. The left plot shows an equal amount of noise for the ohmic and the junction sides, which decreases towards higher strip numbers because of the shorter strip length. The last three chips on the junction side of* LW4 *show a higher than expected noise level.*

5.3.3 Signal gain

Another unknown factor in Eq. 5.5 is the signal gain $k(c)$. Apart from common gain factors for a whole module or chip, the gain can be different for channels within the same chip. Correcting these factors is sensible whenever they exceed the few-percent level because in that case they contribute to the width of the energy deposition distribution which is determined per sensor, not per channel. This section deals with this issue and evaluates the corrections related to the signal gain.

Lambda Wheels sampling time dependent gain

Each channel of the HELIX chip contains a shaper with a peaking time of about 50 ns. The output signal of the shaper is a pulse with a nearly flat top of about 8 ns. The output of the shaper is sampled at every rising edge of the 10 MHz clock signal. This sampling should be done at the flat top of the pulse. Because the T11 beam is continuous during the spill of 600 ms, the 10 MHz sampling clock of the HELIX is asynchronous with respect to passing of the particles and hence with respect to the trigger. Therefore, the trigger circuit can be used to select only those events where the sample is taken at the flat top of the shaped pulse. A 10 ns window of the 100 ns clock period was defined in which a trigger resulted in the acquisition of the event[7]. Ohmic and junction side signals have a different timing due to the difference in charge collection time (see section 3.4.4) which is compensated for by delaying the sampling clock of the junction

[7]Although 90% of the events are rejected by this clock window it did not affect the number of recorded events because the scintillator trigger rate is much higher than the rate that could be recorded by the DAQ.

side with respect to that of the ohmic side by 10 ns. To check the proper tuning of the peak sampling, the most probable energy deposition of pions is shown as a function of the HELIX clock phase in Fig. 5.15 for the ohmic (n) and junction (p) side signals of the four LW silicon planes. If the peak sampling is well tuned, the most probable signal

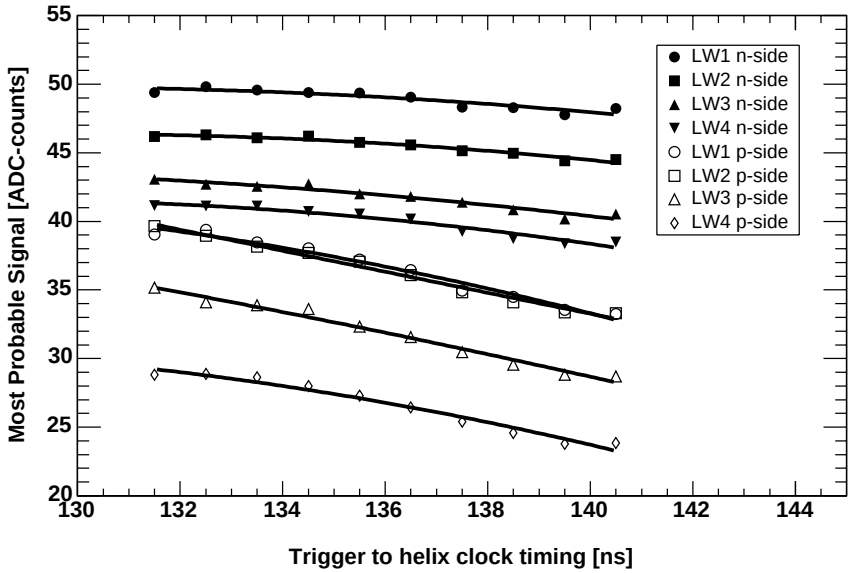

Figure 5.15: *Most probable signal of pions in the ohmic and junction side of the four* LW *sensors as a function of the clock phase. The timing of the peak sampling of the junction side is sub-optimally tuned.*

should hardly depend on the clock timing. The figure shows part of the, time reversed, pulse shape of the HELIX chip near the peak of the pulse. The p-side amplitudes clearly depend on the sampling time and the real peak position is to the left of the plot. Hence, the time window of the clock was not optimally tuned which leads to a larger than necessary amplitude spread of the sampled signals.

The junction sides are more affected by this timing error than the ohmic sides. The spread in signal amplitudes of the junction side is about 15% and is corrected by introducing a HELIX clock dependent gain factor. A drawback of this correction is that it increases the noise by about 8%. Another small smearing effect is caused by the 2 ns jump in the HELIX clock as explained in section 5.2.1. This effect is considered to be insignificant.

Gain variation of the BT detector

The documentation of the BT system [108] reports a variation in gain of almost a factor 2 as a function of channel number. To a large extent, this problem was attributed to an improper reset sequence in the external controller. This has been corrected before the beginning of the present experiment by reprogramming one of the programmable logic devices in the controller. The remaining variation in gain is less than 25% which is corrected for by applying a gain factor per channel. However, first it needs to be investigated whether there is any evidence for a channel dependent gain.

The hypothesis of a channel dependent gain has been investigated by looking at the magnitude of the random noise and the signal amplitude of hits. Since the beam spot only partially illuminates the sensor, the comparison with the signals is only possible for a few chips. Plots of the signal, the common mode noise and the random noise are shown in Fig. 5.16 for strips 128 to 320. For ease of comparison, the y-axes are normalized to

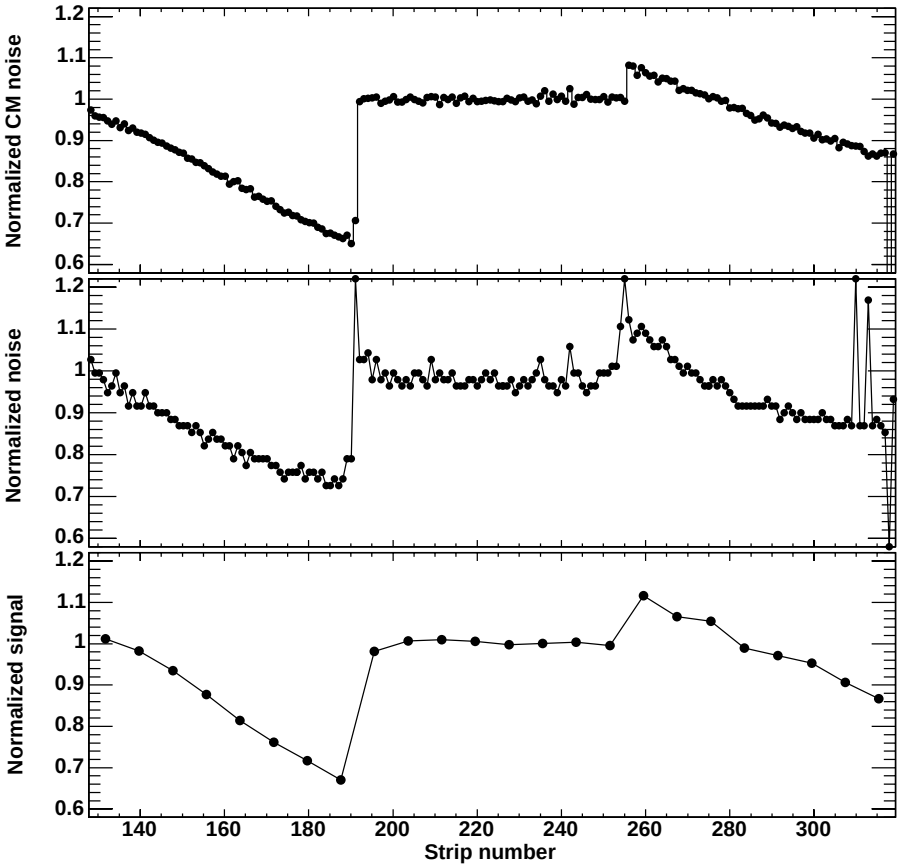

Figure 5.16: *From top to bottom, the plots show the magnitude of the common mode noise, the random noise and the signal from hits for the ohmic side of detector* BT2*. The y-axes are normalized to the mean value of the strip numbers 192 to 255.*

the mean value of the strip numbers 192 to 255. The top plot shows the common mode noise; it is a normalized version of Fig. 5.13. In the center plot, the (random) noise is shown which is obtained by taking the width of the noise distribution of each channel after pedestal and CM noise subtraction. The bottom plot shows the mean of the signal in groups of eight strips; grouping is needed to increase the statistics per bin in order to make a reliable fit to a Landau distribution. All the plots show a similar structure and it is concluded that for the APC chips a channel dependent gain factor should be introduced. The variation in channel gain can best be determined from the common mode noise because of the large statistics and because of the large CM noise amplitudes.

Using the common mode weighting factors ($\omega_{CM}(c,i)$) as gain factors[8] removes the

[8]The method to determine $\omega_{CM}(c,i)$ is discussed in section 5.3.2.

channel to channel signal gain. What remains is a gain factor per APC chip which is an intrinsic property of the chip. Looking at the similarity of the plots in Fig. 5.16, it is fair to assume that the average common mode noise per chip is a measure of the chip gain. In this way, the calibration for all strips and APC chips on one side of the sensor has been determined. Variation of the calibration factor from detector to detector can occur due to different amplification factors in the remaining readout electronics, or variations in the thickness of the sensor. The relative gain factors for the different sensor sides are calculated from fits to the energy deposition distributions.

Another imperfection of the beam telescope readout is the so called *1/32 effect* which is due to a different size of the capacitors in one of the columns of the APC pipeline. If this pipeline column is read out it leads to a too high or too low output amplitude depending on whether the column is used as first or second sample point, respectively. The effect looks like a baseline shift and is therefore, for the greater part, removed by the common mode noise correction in the analysis. However, not only the baseline is affected by the *1/32 effect*, but also the amplitude of the signal changes. Unfortunately, no hardware has been used during the experiment that could detect this state and therefore the gain variation is smeared into the data. The size of the *1/32 effect* is not quantified in [108] and the influence on the quality of the data is therefore unknown.

Signal-to-noise ratio

Now that all channel dependent gain factors are known, the energy deposition signals of different strips can be collected in a single histogram per detector plane. In this way, enough statistics are available to determine the most probable signal for each plane which is needed in order to calculate the signal to noise ratio.

The Signal-to-Noise ratio (S/N) is defined here as the pion signal in a cluster of three strips divided by the sum of the noise in three neighboring strips. This definition differs from the more common definition $S_{cluster}/N_{strip}$ used in tracking applications, which is not useful when looking at energy deposition distributions. The difference between the two definitions for an n-strip cluster is nearly a factor $\sqrt{n}$, but not exactly. Due to correlations, the noise in the cluster is *less* than expected from quadratic addition of random noise. More details are given in appendix B.

An overview of the S/N ratios of all silicon detectors is given in Table 5.9. The average S/N ratio is 7.6 for the BT detectors and 8.2 for the LW detectors.

Table 5.9: *Signal to noise ratio of all* BT *and* LW *detectors for a cluster size of three strips.*

BT1-n	BT1-p	BT2-n	BT2-p	BT3-n	BT3-p	BT4-n	BT4-p	mean BT
7.0	8.0	7.0	7.4	7.3	8.8	6.8	8.5	7.6
LW1-n	LW1-p	LW2-n	LW2-p	LW3-n	LW3-p	LW4-n	LW4-p	mean LW
9.8	8.0	8.7	8.6	9.3	7.0	8.5	5.4	8.2

5.3.4 Hit selection and rejection

The methods described in the previous section helped to retrieve the true signal from the raw ADC data. Hits in the silicon sensor can now be selected by applying a $3\sigma_{noise}$ cut on the data. To reject the remaining noise hits and other spurious signals a very basic track algorithm is implemented. Accurate determination of the track coordinates is not needed because of the low beam intensity. For both the LW and the BT, only hits are accepted that lie within the coordinate range given by the position and dimension of the beam spot.

Figure 5.17 shows the distribution of tracks over the silicon surface of modules BT3 and BT4 for 0.8 GeV·c^{-1} particles. Also shown are the projections of the distribution on the x- and y-axis. The outline of the active area of the trigger scintillator SC1 is clearly visible. The horizontal and vertical lines indicate the projection of the first scintillator onto BT3 and BT4 assuming a 18×10 mm beam spot. The strip-like structure in the

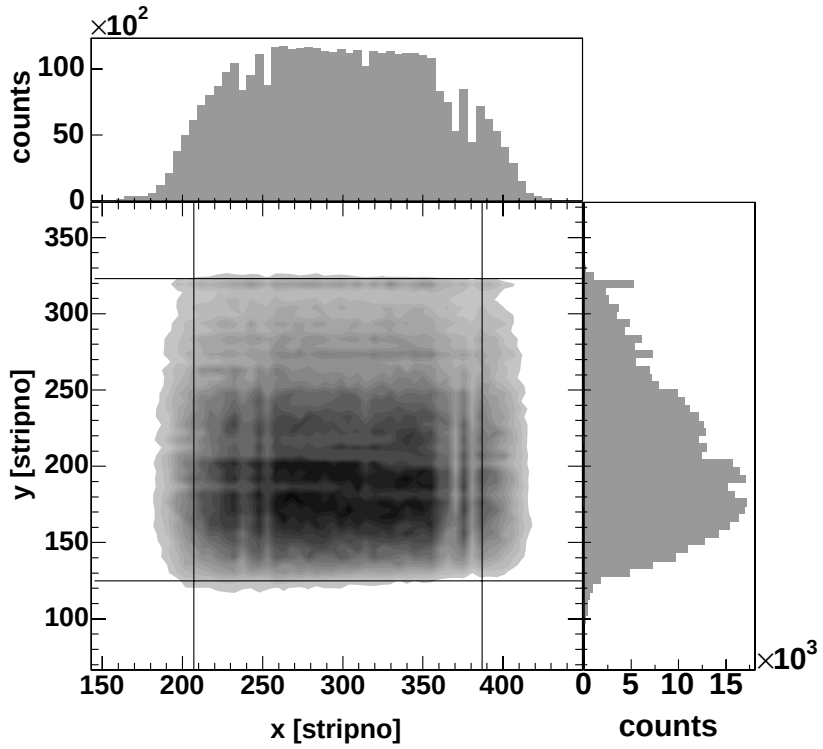

Figure 5.17: *Distribution of tracks over the silicon surface of* BT3 *and* BT4*. The horizontal and vertical lines indicate the projection of the first scintillator on* BT3 *and* BT4 *assuming a 18×10 mm beam spot.*

scatter plot is due to dead strips in either BT3 or BT4. In the x-direction, the beam profile is nearly flat, but in the y-direction the beam-profile has a slope with a lower particle flux in the positive y-direction. This effect could well be caused by the layout of the beam-line. No difference in the profiles was found for different particle species in the beam.

Lambda Wheels hit selection

During data taking several effects deteriorated the quality of the LW data. These effects are not corrected by the common mode noise subtraction algorithm. One of the effects is that some HELIX chips have an alternating baseline for part of the events. Typical for these events is the alternating pattern of a too high and too low pedestal value for two strips in a row. This pattern correlates with the size of the test pulse capacitors and with the (alternating) polarity of the test pulse. Hence the pattern could have been caused by an unintended test pulse injection (as was already mentioned in section 5.3.3). To remove this effect, an extra pedestal subtraction is applied for these chips. The criterion for application of this additional correction is based on the mean value of the signal in two sets of strips, where each set contains all channels with the same test pulse polarity.

Another effect showing up in LW1 and LW2 is the appearance of events with exactly the same strip numbers. As the strip numbering of the LW strips starts from the long strips on both the n- and p-side, combining the p- and n-side hits with equal strip numbers yields x-coordinates belonging to a small region in the center of the detector. By virtue of the misalignment of the beam axis with respect to the optical rail, an exactly equal x coordinate in different LW sensors is unlikely (see Fig. 5.18). The cause of spurious hits of this kind is the interference of the VME readout with the ongoing digitization due to a too early start of the VME readout. The rejection criterion for this type of events is listed below.

The selection of hits that make up a valid candidate track is based on the following four selection criteria:

1. *Probability of the signal amplitude found in the adjacent strips.* Because of the charge sharing due to capacitive coupling, some charge is always transferred to the neighboring channels. The figure of merit is defined as the difference between the charge found in neighboring strips and the expected charge deduced from the signal in the central strip and known coupling factors, divided by the noise. Noise hits in the central strip yield a (large) negative figure of merit. In case of multiple hits, a figure of merit of less than -2 causes the hit to be rejected.
2. *Probability of the signal amplitude found in the back side of the sensor.* Without noise, the signal in the front and back side should be the same. The difference between the two signals divided by the noise is a measure of the probability that the front and backside hits belong to the same track. In case of multiple hits per sensor side, the least probable candidates are removed.
3. *The count of exactly equal strip numbers in* LW*1 and* LW*2.* A high count (3 or 4) is very likely due to the previously described readout error. These hits were rejected.
4. *The difference in the values of Δx and Δy as obtained by combining hits in the first two* LW *sensors and the values of Δx and Δy obtained from hits in the last two sensors.* As Δx and Δy are in first order approximation equal to the angle of the tracks found by the first and second module, hit combinations with matching track angles are kept.

The combination of all criteria removes most of the noise and spurious hits. As a last step, only those events are selected which have exactly one hit in all detector planes.

This last selection step results in a loss of good data as well, which reduces the detection efficiency of the detector as a whole. However, this is considered unimportant for the goal of the present experiment as long as the selection procedure does not introduce a bias in the dataset. Section 5.5.4 deals with the effect of detector inefficiencies on the PID performance.

Beam Telescope hit selection

The first selection of (BT) hits is obtained by combining the information of the ohmic and junction side of each sensor. Because of the small stereo angle, the difference in strip number for the ohmic and junction side hits must be within ± 10 strips. Applying this requirement removes most of the spurious hits and leaves a set of candidate hits. The coordinate (x or y) of these hits is calculated from the charge in the cluster of n strips by the Center-of-Gravity (COG) method

$$x_{cl} = \frac{\sum_i^n q_i x_i}{\sum_i^n q_i}, \tag{5.9}$$

where q_i is the signal charge in strip i and x_i is its position. By combining hits in planes reading the same coordinate, some more hits were rejected.

The difference Δx in x position of tracks recorded in both detector BT1 and BT3 is shown in the left panel of Fig. 5.18, while in the right panel the value of Δy is obtained by combining hits from detector BT2 and BT4. Gaussian fits to the Δx and Δy

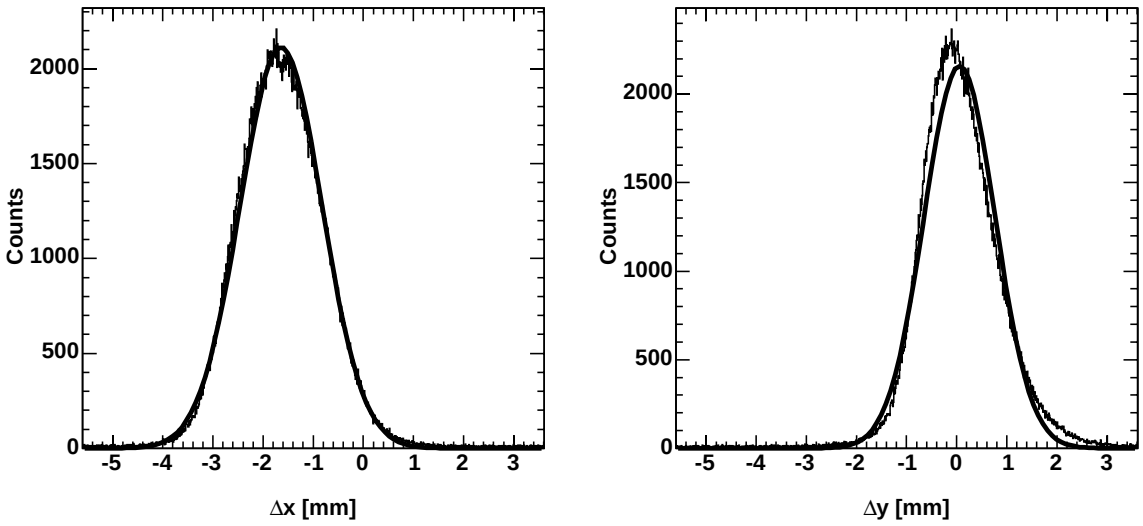

Figure 5.18: *Difference in x- and y-position of tracks passing through the* BT *sensors. The alignment of the tracks with respect to the mounting rail in the x-direction (y-direction) is obtained from sensors* BT1 *and* BT3 *(*BT2 *and* BT4*).*

distribution show that the Δy distribution is skewed. The mean of the Δx distribution is -1.6 ± 0.1 mm which is attributed to a misalignment in the x-direction of the optical rail with respect to the beam. The mean of the Δy distribution is -0.1 ± 0.1 mm and

hence the vertical alignment is correct. The skewness of the distribution is believed to be caused by an asymmetric cut of the beam profile by the scintillators (see Fig. 5.17).

The width of the Δx and Δy distribution is 0.82 ± 0.02 and 0.71 ± 0.02 mm, respectively. Given the distance of 18.1 cm from BT1 to BT3, the width of the Δx distribution translates into an angular spread of 4.5 mrad. The angular spread is due to the combined effect of the divergence of the beam and multiple scattering. The maximum divergence of the beam allowed by the trigger scintillators is given by the geometry of the set-up. If multiple scattering is neglected, the maximum divergence angle is $\pm \arctan(6/416) = 14.4$ mrad, where 6 (cm) is half of the sum of the width of the first and last scintillator and 416 (cm) is the distance between the scintillators[9]. Hence, the observed beam divergence is not limited by the detector geometry.

Multiple tracks

The probability of registering two or more tracks simultaneously by the BT detectors is not negligible because of the long integration time of the APC chip. From Table 5.3 we conclude that the mean time between the passing of two particles in PM1 is 30 μs which gives a probability of $2.6 \cdot 10^{-2}$ that two particles traverse PM1, and hence the silicon, within the 800 ns integration time of the APC[10]. Figure 5.19 shows the number of triggered events containing one, two or three tracks that are observed in the BT sensors. In every plot, bin value zero gives the number of events that have exactly the correct number of hits. To the left of bin zero are the events with one or two hits missing. Similarly, to the right of bin zero the events with extra (noise) hits are shown. For the

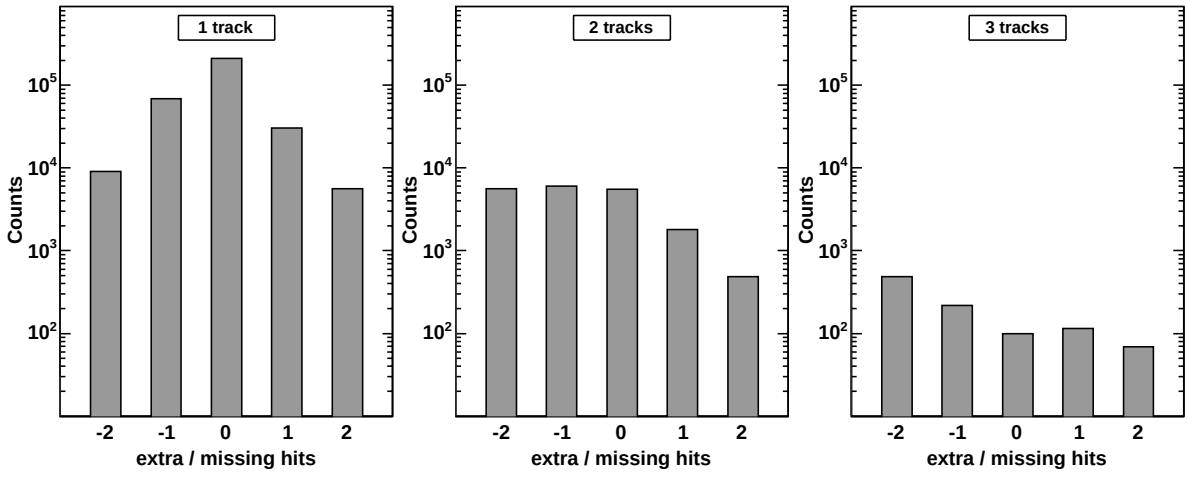

Figure 5.19: *Number of hit combinations in the four* BT *sensors. Most of the entries in the high numbered bins are due to multiple tracks.*

two or three track events, the probability of lacking one hit increases with respect to

[9]This is, however, only true if the focus point of the beam is in front of the silicon set-up (as it was intended). If the focus point lies in between SC1 and SC4, the maximum allowed divergence can be as small as 9.6 mrad, which is still larger than the observed 4.5 mrad.

[10]The probability of observing two tracks in a silicon counter is even larger because the beam spot and the active area of the silicon are both larger than the size of the first scintillator.

the probability to register exactly the correct number of hits.

If we allow a single extra or missing hit, the number of two-track events is 4.1% of the total number of tracks, which has the same order of magnitude as the value calculated from the count rate. Because tracking of particles has not been implemented, the hits from different tracks cannot be distinguished which can lead to errors in the particle identification (which is described in section 5.5). Therefore these events are not used[11].

Efficiency and dead strips

The efficiency of the detectors is lowered by dead and noisy strips. Because total charge collection is important, hits where the maximum signal is found in a strip adjacent to a dead strip are also discarded. Each dead strip thus takes out a region of three neighboring strips. Another source of inefficiency is noisy strips. Strips with more than five times the average number of hits are called noisy. These strips are not used in the hit search, but are, in contrast to dead strips, used when an adjacent strip is hit. Hence, each noisy strip takes out only one strip.

Table 5.10 lists the number of dead and noisy strips for all sensors in the region illuminated by the beam. For the BT sensors, the FWHM of this region is about 170

Table 5.10: *Number of dead and noisy strips in the illuminated region of* BT *and* LW *detectors.*

	BT1-n	BT1-p	BT2-n	BT2-p	BT3-n	BT3-p	BT4-n	BT4-p
dead	0	2	1	2	0	0	2	0
noisy	2	3	2	4	3	5	5	1
	LW1-n	LW1-p	LW2-n	LW2-p	LW3-n	LW3-p	LW4-n	LW4-p
dead	4	1	2	2	1	1	4	2

strips in the x-direction and about 120 strips in the y-direction. The width of the beam in terms of LW strips is about 130. The noisy strips are only shown for the BT detectors because these strips cannot be used as seed in the hit selection mechanism. For the LW modules, the number of noisy channels is small and the hit selection mechanism is more sophisticated. Noisy channels in the LW modules are not marked explicitly but are rejected by step 1,2 or 4 of the hit selection mechanism. The efficiency of detecting a hit in all four sensors (eight sides) of the BT and LW modules, based on the information given in Table 5.10, amounts to 73% and 67%, respectively.

5.3.5 Charge sharing and ohmic-junction side correlations

This section shows some intermediate results from the analysis of the silicon data. The results mainly prove that the signals of the silicon detector are fully understood. Two topics are discussed: the charge sharing among strips for (BT) sensors with intermediate strips, and the correlation of signals derived from the front and back side of BT-detectors.

[11]Removing these events will not affect the accuracy of the particle identification results because they constitute only a few percent of the total number of events.

Charge sharing in the BT sensors

An important difference between the LW and the BT silicon sensors is that the BT sensors have two intermediate strips in between the readout strips. An advantage of intermediate strips is the improvement in position resolution. In the simplest case, that of digital resolution and a high S/N ratio, the position resolution improves by a factor n+1 for n intermediate strips. However, due to the non-zero width of the charge cloud caused by diffusion, the improvement in going from zero to one intermediate strip is less than a factor two. For dE/dx based particle identification, complete reconstruction of the deposited charge in the sensor is important. Due to the extra implanted strips, more charge will remain on the strip-to-backplane capacitance which leads to a loss of signal. A detector optimized for PID should not use such a configuration.

Figure 5.20 shows the charge sharing between the center of the hit (strip n) and its adjacent readout strips. The charge sharing for strip n-1 versus strip n, and n+1 versus n is shown in the upper left and lower right corner of the figure, respectively. In plot (a) two high intensity regions are distinguished which correspond to (i) a hit directly on a readout strip or a hit on the intermediate strip at the n+1 side (lower region), and (ii) to a hit on an intermediate strip on the n-1 side (upper region). If a particle deposits energy in the charge collection region of a readout strip, then still a fraction of the signal is seen on the neighboring readout amplifiers due to charge sharing via the interstrip capacitance and the limited input impedance of the amplifier. The magnitude of this fraction is given by the slope of the line through the readout-hit region. Figure 5.20(c) shows the ratio of the signals in strip n+1 over n. The leftmost peak corresponds to hits on the readout strip. The most probable value for the junction side signal fractions are 8 and 48% for a hit on the readout strip and on an intermediate strip, respectively. On the ohmic side, the equivalent numbers are 13 and 54%. The junction and ohmic side fractions differ due to the larger interstrip capacitance of the ohmic side strips.

If a readout strip is hit, part of the signal is transferred to *both* neighbors. This is indicated in the upper right plot (b) of Fig. 5.20 by the quasi-circular region. Note that the center of this region is offset from zero. If an intermediate strip is hit, not only the two nearest readout strips receive signal but also the readout strips next to these readout strips. This can be seen from the offset of the two non circular regions.

If we look at the most probable energy deposition of a particle as a function of the hit position with respect to the readout strips, we see an 8% loss of signal for a hit on an intermediate strip of the junction side compared to direct hits on a readout strip. The loss of charge on the ohmic side is 2%. The difference between the ohmic and junction side is again due to the larger interstrip capacitance on the ohmic side; less charge remains on the strip-to-back capacitance and more charge is transferred to the readout strips. The 8% loss of signal smears into the energy deposition distribution and thereby adds to its width. However, if tracking is used, the effect can be minimized by introducing a position dependent gain correction factor. This factor is not applied in the analyses.

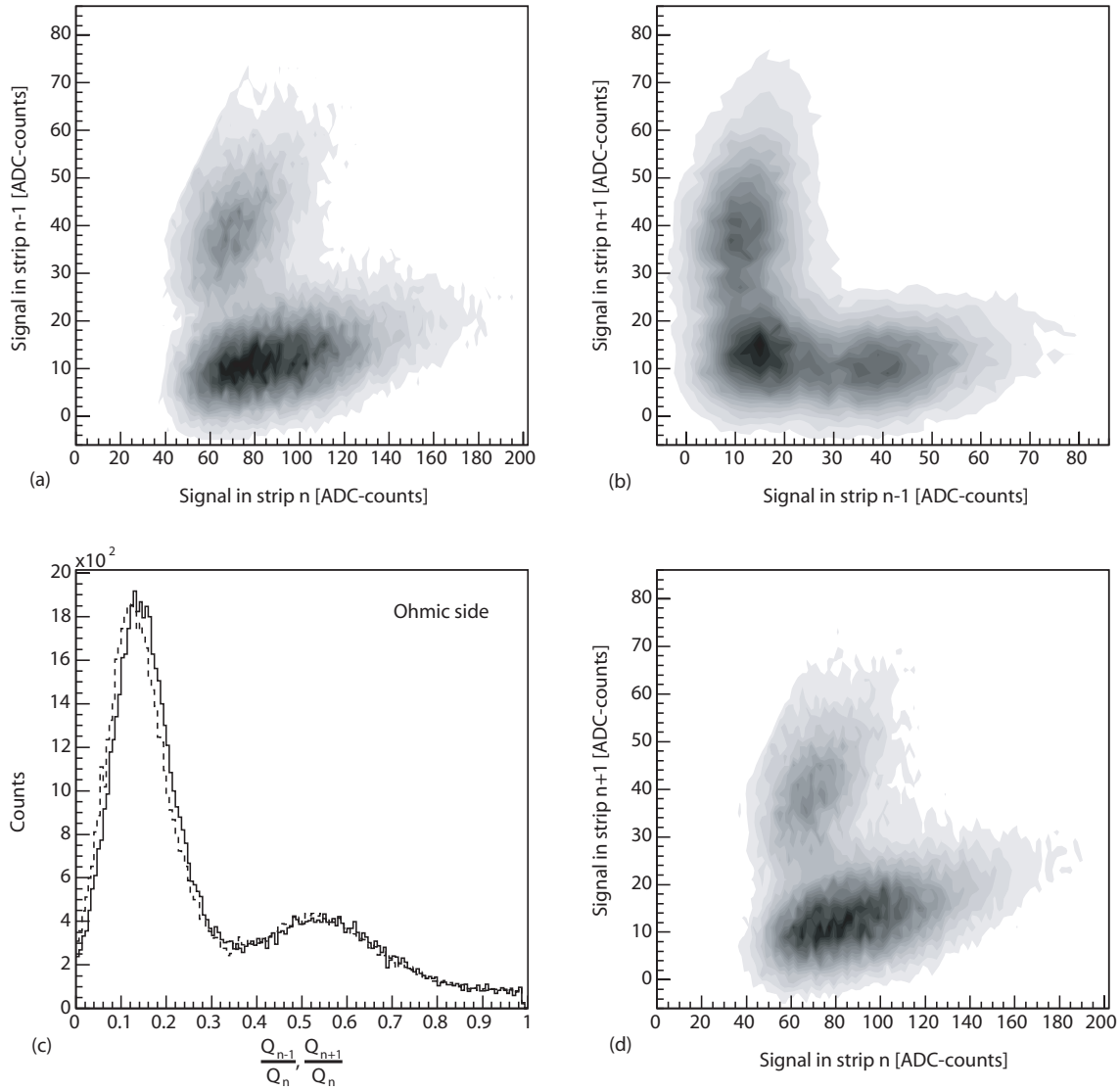

Figure 5.20: *Charge sharing in the ohmic side of a* BT *module. The upper left plot shows the correlation of strip n (center of hit) and strip n-1. Similarly the right plots show the relations n-1 versus n+1 (top), and n+1 versus n (bottom). The bottom left plot shows the ratio of the charges in strip n-1 and n (solid line), and in strip n+1 and n (dashed line), respectively.*

Ohmic and junction side signal correlation

The number of electron-hole pairs liberated by a particle traversing the detector, is a direct measure of the energy deposited by the particle in the active detector volume. Since recombination and trapping of the electrons and holes in (non-irradiated) silicon is negligible, the current induced in the p-strips and n-strips should be the same when

integrated over time[12].

Figure 5.21 shows the ohmic to junction signal correlation for detector BT1 and 0.8 GeV·c^{-1} incident particles. The signal shown is the charge in a cluster, where a cluster is defined as the strip which received most of the charge plus its two neighboring strips. The picture is an overlay of the pion and the proton plots, and therefore the

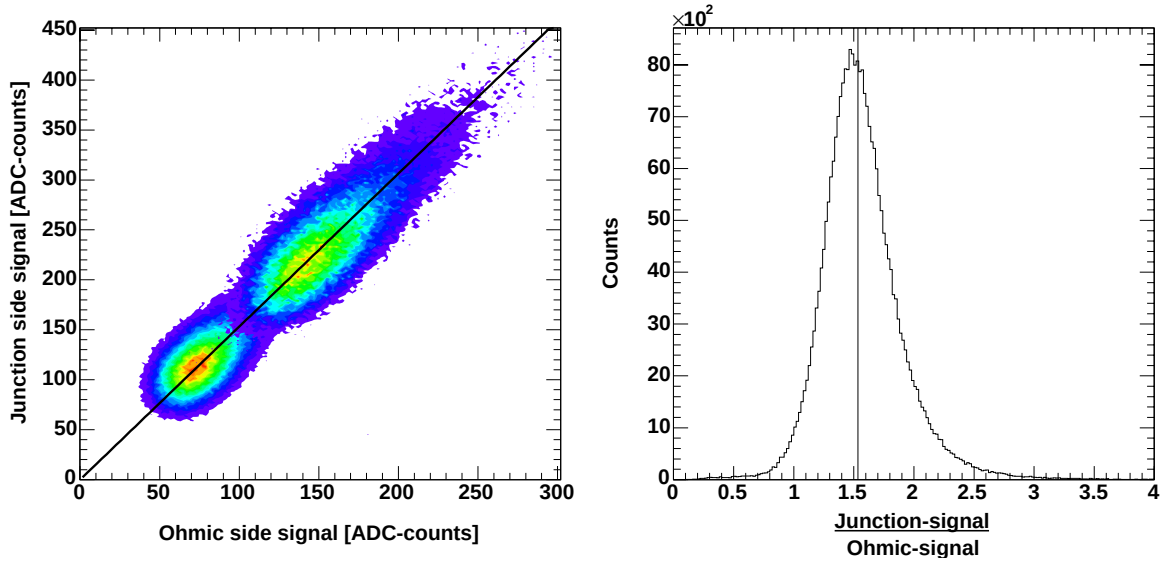

Figure 5.21: *Correlation of ohmic and junction side signals of* BT1 *(left) and the distribution of the ohmic to junction signal ratio. The relative gain (of the ohmic to the junction side) is given by the median value, which is indicated by the vertical line.*

intensities of the two peaks do not correspond to the particle yield. The ohmic and junction side signals are strongly correlated and the relative (junction to ohmic side) gain is given by the slope of the line through the scatter plot. From the ratio of the junction to ohmic side signal for all events, which is shown in the right plot, the relative gain is determined by taking the median value of the distribution; the median value is indicated by the vertical line. The large difference in signal gain of the ohmic and junction side is due to a difference in the line driving electronics of the BT modules.

5.4 Energy deposition distributions

After applying all the corrections and selection criteria as described in the previous sections, the energy deposition distributions for pions and protons can be determined. Distinction between pions and protons is obtained from the TOF information which has a 100% efficiency and a close to 100% purity. Before we can combine the silicon data in order to make a dE/dx based PID, calibration factors need to be calculated. To ease calibration and comparison, the energy deposition distributions of all the silicon planes

[12] A difference could be caused by a ballistic deficit in the amplifiers due to different charge collection times of electrons and holes, but this is only significant when the shaping time of the amplifier is comparable to the charge collection time, which is not the case in this experiment.

are parameterized using a convolution of a Landau function and a Gaussian. The fit used for the parameterization has four free parameters: the most probable value (MP_L) and the width (σ_L) of the Landau distribution, the width of the Gaussian (σ_G) and a normalization factor (k). Note that the term *Most Probable* (MP), which will be used throughout the rest of this chapter, refers to the most probable value of the *convolution* and not to that of the pure Landau function (MP_L), unless specifically stated otherwise.

Two contributions add to the width of the Gaussian: the noise and a contribution to correct for the shortcomings of the Landau function (section 3.2.4). A typical example of a fit with the four free parameters applied to both a pion and a proton energy deposition distribution is given in Fig. 5.22. The example shows that the chosen functional

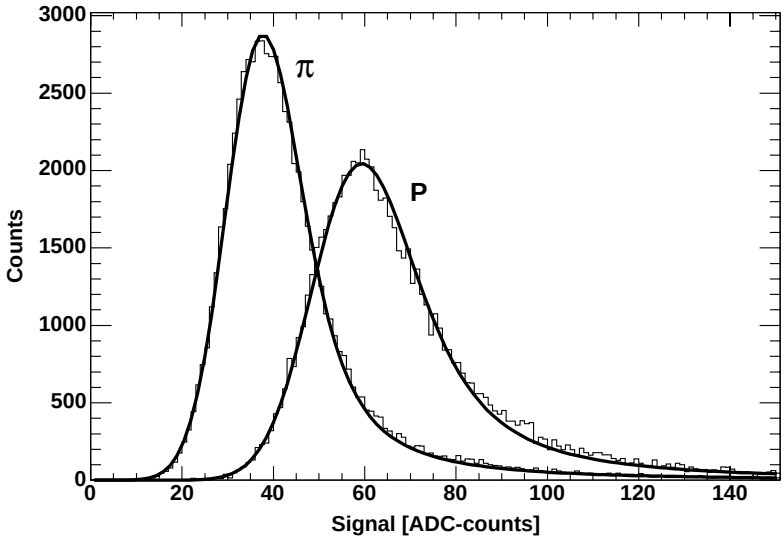

Figure 5.22: *Typical example of a fit, using a Landau function convoluted with a Gaussian, to a pion (left peak) and proton distribution. The signal shown is that of a junction side of a* LW *sensor for a beam momentum of 1.0 GeV·c^{-1}. The pion and proton curves are normalized to the same integral value.*

convolution can be used to describe the measured distributions with good accuracy. For two of the 16 detector sides, the parameterization is less than perfect because of noisy strips or instable behavior of a readout chip. However, even those two parameterizations are good enough to be used in the rest of the analysis.

Strictly speaking, a Vavilov type function should be used in the convolution fit for protons of 0.8 GeV·c^{-1}, because this energy is just outside the region of applicability of the Landau function (see Table 3.3). However, because the difference between a Vavilov and a Landau function is still small for this energy, the Landau function is used which enables direct comparison of the resulting fit parameters.

In the following subsections, the two main characteristics of the energy deposition distributions, i.e. the most probable value and the width, are discussed and compared to the Monte Carlo simulations. First the most probable energy deposition is described in subsections 5.4.1 and 5.4.2. Because of the absence of a real calibration factor (in terms of eV), the ratios of the most probable value of the proton-pion and the positron-pion

distribution are discussed. Subsection 5.4.3 addresses the width of the measured energy deposition distributions.

5.4.1 Ratio of proton and pion MP energy deposition

A direct way to compare a measured energy deposition distribution to the MC distribution is by looking at the ratio of the MP energy deposition of pions and protons. This removes the necessity of absolute calibration constants, which can only be obtained from known energy depositions in the silicon such as from a radioactive source. Absolute calibration factors for the sensor and its associated readout have not been determined for the detectors used in this experiment.

Table 5.11 shows the extracted proton-pion ratios (p/π) for different particle momenta as obtained for all sensors, separately. Although the S/N ratios are slightly different for ohmic and junction sides and also different for Lambda Wheels and Beam Telescope modules, these small differences have almost no influence on the p/π energy deposition ratio.

The simulated distributions are folded with a Gaussian to account for a noise contribution equivalent to a mean S/N value of 7.9 (section 5.3.3). Folding in the noise moves the simulated p/π energy deposition ratio up; the effect is largest for the 0.8 GeV·c^{-1} particles where it moves by 0.03 when going from zero noise (S/N = ∞) to a S/N value of 5. For a beam momentum of 1.3 GeV·c^{-1}, the corresponding shift is less than 0.01.

The simulated ratio is consistently larger than the measured ratio for both the LW and the BT modules and for all five beam momenta. No apparent dependence on ohmic or junction side is visible, neither is there any trend with position along the track of the particle. The uncertainty on the mean measured ratio, which is calculated from the spread in the fit results, is largest for 0.8 GeV·c^{-1} particles.

It has been verified that the difference in measured and simulated p/π ratio cannot be explained by:

- the small difference between the experimental and the simulated momentum;
- small variations in thickness of the sensor or small variations in silicon density;
- different energy loss models in GEANT4. The Photo Absorption Ionization model, for instance, yields the same ratio as the default model[13].
- offset remainders due to flaws in the pedestal subtraction;
- any bias introduced by the common mode noise subtraction algorithm;
- linearity of the preamplifiers and analog to digital converters;
- the size of the charge cluster; the standard 3 strip cluster yields the same p/π ratio as a 5 or 7 strip cluster size;
- noise level in the simulation. At 0.8 GeV·c^{-1} the p/π ratio is most sensitive to the chosen noise level; it decreases by 2% going from a noise level of 0 to a noise level of 4.5ke$^-$. For 1.3 GeV·c^{-1}, the difference is less than 1%;

[13]The Photo Absorption Ionization model in GEANT4.6.2 (a later version of the code) gives a most probable energy deposition for both p and π, which is 25% larger than the values published in the literature (see also section 4.1.2).

Table 5.11: *Ratio of* MP *energy deposition of protons and pions of each* BT *and* LW *sensor at each beam momentum. The mean measured ratio is smaller than the ratio obtained from the simulation.*

sensor	0.8 GeV·c^{-1}	1.0 GeV·c^{-1}	1.1 GeV·c^{-1}	1.2 GeV·c^{-1}	1.3 GeV·c^{-1}
BT1 n-side	1.96	1.55	1.43	1.34	1.26
BT2 n-side	1.96	1.55	1.43	1.33	1.25
BT3 n-side	1.97	1.56	1.43	1.34	1.27
BT4 n-side	2.00	1.56	1.43	1.34	1.27
BT1 p-side	1.93	1.55	1.42	1.33	1.25
BT2 p-side	1.94	1.54	1.42	1.32	1.25
BT3 p-side	1.96	1.55	1.44	1.33	1.26
BT4 p-side	1.94	1.54	1.41	1.32	1.26
LW1 n-side	1.97	1.55	1.44	1.34	1.27
LW2 n-side	2.00	1.57	1.43	1.35	1.27
LW3 n-side	1.97	1.54	1.42	1.34	1.27
LW4 n-side	1.97	1.55	1.42	1.33	1.27
LW1 p-side	2.00	1.57	1.43	1.35	1.28
LW2 p-side	2.03	1.58	1.44	1.36	1.28
LW3 p-side	2.01	1.57	1.43	1.35	1.28
LW4 p-side	2.01	1.56	1.38	1.34	1.29
mean	1.976	1.556	1.426	1.340	1.269
measured	± 0.029	± 0.013	± 0.014	± 0.011	± 0.011
simulated	2.009	1.615	1.490	1.402	1.321
	± 0.002	± 0.002	± 0.002	± 0.002	± 0.002

- experimental effects like the HELIX clock dependence in the LW modules and the *1/32 effect* in the BT modules[14]. These experimental effects modify, to a first order approach, the pion and proton data by the same amount and hence the ratio is not affected.

A possible source of anomalous energy deposition is channeling [113, 114]. Channeling occurs only when a particle traverses the detector with an angle close to one of the major axes of the crystal. For the sensors used in this experiment, the crystal growth direction is known for the LW sensors (<100>), but not known for the BT modules. Hence, the BT silicon will either be of the <111> or <100> type. The critical angle for channeling is given by [38, 53] as

$$\phi_c = \frac{\sqrt{zZa_\infty/(Ad)}}{1670\beta\sqrt{\gamma}}, \tag{5.10}$$

where d is the distance between the rows of atoms, a_∞ is the Bohr radius, and A is the atomic weight of the material. For angles larger than ϕ_c the reduction in stopping power will be negligible.

[14]The influence of the HELIX clock was checked (and found to be negligible) by fitting a distribution using a narrow cut of the allowed HELIX clock phase.

Values of the critical angle, for particles and energies in this experiment, range from 0.05 to 0.23 mrad for <111> silicon. The direction of the BT and LW silicon sensors with respect to the beam axis is 10 ± 2 mrad and 9 ± 5 mrad, respectively, which is much larger than the critical angle. However, the off-axis angle, which is the angle of the crystal axis with respect to the normal of the surface, can be as large as 17 mrad in a typical silicon wafer [115]. Hence, the crystal axis and the beam axis could still have been coplanar.

Assuming the worst case scenario, i.e. with the crystal axis parallel to the beam axis, 4.2% of the 0.8 GeV·c^{-1} protons could have experienced channeling. These channeled protons have a reduced stopping power of up to 30% . By applying fits to MC distributions that included 4.2% of channeled protons, it is found that the effect of channeling on the ratio of the MP energy deposition is negligible. The conclusion is that also channeling cannot explain the difference between the measured and simulated p/π energy deposition ratios.

5.4.2 Ratio of positron and pion MP energy deposition

Because the particle beam also contained a few tens of percents of positrons, enough statistics is available to compare the energy deposition of positrons to that of pions. The ratio of the MP values, from fits to the positron and pion distributions, is given in Table 5.12. The error on the mean measured number is mainly due to the spread in the results from different detectors. Again a S/N level of 7.9 is folded into the simulation

Table 5.12: *Mean measured and simulated ratio of the most probable energy deposition of positrons and pions, compared to the results of a* MC *simulation.*

	0.8 GeV·c^{-1}	1.0 GeV·c^{-1}	1.1 GeV·c^{-1}	1.2 GeV·c^{-1}	1.3 GeV·c^{-1}
mean	1.074	1.069	1.063	1.061	1.058
measured	± 0.004	± 0.005	± 0.006	± 0.007	± 0.007
simulated	1.079	1.077	1.079	1.072	1.070
	± 0.002	± 0.002	± 0.002	± 0.002	± 0.002

results.

Both the measured and simulated e^+/π ratio show a small decrease with increasing momentum, which is due to the relativistic rise in the pion energy loss curve. The γ of the positrons is very high and energy loss by direct ionization for large γ is independent of energy[15]. Although there is a small, consistent, difference in the e^+/π ratio between measurement and simulation, the agreement is good and certainly much better than in the p/π case. It is concluded that the p/π mismatch found in the previous section is probably due to an overestimated proton energy deposition in the Monte Carlo and not due to an underestimation of the pion energy deposition.

[15]This is known as the Fermi plateau in the Bethe-Bloch equation.

5.4.3 Width of the Gaussian in the energy deposition fits

The previous section focused on comparing the MP energy deposition of the measured and MC distributions. Another parameter that can be compared is the width of the distributions. Figure 5.23 shows the fit functions of the measured distribution (solid curves) for pions and protons of 0.8 GeV·c^{-1} together with the expected distribution (dotted curves). The latter is obtained by convolving the Monte Carlo energy distribution with a Gaussian having a width equal to the noise in a three strip cluster. All curves have equal integrated values and the most probable value of the measured and simulated pion distribution is defined as 1 MIP, i.e. the ADC channels of Fig. 5.22 have been converted into an equivalent energy loss scale.

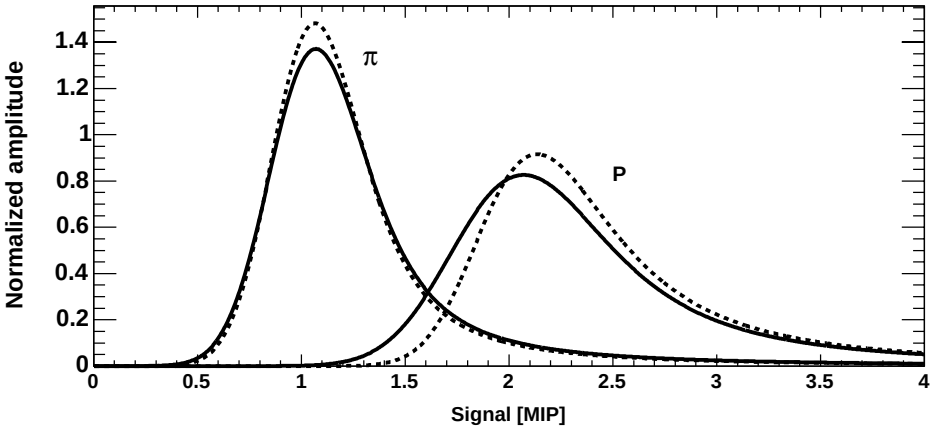

Figure 5.23: *Measured (solid line) and simulated (dotted line) energy deposition of 0.8 GeV·c^{-1} pions (left peak) and protons (right peak). The simulated energy deposition is folded with the noise in a 3 strip cluster. Calibration of the energy deposition is obtained by defining the most probable value of the pion peaks as being equal to 1* MIP. *The curves are normalized to the same area.*

Apart from a shift in position of the measured proton peak, which was the subject of section 5.4.1, both measured peaks are wider than the simulated ones, as can be seen in the figure. By increasing the amount of noise in the simulated distribution, the width of the two peaks can be equalized. Assuming that the results from the Monte Carlo simulations are correct, one would expect the same values for the (electronics) noise. However, the best matching noise level for pions is always lower than the level which is required for the protons.

In the rest of this subsection two slightly different methods to quantify the difference between MC and experiment are pursued. The first method unfolds the noiseless Monte Carlo distribution from the measured distribution. What remains is the excess Gaussian width of the measured distribution which turns out to be larger than the pure electronics noise. The second method unfolds from the measured distribution the measured noise and other known smearing effects. In this case, the remaining distribution is the measured energy deposition straggling. The ratio of the width and the most probable value of the thus obtained 'noiseless' distribution is compared to MC results and to data published in the literature.

Unfolding the excess width of the Gaussian

To determine the excess width (σ_{ew}) of the measured energy deposition distributions with respect to the MC distributions, the parameters of the Landau part of the fit functions are fixed in the fits to the measured distribution. These Landau parameters are obtained from fits to the (noiseless) Monte Carlo distributions. The remaining free fit parameter is the width of the Gaussian σ_{fit} from which the excess width σ_{ew} can be obtained by subtracting the Gaussian width of the simulated distribution σ_{sim}.

The following procedure has been used to remove the gain factors of the different sensors.

- Calibrate the measured and (noiseless) MC curves by setting the most probable value of the corresponding Landau function ($\mathrm{MP_L}$) to unity.
- The normalization parameter (k) is adjusted such that the integral on the distribution is set to unity, for both the measured and the MC curve.
- Fit the normalized *measured* curve with a convolution of a Landau function, using the three fixed parameters of the normalized *simulated* curve, and a Gaussian. The single free parameter of the fit is the width of the Gaussian σ_{fit}.
- Obtain the excess width (σ_{ew}) by using the quadratic relationship $\sigma_{fit}^2 = \sigma_{sim}^2 + \sigma_{ew}^2$, where σ_{sim} is the width of the Gaussian part of the simulated noiseless distribution. This Gaussian (σ_{sim}) is needed to correct for the effect of electronic binding which was discussed in section 3.2.4.

Applying this procedure for all 16 detector sides and taking the mean for each momentum and particle type yields the results for σ_{ew} given in Table 5.13. Also listed are the equivalent numbers for 14 out of 16 detector sides, leaving out the two worst fits. For comparison, the measured noise in a cluster of three strips, obtained from the baseline signal, is also shown. The conversion from ADC-counts to energy is obtained from the most probable energy deposition of GeV positrons in 300 μm silicon (= 85 keV [70]). The uncertainty given is the statistical uncertainty only. In addition, a systematic uncertainty exists due to an uncertainty in the active thickness of the sensors; this uncertainty is estimated to be less than 5%. However, the same calibration uncertainty applies to all measured figures, and hence it is only important when comparing to the simulation results and to data in the literature.

If the measured and the MC distribution would have the same shape, the excess width σ_{ew} of the measured distribution would be equal to the electronics noise. However, the (mean) width σ_{ew} for pions is 33% larger than the pure (measured) electronics noise. The width σ_{ew} from the pion fits is seen to be independent of the particle's energy which is expected because the difference in the MP energy deposition of the pion curves for the various energies is less than 3%. About 8% of σ_{ew} can, at least for the LW modules, be attributed to the clock dependent HELIX gain.

The width of the proton distributions is seen to depend on the momentum. It has been verified that the difference in measured and simulated energy deposition cannot be explained by the presence or absence of multiple scattering in the Monte Carlo. Including inelastic collisions for the primary particles in the MC does not affect the

Table 5.13: *Mean excess width of Gaussian σ_{ew} in keV obtained from fits to the measured distributions using the fit parameters of the noiseless simulated curve. The mean of all 16 detectors sides is listed together with the mean of the best 14 fits. The mean measured electronics noise in a three strip cluster is also shown for comparison.*

	Beam momentum in GeV·c^{-1}				
	0.8	1.0	1.1	1.2	1.3
pion (mean of 16)	13.4 ± 0.5	13.1 ± 0.4	13.4 ± 0.7	13.0 ± 0.5	13.1 ± 0.4
pion (mean of 14)	13.0 ± 0.4	12.7 ± 0.4	12.7 ± 0.5	12.7 ± 0.4	12.7 ± 0.4
proton (mean of 16)	20.6 ± 1.0	17.6 ± 0.7	17.6 ± 1.1	16.5 ± 0.6	16.0 ± 0.6
proton (mean of 14)	19.6 ± 0.7	16.9 ± 0.6	16.3 ± 0.6	15.9 ± 0.5	15.5 ± 0.5
noise (mean of 16)	10.1 ± 0.3	10.2 ± 0.4	10.7 ± 0.6	10.3 ± 0.4	10.1 ± 0.3
noise (mean of 14)	9.8 ± 0.3	9.8 ± 0.3	10.1 ± 0.3	9.9 ± 0.3	9.8 ± 0.3

energy deposition significantly either[16]. Because the electronics noise is the same for all measurements, a reasonable explanation is that the energy deposition straggling in the MC is underestimated for this momentum regime.

Unfolding the electronics noise

An alternative approach is to unfold the electronics noise from the measured energy deposition distribution, which leaves the true energy deposition straggling function. To compare the thus obtained straggling function to results published in the literature, also other effects that lead to smearing of the distribution should be removed, if possible. For the LW sensor, the time dependent HELIX gain factor (see section 5.3.3) increases the width of the distribution by about 8%. This gain factor can be taken out by fitting the distributions for different bins of the HELIX clock timing. For each of the bins, the electronics noise from a three strip cluster is unfolded from the measured distribution. The BT sensors also suffer from a smearing effect, the *1/32 effect* explained in section 5.1.3, but this smearing cannot be unfolded because an independent handle on the effect is lacking. For the BT sensor only the electronics noise from a three strip cluster is unfolded.

Comparison of the present data to results published in the literature is done by evaluating the ratio of the FWHM to the MP. This has the advantage that it takes out the relatively large uncertainty of the thickness of the sensors. This FWHM/MP ratio is almost constant over the energy range explored by the present experiment.

Figure 5.24 shows the FWHM/MP ratio for the LW and BT modules for protons. Additionally, results are shown from calculations by Bichsel [51], measurements from Hancock [68, 69, 51], and simulations from the GEANT4 Monte Carlo. For the signal in the LW and BT modules the charge in the three strips nearest to the track center has been taken. Hence, also the width of the noise that was used for unfolding is that of three strips.

[16]It has been verified that the total inelastic cross section as obtained from the Monte Carlo is in accordance with that found in the literature [116].

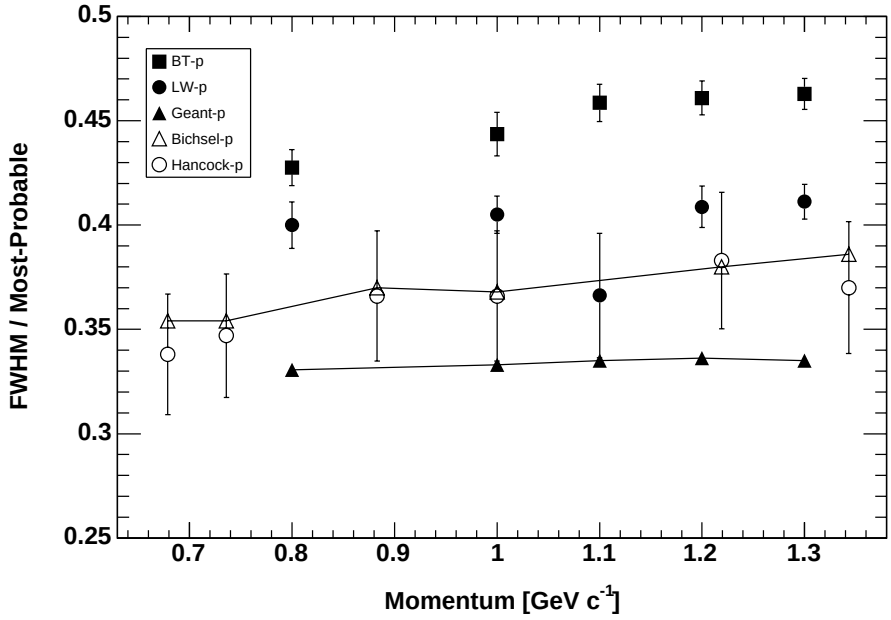

Figure 5.24: *Overview of the* FWHM/MP *ratio of the measured energy deposition distributions (solid squares and circles) in comparison to calculations (open triangles), simulations (solid triangles) and to published measurements (open circles) [68, 69]. The measured ratios are all larger than the calculated values, while the Monte Carlo ratios are smaller than the calculations.*

For both the LW and BT modules, the FWHM/MP ratios are larger than the calculated ratio. The high value of the BT ratio could be due to the *1/32 effect*. There could also be a contribution to the width of the distribution due to incomplete signal collection, which affects the plotted ratio through both the numerator and the denominator. For the LW data, this has been investigated by changing the 3 strip cluster into a 5 strip cluster. It was found that the LW points come down by 0.011, but at the same time the error bars increase due to a larger uncertainty in the noise width.

The MC results based on GEANT4 are consistently lower than the calculations of Bichsel. Assuming that the Bichsel calculations are to be preferred this difference also explains part of the difference in width between the experimental results and the MC results observed in the previous section.

It should be noted that the FWHM/MP of the Bichsel calculations ratio match very well with the Hancock measurements. This is only the case for the ratio, and not for the MP or FWHM value itself. The most probable energy deposition of Hancock's measurement and Bichsel's calculation differ by as much as 10% for the 0.68 GeV·c^{-1} point.

5.4.4 Summary

Before turning to the particle identification capabilities of a multi-layered silicon dE/dx detector, a short summary is given of the results obtained so far.

After applying the time walk corrections, the time-of-flight information from the scintillators gives a close to 100% efficient particle identification of the particles in beam. Also the purity of the TOF decision is close to unity. Hence, the quoted efficiencies and purities in the following sections are those of the silicon system. The numbers need no correction for the inefficiency of the reference PID system.

The energy deposition distribution in all eight silicon sensors has been determined for pions and protons with momenta in the range of 0.8 to 1.3 GeV·c^{-1}. The results of the measurements are mutually consistent, but the measured most probable energy deposition for protons is 1.7 to 4.5% lower compared to the Monte Carlo distributions discussed in chapter 4.

The width of the Gaussian contribution to the measured energy deposition distribution for pions is, after unfolding the MC distribution, about 33% larger than the electronics noise. A part of this extra width (≈8%) is attributed to smearing of the energy deposition distribution due to a sub-optimal tuning of the HELIX peak sampling. For the proton distributions the excess width is even larger and the width is also a function of the momentum.

The FWHM/MP ratios of the measured and simulated energy deposition distributions have been compared to calculations and measured data as reported in the literature. The discrepancy between the MC simulations and the results of this experiment seem to be due, at least partly, to an underestimated width of the simulated energy deposition distribution.

By using the most probable energy deposition of positrons, the calibration factors for all sensors have been determined. The estimated calibration uncertainty, which is mainly due to the unknown (sensitive) thickness of the sensors, is less than 5%.

5.5 Particle identification

From the previous sections it has become clear that the measured energy deposition distributions are wider than the distributions obtained from the MC simulation. In this section it will be studied to what extent this additional width affects the proton-pion identification capabilities. The statistical method used in the analysis of the experimental data is the Kolmogorov-Smirnov (KS)-test, which is described in section 3.3.5. In the KS-test, the probability that a set of energy deposition measurements (samples) belongs to either the proton or pion distribution is determined. The fits to the measured energy deposition distribution, as described in the previous section, are used as probability density functions (PDF) that are needed as input to the KS-test.

Having two sets of four double sided silicon sensors, the PID capability can be determined for different selections of the data. In the rest of this chapter, the KS-test has been applied to the following sensor combinations.

- Four LW sensors.
- Four BT sensors.
- All sensors, both from LW and BT. This configuration is labeled by ALL.

For each sensor, the ohmic and junction side signals are combined into a single number in order to reduce the noise on the measured energy deposition.

Table 5.14: *Particle identification efficiency (ϵ) and purity ($\mathcal{P}$) for 1.3 GeV·c^{-1} particles. The three tables give the result for* LW *only,* BT *only and* ALL *detectors. The number of particles observed as (vertically) and identified as (horizontally) are also shown for each condition.*

		True particle type		
		π	p	$\mathcal{P}$
LW	π	63672	5534	0.920 ± 0.0010
	p	14977	32172	0.682 ± 0.0021
	ϵ	0.810 ± 0.0014	0.852 ± 0.0018	
BT	π	63415	5846	0.916 ± 0.0011
	p	15234	31860	0.677 ± 0.0022
	ϵ	0.806 ± 0.0014	0.845 ± 0.0019	
ALL	π	69736	2845	0.961 ± 0.0007
	p	8913	34861	0.796 ± 0.0019
	ϵ	0.887 ± 0.0011	0.925 ± 0.0014	

Table 5.14 gives the results of the KS-test for one of the 1.3 GeV·c^{-1} beam runs. From top to bottom the three tables show the efficiency (ϵ) and purity ($\mathcal{P}$) for the LW modules, the BT modules and for ALL modules together for the identification of protons and pions. The dataset contains only 36% of the registered events due to the stringent requirement that all 16 out of 16 sensor sides must have a hit. The uncertainties are based on counting statistics only.

Both the LW and BT modules give comparable results with an identification efficiency larger than 80%. A combined analysis pushes the efficiency to the 90% level. The purity depends on the number of particles of each species in the dataset. For a fair comparison, one should quote the purity for e.g. equal number of protons and pions in the dataset. Applying this normalization to Table 5.14 would change the pion and proton purity of the BT data from 0.916 and 0.677 to 0.839 and 0.813, respectively.

5.5.1 Sensitivity to the reference probability density function

In order to investigate the sensitivity of the results to the exact shape of the Probability Density Function (PDF), the proton and pion identification efficiency have been evaluated using different PDFs. Each sample (one per sensor) can be referenced against the Probability Density Functions (PDF) belonging to its own sensor. This method was used in the previous subsection. Alternatively, a single reference PDF per particle type can be used for all samples. Figure 5.25 shows the efficiency of the ALL configuration when using a single PDF per particle type. In this case all samples are tested against the PDF determined for the detector given on the abscissa. In most cases, the KS-test yields

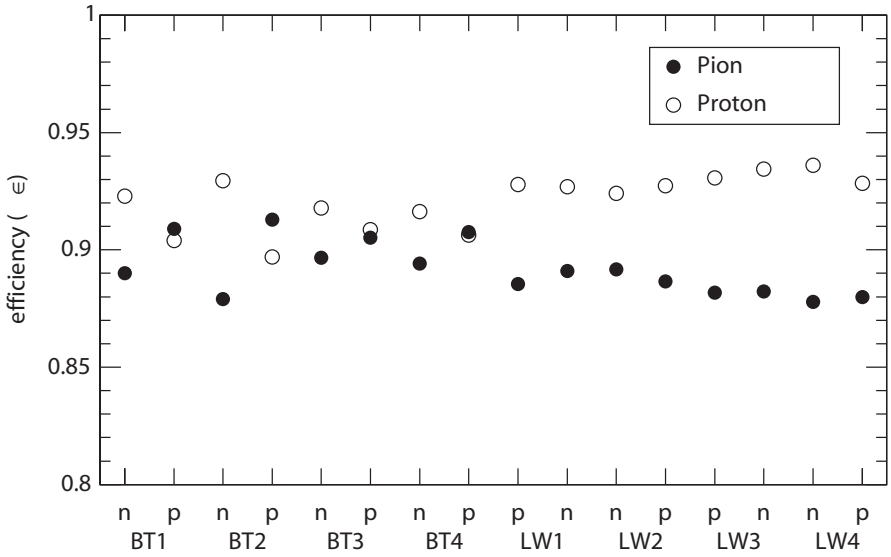

Figure 5.25: PID *efficiency of the* ALL *configuration when using a single reference* PDF *(indicated on the abscissa) for all samples. The higher proton efficiency is due to the long tail of the pion distribution.*

a higher efficiency for protons than for pions. This asymmetry is due to the high-energy tail of the pion distribution. A pion event with many high valued samples is more likely than a proton with many low valued samples. The p-sides of the BT modules are the exception to this rule. These detectors have the largest signal amplification and also the largest pedestals which reduces the dynamic range of these sides to about 3 MIP. The tails of the p-side (proton) distributions are cut off which causes a bias towards low energy samples. Overall the conclusion is that efficiency does not strongly depend on the chosen PDF.

5.5.2 Absolute probability

The KS-test gives the probability (or significance) that a set of samples belongs to a parent distribution. In previous analyses, identification was based on performing two KS-tests (using a pion and a proton PDF) and assigning the particle type from the test giving the highest probability. The absolute value of the probability was not taken into account. In this section the absolute probability returned by the KS-test is discussed in some more detail. To ease the discussion, a dataset consisting solely of pions is considered. A similar analysis carried out for a dataset with only protons, gives comparable results.

Figure 5.26 shows the probability of the KS-test using either a pion or a proton PDF for a dataset consisting solely of pions. An event is assumed correctly identified when the pion probability (P_π) is larger than the proton probability (P_p).

The plots on the left are for a 1.0 GeV·c^{-1} beam and the right hand plots are for a 1.3 GeV·c^{-1}beam. From top to bottom, the plots show the correlation of P_p versus P_π,

the distribution of the pion probability and the distribution of the proton probability. The 1.0 GeV·c^{-1} pions never yield a high proton probability, as shown in plot (e). Wrong identifications are the result of a low probability in both the proton and pion KS-test. Hence, these events do not match well with either the proton or pion PDF. For the 1.3 GeV·c^{-1} pions, on the other hand, a substantial fraction of the wrong identifications is due to a high P_{p} in combination with a low to moderate P_{π} value. These wrong identifications have a high, but wrong, proton probability due to the large number of samples from the tail of the pion energy deposition distribution. The only way to reduce the number of wrong decisions of this type is by increasing the number of dE/dx samples.

Combination of LW and BT probabilities

For each event, three PID decisions are created: a BT decision, a LW decision and an ALL decision. We will now look at the correlation between these collections of decisions. The efficiency of the different decision combinations are listed in Table 5.15.

Table 5.15: *Efficiency of different sets of sensors and for different decision combinations for a 1.3 GeV·c^{-1}run, using only pion tracks.*

set	π efficiency
$\mathrm{LW}_{\mathrm{correct}}$	0.810
$\mathrm{BT}_{\mathrm{correct}}$	0.806
$\mathrm{ALL}_{\mathrm{correct}}$	0.887
$\mathrm{LW}\times\mathrm{BT}_{\mathrm{correct}}$	0.891
$\mathrm{LW}_{\mathrm{correct}} \cap \mathrm{BT}_{\mathrm{correct}}$	0.652
$\mathrm{LW}_{\mathrm{correct}} \cup \mathrm{BT}_{\mathrm{correct}}$	0.964

The first three rows are the pion efficiencies as given in Table 5.14. Intersecting the collections of correctly identified events for LW and BT yields an efficiency of 0.652 which is exactly equal to the product of the BT and LW efficiencies. Hence, no correlation exists between identification decisions taken by the LW and by the BT modules. Similarly, uniting the $\mathrm{LW}_{\mathrm{correct}}$ and $\mathrm{BT}_{\mathrm{correct}}$ event sets gives an efficiency of 0.964 which is again equal to the product of one minus the LW and BT efficiencies. Therefore, also the wrong decisions are not correlated. This absence of correlations shows that the lower efficiency of the individual LW and BT datasets compared to the combination (ALL) is due to the limited number of samples used in the KS-test, and not due to anomalous events.

The efficiency can thus be improved by combining the LW and BT datasets. Two different ways of combining the individual sets have been explored; the use of all eight samples in a single test labeled by ALL, and by multiplying the probabilities of the LW and BT decision. The latter is labeled by LW×BT. Increasing the number of samples in the test (ALL) results in an efficiency of 0.887. The product of the LW and BT probabilities yields essentially the same efficiency.

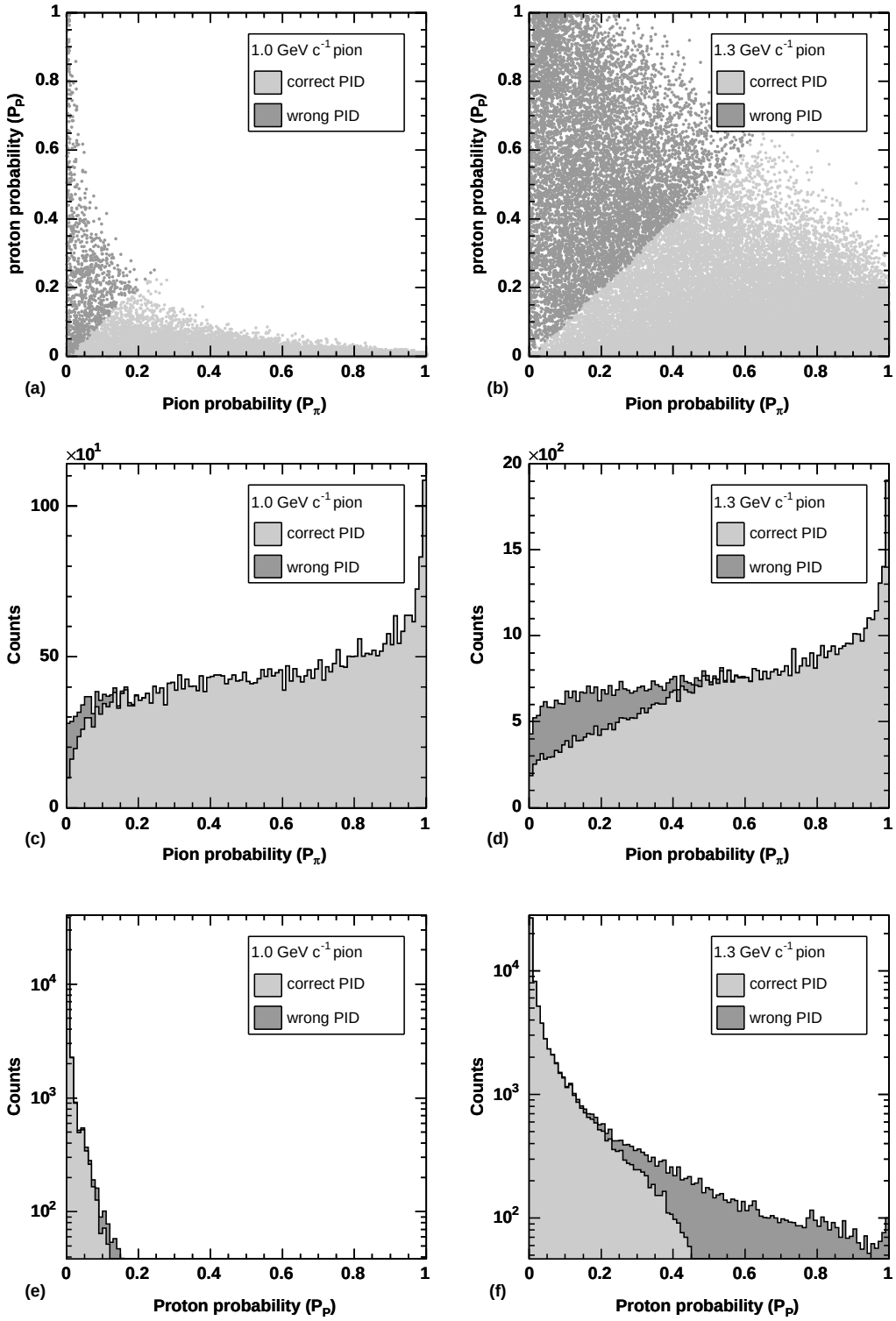

Figure 5.26: *Pion and proton probability distributions for a pion dataset are shown in the middle and lower plots, respectively. The correlation of P_π and P_p is shown in the top panel. The plots on the left side are for 1.0 GeV·c^{-1} incident pions and those on the right side are for 1.3 GeV·c^{-1} pions.*

Probability cuts

In previous sections, the quoted figures on the efficiency and purity were obtained by comparing the significance of the KS-test using either a pion or a proton PDF. Particles are always assigned to either one of the two types. This is possible because of the independent particle identification by means of the time-of-flight system. In absence of the TOF, one should require a minimum value of the probability P. Any event which does not meet this minimum P for either the pion or the proton test, should be labeled as unidentified.

The efficiency as a function of the minimum required P-value for the 1.3 GeV·c^{-1} dataset is shown in Fig. 5.27. A typical value for P, below which the deviation from

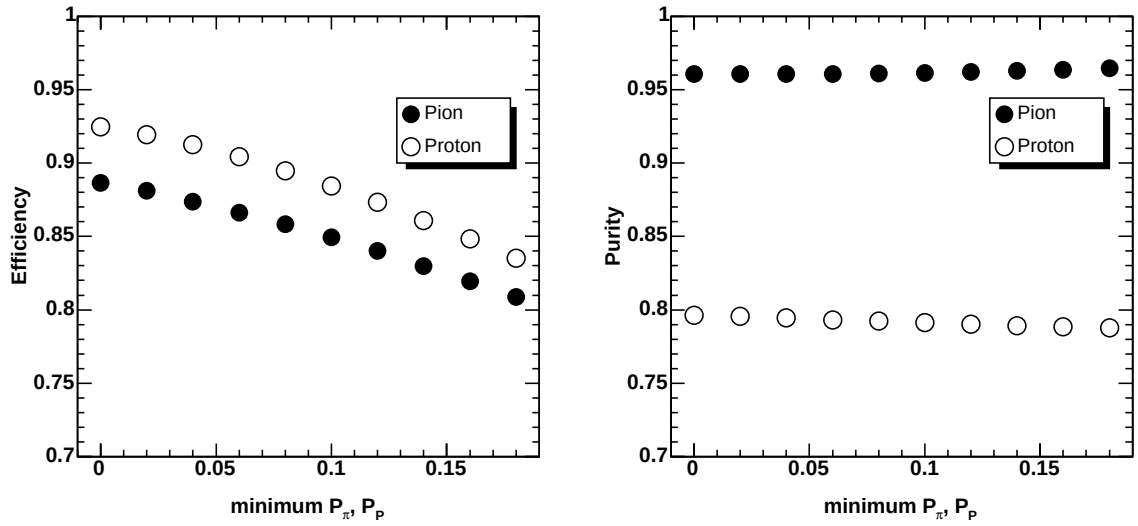

Figure 5.27: *Dependence of efficiency (left plot) and purity (right plot) on the minimum required significance for a 1.3 GeV·c^{-1} dataset.*

the reference distribution is considered substantial, is 0.05 [80]. In the following, a more stringent cut on the P-value of 0.01 will be used. A high cut on the P-value lowers the efficiency but, on the other hand, allows signaling of particles other than the ones examined in the KS-test, as explained below. The purity is virtually independent of the cut of P.

The beam also contained a small fraction of deuterons, but too few to create a deuteron PDF. Applying the KS-tests (with the pion and the proton PDF) to this deuteron dataset, yields P-values smaller than 0.01 for more than 99% of the deuteron events. Hence, requiring a maximum P-value of 0.01 for the complete dataset, filters out almost all deuterons while only a small number of true type pions and protons are selected. Looking at the mean energy deposition of these filtered events, as shown in Fig. 5.28, one can clearly distinguish deuterons from pions. Even the proton peak can be separated from the deuteron peak if the truncated mean is used instead of the arithmetic mean. It is concluded that the use of as many chosen samples as possible and carefully chosen limits on P can substantially improve the PID capabilities of a silicon detector system.

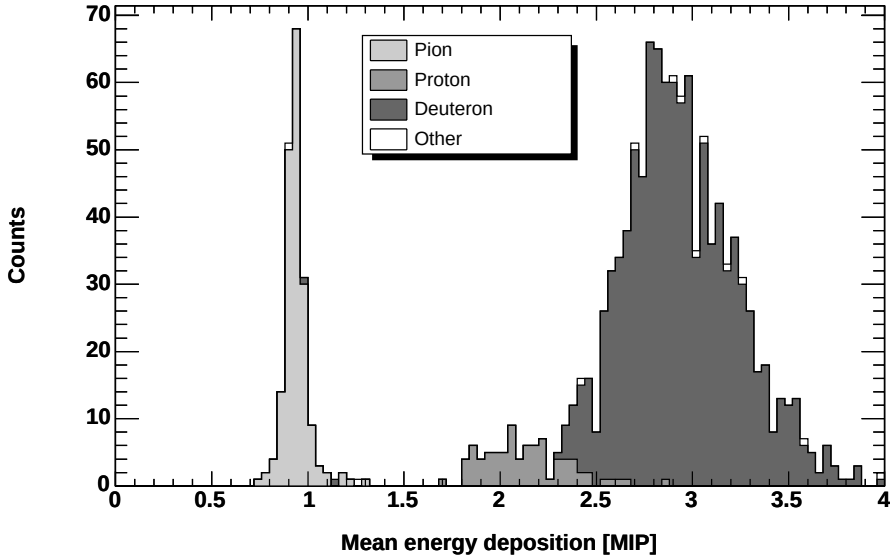

Figure 5.28: *Mean energy deposition of deuterons with a P_π and P_p <0.01. The energy deposition is normalized to the most probable deposition of a* MIP. *Deuterons are well separable from the pions.*

5.5.3 Momentum dependence

Having shown the importance of using combinations of silicon sensors to obtain the highest PID efficiencies, in this section a systematic overview is presented of the efficiencies and purities as a function of the particle momentum. The particle identification efficiency as a function of the momentum is shown in Fig. 5.29 for pions (left) and protons (right), comparing the results from various sensor combinations and from the MC simulations. The efficiency is essentially the same for the two configurations with four sensors and up to 0.08 higher for the eight sensor configuration. As the energy increases, the benefit of using more sensors becomes more pronounced which can be understood from the fact that the closer the two PDFs are, the more samples you need to distinguish the one from the other. The Monte Carlo results are shown as well. They are created using the same techniques as described in section 4.1 but now using only two particle types instead of four and only for perpendicular tracks. The noise level folded into the Monte Carlo data corresponds to a S/N of 8 for minimum ionizing particles, which is very close to the value extracted from the experimental data.

For both the pions and the protons, the efficiency obtained from the Monte Carlo is higher by 3 to 4%. The difference is due to the fact that the measured ratio of the MP pion and proton energy deposition is smaller than the ratio from the Monte Carlo (see Table 5.11).

Nearly the same efficiency is obtained for the 1.2 GeV·c^{-1} measurements as for the 1.3 GeV·c^{-1} Monte Carlo. This can be explained by the fact that the MC energy deposition ratio for 1.3 GeV·c^{-1} is almost equal to the measured ratio for 1.2 GeV·c^{-1} particles. Hence, the difference in efficiency between measurement and Monte Carlo can, to a large extent, be attributed to the difference between the measured and simulated

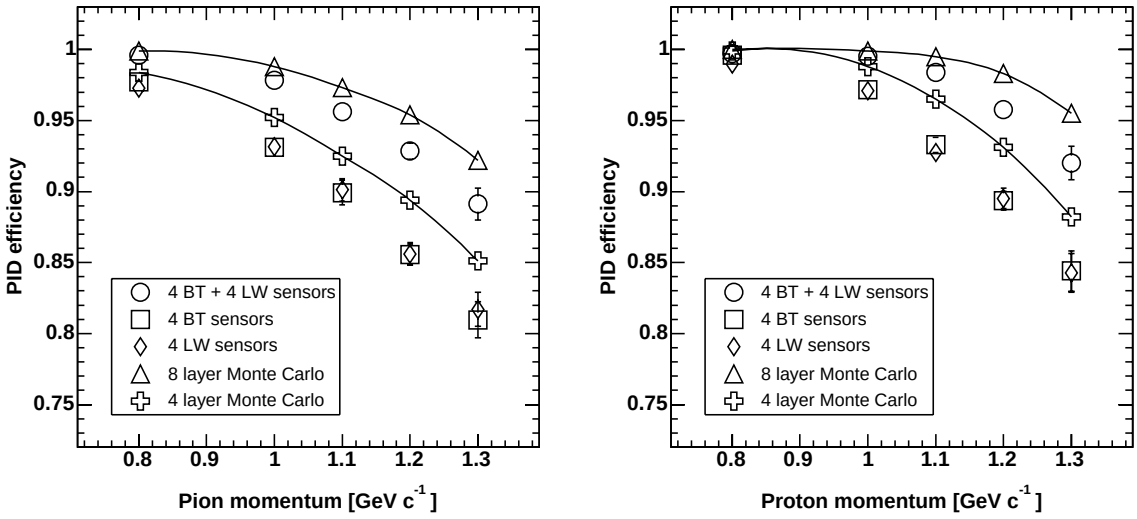

Figure 5.29: *Efficiency as a function of the momentum for pions (left) and protons (right) for various sensor combinations and two* MC *configurations; the latter ones are connected by curves. The efficiency for the* LW *and* BT *datasets is essentially the same. Using a set of eight sensors increases the efficiency by about 0.08 for particles of 1.3 GeV·c^{-1}.*

most probable energy depositions.

The results shown up to now always used a PDF of the proper momentum. In a real experiment, the momentum should be determined from the track of the particle using the same detectors as those used for the dE/dx measurements. Due to the limited detector size and therefore momentum resolution, one will not always determine the exact particle momentum and thus not always use the proper PDF. An estimate of the momentum resolution that can be achieved with a four layer detector in a strong magnetic field has been determined in section 4.2. The momentum resolution ranges from 25 MeV·c^{-1} for 0.8 GeV·c^{-1} protons to 40 MeV·c^{-1} for 1.3 GeV·c^{-1} protons.

The sensitivity of the efficiency to the usage of the correct PDF momentum has been studied by applying the KS-test to a given dataset while using a PDF corresponding to a different momentum. Results of this study are given in Table 5.16; the corresponding normalized purities (i.e. equal flux factors for π and p) are listed in Table 5.17.

The fields on the main diagonal contain the results as presented before and represent the case of a perfect momentum determination. The fields with the light gray background are the efficiencies (purities) of the KS-test when using the nearest available momentum for the PDF; the difference is 100 MeV·c^{-1} in most cases.

As expected, using a higher momentum PDF increases the proton efficiency while at the same time the pion efficiency drops. Similarly, the lower momentum PDF favors pions over protons. The purity dependence on momentum is opposite to the efficiency dependence. Note that the numbers are the result of discrete steps in momentum, while in an actual experiment the calculated momentum will vary around the (correct) mean value. Moreover, a Δp offset gives a much stronger effect than an equal Δp in momentum resolution.

Table 5.16: *Particle identification efficiency of the eight layer configuration when using reference* PDFs *corresponding to different momenta. The figures on the main diagonal represent the results discussed before.*

			particle momentum [GeV·c^{-1}]				
			0.8	1.0	1.1	1.2	1.3
PDF momentum [GeV·c^{-1}]	pion	0.8	0.996	0.994	0.992	0.993	0.994
		1.0	0.984	0.978	0.977	0.975	0.974
		1.1	0.970	0.957	0.956	0.954	0.947
		1.2	0.953	0.930	0.923	0.926	0.914
		1.3	0.937	0.908	0.904	0.902	0.887
	proton	0.8	0.997	0.934	0.732	0.499	0.320
		1.0	0.998	0.995	0.949	0.828	0.672
		1.1	0.999	0.998	0.985	0.920	0.813
		1.2	0.999	0.999	0.992	0.960	0.893
		1.3	0.999	0.999	0.993	0.974	0.925

Table 5.17: *Normalized purities of the eight layer configuration when using reference* PDFs *corresponding to different momenta. The figures on the main diagonal are the same results as were presented before, but now normalized.*

			particle momentum [GeV·c^{-1}]				
			0.8	1.0	1.1	1.2	1.3
PDF momentum [GeV·c^{-1}]	pion	0.8	0.997	0.938	0.787	0.665	0.594
		1.0	0.998	0.995	0.951	0.850	0.748
		1.1	0.999	0.998	0.985	0.922	0.835
		1.2	0.999	0.998	0.991	0.958	0.895
		1.3	0.999	0.998	0.993	0.972	0.922
	proton	0.8	0.996	0.993	0.990	0.986	0.981
		1.0	0.984	0.978	0.976	0.970	0.962
		1.1	0.971	0.959	0.958	0.952	0.939
		1.2	0.955	0.935	0.928	0.928	0.912
		1.3	0.941	0.916	0.912	0.909	0.891

5.5.4 PID efficiency as a function of total detector efficiency

Up to now, the selection of tracks was based on the requirement that a signal was detected in each of the eight double sided sensors. The detectors used in this experiment have, on average, an efficiency of about 95% per sensor side, which is poor. As a consequence the total detector efficiency was only about 45%. Strictly taken, the PID efficiency would have to be multiplied by this detector efficiency, yielding a poor PID efficiency. However, the sensors of this experiment were not selected on the basis of a high efficiency, but on availability.

Alternatively, if a total detector efficiency larger than 99% is required while using double sided sensors with 95% efficiency per side, events with up to three missing hits should be taken into account. Table 5.18 lists the PID efficiency as a function of the number of missing hits for 1.3 GeV·c^{-1} particles both for eight and four double sided sensors. The second column gives the fraction of events in this category, assuming a random distribution of dead strips. Results presented in the previous section are those

Table 5.18: PID *efficiency for a varying amount of missing hits. The efficiency is that of the* KS*-test applied to a 1.3 GeV·c^{-1} run.*

Eight double sided sensors, each 95% efficient			
# missing hits	probability	ϵ_π	ϵ_p
0	0.440	0.887	0.925
1	0.371	0.885	0.923
2	0.146	0.883	0.921
3	0.036	0.880	0.920
total	0.993	0.885	0.923

Four double sided sensors, each 95% efficient			
# missing hits	probability	ϵ_π	ϵ_p
0	0.663	0.808	0.849
1	0.279	0.805	0.845
2	0.051	0.796	0.835
total	0.993	0.807	0.848

listed for zero missing hits. It is clear that missing one, two or three hits has only little influence on the PID efficiency. The total PID efficiency, which is the weighted average of the PID efficiency for zero to four missing hits, is virtually equal to that of a 100% efficient detector. So even though the detector modules used in this experiment are far from perfect, they are good enough to reliably identify particles. It should be noted that the impact of missing hits on the momentum determination is more severe.

5.5.5 Summary

At this point only a short summary of the particle identification results is given. The conclusions are deferred to the next chapter where they are combined with the outlook. With the experiment described in this chapter, it has been shown that particle identification based on dE/dx sampling is possible up to 1.3 GeV·c^{-1} with a few layers of silicon sensors. It is found that with four typical double sided detectors, particle identification at 1.3 GeV·c^{-1} can be achieved with an efficiency of 0.81 and 0.85 for pions and protons, respectively. Increasing the number of layers from four to eight, increases the efficiency by about 0.08 both for pion and proton identification. At lower momenta, the efficiency increases towards 1 for momenta of 0.8 GeV·c^{-1} and below. The normalized purity for 1.3 GeV·c^{-1} is on average 0.83 for a four layer configuration.

The efficiency obtained from the Monte Carlo simulations and the results from the experiment differ by about 0.04, virtually irrespective of the particle type and the number of layers. An explanation for the observed difference is found in the lower value of the most probable energy deposition of protons in the experiment compared to the MC simulation. The simulated most probable energy deposition of protons seems to be too large. Another small contribution to the difference in simulated and experimentally obtained efficiency is due to the difference in width of the simulated and measured energy deposition distributions. Not only is the measured distribution wider than the theoretical prediction from Bichsel, but also is the MC distribution narrower than the Bichsel calculations.

Chapter 6

Conclusions and outlook

6.1 Conclusions

In this thesis it has been investigated to what extent a stack of thin silicon detectors can be used to observe and identify recoil protons produced in Deep Inelastic Scattering. Such observations serve the purpose of enabling measurements of Generalized Parton Distributions. The Monte Carlo studies described in chapter 4 and the experimental investigation of proton-pion separation presented in chapter 5 show that particle identification by means of dE/dx sampling is possible with a stack of silicon detectors up to momenta of 1.3 GeV·c^{-1}, which is considerably higher than the upper limit of 0.8 GeV·c^{-1} commonly used in the most recent applications. The efficiency (purity) that can be accomplished with four silicon sensors with a thickness of 300 μm each is shown to be 0.81 (0.92) and 0.85 (0.68) when separating pions from protons with a momentum of 1.3 GeV·c^{-1} , respectively. Below 0.8 GeV·c^{-1} the efficiency and purity are close to unity. The specifications obtained are close to the intrinsic limits of the chosen particle identification technique for this type of detectors. These specifications fulfill the requirements of a recoil detector in the target area of a future fixed-target deep-inelastic scattering experiment like TESLA-N [27] as described in chapter 2.

The experimental results show that the predictive power of the Monte Carlo simulations is reasonably good; the MC results give a slightly optimistic picture of the detector capabilities compared to the experimental case. The difference in PID performance between simulation and measurement can be attributed to differences in the energy deposition distributions. The most probable value and the width of the energy deposition distribution are the two parameters that describe this difference best. Both the experimental and the Monte Carlo distributions have been compared to the limited amount of data available from literature and to the best known calculations. From this comparison it is concluded that the measured distributions are about 10% wider than expected from the calculations, while at the same time, the simulated distributions are about 10% narrower than those calculations. The difference in measured and simulated energy deposition distribution affects the particle identification efficiency by less than 4% for a four or eight layer telescope. It is therefore considered a minor effect.

Various detector configurations have been explored by means of a Monte Carlo study. The number of detector layers and hence the number of dE/dx samples was varied while

at the same time the total amount of material in the path of the particles and the total number of readout channels was kept constant. Increasing the number of layers from four to eight hardly improves the efficiency, but does increase the purity by about 0.05. Given the high number of background events, a configuration with larger area strips is not desired because of the higher occupancy (which is further discussed in the next section). If not only the number of layers but also the number of readout channels is doubled, the efficiency improves by 0.07 for particles with a momentum of 1.3 GeV·c^{-1}. However, doubling the number of readout channels and hence the costs cannot be justified on the basis of this relatively small increase in efficiency.

It has also been shown by a MC simulation that the performance of a multi-layer silicon recoil detector is not very sensitive to the noise of the readout electronics. The reason for the absence of this sensitivity is that the noiseless energy deposition distributions are already wide and hence the additional broadening due to noise contributes only little to the total width.

The PID determination requires knowledge on the particle's momentum. In the absence of detectors in the target region, the momentum of the particles must be determined from the curvature of the tracks in the strong magnetic field used to keep the target polarized. With a Monte Carlo simulation it has been shown that the resolution of the momentum measurement ranges from 25 MeV·c^{-1} to 40 MeV·c^{-1} for particles with a momentum of 0.8 GeV·c^{-1} and 1.3 GeV·c^{-1} , respectively. The accuracy of the momentum determination affects the PID efficiency only little. In the extreme case of an offset of 50 MeV·c^{-1} of the reconstructed momentum with respect to the true momentum for *all* events, the efficiency changes by at most 0.04.

6.2 Outlook

In this thesis it has been shown that a recoil detector consisting of four layers of silicon strip detectors can be used to separate pions from protons with a momentum up to at least 1.3 GeV·c^{-1} based on the dE/dx information. A point of concern is, however, the number of background events seen by such a detector in the target region. As was calculated in chapter 2, the number of background events for a future high luminosity DIS experiment is very high which requires the use of pixel detectors instead of strip detectors. Pixel-type detectors are needed because the peak count-rate, i.e. the count rate during the bunch train, is very high and not because of a high average count rate. If the lepton beam would be continuous, a detector built from microstrip sensors with a total of several tens of thousands of strips per layer would suffice for the envisaged recoil detector. However, for a beam with the time structure foreseen at the TESLA accelerator the number of background events would yield strip occupancies of nearly 100%.

In this section, the readout of the pixel type detectors is further considered in order to determine whether pixel readout chips, which represent the current state of the technology, could be used for the proposed recoil detector. Several options are explored; fast readout during the bunch train, and temporary storage of the signals in each pixel with readout at regular intervals during the bunch trains. Many other readout schemes could be envisioned but are not addressed because they are essentially combinations of these

two basic options. If temporary storage is used, each stored signal must be accompanied by a time-stamp that is used to select the triggered event from the background events. Given the anticipated rate of 140 hits per ns within the acceptance of the recoil detector together with the several million detector elements per layer, a time stamp with a resolution of a few ns should be enough to resolve tracking ambiguities.

First we recapitulate the main figures regarding the number of background events. As calculated in chapter 2, the number of background events per 0.77 ns long bunch is 108 per layer in the presence of a longitudinal magnetic field. Together with the number of bunches per pulse train of the TESLA accelerator of about $1.25 \cdot 10^6$ it brings the total number of hits in a single 1 ms bunch train to 135 million per detector layer. The average surface area of a detector layer will be in the order of 400 cm^2, which yields a hit rate of 0.35 hits per ns and per cm^2, i.e. a peak rate of 350 MHz·cm^{-2}. In case the experiment is operated with an unpolarized target, no magnetic field is needed in the target area. In that case the number of background events traversing the recoil detector is a factor 15 larger which is prohibitive. It is therefore required to operate a recoil detector always together with a longitudinal magnetic field even if a non-polarized target is used. The magnetic field sweeps out the Møller electrons which are produced copiously in the dense target. The CLAS12 experiment [117] also uses a solenoid to reduce the large number of Møller electrons.

The question is whether the pixel detectors that are currently available are suitable for handling the quoted rate even if a magnetic field is assumed to be present at all times. Pixel chips can roughly be grouped into three categories, (i) counting chips for imaging, (ii) chips with charge integration and (iii) chips with pulse shaping front-ends. The imaging type pixel chips contain a discriminator for each pixel followed by a counter. Because the energy deposition information is lost, these chips are not suited for dE/dx-based particle identification. In the remainder of this section we discuss the suitability of each one of the other two options separately.

Charge integrating front-end chips

In charge integrating chips the charge liberated by the traversing particle is capacitively stored onto an internal node until the readout starts. In case of multiple hits on a single pixel, the individual charges are accumulated. If the occupancy per pixel is low, this does not pose a problem. Well known examples of this type of pixel detectors are Charge Coupled Devices (CCD) and Monolithic Active Pixel Sensors (MAPS). An advantage of these integrating devices is that they are directly suited for application at a continuous beam. Although the proposed TESLA-N beam will be bunched, the bunch frequency of 1.3 GHz cannot be resolved and hence the beam is quasi-continuous during the 1 ms long bunch train.

The current state of the art CCD devices, under development for experiments at the future International Linear Collider (ILC)[1], are so called column parallel CCDs (CPCCD)[118]. In these chips, each column has its own readout circuitry including a

[1] TESLA represented the first fully worked-out design of a future 0.5 - 1.0 TeV e^+e^- collider. Many of the design solutions developed for TESLA are now finding their way into the ILC design. The time structure of the ILC bunch train is the same as the time structure of TESLA.

fast ADC. With this configuration, readout times of about 50 μs can be achieved at an analog to digital conversion speed of 50 MHz. The limiting factor in the CPCCD devices is the charge transfer inside the CCD more than the capabilities of the readout electronics on the periphery of the CCD. The major drawback of CCD-type detectors is the sequential readout of all storage nodes. Data reduction is done at a relatively late stage and hence the readout remains slow.

Another major example of an integrating front-end chip is the Monolithic Active Pixel Sensor (MAPS). MAPS has a matrix type readout which allows random access readout of pixels with a hit. This reduces the number of pixels to be read out by a large factor compared to a CCD. Developments on monolithic pixel sensors for the ILC aim at a readout time of 50 μs for a complete sensor. Because the amount of data to be read is limited, only a small number of outputs per MAPS is used compared to a CPCCD.

For a recoil detector, a readout time of 50 μs is too long, because about 7 million particles will traverse the detector in this time. From experience with the SLD detector [119], tracking is only possible if the occupancy per pixel is less than $1 \cdot 10^{-3}$. Hence, a number of 7 billion pixels per layer would be needed which corresponds to a pixel size of 2.5×2.5 μm^2. This is beyond any currently available device and therefore also monolithic active pixel sensors seem less suited for the envisaged recoil detector. If the readout time per MAPS would be reduced by a factor 10, for instance by increasing the number of outputs by the same factor, a MAPS would be capable of handling the high background rate of the proposed recoil detector. The maximum allowed pixel size then becomes 7.5×7.5 μm^2. Note that the development of CCD and MAPS is driven by the requirements for a vertex detector of an experiment at a high energy linear collider like the ILC [32]. The required position resolution of a vertex detector for the ILC is several micrometers, and hence the amount of material in the vertex detector must be kept very low which favors detectors where the active area and readout are integrated into a single (thin) wafer as in CCDs and MAPS. The estimated hit rate of this vertex detector is only 0.03 hits per mm^2 and per bunch of 337 ns [119], while the equivalent figure for the TESLA-N target region is 1.2, i.e. a factor 40 higher. Therefore, it is not surprising that the developments aimed at a vertex detector for the linear collider do not match with that of a recoil detector for a fixed target experiment at the same collider. The typical size of pixels in CPCCD and MAPS devices is 20×20 μm^2 which is more than sufficient for adequate momentum determination.

Pulse shaping front-end chips

Pulse shaping chips consist of a preamplifier followed by a pulse shaping stage with typical shaping times from several tens to several hundreds nanoseconds. The chips that store binary information like the one used for the ATLAS experiment [120] can only be used for tracking and not for dE/dx particle identification. The pixel chip used in the CMS experiment[121, 122] has a readout architecture that better suits the application studied in this thesis. Each pixel in the CMS chip has, in addition to the preamplifier and shaper, a sample and hold circuit to store the signal charge and a discriminator which is used to notify the readout electronics about the presence of a hit. The hit information is copied almost directly into buffers on the periphery of the chip, where

it is awaiting readout. Only hits are readout which correspond to the correct trigger label. The data are sparsified at an early stage which minimizes the amount of data to be read out. The CMS pixel chip is built in a 0.25 μm technology and has a pixel size of 100×150 μm^2.

Beam tests have shown that the CMS pixel chips can handle a readout rate of 80 MHz·cm^{-2} with an inefficiency as low as 2.7% [121]. This rate is only a factor 4.5 lower than required for a recoil detector operated in a longitudinal magnetic field. By reducing the surface area of each pixel by a factor four while increasing the infrastructure like buffers and interconnects with the same factor, a readout scheme that matches the requirements of the presently discussed recoil detector can be obtained. Increasing the depth of the buffers would increase the dead area of the chip but moving to a smaller integrated circuit technology reduces the problem of the (dead) surface area of the periphery[2]. Fortunately, the required pixel size of about 60×60 μm^2 represents no limitation for bump bonding as indium bumps with a diameter as small as 12 μm have been shown to be possible [123]. In fact, the development of new pixel type detectors with a higher readout bandwidth is being considered for upgrades of the LHC project [124]. In the most ambitious upgrade scenario, the luminosity of the LHC machine will increase by almost a factor 10 and hence the pixel detectors will need higher bandwidth readout schemes to match the higher count-rates. These new pixel detector readout chips can be applied at the recoil detector design discussed in this thesis.

One more issue that needs attention in pulse shaping chips is the capturing of the peak signal of the pulse when the chip is operated with a continuous beam. The above mentioned CMS pixel chip is synchronized to the bunch crossing clock of the LHC machine which allows tuning of the sample time to the peak of the shaped signals which have a peaking time of about 25 ns. For the quasi continuous beam of the TESLA-N experiment, the bunch frequency of 1.3 GHz is much too high to be used as sampling clock. Downscaling the bunch frequency to correspond to the shaping time of the front-end is a possibility, but would introduce a quasi random sampling moment with respect to the peak of the pulse. This effect is similar to the effect described in section 5.3.3 and it leads to a broadening of the energy deposition distribution which in turn leads to a degradation of the PID performance. The simplest way to minimize this effect is to increase the peaking time of the front-end at the cost of an increased probability of signal pile-up.

To conclude, the readout of a recoil detector at a future deep inelastic scattering facility with a luminosity of $1\cdot10^{35}$ cm^{-2}·s^{-1} is a challenging task. Given the developments on pixel detectors that will take place for upgrades of the LHC experiments, a pixel type recoil detector seems a viable option. On-chip data reduction should be accomplished at the earliest possible stage. It is thus concluded that the identification of recoil protons in fixed-target DIS experiments can be realized at the foreseen high-luminosity facilities which are likely to be hosted by the ILC. Such a recoil detector should consist of four to

[2]New circuits for high-energy physics application are being designed in a technology with a 0.13 μm feature size which is a factor two smaller than the technology used for the current version of the CMS pixel chip. Compared to electronics industry this technology is still rather conservative. A modern industrial technology has a feature size of 65 nm while experimental technologies with a feature size as small as 10 nm have been shown to be possible.

eight thin layers of silicon detectors that are readout by new pulse-shaping pixel chips that will be developed for upgrades of the LHC experiments.

Appendix A

Behavior of a Constant Fraction Discriminator

Constant Fraction Discriminators (CFD) were used for PM3 and PM4 in order to reduce time walk. Looking at the time walk of PM4 in Figure 5.8, a clear time walk (Δt_{PM4}) shows up for low ADC values, while for ADC values larger than 200 the Δt_{PM4} is almost independent of the ADC value. The CFD seems to behave like a normal discriminator for ADC values smaller than 200. Note that the time walk for ADC > 200 is less than 100 ps (apart from the last point), which is within specification of the Ortec type 934 CFD [125] (150 ps).

The dual behavior can be explained by looking in some detail at the operation of a CFD. Figure A.1 shows the basic functionality of an Ortec type 934. The input signal

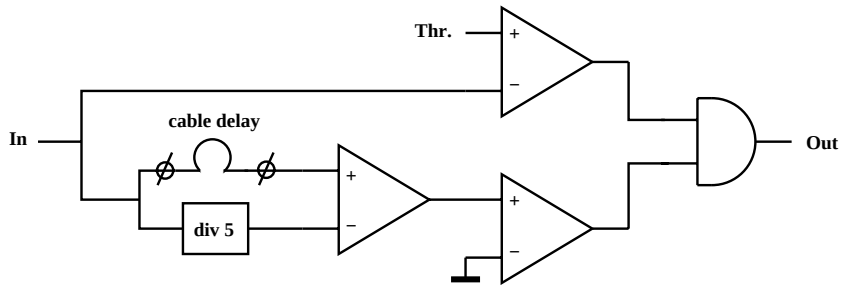

Figure A.1: *Basic functional diagram of a constant fraction discriminator.*

from the photomultiplier is supplied to two circuits, a normal (threshold) discriminator and a constant fraction discriminator. An output pulse is produced from the logic AND of the normal discriminator and the CFD. The output timing of the normal discriminator shows time walk and it should only act as enable for the CFD-output.

The operation of the CFD part is explained with the help of Fig. A.2. The input signal is split in two parts. One part is attenuated by a factor 5 and subtracted from the delayed input pulse. The amount of delay is selectable by cable. Figure A.2 shows that the resulting bipolar signal crosses the baseline at a fixed, but selectable, time with respect to the start of the pulse. The operation principle of the CFD part does not depend on the selected cable delay. However, the cable delay should be chosen such that the output of the CFD determines the timing of the logic AND. If the cable delay is

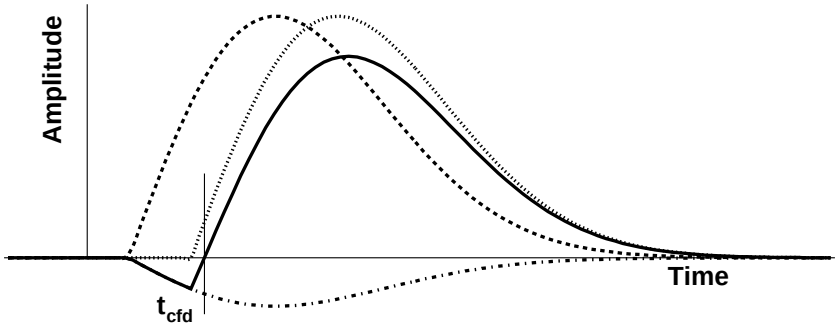

Figure A.2: *Operation of the* CFD. *The input pulse (dashed curve) is delayed (dotted) and added to an attenuated inverted pulse (dash-dot) yielding a bipolar pulse (solid curve). The output of the* CFD *fires when the bipolar pulse changes polarity which is indicated by time* t_{cfd}.

too short, the unit will work as a normal discriminator for signals with a low amplitude because then the output of the normal discriminator fires later than the CFD part. This effect is depicted in Figure A.3. The two dashed curves are the signals going into the

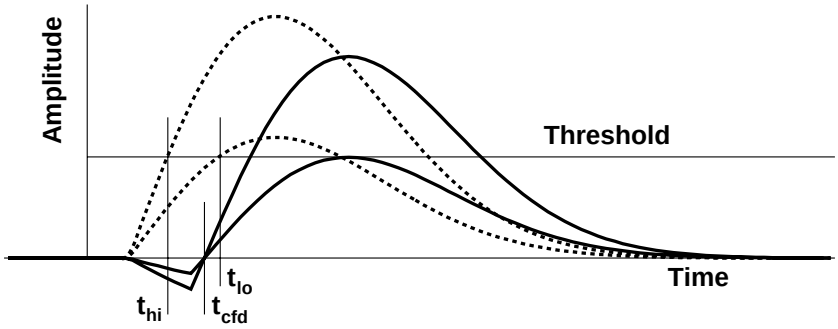

Figure A.3: *The moment at which the threshold discriminator fires depends on the amplitude of the pulse. If the cable delay of the* CFD *is too short, the* CFD *fires too early* (t_{cfd}). *For small input pulses, the timing is determined by the threshold discriminator and not by the* CFD *part.*

threshold discriminator whose output exhibits time walk. For a small input pulse, the threshold discriminator fires at t_{lo} which is later than t_{cfd}, and as a result the output of the CFD unit shows time walk. For large input pulses, the threshold discriminator output fires earlier than t_{cfd}, and no time walk will occur.

Hence, the observed behavior of PM3 and PM4 is probably caused by a too short cable delay. Selection of the cable delay for the CFD was done *before* the experiment with the help of a radioactive source using short coaxial cables for the connection of the photomultiplier to the CFD. At CERN long coaxial cables (> 50 meter) were used which give rise to dispersion of the signals. Dispersion will increase the peaking time of the signals which should have been compensated by increasing the length of the delay cable. This retuning of the delay cables was accidentally omitted.

Appendix B

Noise correlation in strip clusters

For dE/dx based particle identification, the total deposited energy should be known and therefore the signal in a cluster of three strips is accumulated. However, not only the signal but also the noise adds up. Because the noise sources in the three different amplifiers, which are the main contributors to the noise, are uncorrelated a total noise of $\sqrt{3}$ times the noise in a single strip is expected. However, the observed noise in a three channel cluster is smaller than expected which implies a non-zero (negative) covariance of noise sources. This is caused by the cross coupling of the readout amplifiers as will be explained below.

An example of the ratio of the noise in a cluster of three adjacent strips and the noise in a single strip is shown for one the LW modules in the left plot of Fig. B.1. The horizontal line indicates a ratio of $\sqrt{3}$ which corresponds to the addition of three uncorrelated noise sources of equal magnitude. The right hand side of Fig. B.1 shows

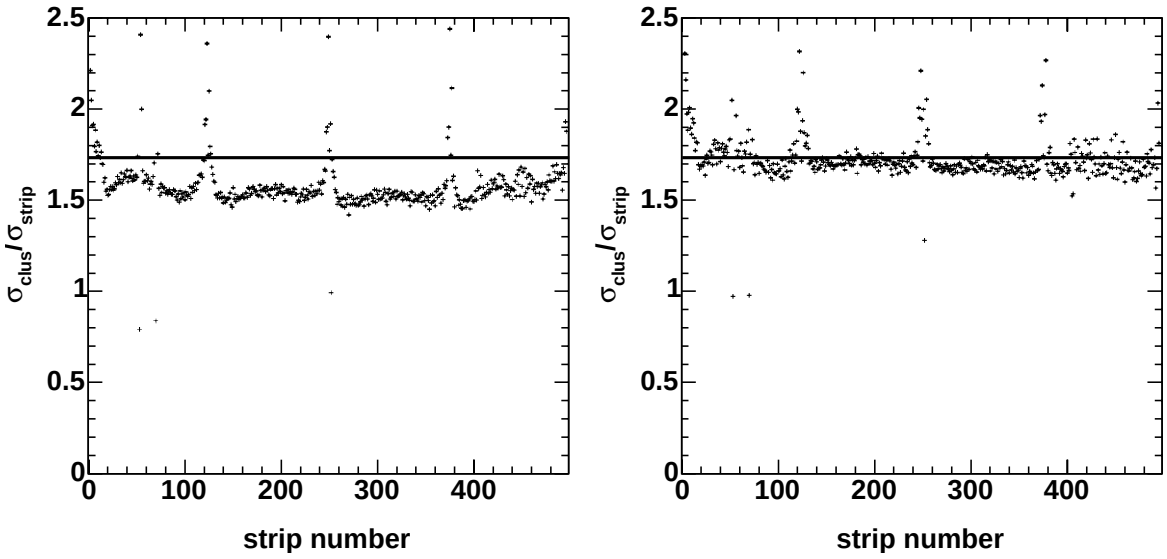

Figure B.1: *Sum of the noise in three adjacent strips (left) and three non-adjacent strips (right). The horizontal line at $\sqrt{3}$ indicates the sum of the noise from three uncorrelated sources of equal magnitude. The noise in three adjacent strips is correlated.*

the sum of the noise in three strips that are not adjacent but have a distance of two strips. In this case the noise is close to the expected level.

The observed difference for the sum of the noise in three adjacent strips can be explained by looking in some detail into the coupling of the electronics to the detector strips. Figure B.2 shows a simplified diagram of this coupling. The diagram only shows the dominant voltage noise sources. A complete treatment of noise sources is given in [126].

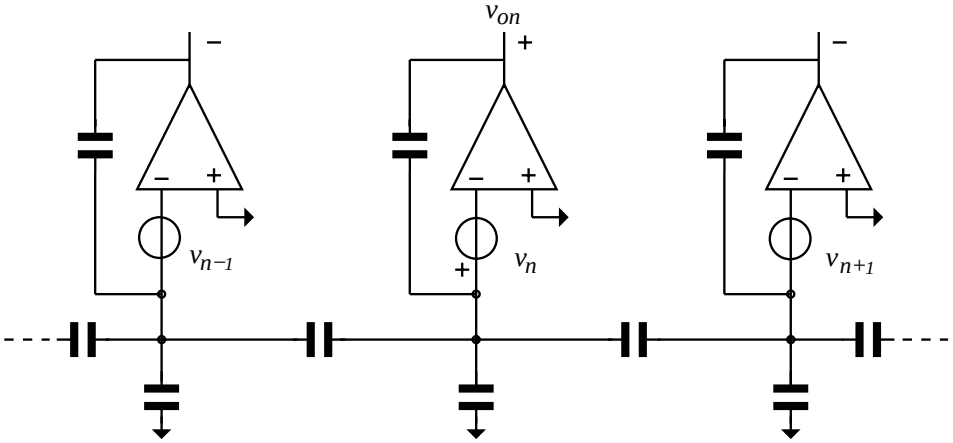

Figure B.2: *Simplified schematic diagram of the coupling between different preamplifiers. The dominant voltage noise source is indicated by* v_n.

The *ac* voltage noise source in the center channel, denoted by v_n, introduces a voltage $k_1 \cdot v_n$ on the output of amplifier n, where the gain factor k_1 depends on the impedances of the network elements. Superimposed on this noise voltage from the amplifier itself is a noise contribution from sources v_{n+1} and v_{n-1}. These contributions are amplified by a factor k_2, where k_2 is, in general, much smaller than k_1[1]. Hence, the noise voltage at the output of amplifier n can be expressed as

$$v_{on} = k_1 \cdot v_n - k_2 \cdot v_{n-1} - k_2 \cdot v_{n+1}. \tag{B.1}$$

The minus signs are due to fact that amplifier n acts as a non-inverting amplifier as seen from voltage source v_n and as an inverting amplifier when looking from v_{n-1} and v_{n+1}. Assuming equal magnitudes (σ) for all noise sources, the magnitude of the noise voltage at the output of amplifier n is

$$\sigma_{on} = \sigma\sqrt{k_1^2 + 2 \cdot k_2^2}. \tag{B.2}$$

Similarly, amplifiers $n+1$ and $n-1$ pick up noise from its neighbors. If we add up the (noise) signal in three neighboring strips, the noise voltage in the cluster becomes

$$\begin{aligned} v_{cl} \;=\; & k_1 \cdot v_n - k_2 \cdot v_{n-1} - k_2 \cdot v_{n+1} + \\ & + k_1 \cdot v_{n-1} - k_2 \cdot v_{n-2} - k_2 \cdot v_n + \\ & + k_1 \cdot v_{n+1} - k_2 \cdot v_n - k_2 \cdot v_{n+2}. \end{aligned} \tag{B.3}$$

[1]The maximum value of gain factor k_2 is $0.5k_1$.

The corresponding noise magnitude is then given by

$$\sigma_{cl} = \sigma\sqrt{3k_1^2 + 6k_2^2 - 8k_1k_2}. \tag{B.4}$$

The first two terms give the noise in case the noise voltages at the amplifier outputs are totally uncorrelated. The third term accounts for the reduction of the noise in a cluster. Because of the non-zero coupling between different amplifiers, which is expressed by a non-zero value of k_2, the noise in a cluster of three strips is less than $\sqrt{3}$ times the noise in a single strip.

Bibliography

[1] P.J. van Heerden. *The crystal counter, a new instrument in nuclear physics*. PhD thesis, Rijksuniversiteit Utrecht, July 1945.

[2] K.G. McKay. A. Germanium Counter. *Phys. Rev.*, 76:1537, 1949.

[3] D.E. Wooldridge, A.J. Ahearn, and J.A. Burton. Conductivity Pulses Induced in Diamond by Alpha-Particles. *Phys. Rev.*, 71:913, 1947.

[4] G.L. Miller, W.M. Gibson, and P.F. Donovan. Semiconductor particle detectors. *Ann. Rev. Nucl. Sci.*, 12:189, 1962.

[5] H.E. Wegner. Semiconductor and Gas-Ion-Chamber Detector System for the Mass Identification of 10- to 30-MeV Particles. *Rev. Sci. Instr.*, 33:271, 1962.

[6] C.A.J. Ammerlaan, R.F. Rumphorst, and L.A.Ch. Koerts. Particle identification by pulse shape discrimination in the p-i-n type semiconductor detector. *Nucl. Instrum. Meth.*, 22:189, 1963.

[7] G. Dearnaley and A.B. Whitehead. The semiconductor surface barrier for nuclear particle detection. *Nucl. Instrum. Meth.*, 12:205, 1961.

[8] W.K. Hofker et al. The checker board counter: a semiconductor dE/dx detector with position indication. *IEEE Trans. Nucl. Sci.*, NS13:208, 1966.

[9] E.H.M. Heijne et al. A silicon surface barrier microstrip detector designed for high-energy physics. *Nucl. Instrum. Meth.*, 178:331–343, 1980.

[10] R. Bailey et al. First measurement of efficiency and precision of CCD detectors for high-energy physics. *Nucl. Instr. Meth.*, 213:201, 1983.

[11] E.H.M. Heijne, P. Jarron, A. Olsen, and N. Redaelli. The silicon micropattern detector: a dream? *Nucl. Instrum. Meth.*, A273:615–619, 1988.

[12] E. Ros. ATLAS inner detector. *Nucl. Phys. Proc. Suppl.*, 120:235–238, 2003.

[13] The HERMES Collaboration. The HERMES Recoil Detector. Technical Report HERMES 02-003, DESY-HERMES, 2002.

[14] E. Maddox. *Study of heavy quark production at HERA using the ZEUS microvertex detector*. PhD thesis, Universiteit van Amsterdam, December 2004.

[15] A. Airapetian et al. Quark Helicity Distributions in up-, down-, and strange-quarks from Semi-inclusive Deep-inelastic Scattering. *Phys. Rev.*, D71:12003, 2005. hep-ex/0407032 and DESY-04-107.

[16] V. Mexner. *Determination of the gluon polarization in the nucleon.* PhD thesis, Universiteit van Amsterdam, December 2005.

[17] R. Devenish and A. Cooper-Sarkar. *Deep Inelastic Scattering.* Oxford University Press, 2004.

[18] F. Halzen and A.D. Martin. *Quarks and Leptons: An Introductory Course in Modern Particle Physics.* John Wiley & Sons, 1984.

[19] C. Adloff et al. Deep-inelastic inclusive *ep* scattering at low x and a determination of alpha(s). *Eur. Phys. J.*, C21:33–61, 2001. hep-ex/0012053.

[20] J. Ashman et al. A measurement of the spin asymmetry and determination of the structure function g(1) in deep inelastic muon proton scattering. *Phys. Lett.*, B206:364, 1988.

[21] J. R. Ellis and M. Karliner. Direct estimate of the gluon polarization in the nucleon. 2005. hep-ph/0501115.

[22] X. Ji. Deeply-virtual Compton scattering. *Phys. Rev.*, D55:7114–7125, 1997. hep-ph/9609381.

[23] A. Airapetian et al. Single-spin asymmetries in semi-inclusive deep-inelastic scattering on a transversely polarized hydrogen target. *Phys. Rev. Lett.*, 94:012002, 2005. hep-ex/0408013 and DESY-04-141.

[24] D. Muller, D. Robaschik, B. Geyer, F. M. Dittes, and J. Horejsi. Wave functions, evolution equations and evolution kernels from light-ray operators of QCD. *Fortschr. Phys.*, 42:101, 1994.

[25] K. Goeke, Maxim V. Polyakov, and M. Vanderhaeghen. Hard exclusive reactions and the structure of hadrons. *Prog. Part. Nucl. Phys.*, 47:401–515, 2001. hep-ph/0106012.

[26] I. Abt, A. Caldwell, X. Liu, and J. Sutiak. A detector for forward physics at eRHIC: Feasibility study. 2004. hep-ex/0407053.

[27] M. Anselmino et al. Electron scattering with polarized targets at TESLA. Technical report, TESLA-N Study Group, 2000. hep-ph/0011299.

[28] L. Merminga et al. ELIC: An electron light ion collider based at CEBAF. Prepared for 8th European Particle Accelerator Conference (EPAC 2002), Paris, France, 3-7 Jun 2002.

[29] D. Ryckbosch. The ELFE project. *Nucl. Phys.*, A699:392, 2002.

[30] T. Walcher. ELFE: An Electron Laboratory For Europe. *Nucl. Phys.*, A666:193–202, 2000.

[31] F. Richard (ed.), J.R. Schneider(ed.), D. Trines (ed.), and A. Wagner (ed.). TESLA Technical Design Report Part I: Executive Summary. 2001. hep-ph/0106314.

[32] The International Linear Collider Communication Group. Technical report. `http://www.slac.stanford.edu/xorg/ilc-trc/2002/2002/report/03rep.htm`.

[33] G. van der Steenhoven. Private communications. 2005.

[34] The COMPASS Collaboration. Common muon and proton apparatus for structure and spectroscopy. Technical report, 1996. Proposal to the CERN SPSLC, CERN/SPSLC/ 96-14, SPSC/P 297, March 1, 1996 and addendum, CERN/SPSLC/96-30, SPSLC/P 297 Add. 1, May 20, 1996.

[35] D. G. Crabb and D. B. Day. The Virginia/Basel/SLAC polarized target: Operation and performance during experiment E143 at SLAC. *Nucl. Instrum. Meth.*, A356:9–19, 1995.

[36] J.J.M. Steijger and G. van der Steenhoven. Recoil detection for a DIS facility at TESLA. Technical Report NIKHEF 2000-013, NIKHEF, 2000.

[37] E.M. Lifshitz L.D. Landau. *Course of theoretical physics. Vol.4. Part 1. Relativistic quantum theory*. Pergamon Press, 1971.

[38] W.R. Leo. *Techniques for Nuclear and Particle Physics Experiments: A How-to Approach*. Springer-Verlag, second revised edition edition, 1993. Berlin, Germany: Springer (1994) 378 p.

[39] R. Maier. Synchrotron radiation. Technical report, 1991. In: General Accelerator Physics Course , Jülich, Germany , 17 - 28 Sep 1990 - pages 97-115, CERN 91-04.

[40] D.E. Cullen, J.H. Hubbell, and L. Kissel. EPDL97: the Evaluated Photon Data Library, '97 Version. Technical report. `http://www-nds.iaea.org/epdl97/index.html`.

[41] M. Huhtinen. Simulation of non-ionising energy loss and defect formation in silicon. *Nucl. Instrum. Meth.*, A491:194–215, 2002.

[42] U. Stange et al. OTIS, A Radiation Hard TDC For LHCb. In *Proceedings of the VIII Workshop on Electronics for LHC Experiments*, 2002.

[43] M. Battaglia and P.M. Kluit. Particle identification using the DELPHI RICH detectors. *Nucl. Instrum. Meth.*, A433:252–256, 1999.

[44] J. Cohen-Tanugi et al. Optical properties of the DIRC fused silica Cherenkov radiator. *Nucl. Instrum. Meth.*, A515:680–700, 2003. hep-ex/0305001.

[45] B. Dolgoshein. Transition radiation detectors. *Nucl. Instrum. Meth.*, A326:434, 1993.

[46] B. Lasiuk. Particle identification in the NA49 TPCs. *Nucl. Instr. Meth.*, A409:402–406, 1998.

[47] S. Wenig. Performance of the large-scale TPC system in the CERN heavy ion experiment NA49. *Nucl. Instrum. Meth.*, A409:100–104, 1998.

[48] J. Visser et al. Design and performance of a silicon test counter for HERMES. *Nucl. Instrum. Meth.*, A521:430–440, 2004.

[49] H. Esbensen et al. Random and channeled energy loss in thin germanium and silicon crystals for positive and negative 2-15 GeV/c pions, kaons and protons. *Phys. Rev.*, B18(3):1039, August 1978.

[50] E. Uggerhøj. Some energy loss and channeling phenomena for GeV particles. *Phys. Scripta*, 28:331, 1983.

[51] H. Bichsel. Straggling in thin silicon detectors. *Rev. Mod. Phys.*, 60:663, 1988.

[52] U. Fano. Penetration of protons, alpha particles, and mesons. *Ann. Rev. Nucl. Sci.*, 13:1, 1963.

[53] S.P. Ahlen. Theoretical and experimental aspects of the energy loss of relativistic heavily ionizing particles. *Rev. Mod. Phys.*, 52(1):121, January 1980. erratum in Rev. Mod. Phys 52, number3, 653 (1980).

[54] E.A. Uehling. Penetration of heavy charged particles in matter. *Ann. Rev. Nucl. Sci.*, 4:315–350, 1954.

[55] G.S. Khandelwal. Shell Corrections for K- and L-Electrons. *Nucl. Phys.*, A116:97–111, 1968.

[56] M.C. Walske. The Stopping Power of K-Electrons. *Phys. Rev.*, 88(6):1283, December 1952.

[57] M.C. Walske. Stopping Power of L-Electrons. *Phys. Rev.*, 101(3):940, February 1956.

[58] R.M. Sternheimer, M.J. Berger, and S.M. Seltzer. Density effect for the ionization loss of charged particles in various substances. *At. Data & Nucl. Data Tabl.*, 30:261, 1984.

[59] B.R. Appleton, C. Erginsoy, and W.M. Gibson. Channeling Effects in the Energy Loss of 3-11-MeV Protons in Silicon and Germanium Single Crystals. *Phys. Rev.*, 161(2):330–349, September 1967.

[60] J.F. Bak et al. Large Departures from Landau Distributions for High-energy Particles Traversing Thin Si and Ge Targets. *Nucl. Phys.*, B288:681, 1987.

[61] C. Erginsoy, H.E. Wegner, and W.M. Gibson. Anisotropic energy loss of light particles of MeV energies in thin silicon single crystals. *Phys. Rev. Lett.*, 13(17):530, October 1964.

[62] W.M. Gibson. The role of particle channelling in detector systems. *IEEE Trans. Nucl. Sci.*, 13:162, June 1966.

[63] O.N. Jarvis, A.C. Sherwood, C. Whitehead, and M.W. Lucas. Channeling of fast protons, deuterons, and alpha particles. *Phys. Rev.*, B19(11):5559, June 1979.

[64] J.J. Kolata, T.M. Amos, and H. Bichsel. Energy-Loss Straggling of Protons in Silicon. *Phys. Rev.*, 176(2):484, December 1968.

[65] H.E. Wegner, C. Erginsoy, and W.M. Gibson. The energy loss by charged particles in silicon as a function of track orientation. *IEEE Trans. Nucl. Sci.*, 12:240, February 1965.

[66] L. Landau. On the energy loss of fast particles by ionisation. *J. Phys. U.S.S.R.*, 8:201, 1944.

[67] P.V. Vavilov. Ionization Losses of High-Energy Heavy Particles. *Sov. Phys. JETP*, 5(4):749–751, November 1957.

[68] S. Hancock, F. James, J. Movchet, P. G. Rancoita, and L. Van Rossum. Energy loss and energy straggling of protons and pions in the momentum range 0.7-GeV/c to 115-GeV/c. *Phys. Rev.*, A28:615, 1983.

[69] S. Hancock, F. James, J. Movchet, P. G. Rancoita, and L. Van Rossum. Energy loss distributions for single particles and several particles in a thin silicon absorber. *Nucl. Instr. Meth.*, B1:16–22, 1984.

[70] K. Hagiwara et al. Review of Particle Physics. *Physical Review D*, 66:010001+, 2002.

[71] H. Bichsel and C. Tschalaer. A range-energy table for heavy particles in silicon. *Nucl. Data*, 3(3):343, October 1967.

[72] D. Buskulic et al. Performance of the ALEPH detector at LEP. *Nucl. Instrum. Meth.*, A360:481–506, 1995.

[73] DELPHI Collaboration. The DELPHI detector at LEP. *Nucl. Instrum. Meth.*, A303:233–276, 1991.

[74] B. Schumm. dE/dx particle identification with a five layer silicon tracker. Technical report, SLAC-BABAR, 1994. SLAC-BABAR-NOTE-126.

[75] H. Bichsel. Particle identification with TPC. Star Note SN0441, May 2000.

[76] S. Agostinelli et al. GEANT4 - a simulation toolkit. *Nucl. Instrum. Meth.*, A506:250–303, 2003.

[77] W.W.M. Allison and J.H. Cobb. Relativistic charged particle identification by energy loss. *Ann. Rev. Nucl. Part. Sci.*, 30:253–298, 1980.

[78] W.H. Press, S.A. Teukolsky, W.A. Vetterling, and B.P. Flannery. *Numerical Recipes in C, The Art of Scientific Computing*. Cambridge University Press, second edition edition, 1992.

[79] G.W. Collins. *Fundamental Numerical Methods and Data Analysis*. `http://astrwww.cwru.edu/personal/collins`, 2003.

[80] E.W. Weisstein. Significance. From MathWorld–A Wolfram Web Resource. `http://mathworld.wolfram.com/Significance.html`.

[81] U. Fano. Ionization Yield of Radiations. II. The Fluctuations of the Number of Ions. *Phys. Rev.*, 72(1):26–29, July 1947.

[82] S.M. Sze. *Semiconductor Devices, Physics and Technology*. John Wiley & Sons, 1985.

[83] E. Belau et al. Charge collection in silicon strip detectors. *Nucl. Instr. Meth.*, A214:253–260, 1983.

[84] S. Heising. *Halbleiterdetektoren für Hochenergie-Experimente bei tiefen Temperaturen und starken Magnetfeldern*. PhD thesis, Universität Karlsruhe (TH), Fakultät für Physik, 1999.

[85] S.M. Sze. *Physics of Semiconductor Devices*. John Wiley & Sons, second edition, 1981.

[86] Z. He. Review of the Shockley-Ramo theorem and its application in semiconductor gamma-ray detectors. *Nucl. Instrum. Meth.*, A463:250–267, 2001.

[87] J.H. Billen and L.M. Young. POISSON/SUPERFISH on PC Compatibles. In *Proceedings of the 1993 Particle Accelerator Conference*, volume 2, page 790, 1993.

[88] N. Demaria et al. New results on silicon microstrip detectors of CMS tracker. *Nucl. Instrum. Meth.*, A447:142–150, 2000.

[89] E. Nygård, P. Aspell, P. Jarron, P. Weilhammer, and K. Yoshioka. CMOS low noise amplifier for microstrip readout; Design and results. *Nucl. Instrum. Meth.*, A301:506–516, 1991.

[90] W. Fallot-Burghardt. *A CMOS Mixed-Signal Readout Chip for the Microstrip Detectors of HERA-B*. PhD thesis, Ruprecht-Karls-Universität Heidelberg, June 1998.

[91] G. Anelli. *Design and characterization of radiation tolerant integrated circuits in deep submicron CMOS technologies for the LHC experiments*. PhD thesis, Institute National Polytechnique de Grenoble, December 2000. `http://rd49.web.cern.ch/RD49/RD49Docs/anelli/these.html`.

[92] C. Da Via et al. Advances in silicon detectors for particle tracking in extreme radiation environments. *Nucl. Instrum. Meth.*, A509:86–91, 2003.

[93] H. Spieler. Introduction to Radiation Detectors and Electronics. `http://www-physics.lbl.gov/~spieler/physics_198_notes_1999`.

[94] D. Baumeister et al. Performance of the Beetle readout chip for LHCb. In *Proceedings of the 7th Workshop on Electronics for LHC Experiments*, 2001.

[95] J. Kaplon et al. Progress in development of the analogue read-out chip for silicon strip detector modules for LHC experiments. In *Proceedings of the 7th Workshop on Electronics for LHC Experiments*, 2001.

[96] D.W. Aitken, W.L. Lakin, and H.R. Zulliger. Energy Loss and Straggling in Silicon by High-Energy Electrons, Positive Pions, and Protons. *Phys. Rev.*, 179(2):393, March 1969.

[97] C. Julliot and M. Cantin. Response of silicon detectors to relativistic pions and electrons. *Nucl. Instrum. Meth.*, 157:235–245, 1978.

[98] H.D. Maccabee, M.R. Raju, and C.A. Tobias. Fluctuations of Energy Loss by Heavy Charged Particles in Thin Absorbers. *Phys. Rev.*, 165(2):469, January 1968.

[99] H.D. Maccabee and M.R. Raju. Fluctuations of energy loss by heavy charged particles in silicon detectors: preliminary measurements. *Nucl. Instrum. Meth.*, 37:176–178, 1965.

[100] N.I. Chernov and G.A. Ososkov. Effective algorithms for circle fitting. *Comp. Phys. Comm.*, 33:329–333, 1984.

[101] R. Kaiser. Conventions for the HERMES RICH Particle Identification. Technical Report HERMES 99-010, DESY-HERMES, 1999.

[102] G. van der Steenhoven. The HERMES experiment. In *Proceedings of the International school of nuclear physics, 26th course, on Lepton Scattering and the Structure of Hadrons and Nuclei, Erice, Italy, 16-24 September 2004*, 2004.

[103] M.G. van Beuzekom et al. Technical design report of the new silicon detector system. Technical report, DESY, 1998. DESY-HERMES-98-14.

[104] D. Heesbeen. *Quasi-real photo-production of hyperons on polarized $^{1,2}H$ targets.* PhD thesis, Rijksuniversiteit Groningen, June 2003.

[105] J.J.M. Steijger. The lambda wheels, a silicon vertex detector for HERMES. *Nucl. Instrum. Meth.*, A453:98–102, 2000.

[106] W. Fallot-Burghardt et al. Helix 128-x User Manual. `http://wwwasic.kip.uni-heidelberg.de/~trunk/projects/Helix`.

[107] J.J.M. Steijger. HADC documentatation. http://www.nikhef.nl/pub/experiments/Hermes/Instrumentation/LambdaWheels/Descriptions_Manuals/hadc.html.

[108] R. Scholte. The NIKHEF beam telescope. Master's thesis, Universiteit Twente, 1998.

[109] R. Horisberger and D. Pitzl. A novel readout chip for silicon strip detectors with analog pipeline and digitally controlled analog signal processing. *Nucl. Instrum. Meth.*, A326:92–99, 1993.

[110] Y. Sugaya et al. Subthreshold antiproton production in pA, dA and αA reactions. *Nucl. Phys.*, A634:115–140, 1998.

[111] I. A. Vorontsov et al. Measurement of Inclusive Cross-sections pi-, pi+, p, H-2, H-3, He-3 at Angle of 3.5-degrees in the Interaction of 10.1-GeV/c Protons with Be, Al, Cu, Ta and Comparison with the Fusion Models. ITEP-85-1983.

[112] P. Egli, D. Galliker, B. Hahn, and E. Hugentobler. Erzeugung energetischer He-Fragmente mit 22 GeV/c Protonen, untersucht in einer Blasenkammer. *Helv. Phys. Act.*, 40:539–558, 1967.

[113] D. S. Gemmell. Channeling and related effects in the motion of charged particles through crystals. *Rev. Mod. Phys.*, 46(1):129–235, January 1974.

[114] A.H. Sørensen. Channeling, Bremsstrahlung and Pair Creation in Single Crystals. *Nucl. Instrum. Meth.*, B119:1–29, 1996.

[115] Virginia Semiconductor Inc. Cutting off-axis wafers. http://www.virginiasemi.com/pdf/cuttingoffaxis80802.pdf.

[116] W. Bauhoff. Tables of Reaction and Total Cross Sections for Proton-Nucleus Scattering Below 1 GeV. *At. Data & Nucl. Data Tables*, 35:429, 1986.

[117] The CLAS12 collaboration. Hall B 12 GeV Upgrade: CLAS12. Technical report, Jefferson Lab., 2005. http://www.jlab.org/Hall-B/clas12/Detector/.

[118] D. Bailey. Studies of Sensors and Vertex Detector Design for the ILC. In *Proceedings of HEP2005 International Europhysics Conference on High Energy Physics, EPS (July 21st-27th 2005) in Lisboa, Portugal*, 2005. to be published, http://www.lip.pt/events/2005/hep2005/talks/hep2005_talk_DavidBailey.ppt.

[119] C. Baltay. Monolithic CMOS Pixel Detectors for ILC Vertex Detectors. In *Proceedings of The 2005 International Linear Collider Workshop (LCWS05), March 18-22, 2005, Stanford, California, USA*, 2005. to be published, http://www.linearcollider.ca/lcws05/h/LCWS05_VTX_Baltay.pdf.

[120] F. Hügging. Front-end electronics and integration of ATLAS pixel modules. *Nucl. Instrum. Meth.*, A549:157–164, 2005.

[121] W. Erdmann. The 0.25 μm front-end for the CMS pixel detector. *Nucl. Instrum. Meth.*, A549:153–156, 2005.

[122] M. Barbero et al. Design and test of the CMS pixel readout chip. *Nucl. Instrum. Meth.*, A517:349–359, 2004.

[123] S. Cihangir and S. Kwan. Characterization of indium and solder bump bonding for pixel detectors. *Nucl. Instrum. Meth.*, A476:670–675, 2002.

[124] F. Ruggiero and F. Zimmermann. Possible scenarios for an LHC upgrade. Prepared for 1st CARE-HHH-APD Workshop on Beam Dynamics in Future Hadron Colliders and Rapidly Cycling High-Intensity Synchrotrons, Geneva, Switzerland, 8-11 Nov 2004.

[125] EG&G ORTEC. Model 934 Quad Constant-Fraction 100-MHz Discriminator, Operating and Service Manual.

[126] Z.Y. Chang and W.M.C. Sansen. *Low-Noise Wide-Band Amplifiers in Bipolar and CMOS Technologies*. Kluwer Academic Publishers, 1991.

Summary

Since roughly 25 years, silicon detectors are commonly used for tracking purposes in high-energy physics experiments. Originally, however, silicon detectors were introduced for the identification of low energy particles. In recent years the original application regained interest in modern high-energy physics experiments. In this thesis it is investigated up to which energy an array of silicon strip (or pixel) detectors can be used to distinguish pions from protons. The use of silicon strip detectors for hadronic particle identification is of particular importance for finding the 'missing link' in studies of the origin of the spin of the proton.

The spin of the nucleon is composed of contributions from the spin and the orbital angular momentum of the quarks and the gluons inside the nucleon. The contribution of the quark spins to the nucleon spin has been determined over the years with great accuracy. More recently also the contribution of the gluon spin to the nucleon has been determined with modest accuracy. It was found that most likely the sum of the quark and gluon spins does not completely account for the nucleon spin of $\frac{1}{2}\hbar$, and hence a non-vanishing contribution from the orbital angular momentum of the quarks and gluons might be expected. To accurately determine the orbital angular momentum of the quarks and gluons, new high-luminosity deep inelastic scattering facilities are needed at a future high-energy lepton accelerator. Currently a new design effort for such an accelerator is ongoing under the name International Linear Collider (ILC), which uses many of the concepts originally developed for the TESLA project at the German institute DESY. The latter project represented the first complete design of such a linear collider and is therefore taken in this thesis as a starting point for all calculations involving the beam of such a facility.

Information on the quark and gluon orbital angular momentum can be obtained by measuring the functions that describe the dynamic correlations between the partons in the nucleon, which are known as the Generalized Parton Distributions (GPD). Measurements of these GPDs can be obtained by studying exclusive processes such as the Deeply Virtual Compton Scattering (DVCS) process. Because the typical forward angle spectrometer used for future deep inelastic scattering experiments at high beam energies lacks the resolution to guarantee exclusivity, a recoil detector in the target area of the experiment is needed. The main task of such a recoil detector is the detection and identification of the recoiling protons from the DVCS process, thus enabling the determination of the exclusivity of the reaction. This recoil detector has to be located close to the polarized target that is used in such experiments. Hence it has to fit in the small volume available inside the target magnet, which is needed to maintain the polarization of the target. The momentum of the recoiling protons from the DVCS process is limited

to about 1.3 GeV·c^{-1} and the polar angle of the recoil protons ranges from 0.2 to 1.3 radians. It thus needs to be investigated whether it is possible to design a recoil detector that meets the kinematic requirements and that can be operated in a magnetic field close to the polarized target and the interaction point.

Many particle identification techniques such as Cherenkov light detection and time-of-flight techniques cannot be used for a recoil detector because of the limited space in the target region or the presence of a high magnetic field. The particle identification technique that is investigated in this thesis is based on measuring the energy deposition, i.e. the dE/dx method. The dE/dx particle identification method makes use of energy deposition information obtained from a stack of silicon detectors. Because multiple layers of silicon sensors are used, statistical techniques can be applied to enhance the particle identification capability of such a silicon telescope. The statistical techniques explored in this thesis are the truncated mean method, the maximum likelihood method and the Kolmogorov-Smirnov test. The advantages and the weaknesses of the various techniques are discussed. The dE/dx technique is used at the limits of its possibilities, and hence a thorough understanding of the physics involved in energy loss processes is very important. The required background information on energy deposition of fast charged particles in silicon and the corresponding energy deposition straggling functions are presented, for that reason.

A future recoil detector of this type will be located in the vicinity of a dense polarized target, and therefore the recoil detector will be exposed to a large number of background events. Most of the background events are electrons from Møller scattering. Many of these low energy Møller electrons are bent away from the recoil detector by the magnetic field in the target area. However, even with this large reduction in the number of background tracks by the magnetic field, the rate of particles traversing the sensitive area of the recoil detector is still so large that microstrip detectors cannot be used. Hence, pixel type detectors must be considered. Various pixel type detectors and readout architectures have been explored. The developments of these detectors are driven by the requirements of the vertex detectors at the LHC machine and at a future linear collider such as the ILC. It turns out that the specifications of readout electronics of pixel detectors developed for the LHC machine better match the requirements of the proposed recoil detector. However, the maximum hit rate that can be handled by the pixel type chips for the current generation of LHC experiments is still a factor four too small. It is very likely, though, that the next generation pixel detectors for the LHC, which are needed if the luminosity of the LHC will be increased by up to a factor 10, will have a readout architecture that can cope with the large number of (background) hits seen by the recoil detector.

In order to find the optimal configuration for the proposed recoil detector Monte Carlo simulations have been performed. The simulations use realistic models to describe experimental effects such as noise of readout electronics, charge sharing in the silicon sensors, and the influence of the magnetic field through the Lorentz angle. Detailed models are presented. Various detector configurations with a different number of detector layers have been explored. It was found that if the total amount of material is kept constant, the benefit of a larger number of layers (i.e. more samples) is largely cancelled out by the reduction in the signal-to-noise ratio of the individual samples due

to the decrease of the thickness of the sensor. On the other hand, if the number of layers is increased while the thickness per sensor is constant, i.e. the total amount of material in the path of the particle increases, the efficiency increases by up to 10%. The influence of the total amount of noise on the PID capabilities has also been studied and it was found that a 50% improvement in signal to noise ratio increases the momentum limit for an 80% identification efficiency by only 3%.

A rough estimate of the particle's momentum is needed to be able to identify particles via a measurement of their energy deposition. The momentum estimate is obtained by determining the curvature of the tracks in the 5 T magnetic field of the polarized target. Monte Carlo simulations have been done to determine the momentum resolution that can be obtained with four silicon detectors placed at equal distances in the bore of the target magnet. A momentum resolution of 25 and 40 MeV·c^{-1} can be achieved for hadrons with a momentum of 0.8 and 1.3 GeV·c^{-1}, respectively. The influence of the momentum determination on the particle identification performance is presented and found to be modest.

Because accurate energy deposition distributions are of decisive importance for particle identification, the results from the Monte Carlo simulations have been verified by conducting an experiment at the Proton Synchrotron facility at CERN. The silicon telescope used in this experimental set-up consisted of eight double sided sensors with a thickness of 300 μm each. The objective of the experiment was to demonstrate that it is possible to separate pions from protons having momenta up to 1.3 GeV·c^{-1} with the highest possible efficiency. Data have been collected with a mixed particle beam, consisting mainly of pions and protons, at momenta of 0.8, 1.0, 1.1, 1.2 and 1.3 GeV·c^{-1}. The energy deposition distributions obtained from these data are compared to the Monte Carlo results and are also compared to the limited amount of data available in literature in this energy regime.

The experimentally determined particle identification efficiency of the four layer silicon telescope is more than 0.8 for pions and protons with momenta up to 1.3 GeV·c^{-1}. The equivalent efficiency for an eight layer telescope is approximately 0.9. As compared to most experiments, proton identification up to 1.3 GeV·c^{-1} with only silicon detectors is a major step forward. Presently one of the most advanced recoil detectors is that of the HERMES experiment. The silicon detector in this recoil project, which is currently being commissioned, is designed to identify protons up to 0.65 GeV·c^{-1}. The capabilities of a four (or eight) layer silicon telescope studied in this thesis fulfill the requirements of a recoil detector at a future deep inelastic scattering facility which aims at studying generalized parton distributions via deeply virtual processes.

Samenvatting

Sinds ongeveer 25 jaar worden siliciumdetectoren veelvuldig toegepast ten behoeve van de reconstructie van sporen in hoge-energie fysica experimenten. Van origine werden siliciumdetectoren echter toegepast voor de identificatie van laag-energetische deeltjes. De originele toepassing heeft sinds enige jaren weer hernieuwde interesse ondervonden van experimenten in de hoge-energie fysica. In dit proefschrift wordt een onderzoek beschreven naar de mogelijkheden om met behulp van een aantal lagen met siliciumdetectoren onderscheid te maken tussen pionen en protonen. Het gebruik van siliciumdetectoren voor hadronische deeltjesidentificatie is met name belangrijk in research dat zich richt op het vinden van de 'ontbrekende schakel' in het onderzoek naar de oorsprong van de spin van het proton.

De spin van een nucleon bestaat uit bijdragen van de spin en het baanimpulsmoment van de quarks en de gluonen in het nucleon. De bijdragen van de quark-spin aan de nucleon spin zijn in de afgelopen decennia met grote nauwkeurigheid bepaald. Recentelijk is ook de bijdrage van de gluon-spin aan het nucleon bepaald, zij het met bescheiden nauwkeurigheid. Het blijkt dat de som van de spins van de quarks en de gluonen niet gelijk is aan de spin van het nucleon, zijnde $\frac{1}{2}\hbar$. Daarom is de verwachting dat er een niet verwaarloosbare bijdrage aan de nucleon spin afkomstig is van het baanimpulsmoment van de quarks en de gluonen. Om het baanimpulsmoment hiervan nauwkeurig te bepalen, zijn er nieuwe diep inelastische verstrooiingsexperimenten nodig met een hoge luminositeit bij een toekomstige hoog-energetische lepton versneller. Op dit moment worden er ontwerpstudies gemaakt voor zo'n versneller die bekend staat onder de naam International Linear Collider (ILC). Dit project is o.a. gebaseerd op vele concepten die ontwikkeld zijn voor het TESLA versneller project bij het Duitse instituut DESY. Dit laatstgenoemde project was het eerste complete ontwerp van zo'n lineaire versneller en daarom wordt dit project als uitgangspunt gebruikt voor zo'n versneller faciliteit.

Informatie over het quark en gluon baanimpulsmoment kan verkregen worden door het meten van de functies die het dynamische gedrag tussen deze partonen[1] in het nucleon beschrijven. De functies staan bekend onder de naam Generalized Parton Distributions (GPD). Gegevens over deze GPDs kunnen verkregen worden uit de bestudering van processen waarbij alle deeltjes uit de reactie worden gemeten, zoals het diep-virtuele Compton verstrooiingsproces. Omdat de gebruikelijke voorwaartse spectrometer in toekomstige diep inelastische verstrooiingsexperimenten onvoldoende resolutie heeft om deze exclusiviteit te garanderen, moet er gebruik gemaakt worden van een 'terugstoot'

[1] Partonen zijn de onderdelen waaruit het nucleon is samengesteld. Hiermee worden zowel de quarks als de gluonen bedoeld.

(recoil) detector in de buurt van de trefplaat van het experiment. De belangrijkste taak van deze recoil-detector is het waarnemen en identificeren van de teruggestoten protonen van het DVCS proces waarmee de exclusiviteit van het proces gewaarborgd wordt. Deze recoil-detector bevindt zich dicht bij de gepolariseerde trefplaat die gebruikt wordt in dit soort experimenten. Daarom moet de detector passen in de beperkte ruimte in de magneet die de trefplaat omhult en die nodig is om de polarisatie van de trefplaat te behouden. De impuls van de teruggestoten protonen afkomstig uit het DVCS proces is maximaal ongeveer 1.3 $\mathrm{GeV{\cdot}c^{-1}}$ en de poolhoek van de protonen heeft een bereik van 0.2 tot 1.3 radialen. De centrale vraag in het in dit proefschrift beschreven onderzoek is of het mogelijk is om een recoil-detector te ontwerpen die voldoet aan de eisen en of die bedreven kan worden in het magnetische veld dicht bij het gepolariseerde target en het interactiepunt.

Vele deeltjesidentificatietechnieken zoals de detectie van Cherenkov licht en vluchttijd technieken zijn niet bruikbaar vanwege ofwel de beperkte ruimte in de trefplaat omgeving danwel de aanwezigheid van het sterke magneetveld. De deeltjesidentificatietechniek die in dit proefschrift onderzocht wordt, is gebaseerd op het meten van de energiedepositie van de deeltjes, oftewel de dE/dx methode. De dE/dx deeltjesidentificatie methode maakt gebruik van de informatie die verkregen wordt van een aantal lagen siliciumdetectoren. Omdat er gebruik gemaakt wordt van meerdere detectorlagen met siliciumsensoren kunnen statistische methoden toegepast worden die het identificerend vermogen van zo'n silicium telescoop verbeteren. De statistische methoden die in dit proefschrift nader bekeken worden, zijn de getrimde gemiddelde waarde methode, de maximum-waarschijnlijkheidsmethode en de Kolmogorov-Smirnov test. De voor- en nadelen van de diverse methodes worden besproken. De dE/dx methode wordt gebruikt op de grens van het maximum haalbare en daarom is een goed begrip van de fysische processen die een rol spelen bij het energieverlies van cruciaal belang. De benodigde achtergrondinformatie over de energie die snelle geladen deeltjes in silicium achterlaten en de bijbehorende verdelingen worden om die reden beschreven.

Een toekomstige recoil-detector zal gebruikt worden in de nabijheid van een gepolariseerde trefplaat met een hoge dichtheid. Daarom zal een recoil-detector blootstaan aan een hoge achtergrondstraling. De meeste van deze achtergrond gebeurtenissen zijn electronen van het Møller verstrooiingsproces. Vele van deze laag-energetische Møller electronen worden door het magnetisch veld in het trefplaat gebied weggebogen van de recoil-detector. Zelfs met deze grote reductie van het aantal achtergrond gebeurtenissen is het aantal deeltjes dat de recoil-detector treft nog zo groot dat het vrijwel onmogelijk is om micro-strip detectoren te gebruiken. Het gebruik van pixel detectoren moet daarom worden overwogen. Diverse typen pixel detectoren en bijbehorende uitleesarchitecturen zijn nader beschouwd. De ontwikkelingen aan dit type detectoren worden gedreven door de eisen van de vertex detectoren bij de LHC versneller en bij een toekomstige lineaire versneller zoals de ILC. Het blijkt dat de specificaties van de vertex detectoren die ontwikkeld zijn voor de LHC versneller beter passen bij de eisen die gesteld worden aan een recoil-detector. De maximale snelheid waarmee gebeurtenissen geregistreerd kunnen worden door pixel chips voor de huidige generatie LHC experimenten is echter nog steeds een factor vier te laag. Het is gelukkig zeer waarschijnlijk dat de volgende generatie pixel detectoren voor de LHC, welke nodig zijn als de luminositeit

van de LHC versneller omhoog gaat met maximaal een factor 10, een uitleesarchitectuur hebben die overweg kan met het grote aantal (achtergrond) gebeurtenissen waaraan de recoil-detector blootgesteld is.

Om de optimale configuratie te vinden voor de voorgestelde recoil-detector, zijn er Monte Carlo simulaties gedaan. Deze simulaties maken gebruik van realistische modellen voor de beschrijving van experimentele effecten zoals ruis van de uitleeselektronica, ladingsverdeling in de siliciumsensoren en de invloed van het magneetveld via de Lorentz hoek. De modellen worden in detail behandeld. Verschillende detectorconfiguraties zijn onderzocht waarbij het aantal detectorlagen gevarieerd is. Het blijkt dat, als de totale dikte van de sensoren constant gehouden wordt, het voordeel van een groot aantal lagen (en dus een groot aantal dE/dx monsters) grotendeels teniet gedaan wordt door de afname in de signaal-ruis verhouding van de individuele monsters tengevolge van de reductie in de dikte van de sensoren. Als echter het aantal lagen groter gekozen wordt bij een constante laagdikte, dan neemt de efficiëntie bij een gekozen impuls toe met maximaal 10%. De invloed van de totale hoeveelheid ruis op de deeltjesidentificatie is ook onderzocht. Een wijziging in de signaal-ruis verhouding van 50% geeft slechts een 3% verandering in de maximale impuls waarbij protonen geidentificeerd worden met een efficiëntie van 80%.

Om deeltjes te kunnen identificeren via het meten van de energie-depositie is een grove indicatie van het impuls van het deeltje nodig. Een goede schatting van de impuls kan verkregen worden door het bepalen van de buigstraal van de deeltjessporen in het 5 T magneetveld van de gepolariseerde trefplaat. Met behulp van Monte Carlo simulaties is bepaald wat de impuls-resolutie is die verkregen kan worden met vier equidistante siliciumdetectoren in het magneetveld van de trefplaat. Een impuls-resolutie van 25 en 40 MeV$\cdot$c^{-1} is haalbaar voor hadronen met een impuls van respectievelijk 0.8 en 1.3 GeV$\cdot$c^{-1}. De invloed van de gevonden impuls-resolutie op de deeltjesidentificatie is zeer beperkt.

Omdat nauwkeurige energie-depositie verdelingen van beslissend belang zijn voor dE/dx deeltjesidentificatie, zijn de resultaten van de Monte Carlo simulaties geverifieerd door middel van een experiment bij de Proton Synchrotron faciliteit op CERN. De bij dit experiment gebruikte silicium telescoop bestond uit acht dubbelzijdige siliciumdetectoren met een dikte van elk 300 μm. De doelstelling van het experiment was het aantonen dat het scheiden van pionen en protonen mogelijk is met een zo hoog mogelijke efficiëntie, waarbij een efficiëntie van 0.8 als minimum gesteld is voor zinvolle identificatie. Er is tijdens het experiment data verzameld van een gemengde deeltjesbundel, voornamelijk bestaande uit pionen en protonen, met een impuls van 0.8, 1.0, 1.1, 1.2 en 1.3 GeV$\cdot$c^{-1}. De energie-depositie verdelingen die verkregen zijn uit de gegevens zijn vergeleken met de resultaten van de Monte Carlo simulaties en zijn tevens vergeleken met de beperkte hoeveelheid gepubliceerde metingen in dit energiegebied.

De experimenteel bepaalde deeltjesidentificatie-efficiëntie van een vierlaags silicium telescoop is groter dan 0.8 voor pionen en protonen met een impuls van ten hoogste 1.3 GeV$\cdot$c^{-1}. Voor een achtlaags telescoop is de overeenkomstige efficiëntie ongeveer 0.9. In vergelijking met soortgelijke experimenten is de gevonden proton identificatie tot een impuls van 1.3 GeV$\cdot$c^{-1} een forse stap voorwaarts. Een van de meest geavanceerde recoil-detectoren van dit moment is die van het HERMES experiment. De siliciumdetector in dit

project, welke zich op dit moment in de opstartfase bevindt, heeft een detectiegrens voor protonen van 0.65 GeV·c^{-1}. De kwalificaties van een vier- of achtlaags silicium telescoop zoals deze bestudeerd is in dit proefschrift voldoen aan de eisen die gesteld worden aan een recoil-detector bij een toekomstig diep inelastisch verstrooiingsexperiment dat zich richt op het onderzoek naar generieke parton verdelingen via diep-virtuele processen.

Acknowledgements

Coming to the end of this project, only one task remains, which is writing the most popular pages of the book. Being an employee of the NIKHEF electronics department, obtaining a PhD in parallel to a daily job is not a paved road (if there even exists such a thing for getting a PhD). Taking a different route certainly has some advantages but on the other hand it also introduces some obstacles. I sometimes found it very difficult to divide my attention between my daily work and my thesis work. Certainly towards the end of this six year project, the challenging work for LHC was so much more attractive than yet another round of reading and modifying the text of my thesis. But let's stop talking about myself and get to what this section is all about.

It is probably needless to say that doing research and writing a thesis is not something you do on your own. Therefore I would like to thank all the people that have contributed in one way or another to this work. There are, however, a few people that should be mentioned especially. Let me start by thanking Eric Heine, Teus van Egdom and the NIKHEF directorate for creating the opportunity to write this thesis in coexistence with my normal job.

The two people that guided me from the beginning to the end, and who encouraged me throughout the years are Jos Steijger and Gerard van der Steenhoven. It is really nice to see that two quite different personalities complement each other in so many different ways. Jos, you were always there to discuss any detail at any time and learned me to be critical even about obvious things, while at the same time you never overlooked the bigger picture and always tried to prevent this work from growing indefinitely. I am amazed by the number and variety of subjects you master. For me you are the textbook example of a critical scientist.

Gerard, I really started to know you better when the actual writing of the thesis started. You always came up with ideas and suggestions to improve the contents and quality of this thesis. I envy your organizational and communicative talents. If I would only have a few tens of percents of it...

A significant part of my time was spent preparing and analyzing the data from the experiment that was conducted at the CERN PS beam. I would like to thank Michael Hauschield and the rest of the SPS/PS team for letting me use the T11 experimental area. I am indebted to 'my testbeam team', Eddy Jans, Michiel Demey, Niels van Bakel and Jos. You guys really helped to make it all possible! Special memories I have on the long, hot and sometimes stressful days in the T11 area at CERN with all of you. Eddy, I really appreciate it that I could always discuss the 'side-effects' of my PhD with someone who is on the same wavelength. I would also like to thank Rob Buis for constructing the various mechanical components needed for the testbeam. During the summer of 2003,

Helena Nowak who worked as a summer student, helped me to analyse the time of flight data from the testbeam. Helena, thank you for your help!

A special bond I have with my fellow PhD students with whom I worked closely on various projects. Jan Visser, Erika Garutti, David Heesbeen, Jaap Velthuis, Niels van Bakel, Sander Klous, Hella Snoek and Michiel Demey, you are pleasant company to hang out with!

I am grateful to the members of my reading comity, Erik Heijne, Herbert Löhner and Hans Wilschut for carefully reading the manuscript and for all the useful suggestions which led to further improvements of this thesis.

Furthermore I would like to thank all the people that I work with in the electronics department and the LHCb group for their patience in working together with me because they were confronted with my sometimes[1] chaotic organization. I especially want to thank Peter Jansweijer, Sander Mos, Wilco Vink and Leo Wiggers because they suffered most.

In general I would like to thank both my mothers, brothers, sisters, other family, friends and colleagues that always kindly asked about my progress on the many occasions. Although I might not always have reacted enthusiastically on the zillions of questions, I surely appreciated your interest and encouragements.

The last words are, of course, for Patricia. Dear Patricia, without you this thesis would not have existed (and don't you dare to deny it). You gave me the opportunity to let me work on it for many, many evenings and weekends while you were doing everything else to keep our life rolling. You never ever complained about the lack of attention (I assume). I really am a lucky guy 'having' you. Thank you very much.

[1] optimist's view!